

Modeling of bending-torsion couplings in active-bending structures. Application to the design of elastic gridshell.



Thèse n.xxxxx
présenté le 01 décembre 2017
à l'Ecole des Ponts ParisTech
laboratoire Navier
Université Paris-Est
pour l'obtention du grade de Docteur ès Sciences
par

Lionel du Peloux

acceptée sur proposition du jury:

Prof Name Surname, président du jury
Prof Name Surname, directeur de thèse
Prof Name Surname, rapporteur
Prof Name Surname, rapporteur
Prof Name Surname, rapporteur

Paris, Ecole des Ponts ParisTech, 2016

“Quia nominor leo.”

A Jacques & Christiane, mes grands-parents bien-aimés.

Acknowledgements

To be provided

Paris, France, 30 septembre 2017

L. du Peloux

Abstract

Summary to be provided

Key words : elastic gridshell, torsion, bending active, composite material

The last decades have seen the emergence of non-standard architectural shapes. Designers find often themselves helpless with the geometrical complexity of these objects. Furthermore, the available tools dissociate shape and structural behaviour, which adds another complication. This dissertation takes the point of view based on invariance under geometrical transformations, and studies several strategies for fabrication-aware shape modelling. Three technological constraints have been identified and correspond to three independent contributions of this thesis. The repetition of nodes is studied via transformations by parallelism. They are used to generalise surfaces of revolution. A special parametrisation of moulding surfaces is found with this method. The resulting structure has a high node congruence. Cyclidic nets are then used to model shapes parametrised by their lines of curvature. This guarantees meshing by planar panels and torsion-free beam layout. The contribution of this dissertation is the implementation of several improvements, like doubly-curved creases, a hole-filling strategy that allows the extension of cyclidic nets to complex topologies, and the generation of a generalisation of canal surfaces from two rail curves and one profile curves. Finally, an innovative method inspired by descriptive geometry is proposed to generate doubly-curved shapes covered with planar facets. The method, called marionette technique, reduces the problem to a linear problem, which can be solved in real-time. A comparative study shows that this technique can be used to parametrise shape optimisation of shell structures without loss of performance compared to usual modelling technique. The handling of fabrication constraints in shape optimisation opens new possibilities for its practical application, like gridshells or plated shell structures. The relevance of those solutions is demonstrated through multiple case-studies. Keywords : structural morphology, generative tool, design process, descriptive geometry, structural optimisation, gridshell, marionette mesh, thin shell. 5

Table of Content

Acknowledgements	v
Abstract (English/Français)	vii
Table of Content	ix
List of Figures	xvii
List of Tables	xxi
Index of notation	xxiii
1 Introduction	1
I Elastic gridshells	3
2 Elastic gridshells	5
2.1 Building free-forms	6
2.1.1 Non-standard forms	6
2.1.2 Importance of free-forms in modern architecture	6
2.1.3 Canonical approaches to build free-forms	6
2.1.4 Main challenges	6
2.2 Elastic gridshell	6
2.2.1 Structural Typology	6
2.2.2 Material Flexibility for Structural Rigidity	6
2.2.3 Erection Process	7
2.2.4 The benefits of composite materials	7
2.3 Built elastic gridshells : a review	8
2.3.1 The beginnings : from the first prototype to the German Pavilion	8
2.3.2 Mannheim Multihalle : the completion of a decade of research	12
2.3.3 The dry period : 25 years from Mannheim to Hannover	13
2.3.4 The signs of a renewal : Dorset and Doncaster	14
2.3.5 The renewal : Hannover, Downland and Savill	15

Table of Content

2.3.6	Gridshell in composite materials : a new perspective	21
2.3.7	Flourishing timber gridshell pavilions	23
2.3.8	Latest experiments	26
2.4	Research works in the field of elastic gridshells : a review	28
2.4.1	Mechanics	28
2.4.2	Geometry	29
2.4.3	Material	30
2.4.4	Technology	31
2.5	Conclusion	32
2.6	References	33
3	Ephemeral cathedral : the first GFRP gridshell building	39
3.1	Introduction	39
3.1.1	Overview	40
3.1.2	Contributions	40
3.1.3	Related work	40
3.2	Project overview	40
3.2.1	Context and challenges	40
3.2.2	Architectural considerations on the form	42
3.2.3	Placing of the building on the site	42
3.2.4	Entrance	43
3.2.5	Daylight	43
3.2.6	Technical description	43
3.3	Construction process	48
3.3.1	Assembly of the grid	48
3.3.2	Deformation of the grid	48
3.3.3	Bracing of the grid	48
3.3.4	Covering of the gridshell	50
3.4	Structural design	50
3.4.1	Overall design process	50
3.4.2	3D modelling of the intended shape	51
3.4.3	Meshing the surface	52
3.4.4	Formfinding and bending prestress	53
3.4.5	As-built geometry	57
3.4.6	Structural analysis	57
3.5	Designing with GFRP materials	59
3.5.1	Properties of the tubes	59
3.5.2	Codes for composite materials	59
3.5.3	Flexural strength of the tubes	61
3.5.4	Partial safety factors	61
3.6	Construction details	63
3.6.1	The swivel coupler	63
3.6.2	The sleeve system	69
3.6.3	Foundations	74
3.6.4	The membrane	74

3.7	Hygrothermal behavior	76
3.7.1	Temperature	76
3.7.2	Moisture	77
3.8	Cost analysis	80
3.8.1	Overall cost for the client	80
3.8.2	Cost details for the building	80
3.8.3	Strengths and weaknesses	81
3.9	Conclusions	90
3.10	Acknowledgements	90
3.11	References	91
II	Rich Kirchhoff beam model	93
4	Geometry of smooth and discrete space curves	95
4.1	Introduction	95
4.1.1	Overview	95
4.1.2	Contributions	96
4.1.3	Related work	97
4.2	Parametric curves	98
4.2.1	Definition	98
4.2.2	Regularity	98
4.2.3	Reparametrization	99
4.2.4	Natural parametrization	99
4.2.5	Curve length	99
4.2.6	Arc length parametrization	99
4.3	Frenet trihedron	100
4.3.1	Tangent vector	100
4.3.2	Normal vector	101
4.3.3	Binormal vector	102
4.3.4	Osculating plane	103
4.4	Curves of double curvature	103
4.4.1	First invariant : the curvature	104
4.4.2	Second invariant : the torsion	106
4.4.3	Fundamental theorem of space curves	106
4.4.4	Serret-Frenet formulas	107
4.5	Curve framing	108
4.5.1	Moving frame	109
4.5.2	Adapted moving frame	111
4.5.3	Rotation-minimizing frame	112
4.5.4	Parallel transport	112
4.5.5	Frenet frame	113
4.5.6	Bishop frame	115
4.5.7	Comparison between Frenet and Bishop frames	117
4.6	Discrete curves	119

Table of Content

4.6.1	Definition	119
4.6.2	Regularity	120
4.6.3	Parametrization	121
4.7	Discrete curvature	122
4.7.1	Definition from osculating circles	122
4.7.2	Benchmarking : sensitivity to non uniform discretization	125
4.7.3	Benchmarking : accuracy in bending energy representation	127
4.8	Discrete tangent vector	130
4.8.1	Circumscribed case	131
4.8.2	Inscribed case	133
4.9	Discrete parallel transport	137
4.9.1	The rotation method	137
4.9.2	The double reflexion method	137
4.10	Conclusion	139
4.11	References	140
5	Elastic rod : variational approach	143
5.1	Introduction	143
5.1.1	Overview	144
5.1.2	Contributions	144
5.1.3	Related work	144
5.2	Kirchhoff rod	145
5.2.1	Description of the motion	146
5.2.2	Inextensibility assumption	146
5.2.3	Euler-Bernouilli assumption	147
5.2.4	Motion of the material frame	147
5.2.5	Material curvatures and twist	148
5.2.6	Material constitutive equations	149
5.2.7	Elastic energy	149
5.3	Curve-angle representation	150
5.3.1	Definition of the representation	150
5.3.2	Measurement of the material twist	152
5.3.3	Vector of material curvatures	152
5.4	Definition of the variational problem	152
5.4.1	Calculus of variations	152
5.4.2	Prerequisite for the computation of energy gradients	153
5.4.3	Coupling between bending and torsion	154
5.4.4	Quasistatic assumption	154
5.5	Energy gradient with respect to θ : twisting moment	154
5.5.1	Derivative of material directors with respect to θ	155
5.5.2	Derivative of the material curvatures vector with respect to θ	155
5.5.3	Computation of the twisting moment	156
5.6	Energy gradient with respect to x : internal forces	157
5.6.1	Derivative of material directors with respect to x	157
5.6.2	Derivative of the vector of material curvatures with respect to x	164

5.6.3	Computation of the forces acting on the centerline	164
5.7	Shear force acting on the rod	167
5.8	Discussion	168
5.9	Conclusion	168
5.10	References	170
6	Elastic rod : equilibrium approach	173
6.1	Introduction	173
6.1.1	Overview	174
6.1.2	Contributions	174
6.1.3	Related work	174
6.2	Introduction to the special Cosserat theory of rods	176
6.2.1	Description of the motion	176
6.2.2	Time evolution	181
6.2.3	Force and moment strains	181
6.2.4	Parametrization of the centerline	182
6.2.5	To go further	183
6.3	Kirchhoff theory of rods	185
6.3.1	Description of the motion	186
6.3.2	Reparametrization	188
6.3.3	Force and moment strains	189
6.3.4	Balance of momentum	190
6.3.5	Equations of motion	196
6.3.6	Hookean elasticity	196
6.3.7	Deformation of cross-sections	197
6.3.8	Strain tensor	199
6.3.9	Stress tensor	199
6.3.10	Constitutive equations for internal forces and moments	199
6.3.11	Discussion	201
6.4	Summary of Kirchhoff theory	202
6.5	Geometric interpretation of Kirchhoff's equations	204
6.6	Conclusion	212
6.7	References	213
7	Numerical Model	217
7.1	Introduction	217
7.1.1	Overview	217
7.1.2	Contributions	218
7.1.3	Related works	219
7.2	Discret beam element	220
7.2.1	Description of the element	221
7.2.2	Modeling of discontinuities	224
7.2.3	Matrix notation	225
7.2.4	Discret extension and axial force	225
7.2.5	Discret curvature and bending moment	226

Table of Content

7.2.6	Discret rate of twist and twisting moment	229
7.2.7	Discret shear force	230
7.2.8	Interpolation of the internal forces and moments	231
7.3	Dynamic Relaxation	233
7.3.1	Overview of the procedure	234
7.3.2	Resultants acting on a particle	234
7.3.3	Equations of motion	235
7.3.4	Explicite time integration	236
7.3.5	Damping	239
7.3.6	Convergence	242
7.3.7	Stability and critical damping	243
7.3.8	Application to the simple plane pendulum	245
7.4	Enriching the model	247
7.4.1	Support	247
7.4.2	Connexion	247
7.5	Software	250
7.5.1	Architecture of the software	250
7.5.2	Key aspects	251
7.5.3	Performance	252
7.5.4	Further guidelines	254
7.6	Test case	256
7.7	Conclusion	257
7.8	References	258
8	Conclusion	261
III	Appendix	263
A	Review of built elastic gridshells	265
A.1	References	268
B	Calculus of variations	269
B.1	Introduction	269
B.2	Spaces	269
B.2.1	Normed space	269
B.2.2	Inner product space	269
B.2.3	Euclidean space	270
B.2.4	Banach space	270
B.2.5	Hilbert space	270
B.3	Derivative	271
B.3.1	Fréchet derivative	271
B.3.2	Gâteaux derivative	272
B.3.3	Useful properties	273
B.3.4	Partial derivative	273
B.4	Gradient vector	274

Table of Content

B.5 Jacobian matrix	274
B.6 Hessian	275
B.7 Functional	275
B.8 References	276
C Parabolic interpolation	277
C.1 Introduction	277
C.2 Lagrange interpolating polynomial	277
C.3 Reparametrization	278
C.4 Characteristic values	278
C.5 Extremum value	279
Bibliography	281

List of Figures

2.1	Known elastic gridshells built by the past.	9
2.2	Steel gridshell built in 1962 in Berkeley, USA	10
2.3	Timber gridshell built in 1962 in Essen, Germany	11
2.4	Timber gridshell built in 1967 in Montreal, Canada	11
2.5	Timber gridshell built in 1962 in Essen, Germany	13
2.6	Roundwood gridshell built in 1995 in Dorset, England	15
2.7	Timber gridshells built in 1998 in Doncaster, England	15
2.8	Carboard gridshell built in 2000 in Hannover, Germany	16
2.9	Timber gridshell built in 2003 in Downland, England	17
2.10	Timber gridshell built in 2002 in Pishwanton, England	18
2.11	Timber gridshell built in 2003 in Filmwell, England	19
2.12	Timber gridshell built in 2006 in Savill, England	20
2.13	Timber gridshell built in 2007 in Kent, England	21
2.14	GFRP gridshell built in 2007 in Noisy-Champs, France	22
2.15	GFRP gridshell built in 2011 in Paris, France	23
2.16	GFRP gridshell built in 2013 in Cr��teil, France	23
2.17	Timber gridshells built by gridshell.it in Italy	24
2.18	Timber gridshell built in 2013 in San Antonio, USA	25
2.19	Timber gridshell built in 2016 in Montpellier, France	26
2.20	Recent experiments built in 2016 in Champs-sur-Marne, France	26
3.1	Situation map	41
3.2	Architectural sketch	41
3.3	Exterior view	44
3.4	Interior view	44
3.5	Entrance	45
3.6	Key elements of the structural system	45
3.7	Transversal section of the building	47
3.8	Top view of the building	47
3.9	Construction process of the gridshell.	49
3.10	Benchmarking shapes regarding their curvature	51
3.11	How the compass method works	52

List of Figures

3.12 The compass method step by step	54
3.13 Each set of directrices leads to a different grid.	55
3.14 Meshing software as a plugin for <i>Grasshopper</i>	56
3.15 Permanent bending stresses in the structure under self-weight	58
3.16 Reconstruction of the full 3D geometry	58
3.17 Flexural test of the GFRP tubes	62
3.18 Technical drawing of the swivel coupler	64
3.19 Influence of the interface layer on the sliding resistance	66
3.20 Influence of the tightening on the sliding resistance	67
3.21 Influence of the temperature on the sliding resistance	68
3.22 Technical drawing of the sleeve system.	69
3.23 Design and behavior of the the sleeve system	71
3.24 Typical failure modes when testing the sleeve system in traction	71
3.25 Tensile test of the pinned connection	72
3.26 Typical failure modes of a bolt in a pultruded element	73
3.27 Technical drawing of the footing.	75
3.28 Weather data at site location during opening hours	78
3.29 Temperature inside the building during opening hours	79
3.30 Cost allocation for the whole project	83
3.31 Cost allocation per square meter of covered area	83
3.32 Allocation of the man-hours spent by the volunteers	84
3.33 Cost allocation for masonry works	86
3.34 Cost allocation for the superstructure	88
 4.1 Definition of the tangent vector and the osculating circle of a curve	101
4.2 Osculating circles for a spiral curve at different parameters	104
4.3 Discontinuity of the Frenet trihedron at an inflexion point	108
4.4 Geometric interpretation of the angular velocity vector of a moving frame	110
4.5 Adapted moving frame on a circular helix	111
4.6 Angular velocities of Frenet and Bishop frames for a circular helix	118
4.7 Discrete curve representation and parametrization	120
4.9 Comparison of circumscribed and inscribed osculating circles	126
4.10 Sensitivity of discrete curvatures to non uniform discretization	126
4.11 Discretization of a semicircle and evaluation of its bending energy	128
4.12 Relative error in the estimation of the bending energy of a semicircle	128
4.13 Discretization of an elastica curve and evaluation of its bending energy	129
4.14 Relative error in the estimation of the bending energy of an elastica	129
4.15 Definition of the tangent vector associated to the circumscribed curvature	132
4.16 Definition of the tangent vector associated to the inscribed curvature	134
4.17 Two methods to parallel transport a vector	138
 5.1 Curve-angle representation of the rod	151
5.2 Succession of the degrees of freedom	153
5.3 Variation of the Bishop frame for a perturbation of the centerline	159
5.4 Measuring the variation of parallel transport : rotation of angle α_ϵ	160
5.5 Measuring the variation of parallel transport : rotation of angle Ψ_ϵ	160

6.1	Description of the motion for a Cosserat rod : longitudinal section	178
6.2	Description of the motion for a Cosserat rod: transverse section	179
6.3	Equilibrium of an infinitesimal slice of rod.	191
6.4	Typical deformation modes of cross-sections in Kirchhoff's theory	198
6.5	Geometric interpretation of Kirchhoff's equations	205
6.6	Interpretation : influence of the curvature (κ)	206
6.7	Interpretation : influence of the first material curvature (κ_1)	208
6.8	Interpretation : influence of the second material curvature (κ_2)	210
7.1	Biarc model for a discrete beam element	222
7.2	Parabolic interpolation of the kinetic energy peak	240

List of Tables

3.1	Key numbers	46
3.2	Technical properties of the tube.	60
3.3	Technical properties of the membrane.	60
3.4	Flexural tests of the GFRP tubes	61
3.5	Short-term and long-term values for material resistance	63
3.6	Man-hours spent by the volunteers on the fabrication	85
3.7	Cost details for masonry works	87
3.8	Cost details for the superstructure	89
4.1	Review of several discrete curvature definitions	123
6.1	Summary of the notations	184
7.1	Simple cost model for arithmetic operations	251
A.1	Project review - general informations.	266
A.2	Project review - key numbers	267

Index of notation

Geometry of curves

- t The unit tangent vector.
 n The unit normal vector.
 b The unit binormal vector.
 τ_f The torsion of Frenet.
 κb The curvature binormal vector.
 Ω The darboux vector.

Mechanics of rods

- $\gamma, \bar{\gamma}$ Centerline curve – reference configuration.
 γ The centerline curve – actual configuration.
 s The arc length of the centerline – reference configuration.
 s_t The arc length of the centerline – actual configuration.
 \bar{x} The centerline position vector – reference configuration.
 x The centerline position vector – actual configuration.
 $\bar{\nu}$ The force strain vector – reference configuration.
 ν The force strain vector – actual configuration.
 $\bar{\varkappa}$ The material curvature (or moment strain) vector – reference configuration.
 \varkappa The material curvature (or moment strain) vector – actual configuration.
 \mathcal{E}_s The streching energy.
 \mathcal{E}_b The bending energy.

List of Tables

\mathcal{E}_t The twisting energy.

voir Timoshenko 1951 pour exemple.

1 Introduction

Introduction

Elastic gridshells Part I

2 Elastic gridshells

This chapter presents a critical literature review on different disciplines that deal with the rationalisation of free-form architecture. The review includes both structural and geometrical considerations and identifies potential areas of development that are studied in the next chapters of this dissertation.

At present, the architectural significance of grid shells can hardly be fully envisioned. Too little experience has been gained as yet. However, the first signs of a grid shell architecture are already apparent. The projects planned and executed to date and the results of this research work indicate possibilities that open up a wide field of applications for grid shells. Two things stand out above all. The first is the nearly unlimited variety of forms that can be realized with grid shells, the second is the fact that there is no closed shell surface, but rather a simple, spatially curved grid composed of rods. Both features are of fundamental significance. They fully characterize the architectural essence of the grid shell support structure. [1, p. 250]

2.1 Building free-forms

2.1.1 Non-standard forms

2.1.2 Importance of free-forms in modern architecture

2.1.3 Canonical approaches to build free-forms

2.1.4 Main challenges

2.2 Elastic gridshell

The invention of the gridshell concept is commonly attributed to Frei Otto, a German architect who devoted several years to gridshells. In 1975 he achieved the famous *Mannheim Multihalle* [2], a wooden shell of 7500 m², in collaboration with the engineer Edmund Happold (Arup). Literally, the word “gridshell” refers to grids behaving like shells : from a mechanical point of view that means stresses acting on the structure are mainly transmitted through compression and traction. These structures can cross large-span with very little material.

However, according to the historic evolution of the concept, characterizing a gridshell as the combination of a structural concept – a grid behaving like a shell – and a specific construction process – using the bending flexibility of the material – seems to be more accurate. The Mannheim project (in which a wooden regular and planar grid, lacking shear stiffness, is elastically deformed up to a targeted shape with the help of stays, and then braced and covered) is regarded as the starting point of this new concept.

The Mannheim project is regarded as the starting point of this new concept for which a wooden regular and planar grid, lacking shear stiffness, is elastically deformed up to a targeted shape with the help of stays, and then braced and covered. This type of gridshell, known as elastic gridshell, offers a very elegant manner to materialize freeform shapes from an initially flat and regular grid, which obviously has many practical benefits: planar geometry, standard connection nodes, standard profiles and so on.

2.2.1 Structural Typology

Their mechanical behaviour is very similar to the one of real shells even if the material is discrete and located in a grid more or less open. Moreover, gridshells benefit from the same advantages as the ones showed by an eggshell : they can cross large span using a low amount of material. Their stiffness is mainly linked to their double-curved shape.

2.2.2 Material Flexibility for Structural Rigidity

In this field of application, composite materials like glass fibre reinforced polymer (GFRP) could favourably replace wood, where both resistance and bending ability of the material

is sought [3]. The stiffness of the structure does not derive from the intrinsic material rigidity but principally from its geometric curvature. Ideally, the composite profiles are produced by pultrusion, an economic continuous moulded process. The standardization of the process guarantees very stable material and mechanical properties. It frees designers from the painful problematic of wood joining and wood durability. The characterization of this material is presented further in the paper.

2.2.3 Erection Process

Usually, the grid morphology is not trivial and leads to design numerous costly and complex joints. To overcome this issue, an original and innovative erection process was developed that takes advantage of the flexibility inherent to slender elements. A regular planar grid made of long continuous linear members is built on the ground (??a). The elements are pinned together so the grid has no in-plane shear stiffness and can accommodate large-scale deformations during erection. Then, the grid is bent elastically to its final shape (??). Finally, the grid is frozen in the desired shape with a third layer of bracing members (??b) and the structure becomes a shell.

“From the inverted form to the gridshell” [1, p. 179]

2.2.4 The benefits of composite materials

The benefits of GFRP gridshells have been covered previously. We just recall the main aspects.

The gridshells built in composite material, being at the heart of this paper, are consistent with the framework defined previously, that is to say :

Glass fiber reinforced polymer (GFRP) tubes are at the heart of the presented technology. They can favorably replace wood where both resistance and bending ability of the material is sought [**Douthe2010**].

The tubes are made by pultrusion, “a continuous molding process whereby reinforcing fibers are saturated with a liquid polymer resin and then carefully formed and pulled through a heated die to form a part. Pultrusion results in straight constant cross section parts of virtually any shippable length”.¹ This process is very economic and its standardization guarantees very stable material and mechanical properties. It frees designers from the problem of joining wood pieces with finger joints to obtain long and continuous members and of wood durability.

¹Video explaining the pultrusion process : https://www.youtube.com/watch?v=4MoHNZB5b_Y

2.3 Built elastic gridshells : a review

No thorough historic review is available about executed projects of elastic gridshells although some partial reviews have been done time to time on the occasion of scientific works or construction projects. This review aims at filling this gap by giving an overview of the development of the concept from the very beginning to the very last experiments. Only known built projects have been identified and reported here. The only condition for a project to belong to this review is to comply with the definition of what an elastic gridshell is (see ??), independently to any other consideration (material, fabrication, size, cladding, ...).

The informations collected during this research work are given in table format in appendix (see ??). A synthetic presentation of these datas is proposed to the reader in fig. 2.1, where projects are ordered by date, span, covered area and material.

The books edited by the *Institut für leichte Flächentragwerke* are of great interest to understand the beginnings. *IL10 Grid Shells* [1] has a precise inventory of the first experiments from 1962 to 1976, while *IL13 Multihalle Mannheim* [4] focuses on the construction of the Multihalle in Mannheim. *Timber Gridshells: Architecture, structure and craft* [5] is a significant effort but focuses exclusively on medium to large scale projects in timber. A small but general partial review is also available in [6]. An interesting review is also given by Quinn and Gengnagel [7] as part of his research work on new erection methods. A review of bracing and cladding systems is done in [8]. A review of formfinding methods is done in [9]. Finally, various valuable reviews are available in the thesis by Douthé [10], Bouhana [11], Tayeb [12], and Lafuente Hernández [13].

2.3.1 The beginnings : from the first prototype to the German Pavilion

Frei Otto started his studies in architecture in 1947 in Berlin, Germany, and completed his doctorate on tensile structures in 1953. This first work was published and translated later in the 60's. He then began to work in the field of lightweight structures using physical models such as soap films or hanging nets, and photographic measurements.^{2,3} These tools were essentials for his exploration of forms and structures as there were no computers at that time.

²In the 19th and 20th centuries model testing was at the heart of structural innovation [14]. Analog models were employed successfully by well-known architects and engineers to go beyond the limits of existing knowledge (A. Gaudi, H. Isler, F. Candela, F. Otto, ...) and are still employed today where numeric models failed to represent accurately some physical phenomenons (for instance in wind analysis for high rise towers and bridges).

³"Photography is the medium through which the form and content of a model are communicated. It is one of our most important tools in that it provides the basis for documentation and information, supplements our creative potential [...] " [1, p. 56]

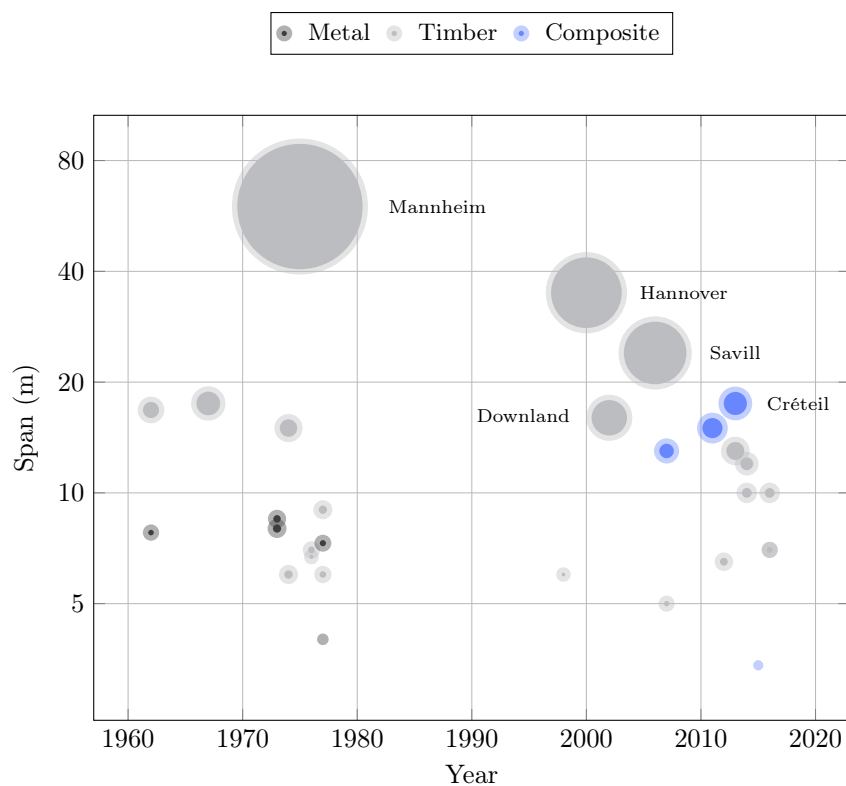
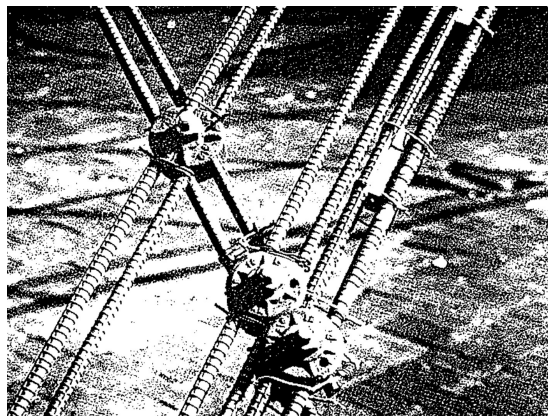


Figure 2.1 – Known elastic gridshells built by the past. The surface of the bubbles is proportional to the covered area. Color indicates the material employed for the rods.



(a) Knot detail



(b) Steel lattice

Figure 2.2 – Steel gridshell built in 1962 in Berkeley, USA.

Steel Gridshell, Berkeley, USA, 1962

Simultaneously, he became interested by the study of lightweight shells and the way they were form-found. One of his very first elastic gridshell was built in 1962 with students at Berkeley, USA [1, p. 270]. It is funny to remark that this first gridshell was not a timber gridshell but a steel gridshell made out of twin steel rods linked in a grid fashion by bolts with clamping plates (see fig. 2.2a). This first experiment demonstrated at small scale the ability to bend a regular grid with no shear rigidity into a curved shape (see fig. 2.2b). The grid was loosely braced and shell effects were not investigated.

Essen Gridshell, Essen, Germany, 1962

The same year he designed and built a first timber gridshell at Essen, Germany [1, p. 272]. The prototype – a single-layer gridshell spanning 17 m and covering an area of 198 m^2 – was made with 3-ply laminated timber profiles in hemlock pine (see fig. 2.3a). The cross-section of the profiles was rectangular (60 mm x 40 mm) and the elements were assembled in a grid fashion with simple steel bolts. Once erected, nothing was specifically done to improve the in-plane shear stiffness of the grid and activate a shell behavior. Finally, the structure was covered with a transparent plastic foil nailed directly on the grid's profiles (see fig. 2.3b).

German Pavilion Auditoria, Montreal, Canada, 1967

Fiver years later, on the occasion of the *1967 International and Universal Exposition* in Montreal, Canada, Frei Otto was appointed to design the German Pavilion : a large cable

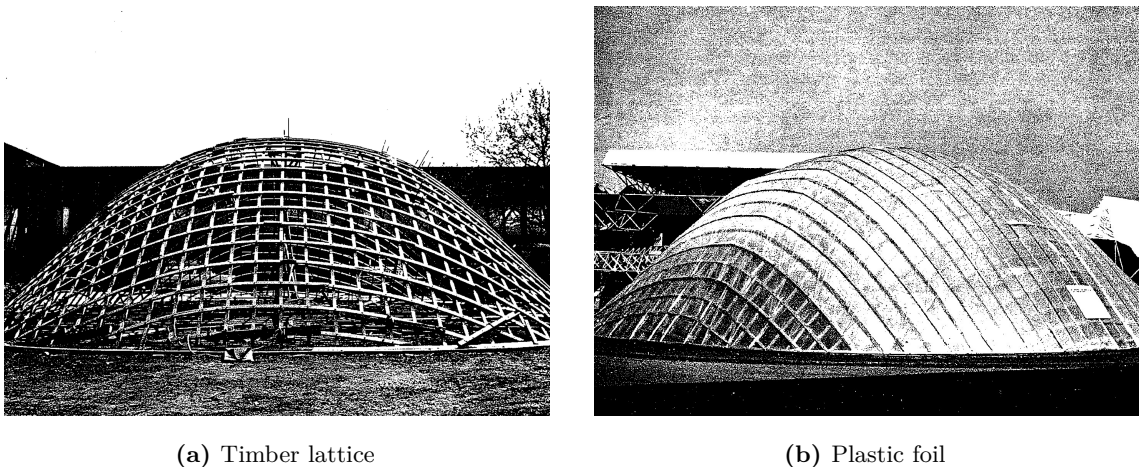


Figure 2.3 – Timber gridshell built in 1962 in Essen, Germany.

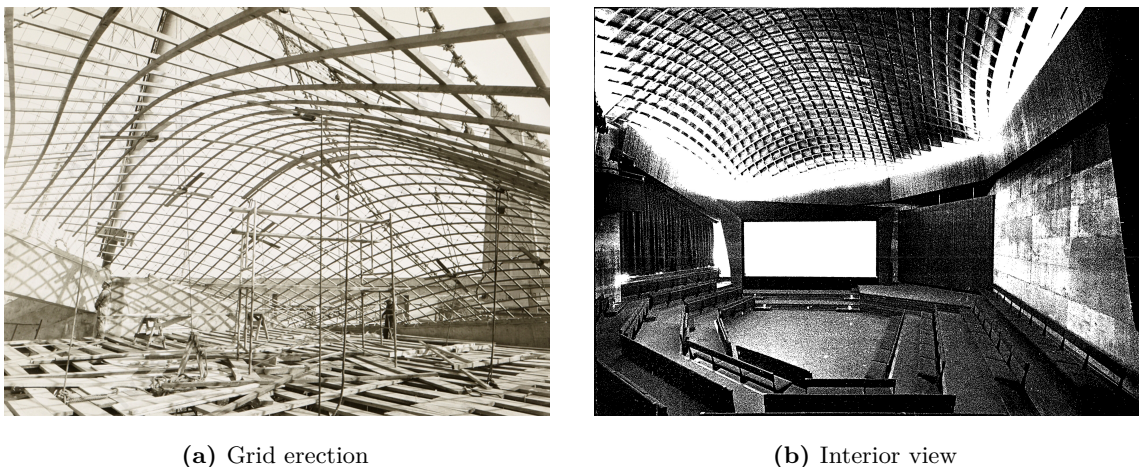


Figure 2.4 – Timber gridshell built in 1967 in Montreal, Canada.

net tent prefiguring the realization of the olympic stadium of Munich, Germany, in 1972.^{4,5}

The pavilion required two auditoria and these were designed using the principle of elastic gridshell [1, p. 274]. All together, the auditoria covered an area of 365 m^2 and spanned 17.5 m. The construction technique employed in Montreal was quite similar to the one developed in Essen, but this time the grid was fully braced with a layer of nailed plywood boards and offered a proper roofing made out of insulation panels covered with a PVC coated fabric (see figures 2.4a and 2.4b).

The two gridshells built in Montreal mark a significant step in the maturation process of

⁴Actually, Frei Otto became the director of the newly founded *Institute for Lightweight Structures* (Institut für Leichte Flächentragwerke or IL) at the University of Stuttgart in 1964. It was the IL that was commissioned by the German government to conduct research in connection with the planning of the German pavilion for the exposition in Montreal.

⁵Video of the construction of the German pavilion : <https://www.youtube.com/watch?v=Z0mtFMoseUk>.

the technique leading to the major realization of Mannheim in 1976 : a methodology has emerged to progress “from the inverted form to the gridshell” [1, p. 179] ; main construction details have been validated ; various erection methods have been tested ; mid-scale buildings have been built to host public. However, due to the over complexity of these structures, lots of unknowns remained unsolved at this stage and the behavior of the structures could not be fully predicted.⁶

It is worth to mention that several unexecuted large-scale projects were studied by Frei Otto between 1967 and 1973 at the *IL* or at the *Atelier Warmbronn*.⁷ These projects are basically documented in [1, pp. 278 - 288] and reveal that he was training his capacity to master large-scale projects with the technique of elastic gridshells for more conventional building projects (wave pool, swimming hall, multi-purpose hall, auditorium, . . .).

2.3.2 Mannheim Multihalle : the completion of a decade of research

The project of the Multihalle started in 1970, when the decision was made that Mannheim, Germany, would hold the Bundesgartenschau in 1975.⁸ The architects of the project, *Carl Mutschler & Partners*, consulted Frei Otto at *Atelier Warmbronn* as he was starting to get known in the field of innovative lightweight structures. This is how the idea of the gridshell was introduced in the project [15].

A thorough report on the project is available in [4]. A more condensed but still precise description of the engineering problematics related to this projects are availables in the excellent papers from Happold and Liddell [2] and Liddell [15].

Multihalle, Mannheim, Germany, 1975

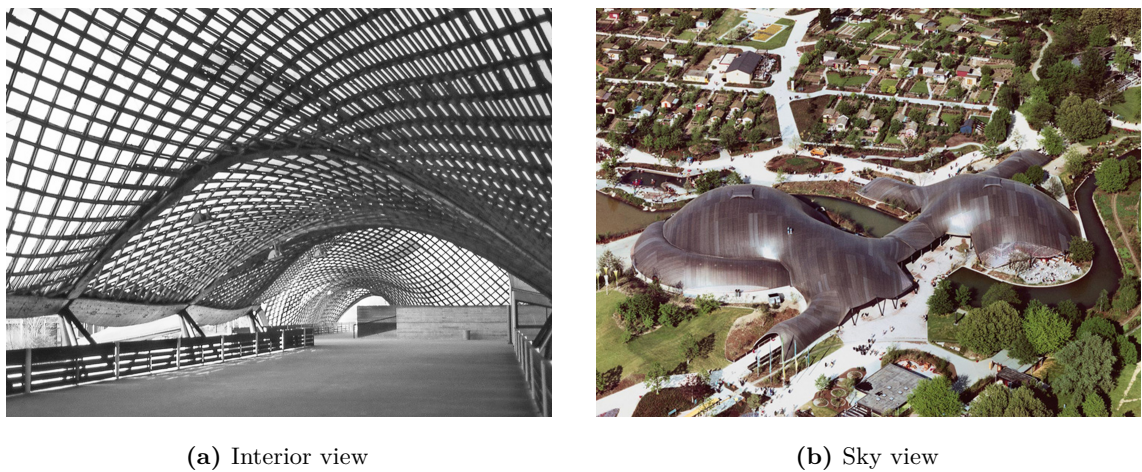
Mannheim is an unprecedented realization because it is more than twenty times larger than the previously built gridshells in Montreal and is meant to last many years and not only for the duration of a short-term exhibition. The timber lattice, still existing in 2017, covers an area of 7400 m² (see fig. 2.5b). It is composed of two interconnected domes, one for the multi-purpose hall (span : 60 m | height : 20 m) and one for the restaurant (span : 50 m | height : 18 m).

Although the constructif system deployed at Mannheim clearly inherited from the previous developments, the challenge was such that it had to be revisited. In particular the main additions were the introduction of the double-layer system and the proper bracing of the grid. A major advance was also the use of the very first numeric models to study the structure.

⁶“Snow accumulations in the throat of the common edge beam probably caused one of the two grid shells of project Montreal to buckle in a relatively flat region. The diameter of the buckled area was about 3 meters. Neither grid rod was broken, i.e. the buckling progressed elastically. It might have been possible to press the buckled area back into shape.” [1, p. 219]

⁷Atelier Warmbronn is the architectural studio founded by Frei Otto in 1969.

⁸The Bundesgartenschau is a national horticultural exhibition that takes place every two years in Germany.



(a) Interior view

(b) Sky view

Figure 2.5 – Timber gridshell built in 1975 in Mannheim, Germany.

The double-layer system was introduced to tackle two issues : the grid needed some flexibility to be bent into the desired shape, but once erected it should provide sufficient bending stiffness to resist disturbing loads and avoid a buckling collapse.⁹ One erected, the two grids, one sliding on top of the other one, were connected together to form a single grid with much higher ladder profiles (from 50 mm to 150 mm), increasing their bending stiffness by 26 (see fig. 2.5a).

Because the in-plane stiffness of the grid also plays a major role in the resistance to buckling, this question was considered with care. The bracing of the grid was first achieved by preventing the nodes to turn once the grid was erected. This was done by creating some friction in the nodes when tightening the bolts linking the laths, after the grid was erected. Additional bracing cables were put in the grid.

Finally, the project of Mannheim was a key project in the development of modern lightweight structures. Great engineers were born in touch with Frei Otto, following its footsteps or collaborating with him. This heritage has irrigated for several decades the engineering of lightweight structures in Europe and gave birth, directly or indirectly, to several studios among which we can cite *Buro Happold*, *Schlaich Bergermann & Partner* and *RFR*.

2.3.3 The dry period : 25 years from Mannheim to Hannover

Although the experience of Mannheim proved the feasibility and the potential of gridshell structures for large-scale projects, it also revealed that these projects were subject to an incredible complexity in terms of structural design, geometry, modeling, testing, team work, construction methods, ... At that time, very few people could pretend to master all the knowledge and techniques required to design and built timber gridshells and developed in the bosom of the *Institute for Lightweight Structures* in Stuttgart.

⁹Theoretically, self-weight loads would produce only compression in the members because the (funicular) form of the grid resulted from the inversion of a hanging chain model in pure tension.

This project was obviously well ahead of its time and the engineering cost to design such structures was probably prohibitive considering the tools available at that time. This certainly explains why no elastic gridshells were built during the 25 following years, despite the optimism of the pioneers of the Multihalle.¹⁰

Note that around 1975 small workshop and experiments lead to the construction of several but small elastic gridshells, as reported in [1]. A non-exhaustive but quite extensive list of known executed gridshell projects is presented in fig. 2.1. The dry period is clearly visible.

2.3.4 The signs of a renewal : Dorset and Doncaster

It is only 20 years later that gridshells started to reappear, in the late 90's mainly in the United Kingdom, and for projects that had interest in environmental problematics.

Westminster Lodge, Dorset, England, 1995

In 1995, a small student residence named *Westminster Lodge* was built in Dorset, England. This dwelling was part of a larger project – Hooke Park – aiming at investigating how the local forest resources, in particular immature roundwood thinnings, could be better utilized. The project was lead by ABK, Frei Otto, Buro Happold and Cullinan Studio. Unlike Mannheim, the timber shell was bent and weaved rod by rod on a scaffold platform. But the structural system exhibited a double-layer gridshell pattern very similar to the one employed for the Multihalle (see fig. 2.6a). The rods were made out of splice-jointed roundwood to form long-length poles of diameter 200 mm. The development of this jointing technique, which could be produced directly in the forest, was part of the project's investigations [17]. The grid was braced by a layer of diagonal boards nailed to the roundwoods. The structure was finally cladded with a planted turf roof (see fig. 2.6b).

Earth Center, Doncaster, England, 1998

At the same time, a project of a similar spirit arose for the *Earth Center* in Doncaster, England.¹¹ The project planning started in 1994 and a series of small timber gridshells were designed by Buro Happold and then built in 1998. The landscape structures were single-layer timber gridshells made with oak laths. Once erected with a crane, the grids were braced with crossing diagonal stainless steel cables (see fig. 2.7a). Openings were possibly reinforced with curved timber frames (see fig. 2.7b).

These projects definitely trailed the technique in England and initiated the renewal period (see §2.3.5). Although they remained small-scale projects for which modeling was achieved

¹⁰“For many years after its completion, Happold promoted the benefit of the timber gridshell as a construction technique and stated that he could not understand why it had not been adopted more widely. He perceived the benefits to be in the efficiency of the construction method to enable doubly curved (shell) structures to be constructed quickly and cost effectively.” [16].

¹¹“The Earth Centre Forest Garden was intended to demonstrate how managed woodland could supply the vast majority of all natural resources needed for human survival.”



Figure 2.6 – Roundwood gridshell built in 1995 in Dorset, England.



Figure 2.7 – Timber gridshells built in 1998 in Doncaster, England

through physical models, they trained and restored partially the operational ability of Buro Happold to design timber gridshells as pointed by Harris et al. [16].

2.3.5 The renewal : Hannover, Downland and Savill

What was missing for elastic gridshells to re-emerge after the major experiment of Mannheim was probably the development of modern numeric tools to ease and speed up the design process.¹² Amongst those tools we should identify two main categories : geometry processing

¹²“The key to the modern use of timber gridshells is the development of computer methods in modelling complex three-dimensional shell structures. For the Mannheim structure, the primary method of form finding was the use of physical models. The Earth Centre structures were small and easily modelled using wire mesh, but when Buro Happold were commissioned to design the Japanese Pavilion for Expo 2000 in Hannover (Architect Shigeru Ban), it was apparent that much more sophisticated computer form finding and analysis would be necessary.” [16]



(a) Interior view



(b) Sky view

Figure 2.8 – Carboard gridshell built in 2000 in Hannover, Germany.

softwares and structural analysis softwares. Recall that in the 70's, geometry processing was done through physical models and photographic measurements [1, pp. 130-135] while structural analysis was conducted through a compound of physical model testing with scaling techniques [4, pp. 130-135], hand calculations and the very first numerical formfinding calculations [1, pp. 184-193] and finite element calculations [1, pp. 210-217].

In the late 90's, the rise in importance of computer methods offered new possibilities.

Japan Pavilion, Hannover, Germany, 2000

In 1997, architecte Shigeru Ban began to collaborate with Frei Otto and Buro Happold to design the *Japan Pavilion* for *Expo 2000* in Hannover, Germany [18]. This pavilion was a large-scale corrugated gridshell made out of cardboard tubes, about 75 meters long and 25 meters wide. Corrugations bring curvature, and therefore enhance the strength of the shell. The tubes were tied together with a fabric tape, a very low-tech joint (see fig. 2.8a). The structure was covered with a paper membrane specially developed for the project to meet the requirements of the german fire regulations (see fig. 2.8b). For the occasion, a new erection method was set up in which the grid was laid out not at the ground level but at a higher level on a hydraulic scaffold platform. From there, the grid was pushed up into position using the platform's jacks. It was found late that the cardboard tubes were subject to a high level of creep. This required the introduction of new timber arches to reinforce the gridshell and to enlarge the existing timber rafters intended to brace the grid and support the paper membrane (see fig. 2.8a).

Weald and Downland, Singleton, England, 2002

The design of the *Downland* gridshell began right after the completion of the Westminster Lodge (see §2.3.4) where architects from E. Cullinan Studio became acquainted with the engineers from Buro Happold. At Downland, the project team truly revived the technique of large-scale timber gridshells while bringing lots of improvements to the system. The

building opened to the public in 2002. Its corrugated shape recalls the one of the Japan Pavilion from which it was inspired (see fig. 2.9b).

The building is 50 meters long and 12.5 to 16 meters wide, covering an area of about 675 m² for a height varying from 7 to 9.5 meters [19]. The structure is a double-layer gridshell made of rectangular oak laths of cross-section 50 mm x 35 mm (see fig. 2.9a). To produce high grade timber elements, the continuous laths were re-formed from small carefully selected wood pieces, finger-jointed every 60 cm in 6.0 m length pieces. These pieces of lath were then scarf-jointed on site every 6 m to obtain the desired length, up to 50 m.



(a) Interior view



(b) Exterior view

Figure 2.9 – Timber gridshell built in 2003 in Downland, England.

The grid pitch is 1.0 m except in weaker areas where it is 0.5 m. There, the grid is twice denser to achieve the required buckling resistance [16]. Rib-lath bracing was preferred to steel cable bracing as ribs were deemed to offer a more convenient support for the cladding elements and to reduce the complexity of the connection. A new connection system was developed to avoid the cost of drilling thousands of slotted holes that would, in addition, reduce the cross-section area, while maintaining the required scissor behavior for the deformation of the timber lattice.¹³

The flat lattice was laid out on a scaffold platform. Unlike the Japan Pavilion, the lattice was progressively lowered down into position. This stage took 6 weeks. Once deformed, the shear blocks were introduced in the grid and bracing rib-laths were installed, giving its full strength to the shell. Finally the gridshell was cladded with a mix of polycarbonate plates (to let the light in) and timber boards on top of insulation panels and a rain screen.

It is worth mentioning that for the first time the form was not found by inverting some sort of hanging chain model that would produce a pure funicular shape where only compression occurred. Instead, the shape was the result of a numerical computation that took into account the bending behavior of the laths.¹⁴ Harris et al. [16] argued that

¹³This detail was patented by the design team and the client.

¹⁴This software was developed by Chris Williams of the University of Bath.

computer models enabled some interactivity in the formfinding process that would not be possible with physical models, leading to a better synergy between architectural and structural requirements. They also argued that physical models contributed invaluable to the development of a creative and efficient design throughout the project.

Lothian Gridshell, Pishwanton, Scotland, 2002

This project deserves some attention because the developed approach was completely different from the projects exposed until now : “Previous projects have portrayed the method as a highly technical use of a low tech resource. This, however, need not be the case as we see with this project [...]” [20]. The structure was the result of “[...] an unusual collaboration between sole practitioner Christopher Day, engineer David Tasker, a crowd of local volunteers and (more unusually) the philosophies of Rudolf Steiner and Johann Wolfgang Goethe” [21].¹⁵ The single-layer gridshell was made out of local larch. Once



(a) Interior view



(b) Exterior view

Figure 2.10 – Timber gridshell built in 2002 in Pishwanton, England.

erected by hands, the dome-like shape covered about 80 m² and spanned 10 meters. The grid was braced with timber boards (see fig. 2.10a) and covered with a planted turf roof (see fig. 2.10b). Some calculations were made but in the end, it had to carry load testing to prove its safety and gain its regulation approval.¹⁶

¹⁵From the online paper “The other gridshell” : <http://www.bdonline.co.uk/the-other-gridshell/1020435.article>

¹⁶“There were a lot of calculations but no computer-generated models to show they all added up. In fact, the form was previously established with scale models. When it came to gaining Building Regulations approval, the team needed to prove that the building would be strong enough. So Tasker arranged for the unfinished structure to be loaded with about 18 tonnes of sand from a local quarry – equivalent to the maximum predicted snow load, plus a safety factor.” [21]

Woodland Centre, Filmwell, England, 2003

The gridshell of the Woodland Center was built 7 years after the project had started (fig. 2.11a).¹⁷ The building was designed by architect Feilden Clegg and engineers from Atelier One. It was part of a larger research and development project that aimed at developing chestnut – a low grade wood – as a construction material.¹⁸



Figure 2.11 – Timber gridshell built in 2003 in Filmwell, England.

The building, still existing, is composed of 5 barrel vaults spanning 12 meters and about 5 meters wide (see fig. 2.11b). It covers about 300 m^2 [22]. Each vault module is a transportable unit composed of two curved arches. A single layer gridshell was then applied to this primary frame and braced with chestnut panels. The grid was made of laths with $75 \text{ mm} \times 25 \text{ mm}$ rectangular cross-section, assembled with simple bolts. On top of that, insulation materials and a membrane as rainscreen [23].

Savill Garden, Englefield Green, England, 2006

This project saw the light of day thanks to the reputation of the gridshell built in Downland. Again, Buro Happold did the structural design while Green Oak Carpentry realized it. But this time, the architect was Glenn Howells.

The *Savill* gridshell is 90 meters long and 25 meters wide. It covers an area of about 2000 m^2 , and is therefore almost three times larger than the gridshell in Downland. Once again, the corrugated shape was defined by a parametric equation ($z = f(x, y)$) to enable interactivity between architects and engineers during the formfinding process (see fig. 2.12b). Chris Williams was responsible for this job.

In Savill, the forming strategy was quite different than those employed in Mannheim,

¹⁷More to be found at : [Growing and making Flimwell's chestnut gridshell](#).

¹⁸This project was conducted by the Building Research Establishment.



(a) Interior view



(b) Exterior view

Figure 2.12 – Timber gridshell built in 2006 in Savill, England.

Hannover or Downland [24]. Firstly, a single layer gridshell – constituted by the bottom two laths jointed with simple bolts – was deformed into the target shape. Secondly, the shear blocks were screwed on these laths. Thirdly, the upper two laths were positioned and screwed on top of the shear blocks to re-form a double-layer gridshell. Finally, the grid was then braced with two alternate layers of plywood boards, 12 mm thick each. Bracing the grid with continuous panels instead of cables or diagonal elements was a major architectural choice (see fig. 2.12a). Moreover, it gave a well-defined surface for the cladding composed of 160 mm of insulation, covered by a waterproof aluminium layer made with standing-seam profiles supporting the oak boards [25].

Another consequence of this forming process was the drastic simplification of the connexion. The system developed for Downland was of no utility in that case and only simple bolts and screws were required. In this project, the pitch of this grid is 1.0 m. The 20 kms of laths are made from larch and have a 80 mm x 50 mm rectangular cross-section. They are spaced from 100 mm to 150 mm by the shear blocks.

Of course, the steel perimeter is a major component of the project but is not in the scope of this thesis. For further details the reader is invited to refer to Harris et al. [24] and Trada [25].

Chiddington Castle Orangery, Kent, England, 2007

The gridshell covering the orangery of Chiddington Castle is a very small one. Built in 2007, it is 12 meters long, 5 meters wide and covers about 50 m² (see fig. 2.13b). The structural system is derived from the one employed in Downland and is, once again, developed by Buro Happold and the Green Oak Caprentry. But this time the architect is Peter Hulbert.

However this project embed some interesting innovations. Indeed, this time the gridshell is



(a) Glazing support

(b) Exterior view

Figure 2.13 – Timber gridshell built in 2007 in Kent, England.

braced with a bidirectional cable network. Twin cables are employed to facilitate clamping on the node connection, which has been adapted from the previous version developed in Downland. This connection is now equipped with an additional threaded hole which can receive the clamping supports for the glazing (see fig. 2.13a). The timber shell is then glazed with triangular panels. Note that the quadrangles of the mesh are not planar any more in the deformed configuration and therefore triangulation of the panels is mandatory.

2.3.6 Gridshell in composite materials : a new perspective

Since 2002, the laboratory [Navier](#) at the Ecole des Ponts ParisTech develops a research program on elastic gridshells that is still ongoing. It focuses on both the use of new materials such as composite materials and the development of modern computer design methods for the generation of complex shapes, the formfinding and the structural analysis.

Douthe et al. [3] proved that composite materials in glass fiber reinforced polymers (GFRP) are very suitable for this type of structures where both flexibility and strength of the profiles are required. On the level of mechanical behavior GFRP surpass wood. They are easy and cheap to produce in long length when they are manufactured by pultrusion, thus avoiding complex jointing issues.¹⁹.

The first gridshells in composite material, Champs-sur-Marne, France, 2007

These developments have been validated by the construction of two prototypes in 2007 (see fig. 2.14a) and in 2008 (see 2.14b) [26]. These structures were left outside for about 7 years. They covered about 150 m² each, spanning around 13 meters. The structures were single-layer gridshells made with pultruded GFRP tubes ($\varnothing 41.7 \text{ mm} \times 3.5 \text{ mm}$) assembled with a standard scaffold swivel connector. The grid were braced with a third layer of tubes

¹⁹Video explaining the pultrusion process : https://www.youtube.com/watch?v=4MoHNZB5b_Y

an covered with a PVC coated fabric membrane providing full waterproofness.



(a) First prototype (2007)



(b) Second prototype (2008)

Figure 2.14 – GFRP gridshell built in 2007 in Noisy-Champs, France.

Here, the performance of composite materials is of real benefit. A single-layer gridshell is enough for this span. The hollow circular cross-section make optimal use of the material. Tubes are provided in 12 meters length and therefore no joints are required for this span. In the end, all these benefits make the constructive system a lot more lighter, simpler and efficient than what a timber gridshell would offer.

Solidays, Champs sur Marne, France, 2011

In 2011, [Navier](#) used its knowledge to design with a team of students a temporary pavilion for a music festival in Paris, France (see [fig. 2.15b](#)).²⁰ Although the constructive system was similar to the one employed for the two prototypes, the size and the span were more than twice larger [27]. In addition, it was the first gridshell in composite material that hosted some public and therefore had to comply with strict building regulations.

To our knowledge, it is also the first gridshell that was designed using the compass method [1], thus providing an inverse method to design the structure directly from the shape given by the architect. The single-layer gridshell covered about 280 m² and was erected by two mobile cranes (see [fig. 2.15a](#)).

Ephemeral Cathedral, Crêteil, France, 2013

The *Ephemeral Cathedral* of Crêteil is the last achievement of this kind [28].²¹ It was designed by [T/E/S/S](#) with the assistance of [Navier](#). This time the structure is a real building meant to last a decade and is still in activity since its construction in 2013. A

²⁰Photos and videos of the construction process at : <http://thinkshell.fr/gridshell-solidays-2011/>

²¹Photos and videos of the construction process at : <http://thinkshell.fr/gridshell-cathedral-2013/>

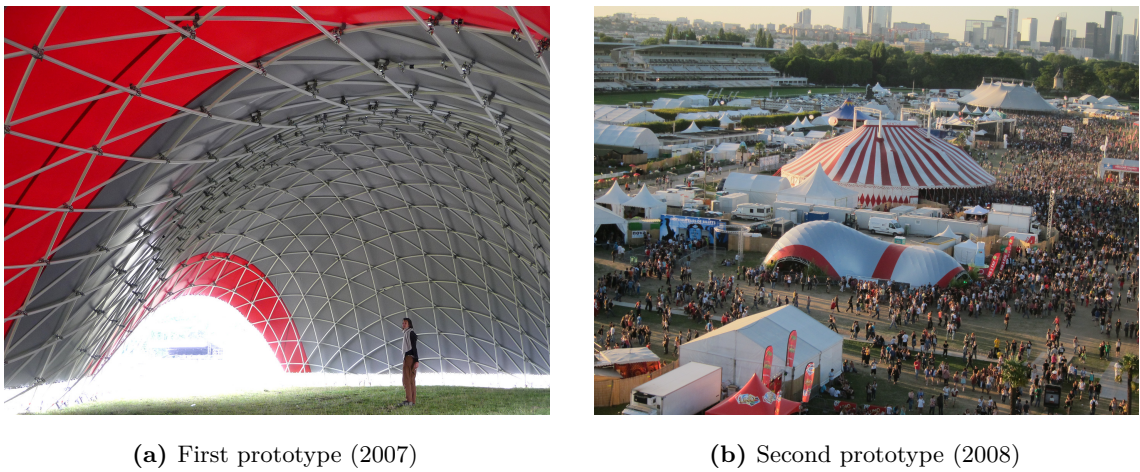


Figure 2.15 – GFRP gridshell built in 2011 in Paris, France.

complete review of this project is given in the next chapter of this thesis (see ??).

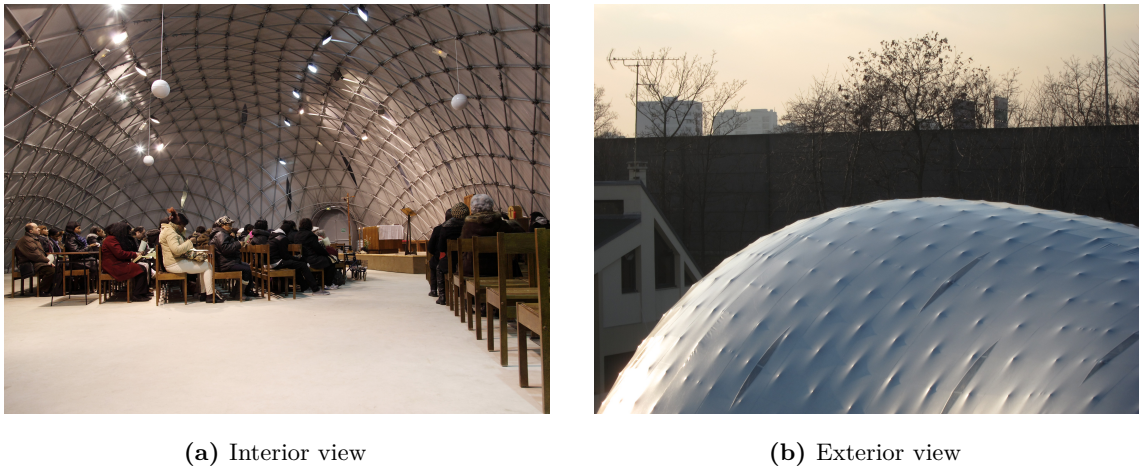


Figure 2.16 – GFRP gridshell built in 2013 in Créteil, France.

The single-layer gridshell covers about 350 m² and spans 17 meters (see fig. 2.16a). It is covered by a PVC coated fabric membrane (see fig. 2.16b). It was erected by two mobile cranes.

2.3.7 Flourishing timber gridshell pavilions

Since 2010, about 20 timber gridshell pavilions were built around the world, mainly during workshops. Here, we do not review all this pavilions in detail because they are quite similar although each one has its specificities.

The impetus given by gridshell.it

Around 2010, a research group gathering architectural and engineering skills appeared under the name [gridshell.it](#) in Italy. Inspired by the work of Frei Otto, they revisited the structural system developed at Mannheim and adapted it to a range of small-scale timber pavilions.



(a) Lecce, 2010



(b) Toledo 2.0, 2014

Figure 2.17 – Timber gridshells built by gridshell.it in Italy.

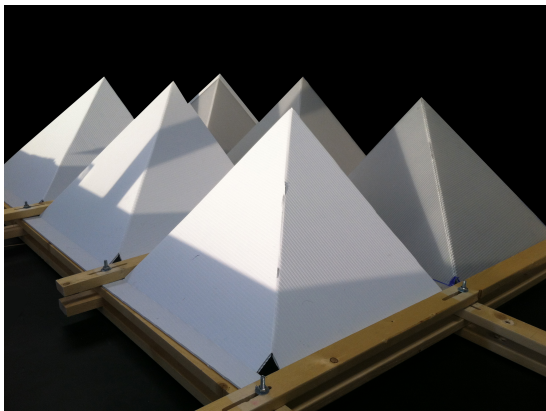
These pavilions have in common to be double-layer timber gridshells. The structural system is always composed of laths with rectangular cross-section. The laths come in short length from the sawmill (about 3 to 4 meters). They do not try to re-form long-length laths with complex jointing techniques. Instead, they use a simple splice system. Although it is not very pleasant visually, it is efficient enough for this kind of project. As the laths are short, this detail is repeated frequently in the grid. However the splice system enable a higher level of prefabrication of the grid. Thus, small modules of the size of the laths can be preassembled and connected with the splice system to re-form the full gird. This gridshells are braced either with cables or with individual diagonal elements in each cell.

These structures were never meant to provide full waterproofness although some were an occasion to experiment different types of cladding with boards (Lecce 2010, Toledo 2012, Milano 2013,) or with textile membranes (Lecce 2009).

One of their first pavilion was built in 2010 in Lecce, Italy (see [fig. 2.17a](#)). Their most known project is probably the Toledo pavilion built in 2012 in Naples, Italy. A new pavilion called Toledo 2.0 was built in 2014 in Naples, Italy (see [fig. 2.17b](#)). Although it seems that their initial approach focused more on the architectural aspects and the construction process, they rapidly tried to develop dedicated computer design methods [29] and did serious wood testing [30].

Other similar timber pavilions

The ideas of the gridshell.it group spread rapidly and similar projects were achieved outside of Italy. Amongst them, we can point out the ZA pavilion built in 2013 in Cluj, Romania [31] ; the F² pavilion built in 2014 in San Antonio, USA, with an interesting folding skin (see figures 2.18a and 2.18b) ; and the pavilion built in 2016 in Trondheim, Norway, which is made of very short length laths spliced every two cells [32, 33].



(a) Folding skin



(b) Pavilion

Figure 2.18 – Timber gridshell built in 2013 in San Antonio, USA.

Specific inputs from the laboratory Navier

In that vein, Navier and engineers from Terrell helped two students from the ENSA Grenoble and ENSA Toulouse to design a modular pavilion system for their final year project (2016). These pavilions were designed similarly to the pavilions of gridshell.it but improvements were made. Firstly, a new cable bracing system was developed. It was embedded in the grid and tensioned with spacer plates once the grid was erected (see fig. 2.19a). This system proved its efficiency on site compared to bracing with diagonal elements. Secondly, the grid was designed and fabricated so it could be dismantled and reassembled in a different shape. And indeed, a first pavilion was erected in Toulouse the 3rd of June, dismantled, reconfigured, and re-erected in Montpellier the 15th of June. The pavilions shared the same standard grid modules (2.40 m x 2.40 m). Dedicated modules were used to adapt the change in shape.²²

²²For these projects, I did the gridfinding with the compass method, the formfinding with my own dynamic relaxation software, wood testing and specification, grid system detailing (nodes, cross-sections, grid pitch, bracing, slotted holes, shear blocks, ...) and provided a valuable assistance all along the project.



Figure 2.19 – Timber gridshell built in 2016 in Montpellier, France.

2.3.8 Latest experiments

In 2016, a one-week workshop called [Building Freeform 2016](#) was held at the Ecole des Ponts ParisTech, France. The brief was to explore some innovative methods, including the generation of forms authorizing the coverage by flat panels as well as the automation of some production tasks with the use of a robot arm (see [fig. 2.20a](#)). The draft studies were conducted upstream of the week, so that students can focused on design issues, implementation and practical achievement.²³

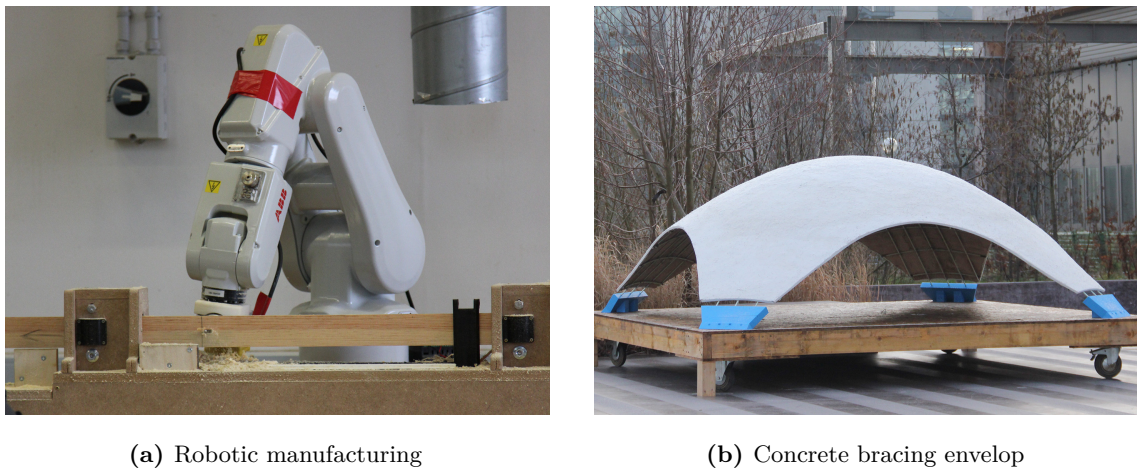


Figure 2.20 – Recent experiments built in 2016 in Champs-sur-Marne, France.

The second experiment is a hybrid structure (see [fig. 2.20b](#)). It is part of our reflexion

²³The co-development of this week was part of my research work. In particular, I provided the formfinding and structural analysis tools and developed the upstream software to generate the fabrication informations required by the milling station. This software was largely parametric so students can truly implement their own design. I was also involved in the planning of the week.

2.3. Built elastic gridshells : a review

at [Navier](#) on how to brace and clad gridshells. Indeed, the bracing of the grid in its final form remains a time consuming step with a lot of manual work. The lack of alternatives to membrane covering is also an important limitation to the development of such technology. The proposed experiment tries to tackle both issues through a novel concept of a hybrid structural skin made of an elastic gridshell braced with a concrete envelope. The idea is to use the gridshell as a formwork for the concrete and to guarantee a mechanical connection between the thin concrete skin and the main grid, so that the concrete ensures the bracing of the grid and that the thickness of the concrete is reduced to a minimum. To demonstrate the feasibility and interest of this structural concept, a 10 m^2 prototype was built at the Ecole des Ponts ParisTech, France (see [fig. 2.20b](#)). The main aspects of the design and of the realization of the prototype are presented by Cuvilliers et al. 2017 [8]

2.4 Research works in the field of elastic gridshells : a review

In this section we depict the research works that are related to elastic gridshells. Several topics have been identified to organize the review.

Toussaint 2007 [34] Olsson and Fisher 2012 [35] Poulsen 2015 [36]

2.4.1 Mechanics

Formfinding

Adriaenssens 2000 [37] propose a 6-DOF discrete beam element that integrates in a dynamic relaxation solver. This element is meant for the numerical analysis of bent elements in cable net and gridshell structures.

Adriaenssens et al. 1999 [38] present a 3-DOF discrete beam element for the formfinding of elastic rods. This element is valid only for rods that are straight in their rest configuration and that have an isotropic cross-section. Barnes 1999 [39] integrate this element for numerical analysis based on dynamic relaxation. Adriaenssens and Barnes 2001 [40] observe a better stability of this element compare to their previous 6-DOF element.

Barnes et al. 2013 [41] try to take account for torsional behavior in slender rods with anisotropic cross-section. They do not resort to any additional degree of freedom. Instead, they monitor the (geometric) torsion of a discrete space curve by computing the rotation rate between two consecutive osculating planes. This is valid only in rare specific cases where geometric torsion and mechanical torsion agree and is of little practical use.

D'Amico et al. 2014 [29] and later Poulsen 2015 [36] implement the 6-DOF beam element developed earlier by Adriaenssens 2000 [37] and use it for the formfinding of gridshells.

du Peloux et al. 2015 [42] propose a new 4-DOF element that takes account for both bending and torsion behaviors of slender rods. It relies on the Bishop frame and the notion of parallel transport. It is based on a circular spline interpolation. This element is valid for rods with anisotropic cross-section as well as for rod that are not straight in their rest configuration. They also formulate an elastic joint for the modeling of grids of interconnected beams.

D'Amico et al. 2016 [43] propose a similar approach but use a Catmull-Rom spline interpolation. However, dealing with boundary conditions is harder with this interpolation as it requires an additional node.

Kim-Lan Vaulot 2016 [9] revisit the benefits of using scale physical models for the formfinding of elastic gridshells. The grids are made out of Nitinol, a superelastic material, to make sure the models will always work in the elastic domain of the material.

Stability

Bulenda and Knippers 2001 [44] investigate for dome and barrel vault gridshells how imperfections can influence buckling.

Mesnil et al. 2015 [45] explore the influence of permanent bending pre-stress on the buckling capacity of strained gridshells. They show that for reasonably sized single-layer elastic gridshells the bending pre-stress does not influence the shape of the buckling modes. They give a simplified formula to estimate the buckling capacity of elastic gridshells under funicular loading.

Mesnil et al. 2015 [45] compare the linear buckling of non braced quadrangular gridshells and kagome gridshells.

Lefevre et al. [46] explore the buckling of triangulated single-layer elastic gridshells with a dome-like shape. In there analysis they take into account the eccentricity that exists between layers and the anisotropy of the grid. They propose a simplified formula to evaluate the buckling load of such gridshells.

Form-structure interaction

Malek 2012 [47] study how corrugation in shapes affect the mechanics of gridshells.

Jensen et al. 2013 [48] propose to interconnect several gridshells to form a stronger structure. Filz and Naicu 2015 [49] also investigate the properties of interconnected gridshells but for the purpose of kinematic effects.

Robustness

Tayeb et al. [50] study how the high level of redundancy in a gridshell enhance its resistance to collapse. They show that because of the redundancy, a pseudo ductile behavior of the structure is still observable when a brittle material is used (such as GFRP).

2.4.2 Geometry

Generation of Chebychev nets

In *IL10 Grid Shells*, Burkhardt et al. 1974 [1] study the uniform mesh net with square cells. They propose a classification for suspended nets (pp. 68-69) and give an inventory of common problems such as overlapping and singularities. They explain how to build valuable physical models for hanging nets (pp. 50-55) and how to measure them with either close-range stereo-photogrammetry, a simple measuring table or the parallel light measurement technique (pp. 130-134). Finally, they propose a geometric method to find Chebyshev meshes from a given curved shape called the *compass method* (pp. 140-141).

Bouhaya et al. 2009 [51] propose an alternative to the compass method for finding gridshell

meshes on an imposed surface. This method consists in numerically dropping a grid onto a fixed shape. The simulation is achieved with a dynamic explicit finite element solver. Therefore, the proposed method can take into account the real mechanics of the grid, which is not possible with the compass method.

Bouhaya et al. 2014 [52] implement the compass method in a geometry software. For a fixed mesh pitch and starting point they parametrically generate a large number of discrete guidelines on the surface. The generation of a guideline is controlled by a vector of angles controlling the expansion on the surface. The method is then coupled with a genetic algorithm to find meshes where the curvature of the elements is minimized.

Lafuente Hernández et al. 2012 [53] propose a variational approach to find grids that minimize the curvature of the elements. This is done by introducing penalty energies. Consequently, the mesh is allowed to move away from the imposed shape and the bars are allowed to dilate from their initial length.

du Peloux et al. 2011 [54] implement the compass method in *Grasshopper*. They use it to design two large-scale gridshells in composite material in 2011 [27] and 2013 [28].

Lefevre et al. 2015 [46] propose and extended compass method that take into account the eccentricity between the layers of rods. This gap is generally due to the connection system.

Masson and Monasse 2017 [55] prove the existence of a global smooth Chebyshev net on complete, simply connected surfaces when the total absolute curvature is bounded by 2π . In his thesis, Masson 2017 [56] study the conditions of existence of Chebyshev nets with singularities and give methods to construct them.

Pone et al. 2016 [57] propose a tool similar to the ones developed by du Peloux et al. 2011 [54] and Bouhaya et al. 2014 [52].

Morphogenesis

Douthe et al. 2016 [58] propose a reverse approach. Instead of trying to fit a mesh on an imposed surface, they construct discrete surfaces that embed the required properties. They show that the dual mesh of an isoradial mesh is a Chebyshev net. They give a method to construct such nets.

Mesnil 2017 [59] propose various methods to generate construction-aware discrete surfaces. Some of them are applicable to gridshells, for instance to produce twist-free grids of grids with planar quadrangular panels.

2.4.3 Material

Douthe et al. 2010 [3] look for new materials that could surpass wood when building elastic gridshells. They use Ashby's selection method to show that composite materials in glass fibre reinforced polymers are good candidates. Douthe et al. 2006 [26] build the first

2.4. Research works in the field of elastic gridshells : a review

structure of this kind.

Kotelnikova-Weiler et al. 2013 [60] extend the previous approche to draw somme recommendations for the selection of materials for actively-bent structures.

Kotelnikova-Weiler 2012 [61] studies the long term behavior of pultruded GFRP rods subject to permanent combined bending and torsion stresses.

2.4.4 Technology

Erection

In *IL10 Grid Shells*, Burkhardt et al. 1974 [1] propose various methods for erecting elastic gridshells. Quinn and Gengnagel 2014 [7] review several gridshell projects and their erection methods. They question the potential of air-inflated membrane cushions for the erection of strained gridshells. Quinn et al. 2016 [62] investigate the benefits of pneumatic falseworks to erect strained grid shells.

Liuti et al. 2016 [63] present an inflatable membrane technology for the erection of post-formed timber gridshells. They test it on a small-scale structure.

Cladding

Lafuente Hernández and Gengnagel 2014 [64] try to further improve the efficiency of deployable gridshells by using the cladding membrane to brace the structure. Although this solution is less stiff than the usual ones, it does enhance the deployability and reduce the work spent in the bracing stage.

Cuvilliers et al. 2017 [8] develop a concept of a hybrid structural skin, that is an elastic gridshell in composite material braced by a thin fibre reinforced concrete skin. The gridshell serves as a formwork to the concrete skin and the concrete skin is pored directly on the deformed grid. The connection enable a tight collaboration between the structural grid and the concrete, so that the skin is bracing the gridshell.

Optimization

D'Amico et al. 2015 [65] describe a procedure to optimize timber gridshell cross-sections. The optimization is done for a given load case and relatively to the generated stresses. Nevertheless, this optimization process does not take into account the buckling behavior of the structure, which is usually prevails in such lightweight structures.

Robotisation

Robotisation is investigated in recent timber gridshell projects such as the ZA pavilion [32] and the pavilion built at the ENPC in 2016.²⁴ Robotic design and manufacturing of timber structures is further explored by Menges et al. 2016 [66].

2.5 Conclusion

²⁴This pavilion has been published on the web : <http://thinkshell.fr/freeform-wooden-gridshell-2016/>.

2.6 References

- [1] B. Burkhardt, J. Hennicke, and E. Schauer, eds. *IL10 Grid Shells*. Institut für leichte Flächentragwerke (IL). Stuttgart, 1974.
- [2] E. Happold and I. Liddell. “Timber lattice roof for the Mannheim Bundesgartenschau”. In: *The structural engineer* 53.3 (1975), pp. 99–135.
- [3] C. Douthe, J.-F. Caron, and O. Baverel. “Gridshell structures in glass fibre reinforced polymers”. In: *Construction and Building Materials* 24.9 (2010), pp. 1580–1589.
- [4] B. Burkhardt, M. Chaitos, J. Langner, W. Langner, and G. Lubberger, eds. *IL13 Multihalle Mannheim*. Institut für leichte Flächentragwerke (IL). Stuttgart, 1978.
- [5] J. Chilton and G. Tang. *Timber Gridshells: Architecture, structure and craft*. Routledge, 2017.
- [6] M. Collins and T. Cosgrove. “A Review of the State of the Art of Timber Gridshell Design and Construction”. In: *Civil Engineering Research in Ireland*. 2016.
- [7] G. Quinn and C. Gengnagel. “A review of elastic grid shells, their erection methods and the potential use of pneumatic formwork”. In: *WIT Transactions on the Built Environment* 136 (2014), pp. 129–144.
- [8] P. Cuvilliers, C. Douthe, L. du Peloux, and R. Le Roy. “Hybrid structural skin : prototype of an elastic gridshell braced by a fibre-reinforced concrete envelope”. In: *Journal of The International Association for Shell and Spatial Structures* (2017), pp. 1–12.
- [9] L. Kim-Lan Vaulot. “Form-Finding of Elastic Gridshells”. PhD thesis. Massachusetts Institute of Technology, 2016.
- [10] C. Douthe. “Etude de structures élancées précontraintes en matériaux composites : application à la conception des gridshells”. PhD thesis. Université Paris Est, 2007, p. 274.
- [11] L. Bouhaya. “Optimisation structurelle des gridshells”. PhD thesis. Université Paris-Est, 2010, p. 154.
- [12] F. Tayeb. “Simulation numérique du comportement mécanique non linéaire de gridshells composés de poutres élancées en matériaux composites et de sections quelconques”. PhD thesis. 2015.
- [13] E. Lafuente Hernández. “Design and Optimisation of Elastic Gridshells”. PhD thesis. Universität der Künste Berlin, 2015.
- [14] B. Addis. “‘Toys that save millions’ - A history of using physical models in structural design”. In: *The Structural Engineer* 91.4 (2013), pp. 12–27.
- [15] I. Liddell. “Frei Otto and the development of gridshells”. In: *Case Studies in Structural Engineering* 4 (2015), pp. 39–49.
- [16] R. Harris, J. Romer, O. Kelly, and S. Johnson. “Design and construction of the Downland Gridshell”. eng. In: *Building research and information* 31.6 (2003), pp. 427–454.

- [17] R. Burton, M. Dickson, and R. Harris. “The use of roundwood thinnings in buildings : a case study”. In: *Building Research & Information* 26.2 (1998), pp. 76–93.
- [18] M. McQuaid, F. Otto, and S. Ban. “Building the Japan pavilion”. In: *Shigeru Ban*. Phaidon Press, 2006, pp. 8–11.
- [19] R. Harris and O. Kelly. “The structural engineering of the Downland gridshell”. In: *Space Structures 5* 1.April 2002 (2002), pp. 161–172.
- [20] O. Lowenstein. “Lothian Gridshell”. In: *Building for a Future Winter* (2002), p. 29.
- [21] Bdonline.co.uk. *The other gridshell*. 2002.
- [22] O. Lowenstein. “Gridshells in England. Ideas from the U.K. make stunning use of small timber”. In: *Wood Design & Building* (2004).
- [23] Fourthdoor.org. *Growing and making Flimwell's chestnut gridshell*. 2003.
- [24] R. Harris, S. Haskins, and J. Roynon. “The Savill Garden gridshell : Design and construction”. In: *The Structural Engineer* 86.17 (2008), pp. 27–34.
- [25] Trada. “The Savill Building. A visitor centre with a timber gridshell roof Gridshell structures”. In: *TRADA* (2006), pp. 1–7.
- [26] C. Douthe, O. Baverel, and J.-F. Caron. “Formfinding of a grid shell in composite materials”. In: *Journal of the IASS* 47 (2006), pp. 53–62.
- [27] O. Baverel, J.-F. Caron, F. Tayeb, and L. du Peloux. “Gridshells in composite materials : construction of a 300 m² forum for the solidays' festival in Paris”. In: *Structural Engineering International* 22.3 (2012), pp. 408–414.
- [28] L. du Peloux, F. Tayeb, O. Baverel, and J.-F. Caron. “Construction of a large composite gridshell structure: a lightweight structure made with pultruded glass fibre reinforced polymer tubes”. In: *Structural Engineering International* 26.2 (2016), pp. 160–167.
- [29] B. D'Amico, A. Kermani, and H. Zhang. “Form finding and structural analysis of actively bent timber grid shells”. In: *Engineering Structures* 81 (2014), pp. 195–207.
- [30] B. D'Amico, A. Kermani, H. Zhang, A. Pugnale, S. Colabella, and S. Pone. “Timber gridshells: Numerical simulation, design and construction of a full scale structure”. In: *Structures* 3.May 2016 (2015), pp. 227–235.
- [31] D. Naicu, R. Harris, and C. Williams. “Timber Gridshells: Design methods and their application to a temporary pavilion”. In: *World Conference on Timber Engineering* (2014), pp. 1–2.
- [32] J. Haddal Mork, S. Dyvik Hillersøy, B. Manum, A. Rønnquit, and N. Labonnote. “Introducing the Segment Lath - a Simplified Modular Timber Gridshell Built in Trondheim Norway”. In: *World Conference on Timber Engineering*. 3. Vienna, Austria, 2016.
- [33] N. Labonnote, J. H. Mork, S. H. Dyvik, A. Rønnquist, and B. Manum. “Experimental and Numerical Study of the Structural Performance of a Timber Gridshell”. In: *World Conference on Timber Engineering*. 2. Vienna, Austria, 2016, pp. 3–10.
- [34] M. Toussaint. “A design tool for timber gridshells”. PhD thesis. Technische Universiteit Delft, 2007.

- [35] J. Olsson and A. Fisher. "Form finding and size optimization - Implementation of beam elements and size optimization in real time". PhD thesis. Chalmers University of Technology, 2012, p. 97.
- [36] E. Poulsen. "Structural design and analysis of elastically bent gridshells". PhD thesis. Chalmers University of Technology, Gothenburg Sweden, 2015.
- [37] S. Adriaenssens. "Stressed spline structures". PhD thesis. University of Bath, 2000.
- [38] S. Adriaenssens, M. Barnes, and C. Williams. "A new analytic and numerical basis for the form-finding and analysis of spline and gridshell structures". In: *Computing Developments in Civil and Structural Engineering*. Ed. by B. Kumar and B. H. V. Topping. Edinburgh: Civil-Comp Press, 1999, pp. 83–91.
- [39] M. Barnes. "Form finding and analysis of tension structures by dynamic relaxation". In: *International Journal of Space Structures* 14.2 (1999), pp. 89–104.
- [40] S. Adriaenssens and M. Barnes. "Tensegrity spline beam and grid shell structures". In: *Engineering Structures* 23.1 (2001), pp. 29–36.
- [41] M. Barnes, S. Adriaenssens, and M. Krupka. "A novel torsion/bending element for dynamic relaxation modeling". In: *Computers & Structures* 119 (Apr. 2013), pp. 60–67.
- [42] L. du Peloux, F. Tayeb, B. Lefevre, O. Baverel, and J.-F. Caron. "Formulation of a 4-DoF torsion / bending element for the formfinding of elastic gridshells". In: *Proceedings of the International Association for Shell and Spatial Structures*. August. Amsterdam, 2015, pp. 1–14.
- [43] B. D'Amico, H. Zhang, and A. Kermani. "A finite-difference formulation of elastic rod for the design of actively bent structures". In: *Engineering Structures* 117 (2016), pp. 518–527.
- [44] T. Bulenda and J. Knippers. "Stability of grid shells". In: *Computers and Structures* 79.12 (2001), pp. 1161–1174.
- [45] R. Mesnil, J. Ochsendorf, and C. Douthe. "Stability of Elastic Grid Shells". In: *International Journal of Space Structures* 30.1 (2015), pp. 27–36.
- [46] B. Lefevre, C. Douthe, and O. Baverel. "Buckling of elastic gridshells". In: *Journal of the IASS* September (2015).
- [47] S. R. Malek. "The effect of geometry and topology on the mechanics of grid shells". PhD thesis. MIT, 2012.
- [48] T. Jensen, O. Baverel, and C. Douthe. "Morphological and mechanical investigation of interconnected elastic gridshells". In: *International Journal of Space Structures* 28.3-4 (2013), pp. 175–186.
- [49] G. Filz and D. Naicu. "2 Landscapes – interaction of 2 gridshells based on a modified Stewart - Gough - principle". In: *Proceedings of the IASS Working Groups 12 + 18*. Tokyo, Japan, 2015.
- [50] F. Tayeb, J.-F. Caron, O. Baverel, and L. du Peloux. "Stability and robustness of a 300m² composite gridshell structure". In: *Construction & Building Materials* (2013).

- [51] L. Bouhaya, O. Baverel, and J.-F. Caron. “Mapping two-way continuous elastic grid on an imposed surface : application to grid shells”. In: *IASS 2009*. Valencia, Spain, 2009, pp. 989–998.
- [52] L. Bouhaya, O. Baverel, and J.-F. Caron. “Optimization of gridshell bar orientation using a simplified genetic approach”. In: *Structural and Multidisciplinary Optimization* 50.5 (2014), pp. 839–848.
- [53] E. Lafuente Hernández, S. Sechelmann, T. Rörig, and C. Gengnagl. “Topology optimisation of regular and irregular elastic gridshells by means of a non-linear variational method”. In: *Advances in Architectural Geometry*. 2012, pp. 147–160.
- [54] L. du Peloux, O. Baverel, J.-F. Caron, and F. Tayeb. “From shape to shell : a design tool to materialize freeform shapes using gridshell structures”. In: *Design Modelling Symposium*. Berlin, Deutschland, 2011.
- [55] Y. Masson and L. Monasse. “Existence of global Chebyshev nets on surfaces of absolute Gaussian curvature less than 2 pi”. In: *Journal of Geometry* 108.1 (2017), pp. 25–32.
- [56] Y. Masson. “Existence et construction de réseaux de Chebyshev avec singularités et application aux gridshells”. PhD thesis. Université Paris-Est, 2017.
- [57] S. Pone, G. Mirra, E. Pignatelli, D. Lancia, and S. Colabella. “Specialised algorithms for different project stages in a post-formed timber gridshell design”. In: *Structures and Architecture* September (2016), pp. 259–266.
- [58] C. Douthe, R. Mesnil, H. Orts, and O. Baverel. “New shapes for elastic gridshells covered by planar facets”. In: *Proceedings of the IASS Annual Symposium*. October. Tokyo, Japan, 2016, pp. 1–9.
- [59] R. Mesnil. “Structural explorations of fabrication-aware design spaces for non-standard architecture”. PhD thesis. Paris-Est University, 2017, p. 231.
- [60] N. Kotelnikova-Weiler, C. Douthe, E. Lafuente Hernández, O. Baverel, C. Gengnagel, and J.-F. Caron. “Materials for actively-Bent structures”. In: *International Journal of Space Structures* 28.3-4 (2013), pp. 229–240.
- [61] N. Kotelnikova-Weiler. “Optimisation mécanique et énergétique d’enveloppes en matériaux composites pour les bâtiments”. PhD thesis. Université Paris-Est, 2012, p. 310.
- [62] G. Quinn, C. Gengnagel, and K.-U. Bletzinger. “imulatin ng Pneum matic Er rection of o Strain ed Grid Shells via v Dynam mic Rela”. In: *Proceedings of the IASS Annual Symposium*. October. Tokyo, Japan, 2016.
- [63] Liuti, A. Pugnale, and B. D’Amico. “Building timber gridshells with air : Numerical simulations and technique challenges”. In: *Structures and Architecture* (2016).
- [64] E. Lafuente Hernández and C. Gengnagel. “A new hybrid: Elastic gridshells braced by membranes”. In: *WIT Transactions on the Built Environment* 136 (2014), pp. 157–170.
- [65] B. D’Amico, A. Kermani, H. Zhang, P. Sheperd, and C. Williams. “Optimisation of cross-section of actively bent grid shells with strength and geometric compatibility constraints”. In: *Computers & Structures* 154 (2015), pp. 163–176.

2.6. References

- [66] A. Menges, O. D. Krieg, and T. Schwinn. *Advancing Wood Architecture. A computational approach*. Routledge, July 2016, p. 256.

3 Ephemeral cathedral : the first GFRP gridshell building

3.1 Introduction

The Ephemeral Cathedral of Créteil, France, is an elastic gridshell structure made of composite materials [28]. Built in 2013, this 350 m² religious edifice was initially a temporary church meant to gather the parishioners during the two years renovation (2013 - 2015) of their permanent cathedral (see fig. 3.1). At the time of writing, this building is still in activity and has been erected for almost five years. Although this structure is no more a church it has entered in a reconversion process to become a space for community activities and is now the property of the city of Créteil, France.

This large-scale prototype represents a first in the building industry which still shows excessive apprehension for the use of non-traditional materials such as composites, especially when it comes to structural applications. This is emphasized by the fact that only pre-norms or professional recommendations exist for composite materials, which is quite insufficient when one has to deal with insurers and legal technical controls. Although this structure is not the first elastic gridshell ever built in *Glass Fiber Reinforced Polymer* (GFRP) composite material, it should be regarded as the first true building using this technology. Indeed, this prototype – which can legally accommodate up to 500 people – complies with all the required performances : structural stiffness, fire safety, waterproofness, lightning, thermal comfort, etc. To our knowledge, this building is still the only one of this kind ever built.

It is worth to mentionne that this project arises thanks to a long-term collaboration between T/E/S/S atelier d'ingénierie¹ and the laboratory Navier² and marks the accomplishment of a ten years research project in this field.³ More over, this challenge was both technical

¹A structural design firm based in Paris, France : <http://tess.fr>

²Architected Materials and Structures (AMS) research team, specializes in the field of mechanics of materials and structures : <http://navier.enpc.fr/Materiaux-et-Structures?lang=en>

³Note that I developed this project in 2012 while I was a structural engineer at T/E/S/S, using the

and human as the structure was built by the parishioners them selves.

3.1.1 Overview

3.1.2 Contributions

This project was at the heart of the motivations for this thesis as it acted as a proof of feasibility and as a validation of the design tools and methods developed until then. The gained experience has highlighted further research directions that are presented in this manuscript.

In this chapter, we present the key aspects of the design and construction of this building. The main contribution of this work is to exhibit a method to design and build gridshells in a shape-driven design process. In such a process, architecture plays its full role as it is less dependent on purely structural considerations. Moreover, a building is much more than a shelter and has to satisfy serious requirements. To fill this gap, a meticulous attention was brought to the development of construction details. These technical developments lead to numerous testings. This chapter focus on this fundamental aspect as it is also a key contribution. Finally, we point out and analyze our experience, and we draw up some recommendations for further developments.

3.1.3 Related work

A thorough review is given in ??.

3.2 Project overview

3.2.1 Context and challenges

Créteil is a city of 90.000 inhabitants in the southeast suburb of Paris. Its urbanization began in the late 50's, impelled by the French architect Charles-Gustave Stoskopf. In 1976 he designed Notre Dame of Créteil, a modest catholic church made of concrete, which became a cathedral 10 years later (see item 2 in fig. 3.1). Recently, the diocese of Créteil has undertaken a major architectural redevelopment project of its cathedral, including a timber shell covering the religious area and the creation of a new cultural area. Once transformed, the edifice shall be more visible, more hospitable and livelier for citizens. Inevitably, such a molt takes time and a temporary place of worship was required to ensure liturgical services during the two-years work. In November 2011, T/E/S/S, the structural design office in charge of the cathedral renovation project, made an ambitious proposal to the diocese : based on a previous successful experience – the construction of a composite gridshell for the festival Solidays [27] – T/E/S/S suggested that rather installing a basic

knowledge I had previously gained on the gridshell project for the Solidays music festival in 2011 while I was a research engineer at Navier. I started this thesis in octobre 2014, 18 months after the opening of the temporary cathedral to pursue my research on this topic started in may 2010.



Figure 3.1 – Situation map. The temporary gridshell (1) was built very close to the permanent cathedral (2). Remark that the two buildings cover a quite similar projected area.

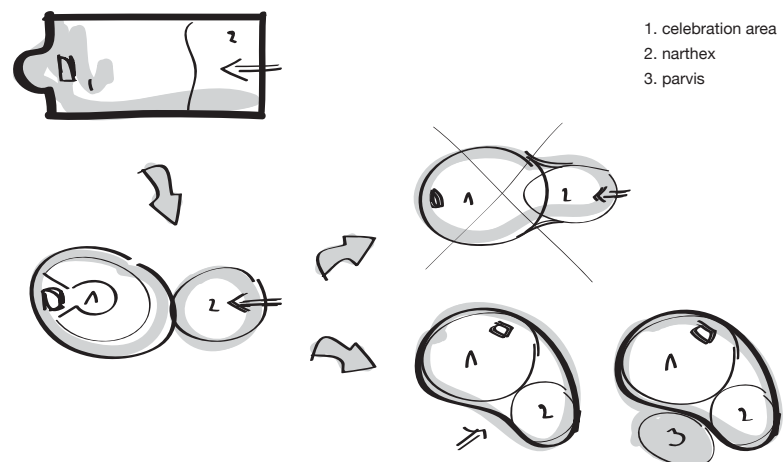


Figure 3.2 – Architectural sketch. Major and minor volumes are agglomerated into one volume. Here, the morphological register allowed by elastic gridshells appears to be relevant.

tent, the parishioners should construct themselves a temporary cathedral.^{4,5}

3.2.2 Architectural considerations on the form

The origin of this building form was driven by two objectives, that is, to provide a variety of appropriate internal spaces within which the community could assemble, and to provide an externally welcoming and visually interesting form. According to the architect Tom Gray, today, the internal organization of a roman catholic church is in large part driven by the post Vatican II vision of a religious celebration being a collective gathering of the community around the Eucharist, center of spiritual life. A circular seating arrangement is often considered the most convivial form to create a sense of belonging while minimizing a sense of hierarchy. However the community is not only using the building for religious celebration but also for encounters on a more informal manner, for example spontaneous gatherings after religious ceremonies. In the early Roman church, such gathering of the community was facilitated by the presence of an anti-space to the main space called a *narthex*, through which one passed on entering the church. It was therefore felt appropriate that the formal freedom which the gridshell system offered would be used to explore forms composed of an agglomeration of major and a minor volumes which contain the two functions : formal and informal gatherings (see item 1 and 2 in [fig. 3.2](#)).

Formal explorations were undertaken using modeling clay. The final form is based loosely on two adjacent semi spherical volumes of different size, which are merged into one complex form. Externally the fear of the design team was that the totally convex blob form could look intimidating. It was therefore decided that the two spherical virtual forms, which would be joined to make the final form, would be arranged not in a symmetrical axial manner, but in an asymmetrical curved composition. The resulting form seen in plan is convex on one side and concave on the other. The concave form in plan allows for double curvature to be introduced into what would be otherwise a simpler blob and gives sensuality and visual interest to the building.

3.2.3 Placing of the building on the site

The temporary cathedral is located on a land owned by the municipality, which is used for sporting and other communal gatherings. The curve in the building defines an external area where the church community could meet in the open air and this is where the entrance to the church is situated. The building was positioned on the site so that the entrance addresses a grass planted area forming a garden forecourt or “parvis” (see item 3 in [fig. 3.2](#)). A service building housing plant, toilets and vestry are housed in a port cabin positioned to the rear of the building (see [fig. 3.8](#)).

⁴See the video of the construction of Solidays’ gridshell here : <https://youtu.be/24LLfcVIZWw>.

⁵See the video of the construction of Creteil’s gridshell here : <https://youtu.be/jLq-UfOdnQQ>.

3.2.4 Entrance

It is formally quite difficult to integrate doors, which must be verticals, into a complex geometry. Either the gridshell could be deformed to accommodate the geometrical requirements of doors, or the doors could be integrated into an independent form. The latter approach was chosen. In looking for forms to house the doors, reference was made to the conical monumental doorways with rings of concentric decoration, which welcome the faithful to romanesque and gothic churches in France. The conical forms were found to be coherent to the overall geometry of the building. The entrance doors were therefore inserted into a conical hooded form made of rolled steel plates and stiffened by concentric steel tubes, which not only make reference to historic precedence but also refer to the gridshell to be discovered inside (see [fig. 3.5b](#)). The cone of the entrance doors was positioned in the concave side of the building giving access directly to the narthex part of the internal volume. To the rear of the church is situated a service door. The steel hood, which houses this door, is curved tightly around the door and takes up an ovoid form.

3.2.5 Daylight

The gridshell is covered in a PVC membrane, which is opaque. How to introduce daylight into the interior was a major subject of reflection. The simplest way found was to use transparent membrane placed occasionally on the membrane. A small amount of light was required in the interior to create a contemplative atmosphere. The lights would in consequence glow and would be seen as luminous insertions in the vault, like stars in the celestial vault or the apse of some Romanesque churches. The stars were patterned on the joints of the PVC membrane. The almond shape came from simplification of the cutting into the panels either side of the joints and to avoid stress concentrations around cuts in the membrane. This shape, known as Mandela, is frequently used in Marian religious imagery. The distribution of the transparent insertions is quite uniform but gets denser above the pinnacle.

3.2.6 Technical description

The gridshell structure is made of long glass fibre tubes ($\varnothing 42$ mm) fastened together with scaffold swivel couplers (see, [fig. 3.6a](#)). The structural members of the grid, all of different lengths, are built from one, two or three composite tubes connected with steel sleeves (see [fig. 3.6b](#)). The length of the tubes is limited to 12 m to enable transportation through standard trucks. The tubes are organized in three layers. During assembly, the first two layers are first placed perpendicular to one another on the ground. They form the *quadrangular primary grid*. The distance between the tubes of these two layers is constant, resulting in a regular grid. This primary grid is elastically deformed to obtain the final shape. The third layer of tubes acts as bracing. It gives the structure a shell-like behavior. The tubes are fixed to the primary grid once the shape has been obtained

The structure is anchored to a concrete strip footing with a special anchorage system, which ensures transfer of loads from the composite structure to the ground (see [fig. 3.6c](#)).



Figure 3.3 – Exterior view. The connections mark the fabric suggesting the interior grid structure. This texture enriches the perception of the building viewed from the outside and creates effects with the light reflections – © L. du Peloux for T/E/S/S.



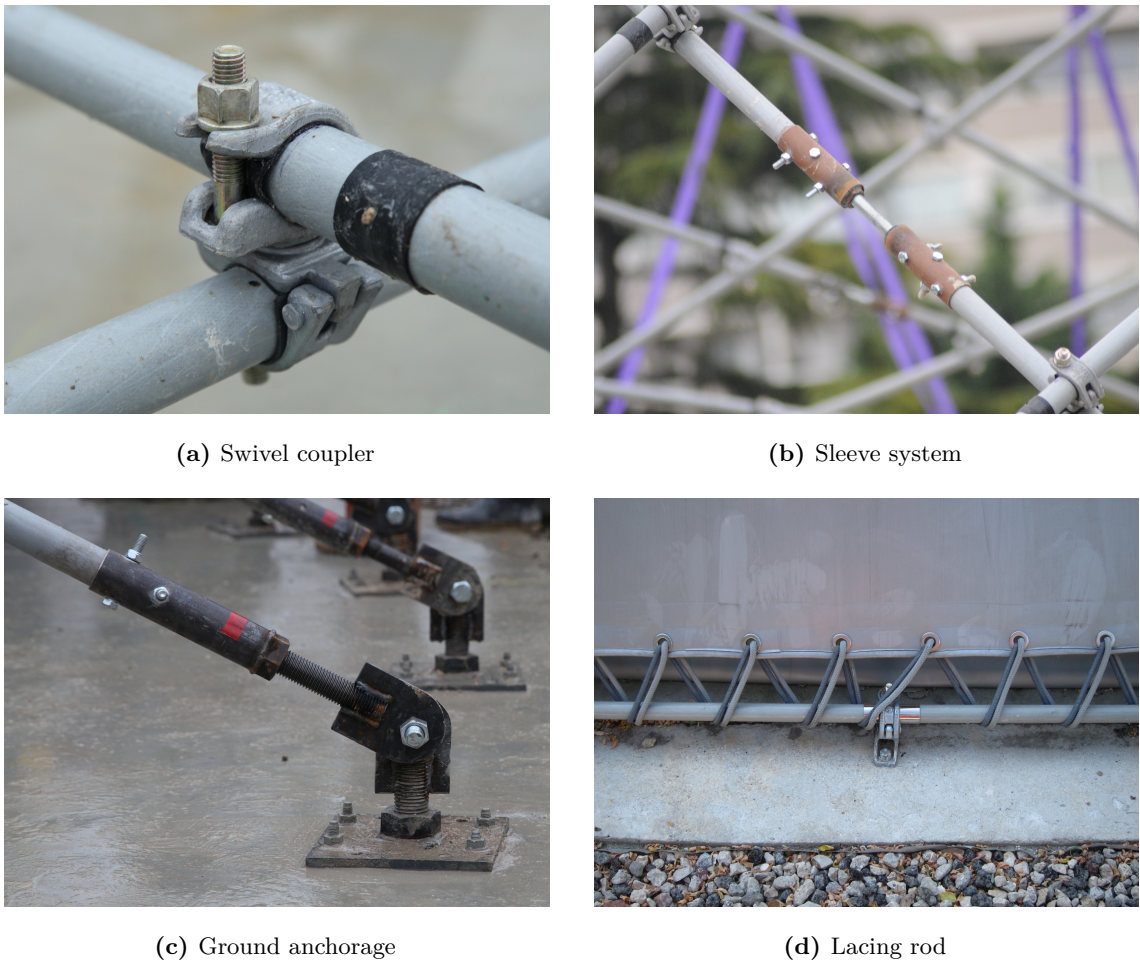
Figure 3.4 – Interior view. The grid pattern highlights the lightness of the structure and gives its tempo to the internal space. Lines converge to the altar, the heart of the liturgical area where the mass is offered on – © C. Moissinac for T/E/S/S.



(a) Exterior

(b) Interior

Figure 3.5 – Entrance. Two steel doors allow the entrance inside the building.



(c) Ground anchorage

(d) Lacing rod

Figure 3.6 – Key elements of the structural system.

A similar system enables fixation of the structure to the doors (see [fig. 3.5b](#)).

A PVC coated fabric (see [fig. 3.3](#)), tailor-made for the purpose, covers the structure. The transparent portion of the structure allows daylight inside the gridshell. The fabric is stretched on the peripheral edge of a dedicated beam with a double-lacing system (halyard and strap, see [fig. 3.6d](#)). At the ground level, the lacing edge of the beam is made of a bent, composite rod nailed to the concrete slab. At the grid–door junction, a steel arch is welded to the doorframe (see [fig. 3.5a](#)).

The PVC fabric is waterproof and, since it is a continuous membrane, has no joints except at the perimeter. At the perimeter, a continuous strip of membrane is prefixed to the internal surface of the membrane and fixed to the ground slab. At the doors, a flexible strip of the membrane is riveted to the doorframe.

Category	Item	Unit	Quantity
Public	seating	p	360
	standing	p	500
Dimensions	length	m	29
	width	m	17
	height	m	7
	contour	lm	75
	area	m^2	350
	volume	m^3	1600
Gridshell	tubes (x176)	lm	1775
	connections		1130
	sleeves		125
	anchorage		127
	<i>ground (single)</i>		77
	<i>ground (double)</i>		16
	<i>door (single)</i>		18
	weight	kg/m^2	5
Fabric	opaque	m^2	530
	transparent	m^2	12
	lacing rod	lm	67
	weight	kg/m^2	1

Table 3.1 – Key numbers.

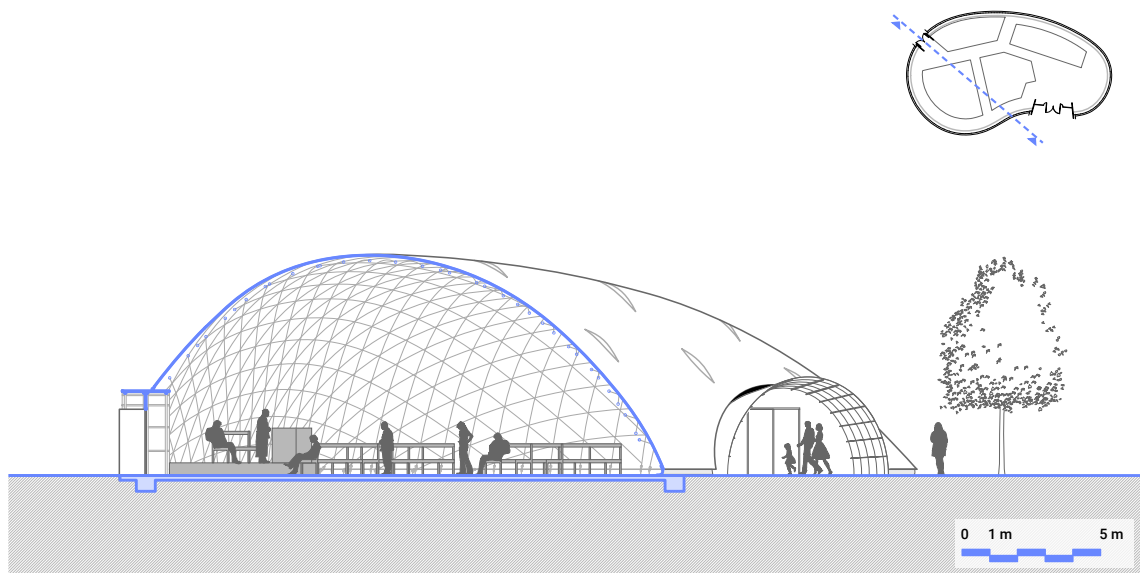


Figure 3.7 – Transversal section of the building. Observe how the grid gets denser at the choir. Two doors give access to the building. The height at the pinnacle is about 7 m.

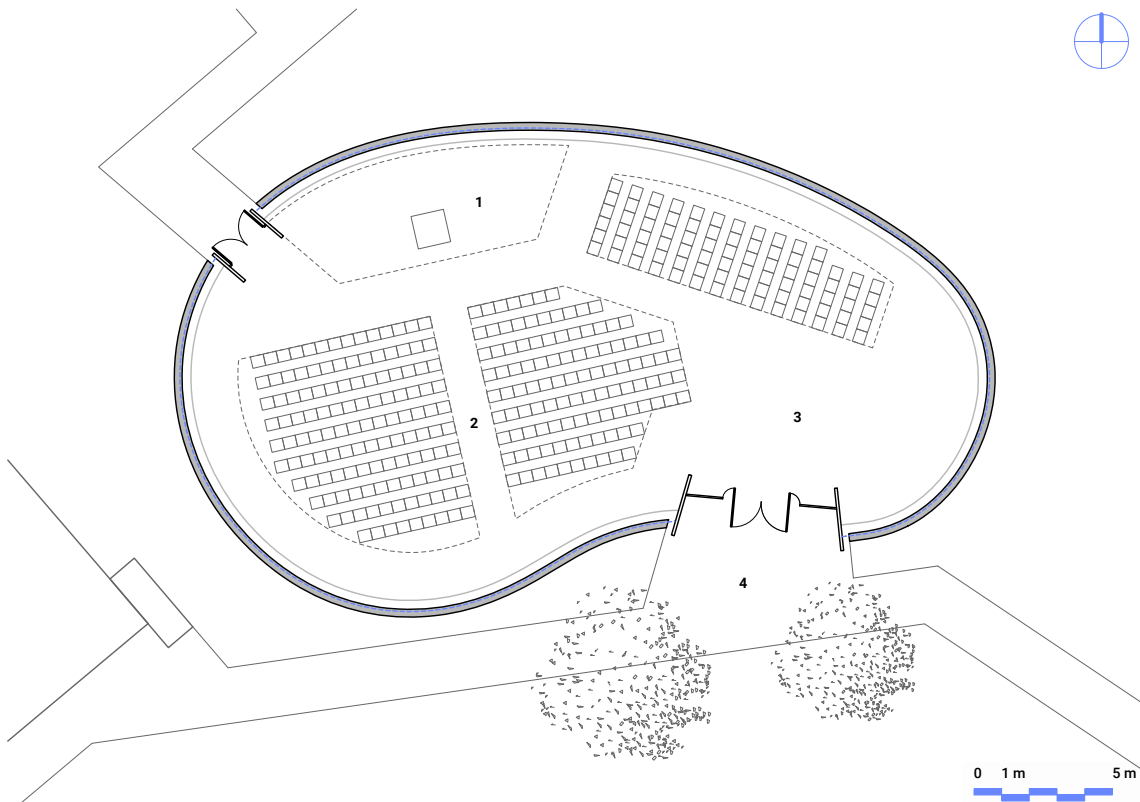


Figure 3.8 – Top view of the building. The interior space is composed of a choir (1), a place of assembly (2) and a narthex (3). The main entrance overlook the parvis (4). The shell spans about 29 m in the longitudinal direction and about 17 m in the transversal direction. The covered area is about 350 m². The space can accommodate 360 seating people or 500 standing people.

3.3 Construction process

3.3.1 Assembly of the grid

The first two directions of tubes were assembled perpendicularly on the ground with the swivel couplers (see [fig. 3.6a](#)) to form the *primary grid*. The resulting grid covered about 600 m² (see [fig. 3.9a](#)). At each intersection, the tubes were fastened together with a coupler, installed manually by the volunteers. They were asked not to tighten the bolts but just to engage the collars in order to prevent potential damages from the collar over the tube. Once the assembly of the primary grid was complete, the swivel couplers were tightened with a torque wrench to the optimal torque specified by the laboratory Navier. The whole stage took two full days. Note that because the anchorages stucked out from the slab, it was decided not to assemble the grid on the concrete slab to ensure that the grid would be able to slide freely on the ground and not get clung in the anchorages during the erection stage.

3.3.2 Deformation of the grid

The next stage consisted in lifting the grid simultaneously with two mobile cranes (35t). Once lifted up, the grid took nearly its final form (see [fig. 3.9b](#)). The structure was slowly moved above the slab until tube endings faced at best their respective anchor points. Then, tube after tube, the workers pinned the grid to the ground anchorages (see [fig. 3.9c](#)). This stage is tricky, especially at the beginning because only few tubes are connected to the ground. If the grid moves it can easily break these few tubes. The action of pinning a tube is done with a single bolt. The end of each composite tube is equipped with a rotating steel clevis. Similarly, each ground anchorage is composed of a steel plate fixed to the concrete slab and a rotating clevis. To pin a tube to an anchorage, their clevis are aligned one to each other and a pin is positioned in their central hole (see [fig. 3.6c](#)). When all the tubes were pinned to their anchorage, the grid was stable and secured and the cranes were removed (see [fig. 3.9d](#)). The stage lasted one full day.

3.3.3 Bracing of the grid

Once the primary grid was deformed into the final shape, it was braced by a third direction of tubes called the *triangulation*. The triangulation tubes split the quadrangular mesh of the primary grid into triangles (see [fig. 3.9e](#)). This work was tedious as it required working at height in aerial buckets. Tubes were hand-conveyed in the structure and attached to the tubes of the second layer with an additional swivel coupler. Each node of the structure would then be composed of two connections (see [fig. 3.18](#)). Once triangulated the structure behaves like a shell and its stiffness increases largely.

3.3. Construction process



(a) Flat grid



(b) Erection



(c) The grid is anchored



(d) Deformed grid



(e) Grid is braced



(f) Membrane

Figure 3.9 – Construction process of the gridshell.

3.3.4 Covering of the gridshell

Finally, the structure is covered with a PVC coated fabric. The membrane comes rolled up. The roll is positioned at one side. Then it is progressively unrolled toward the other side (see [fig. 3.9f](#)). This step requires professional rope workers. Once the membrane is in place, it is hand tensioned with a system of halyard and strap (see [fig. 3.6d](#)). All included, this stage lasted no more than a single day for a team of six workers.

This step appears as the moment of truth : if the membrane perfectly fits the gridshell, making no crease, that means the structural analysis were successfully conducted with the required accuracy (see ??).

3.4 Structural design

In this section, we exhibit a methodology to design a gridshell with a shape-centered approach. This is one of the key originality of this work and it was first implemented for the Solidays gridshell in 2011. The idea is to identify a grid and a set of supports that once the grid is bended and anchored to its foundations has a geometry as close as possible to the target shape designed by the architect.

Solving this inverse problem is quite a challenge. It requires a lot of back-and-forth between architects and engineers about the definition of the shape. To build a suitable solution the designers need agile tools to get deep insights quickly and adapt their design iteratively until convergence is reached. Unfortunately, existing structural analysis softwares are more validation tools than agile design tools. Although they are necessary to fully validate the feasibility of a given structure, they are quite limited to explore the space of solutions.

The presented methodology tackles this issue by providing appropriate design criteria to the designer. These criteria can be implemented in real-time softwares, thus approaching the agility of the physical models employed in the past [14].

3.4.1 Overall design process

The goal of the design process is to identify a gridshell structure that works and respects as faithfully as possible the architectural project with respect to the shape and program. The design of the gridshell represents “the path from shape to structure”. Its progress is iterative and revolves around three major stages :

- shape : modeling a shape from the architectural brief
- mesh : meshing the shape to obtain the geometry of the grid
- structure : analyze the structural efficiency of the grid

Developing this structural design was a complex process. Indeed, for each step, the method, the tool and the criteria that offer both a sufficient explorative richness in order to find

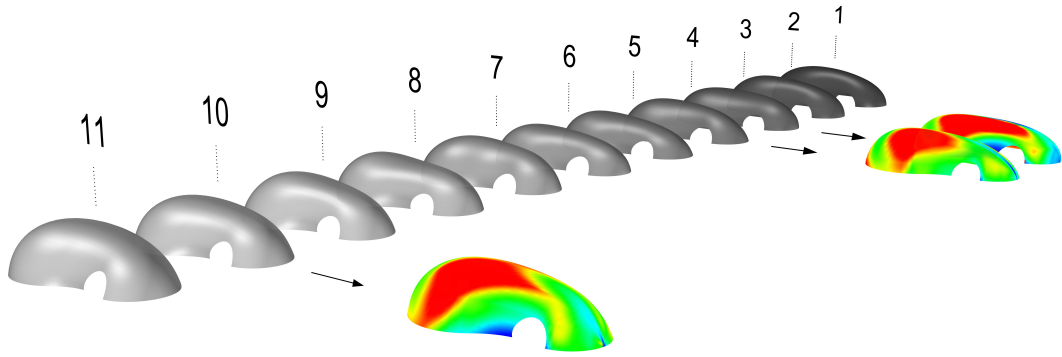


Figure 3.10 – Benchmarking shapes regarding their minimum principal curvature.

potential candidate solutions, and the means to evaluate and compare the suitability of those solutions, had to be found. In the next part of this section, the studied options and the selected evaluation criteria for each previously mentioned stage are presented.

3.4.2 3D modelling of the intended shape

The first step of the process consists in building a precise geometric model from the sketch of the architect and evaluating its mechanical potential (see [fig. 3.10](#)). At this stage, the goal is to estimate quickly the probability a given shape would lead to the generation of a structurally feasible gridshell.

Stresses in the grid are mainly due to the bending of the tubes. Therefore, they can be derived directly from the measurement of the geometric curvature of the tubes. Because the principal curvatures of the surface give a quantitative measurement of the local curvature of any curve drawn on a surface, they are relevant indicators to evaluate the stress rate of laying a grid on the said surface.⁶ Particularly, the following condition has to be satisfied everywhere :

$$E \cdot \frac{r}{R_{min}} < \frac{\sigma_{k,flex}}{\gamma_{lt}} \quad (3.1)$$

where, r is the tube's outer radius, R_{min} is the minimum principal radius of curvature of the surface, E is the flexural modulus, $\sigma_{k,flex}$ the characteristic flexural strength and γ_{lt} the long-term partial coefficient of material resistance (see [§3.5.4](#)).

Ideally, the shape is controlled by few key parameters. Thus, it is easier to adapt and optimize the shape through an iterative process towards the above criterion [eq. \(3.1\)](#).

⁶Indeed, any normal section of the surface will have its curvature bounded by the principal curvatures of the surface. Therefor, this seems reasonable to seek grids that fulfill this criterion as the structural elements would probably not resist too large variations of curvatures in the plane of the surface.

3.4.3 Meshing the surface

During the second step, the candidate surface is meshed and the mechanical potential of the resulting grid is evaluated. At this stage, the probability of a given mesh leading to the generation of a viable gridshell structure is estimated. Simultaneously, meshes are compared according to their architectural relevance.

In this step, the geometric curvature of the polylines drawn on the surface is an appropriate criterion to characterize the mechanical potential of the grid. Unlike the previous step, this criterion takes into account the curvature of the studied mesh and not the minimum principal curvature. In particular, it has to be ensured that the following condition is satisfied everywhere :

$$E \cdot \frac{r}{R_{\text{spline}}} < \frac{\sigma_{k,\text{flex}}}{\gamma_{lt}} \quad (3.2)$$

where R_{spline} is the spline's local curvature radius. The mesh is obtained by the compass method (see §3.4.3), which develops a regularly spaced grid on a surface from two secant curves lying on the surface and called *directrix*. This method, proposed by Burkhardt et al. [1], was first implemented for the Solidays gridshell in 2011. The method guarantees that the grid is made of parallelograms when developed in a plane. This geometric property is exactly what we are looking for to ensure the necessary degree of freedom of the grid responsible for its deployment (see §3.6.1). For a given shape, there are an infinite number of possible meshes (see fig. 3.13). The aim is to identify at least one grid which satisfies both the architectural and the structural requirements.

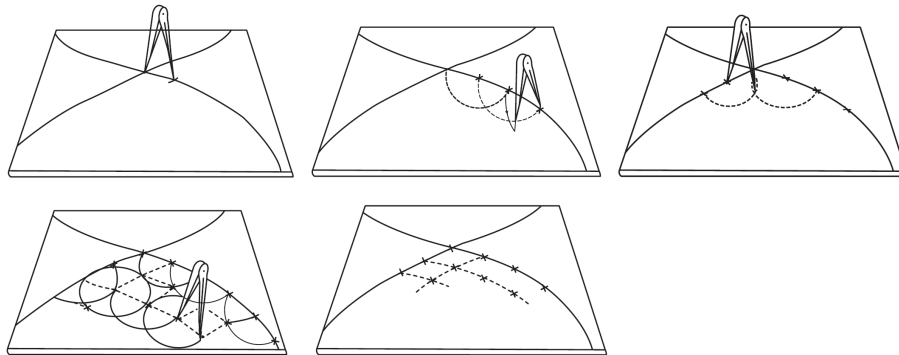


Figure 3.11 – How the compass method works.

Compass method

This process propagates a two way mesh of constant pitch on any NURBS surface (see fig. 3.11). Two secant directrices are drawn on the surface to mesh. These curves mark the boundary of four quarters. Each half directrix is then subdivided with a compass of constant distance (the pitch). Finally, from two consecutive half directrix quadrants are meshed with the same compass distance.

The compass method does not allow to spread the mesh everywhere on a given surface

because it stops when a directrix reaches the boundary of the surface. Only a portion of the surface can be meshed and the covered area varies according to the chosen set of directrices. To overcome this difficulty, we consider the gridshell surface (see [fig. 3.12a](#)) as a part of a larger domain surface (see [fig. 3.12c](#)). Trimmed by a plane, this domain surface should give back the intended shape to build (see [fig. 3.12b](#)). Therefor, it is possible to mesh the domain surface (see [fig. 3.12d](#)) and to retrieve a Chebyshev net that cover completely the initial surface (see [fig. 3.12f](#)).

The method is easily extended to meshes with variable pitch. This idea was explored to find optimal grids with genetic algorithm by Bouhaya et al. [52]. It is worth to mention an attempt to extend this method for multilayer Chebyshev grids by Lefevre et al. [46].

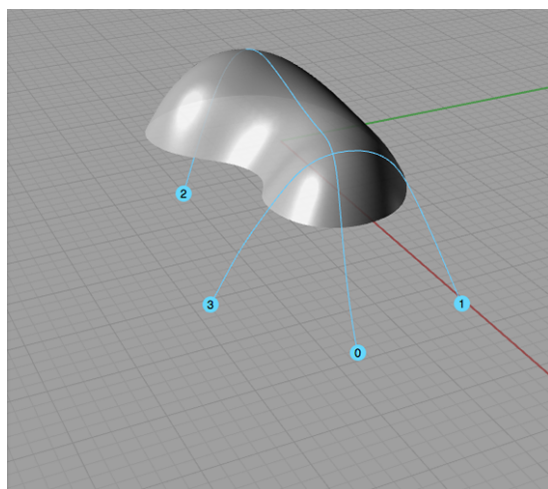
Numerical tool

Here, a specific software developed by du Peloux et al. [54] for *Rhinoceros* and *Grasshopper* allows generating this kind of mesh on any non-uniform rational B-spline surface (NURBS). It performs the following elementary operations : surface meshing with the compass method, trimming, control of the geometry's integrity and flattening of the grid (see [figures 3.12](#) and [3.13](#)). The tool also generates automatically a text file, which can be imported into a structural analysis software, containing all the required information to build programmatically the analysis model and then perform the formfinding of the structure (see [fig. 3.14](#)). In particular, an add-on feature facilitates loads application of various complexities (snow, wind, etc.), which is otherwise difficult in conventional analysis softwares for freeform structures. However, the tool does not provide any computation facilities itself and this is exactly the goal of the second part of this thesis.

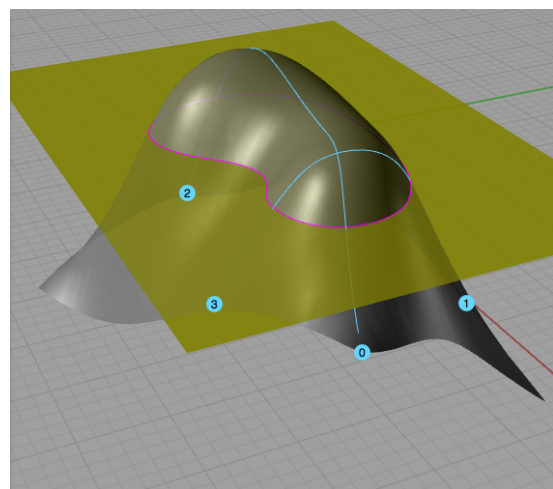
3.4.4 Formfinding and bending prestress

In the previous steps, the initial form was optimized and promising meshes for the materialization of the future gridshell were identified. However, the produced meshes do not take into account any of the mechanical reality, because only geometrical rules were used in their generation. The formfinding step consists precisely in finding the geometry of the grid at mechanical equilibrium, and the corresponding permanent bending stresses. The calculation is performed numerically thanks to a dynamic relaxation algorithm with kinetic damping and comprise the following steps :

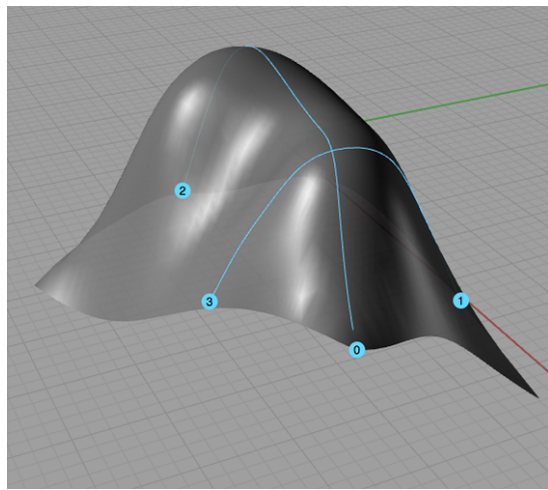
1. The grid is bent by a set of applied displacements from its resting position to the compass position.
2. The grid is then relaxed until it falls in its mechanical equilibrium.
3. Bending stresses of the triangulation are calculated relative to the geometry of the equilibrium.
4. Geometry and bending stresses of the triangulation are re-injected into the model in step 2.



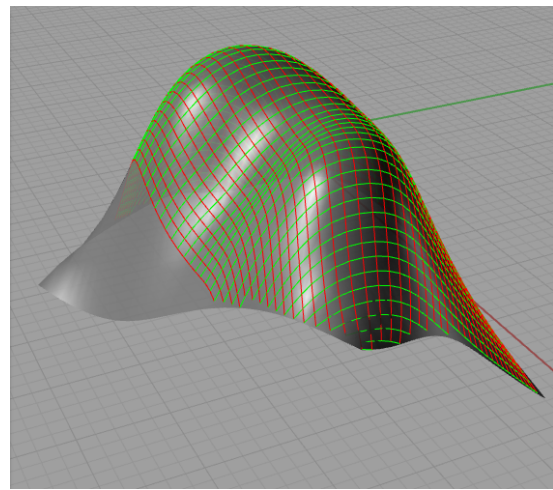
(a) Target shape



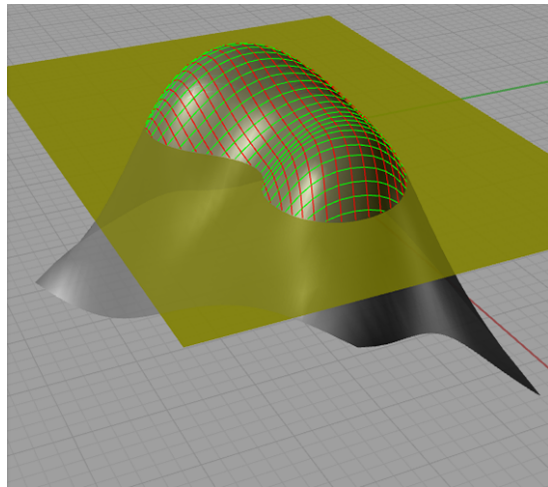
(b) Domain and trimming surfaces



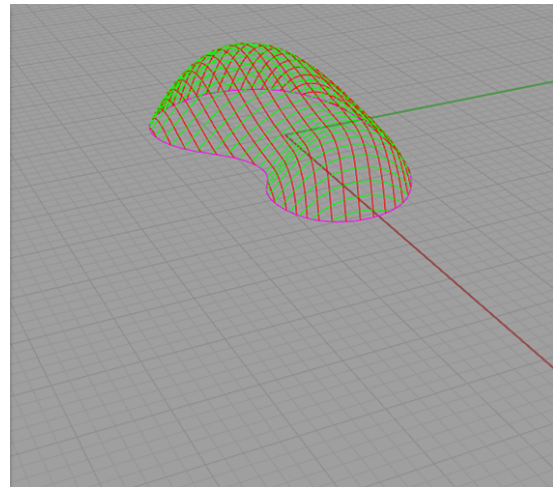
(c) Secant directrices



(d) Resulting mesh

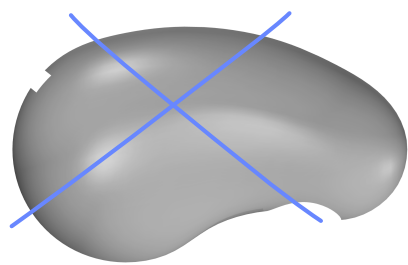


(e) Trimmed mesh

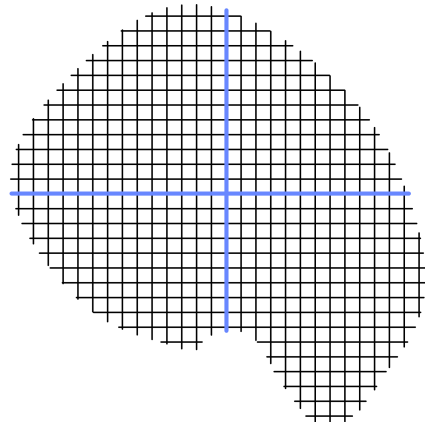


(f) Final grid

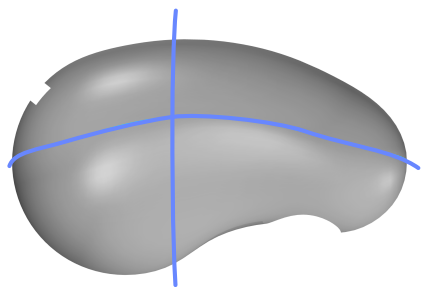
Figure 3.12 – The compass method step by step.



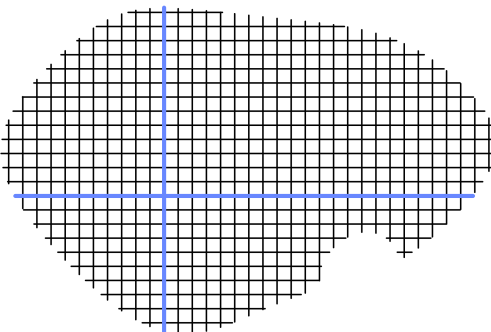
(a) First set of directrices



(b) First grid



(c) First set of directrices



(d) Second grid

Figure 3.13 – Each set of directrices leads to a different grid.

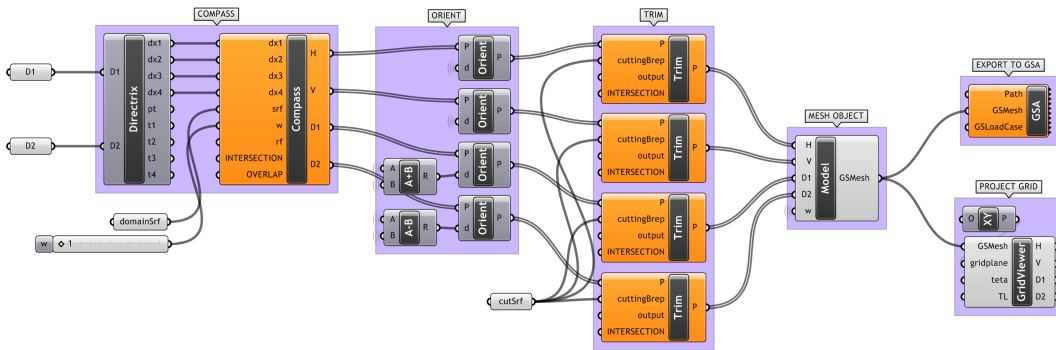


Figure 3.14 – Meshing software as a plugin for *Grasshopper*.

Two analysis models were built during this process to study the structure with and without bracing tubes.

The computations were realized with the formfinding module of the software Oasys GSA.⁷ It relies on a 6-DOF dynamic relaxation algorithm with either viscous or kinetic damping such as the one introduced in 2000 by Adriaenssens [37]. In practice, making the computations to converge was a really difficult and time-consuming task, highlighting the necessity of a dedicated formfinding tool with a higher level of interactivity. This issue that the coupling between rotational and translational degrees of freedom could cause ill-conditioning problems was already noticed by Adriaenssens and Barnes [40]. In the same paper, they proposed a 3-DOF element valid for torsion-free cases. Simpler and faster, it is also a lot more stable. This element was reused and extended lat1er for the formfinding of elastic gridshells in composite materials with complex connections by Douthe [10].

To tackle numeric instabilities the model had to be simplified :

- Connections between elements were modeled as rotation-free joints, enforcing only position constraints without taking into account the eccentricity between the tubes. This becomes a problem when it comes to evaluating the stability of the gridshell as eccentricity can play a major role [46]. This is also problematic when determining the production length of the tubes and the position of the anchorages (see §3.4.5).
- The triangulation could not be embedded from the start in the model and had to be treated separately and re-injected later on.

The formfinding process should not be regarded as a pure computational stage where only the equilibrium shape has to be found while all other design parameters are fixed. Indeed, as the goal is to find a suitable geometry with the most relaxed permanent bending stresses in the structure, this process could itself be employed to explore optimal geometries that will lead to more relaxed static equilibriums. In the present project the supports were allowed to move slightly around their target position by the mean of spring supports with

⁷<http://www.oasys-software.com/products/engineering/gsa-suite.html>

orthotropic stiffness. This allowed to decrease the overall level of permanent bending stress in the tubes while granting very minor changes in the geometry.

Finally the process converges when the shape and the pattern drawn by the mesh are suitable for the architect while the permanent bending stresses are acceptable for the tubes (see §3.5.4). The end results for this stage are presented in fig. 3.15. Note the smoothness of the mesh and the convergence of the tubes near the altar. Bending stresses are well distributed and inferior to the maximum design stress allowed (133 MPa in that case). Only few tubes are heavily loaded, in the areas where the curvature is the highest.

3.4.5 As-built geometry

Although, the eccentricity ($e = 136$ mm) remains small compared with the span of the shell ($l = 17$ m), it is not negligible compared with the mesh size ($w = 1.0$ m). Thus, the tube lengths and anchorage positions could not be determined with sufficient accuracy without taking into account the thickness of the structural grid due to this eccentricity. The employed method, purely geometrical, assesses that the neutral fibre of the shell is equidistant from the first two layers of pipes. The form-finding is performed only with those two layers. Connection axes has to be parallel to the local normal of the shell surface. This assumption was not exact, but, in this case, gave sufficient accuracy. The red pipe was offset by $-e/2$, the green by $+e/2$ and the blue by $+e/2$ along the surface normal.

3.4.6 Structural analysis

A full structural analysis is finally performed on the gridshell, using the two mechanical models created previously during the formfinding stage. The non-braced model is used to check the grid's behavior during the construction stages. In particular, it must be verified that the primary grid - the one with no triangulation tubes - has no risk of buckling, both for obvious safety reasons and to ensure the accuracy of the final geometry. Indeed, the more the form is likely to buckle, the more it can be triangulated in a buckled geometry different to the targeted geometry. The model with the triangulated grid is used to confirm the gridshell complies with all the structural requirements during its lifetime. Its behavior under standard loadings is evaluated.

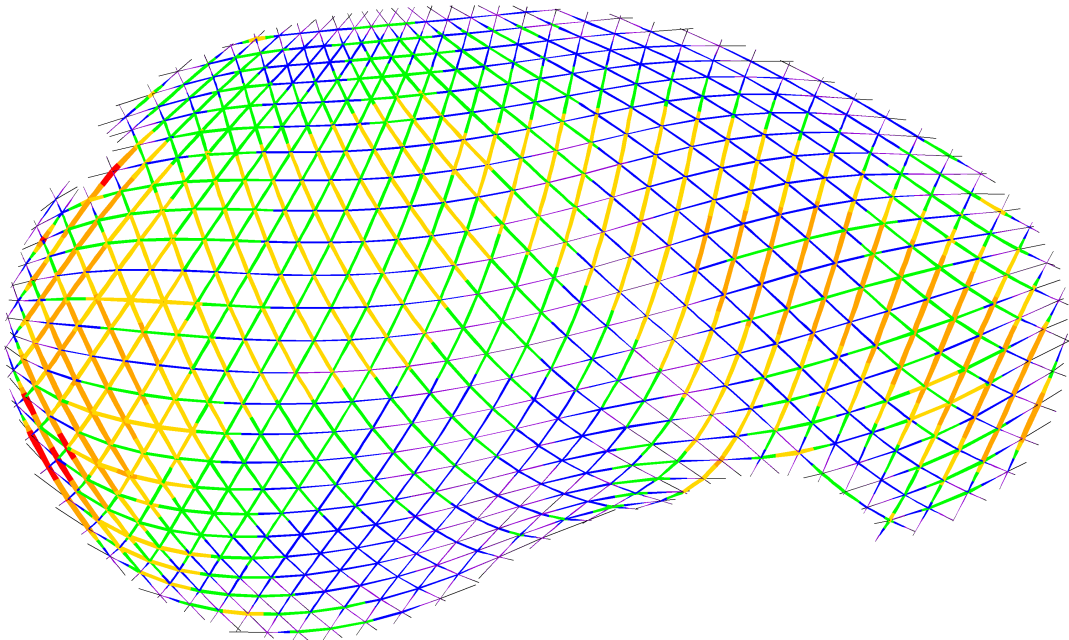


Figure 3.15 – Permanent bending stresses in the structure under self-weight (red tubes : 130 MPa).

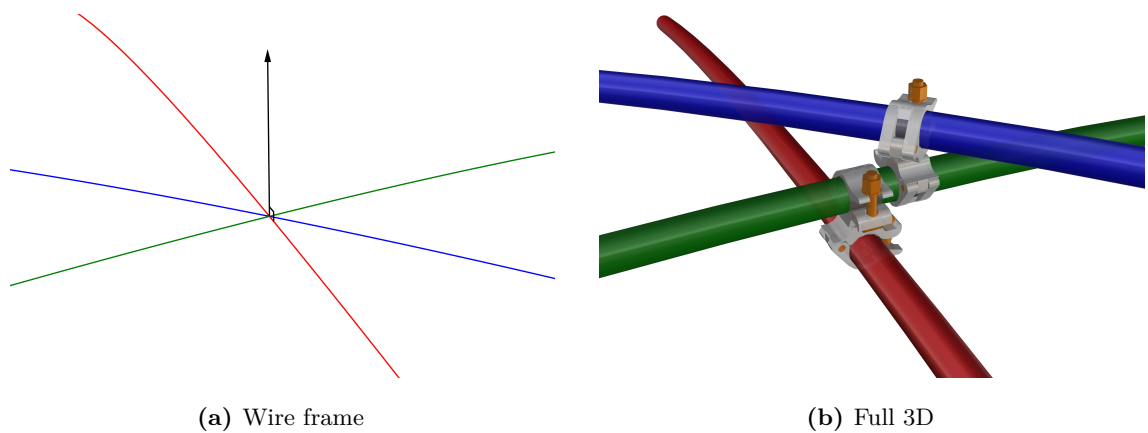


Figure 3.16 – Reconstruction of the full 3D geometry.

3.5 Designing with GFRP materials

This section focuses on the GFRP tubes employed for the structure. We present how we managed to deal with this composite material in the eyes of the existing regulatory framework although there is no applicable norms for composite materials (see §3.5.2). Beyond the administrative strategy, we present how their flexural strength was evaluated (see §3.5.3) and how the corresponding partial safety factors were determined (see §3.5.4).

3.5.1 Properties of the tubes

The technical properties of the tube employed for this project are given in tab. 3.2. Although these data were provided by the manufacturer at the time of the project, a test campaign was done to verify the flexural resistance of the tubes taking into account the influence of the swivel couplers clamped on the tubes (see §3.5.3).

3.5.2 Codes for composite materials

Beyond the technical difficulties related to both design and structural analysis of the shell, the regulatory framework was a vital issue for the success of the project. As it was the first time a structure of this kind was going to host a large number of people for over two years, the question of its reliability over time was a major issue. In order to be built, the gridshell had to comply with existing standards, which do not take into account such an innovative edifice, all in composite material. The strategy adopted to bypass this obstacle is presented herafter.

First level : administrative classification of the building

The first level, administrative, consisted of obtaining from the French authorities an appropriate classification for the building, taking into consideration the project's real-time requirement : a light-weight structure with a short lifespan. As expected, the structure was classified as a "building open to the public" (EPR in French) from the category "big tops and tents" (CTS in french) [67]. In this classification, construction procedures and regulations are adapted to the short lifespan of buildings.

Second level : compliance with existing standards

The second level, normative, consisted of ensuring that most of the existing regulatory framework justified the compliance of a structure that would not, at first sight, be considered by standards that do not include composite materials.

As far as possible, the design was made in compliance with the Eurocode, where the structural design is done according to the limit states under normalized loadings (self-weight, snow, wind, etc.). Although, the Eurocodes do not directly take into account composite materials, they propose some probabilistic methods to introduce new materials

Item	Standard	Polyester Mat-Roving-Mat
External diameter		41.7 mm
Internal diameter		34.7 mm
Wall thickness		3.5 mm
Section area		$4.20 \times 10^{-2} \text{ m}^2$
Section moment of inertia		$7.7259 \times 10^{-4} \text{ m}^4$
Torsion constant		$15.4518 \times 10^{-4} \text{ m}^4$
Shipping length		12.0 m
Glass content by weight	ISO 1172	60 %
Specic weight	ASTM D792	1.75 kg/m^3
Linear weight		0.735 kg/lm
Coefficient of thermal expansion	ASTM D696	$11 \times 10^{-6} \text{ K}^{-1}$
Tensile strength	ASTM D638	400 MPa
Tensile modulus	ASTM D638	26 GPa
Flexural strength	ASTM D790	400 MPa
Flexural modulus	full bending	25 GPa
Compressive strength	ASTM D695	220 MPa
Compressive modulus	ASTM D695	20 GPa

Table 3.2 – Technical properties of the tube.

Item	Standard	Précontraint 702 Opaque Alu
Yarn		1100 dtex PES HT
Weight	EN ISO 2286-2	830 g/m^2
Width		267 cm
Standard jumbo roll		50 lm or 300 lm
Finish		2-face acrylic varnish
Tensile strength (warp/weft)	EN ISO 1421	280/280 daN/5 cm
Tear strength (warp/weft)	DIN 53.363	30/28 daN
Elongation under load (warp/weft)	NF EN 15619	< 1 % / < 1 %
Adhesion	EN ISO 2411	10 daN/5 cm
Solar transmission	NFP 38511	13.5 %
Flame retardancy	NFP 92-507	M2
	DIN 4102-1	B1
Euroclass	EN 13501-1	B-s2, d0
Cold resistance	ISO 4675	-30 °C
Heat resistance	DIN 4102-1	70 °C

Table 3.3 – Technical properties of the membrane.

(EN1990, Annexe D). The mechanical properties of the GFRP pipe were determined as far as possible by tests in conformance with these methods. Alternatively, values were taken according from the Eurocomp [68].⁸ In some cases, such as for the sleeve, the construction design also benefited from this approach.

3.5.3 Flexural strength of the tubes

The characteristic flexural strength ($\sigma_{k,flex}$) of the GFRP tube was used to verify if the structure complied with the Eurocode. This parameter had a critical impact on the structure's reliability because in this particular application stresses in the tubes are mainly due to the bending. Thus, it was important to confirm the manufacturer's permitted value through testing. Three-point flexural tests were carried out with and without connections (see fig. 3.17) to determine the characteristic strength according to the Eurocode protocol (Annex D) :

$$\sigma_{k,flex} = \bar{\sigma}(1 - k_n \sigma_x) \quad (3.3)$$

For five tests, the factor $k_{n,5\%}$ is 1.80 assuming a normal distribution. It has been proved in [12] that the connections caused more scattering in the results. Finally, the manufacturer allowed value of 400 MPa was confirmed and retained for further calculations.

Connection	σ_1	σ_2	σ_3	σ_4	σ_5	σ_k
Without	456	441	445	460	477	430
With (20 Nm)	444	478	434	479	427	408

Table 3.4 – Flexural tests of the GFRP tubes (MPa).

3.5.4 Partial safety factors

The partial coefficients of material resistance (see tab. 3.5) used in the project were calculated according to the Eurocomp. The short-term coefficient proposed in Eurocomp ($\gamma_{st} = 1.3$) was increased to consider the critical stage of erection, where the deformations could not be controlled accurately. When dealing with long-term effects in permanently loaded, pultruded composite materials subjected to creeping and relaxation designers should be careful [61, 69]. In this project, this was reflected in the high partial coefficient for long-term effects.

⁸The Eurocomp is a kind of pre-standard intended for the structural design of buildings and civil engineering works using GFRP composites, consistent with the Eurocode approach. It is considered as the reference design code for GFRP materials.

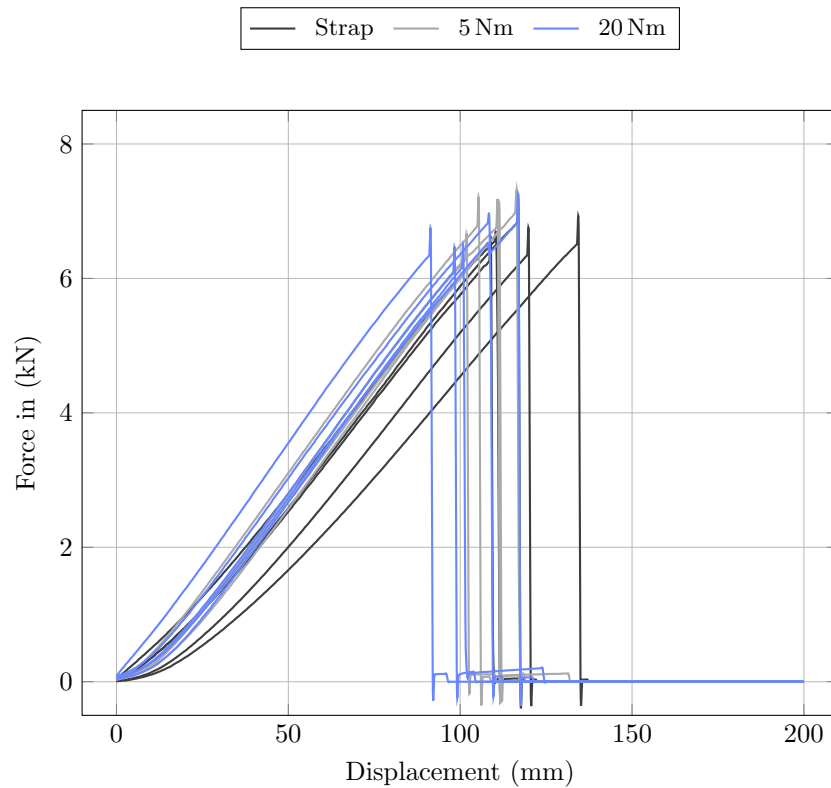


Figure 3.17 – Flexural test of the GFRP tubes. Results from [12].

Time scale	γ	σ_d
Short-term	2.0	200
Long-term	3.0	133

Table 3.5 – Short-term and long-term values for material resistance. γ is the partial coefficient for safety factor. σ_d is the flexural design strength.

3.6 Construction details

In this project, one can identify 4 major structural details : the swivel coupler for connecting composite tubes to assemble the grid (see fig. 3.6a) ; the steel sleeve for connecting several composite tubes to obtain long members from initially short pieces of tubes (see fig. 3.6b) ; the ground anchorages for fixing the structure to the concrete slab (see fig. 3.6c) and the lacing edge beam of the fabric (see 3.6d). The challenging issue of connecting the steel and composite parts was solved similarly sleeve and anchorage details.

3.6.1 The swivel coupler

Tubes are connected together with scaffold swivel couplers (see fig. 3.6a). Each connection is composed of two collars ($\varnothing 42$ mm and 38 mm wide) linked by a steel axis (see fig. 3.18). Thus the collars can freely rotate around the axis of the connection. This degree of freedom is responsible for the lack of in-plane shear stiffness of the primary grid and this is precisely this mechanism that allows the flat grid to deform into a free form surface. Each collar is itself composed of two hemicylindrical parts so that it can be opened to easily engage a tube. A M12 nut and a swivel T-bolt allow to lock the tube in the collar using friction. Collars are positioned over a 1.5 mm thick epdm ribbon wrapped around the tubes (see fig. 3.18). Once clamped in the connection, the tubes are spaced by a 68 mm distance from axis to axis. Although the mechanical consequences of this eccentricity could be neglected to a first-order approximation, this is not the case for the geometric consequences it induces as explained in §3.4.5.

Interface layer

This coupler is made to assemble two scaffold steel tubes together. Workers should tight strongly the collars of the coupler to ensure that the steel tubes won't slide in their collar. Here, it is clearly impossible to do that. Indeed the GFRP tube is to thin (only 3.5 mm thick) and tightening the collars to the maximum would damage it or even make it collapse. However, preventing the connections to slide along the tubes is critical to maintain the in-plane shear degree of freedom of the grid. If connections would slide, the grid would probably not deploy in space as intended. The grid kinematic would be blocked at some points, developing high stresses that would lead to breakages. To maintain a sufficient level of sliding resistance while preserving the material integrity it was decided to introduce an interface layer to :

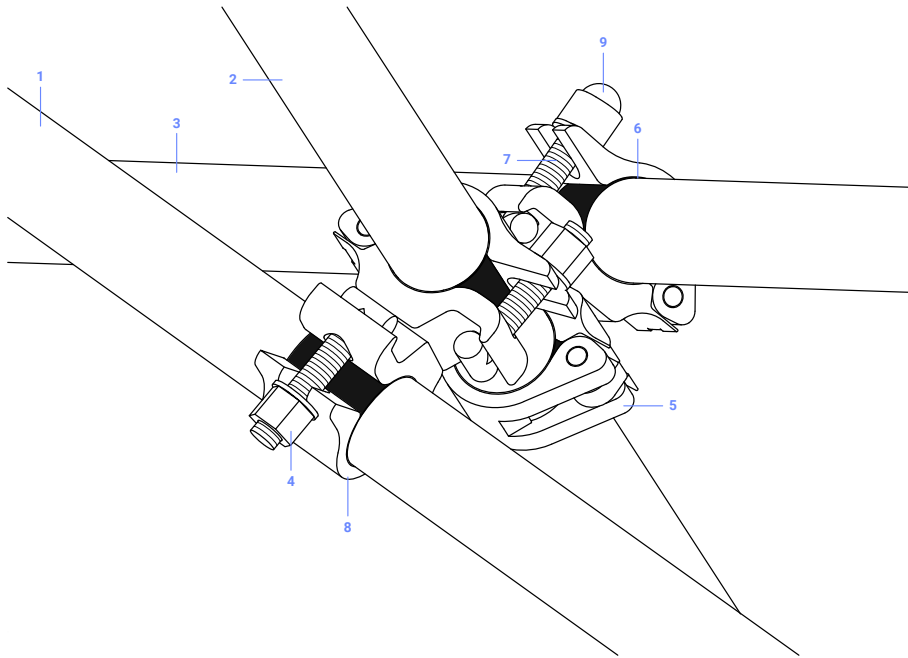


Figure 3.18 – Technical drawing of the swivel coupler. GFRP tubes (1, 2, 3). Swivel couplers (5, 8). EPDM layer (6). M12 swivel T-bolt (7). M12 nut (4) and plastic cap (9).

- increase the poor friction coefficient between the steel collar and the GFRP tube ;
- improve the distribution of stresses generated by the transverse compression of the collar over the tube, thus allowing a stronger clamping of the collar.

Several materials were tested in different thickness. Some of the results are presented in [fig. 3.19](#). A 1.5 mm thick EPDM ribbon was found to be suitable for the design requirements of the project. This layer improves significantly the sliding resistance from about 300 N to about 1200 N. Once the interface layer had been chosen, further tests were conducted to determine the appropriate clamping for the connections. The aim was to maximize the clamping to get the best sliding resistance (see [fig. 3.20](#)) while preserving the integrity of the tubes. It was found that a tightening torque between 15 Nm to 20 Nm was the optimal solution [12].

Finally, the ribbons were ordered with a double sided tape (DST) face to facilitate their placement on the tubes. The influence of the temperature regarding the presence of the adhesive has been investigated. The results show that after 40 °C the scotch creeps and a loss of resistance occurs (see [fig. 3.21](#)). A recent thermal study of the structure has demonstrated that with no cooling system the temperature inside the building could rise up to 70 °C (see §3.7.1 and [figures 3.29a](#) and [3.29b](#)).

Benefits and drawbacks

This connection has the advantage to be available almost every where, to be really cheap and indestructible compare to the GFRP members. However, there are some drawbacks as

it is not tailor-made for this application :

- The weight of this part is 1.16 kg, which is very heavy compare to the lightness of the system. In this project, the weight of the swivel couplers represents one third of the overall weight of the structure. This could easily be reduced with a dedicated design.
- The actual design is not adapted to resist sliding. This is critical as explained previously. This problem occurred locally during the lifting of the grid and it was a pain to finish the deployment of the structure (see ??).
- Although the clamping of the collars enhance the resistance to sliding of the couplers, they also activate the ability to transfer some torsion to the tubes. Unfortunately, the tubes are very weak regarding this type of sollicitation (see tab. 3.2). A better design would propose a kinematics that allow the rotation of each collar around the axis of the connection and the axis of the tube.
- As the number of connections is quite huge, the clamping process should be at the heart of the design. The later has to guarantee that the workers will not damage unintentionally the structural members. If clamping would be found to be the way to go – which indeed might be an relevant option – the structural elements will have to be stronger to resist both clamping and torsion.

Furthermore, other design criterion should be taken into account such as the fact that the connection must not damage the membrane. This was resolved in the project thanks to plastic caps (see fig. 3.22). It is worth to mentionne that the problematic of the connection should be treated in symbiosis with the difficult question of the bracing and the covering as it interacts with all the key parts of the system : grid, bracing and membrane. Some propositions to this complex problem were designed and tested during this thesis and are presented in ??. A noticeable design attempt was proposed in the roof of Chiddingstone's orangery ??.

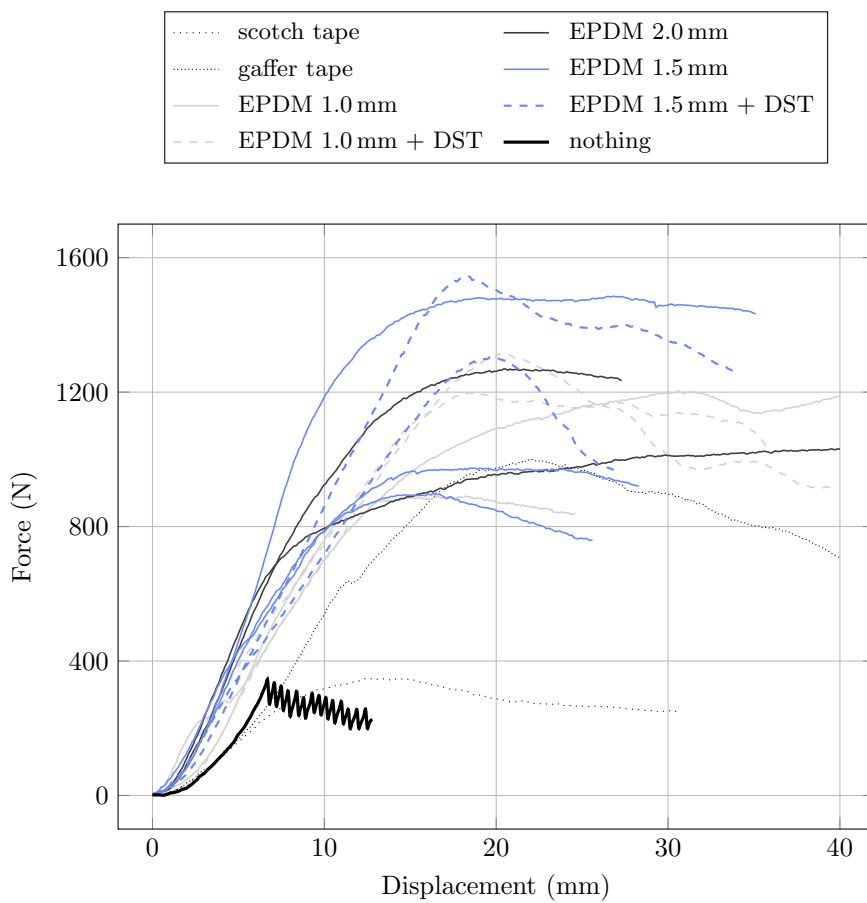


Figure 3.19 – Influence of the interface layer on the sliding resistance (5 Nm). Results from [12].

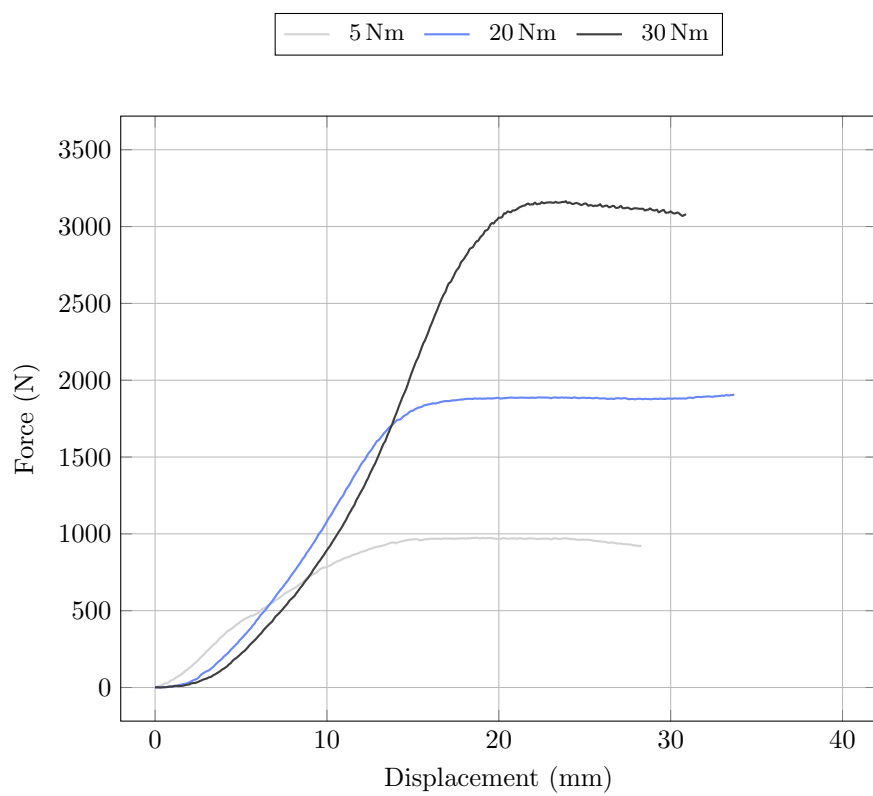


Figure 3.20 – Influence of the tightening on the sliding resistance for a 1.5 mm EPDM layer. Results from [12].

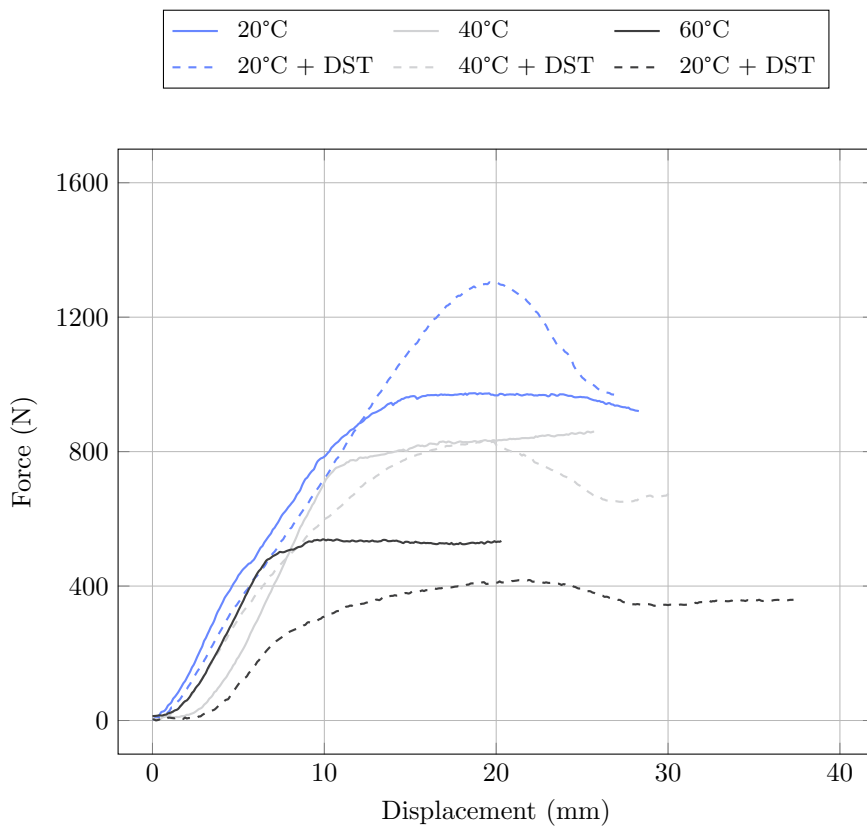


Figure 3.21 – Influence of the temperature on the sliding resistance for a 1.5 mm EPDM layer.
Results from [12].

3.6.2 The sleeve system

Sleeves are major components in the structural system. The presented design is an important innovation compared with the composite gridshells built previously, where members were simply interrupted or overlapped (see [fig. 3.23a](#)). By establishing mechanical and architectural continuities between tubes, the new sleeve system brought the real behavior of the shell closer to its theoretical behavior (see [fig. 3.23b](#)).

The sleeve is a steel system that provides mechanical continuity between two adjacent composite tubes for both tension and bending. It is made of three parts : two connectors linked by a threaded rod (see [fig. 3.22](#)). Each connector is a 48.3 × 2.9 mm steel tube, slightly larger than the composite tubes it connects, with a welded M20 nut at one end. The connector is pinned to the composite tube with three 10 mm bolts. Some structural adhesive was also employed to fill the gaps and to guarantee good rigidity of the assembly. However, the sleeve is designed to ignore the contribution of the adhesive to the mechanical strength of the system. A M20 threaded rod links the two connectors. It allows tension forces and bending moments to pass from one tube to the other. It does not transfer any torsion.

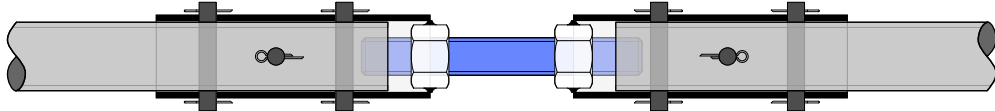


Figure 3.22 – Technical drawing of the sleeve system.

Mechanical behaviour

Tension forces are transferred from the composite tube to the connector through shear in the pins. Owing to a lower bearing resistance in the composite than in the steel, each of the three pins could be gradually loaded. When loading the system, initially, only one of the three pins is in contact with both the steel tube and the composite tube, because of inevitable minor manufacturing gaps. When the axial load is increased, this pin started to “eat” into the composite tube until the second pin also comes in contact. Thus, the axial load is transferred equally between the two pins. This scheme could work for more until another failure mode occurs. For this mode of composite failure, which prevailed in this case, the total bearing capacity of the assembly was thus three times the capacity of a single pin. This total bearing capacity can be calculated from the compressive strength, the composite thickness and the pin diameter :

$$F = 3 \times f_{u,c} \cdot d \cdot t = 3150 \text{ daN} \quad (3.4)$$

In the next section, tests carried out at the Navier laboratory to confirm the predicted value are presented. Bending moments were transferred through the threaded rod of the sleeve. This part was designed to reach the two following qualitative criterions simultaneously :

- Firstly, the bending stiffness of the rod should be roughly equivalent to the composite bending stiffness to preserve the curvature's continuity along the system (see [fig. 3.23c](#)). This continuity was of prime importance from an architectural point of view.

$$\frac{EI_{rod}}{EI_{gfrp}} \simeq 1 \quad (3.5)$$

- Secondly, the steel quality of the rod should be adjusted such that plastification begins when the composite tube tends to approach its maximum design stress (a third of the yield stress). Thus the rod acted as a “fuse” : if the curvature of the system reaches the maximum allowed curvature, the steel rod starts their plastification. The plastic hinge accumulates the rotation thus preventing the curvature to increase in the composite tubes (see [fig. 3.23d](#)).

$$\frac{M_{rod}^{elastic\ max}}{M_{gfrp}^{\sigma=133\ MPa}} \simeq 1 \quad (3.6)$$

In this project, the numerical values for the ratios in [eq. \(3.5\)](#) and [\(3.6\)](#) were 0.79 and 0.96 respectively.

Testing the load-bearing capacity of the pinned connection

[fig. 3.25](#) shows the tensile test of a three-pin connection between a connector and the corresponding composite tube. The graph reflects the elastic behavior of the composite tube up to 35 kN, with slight deviations corresponding to the rearrangement of the pins. The compressive stress applied by each pin to the composite tube exceeds its compressive strength. Progressively, the pins are pulled through the tube under a residual force that tends to stabilize at around 20 kN.

The theoretical failure modes of a bolt in a pultruded profile are given in [70] and are illustrated in [fig. 3.26](#). For the present design of the sleeve system, the observed failure modes were tearing (see [fig. 3.24a](#)) and contact compression (see [fig. 3.24b](#)). Note that this last failure mode is necessary to cumulate the load bearing capacity of each pin.

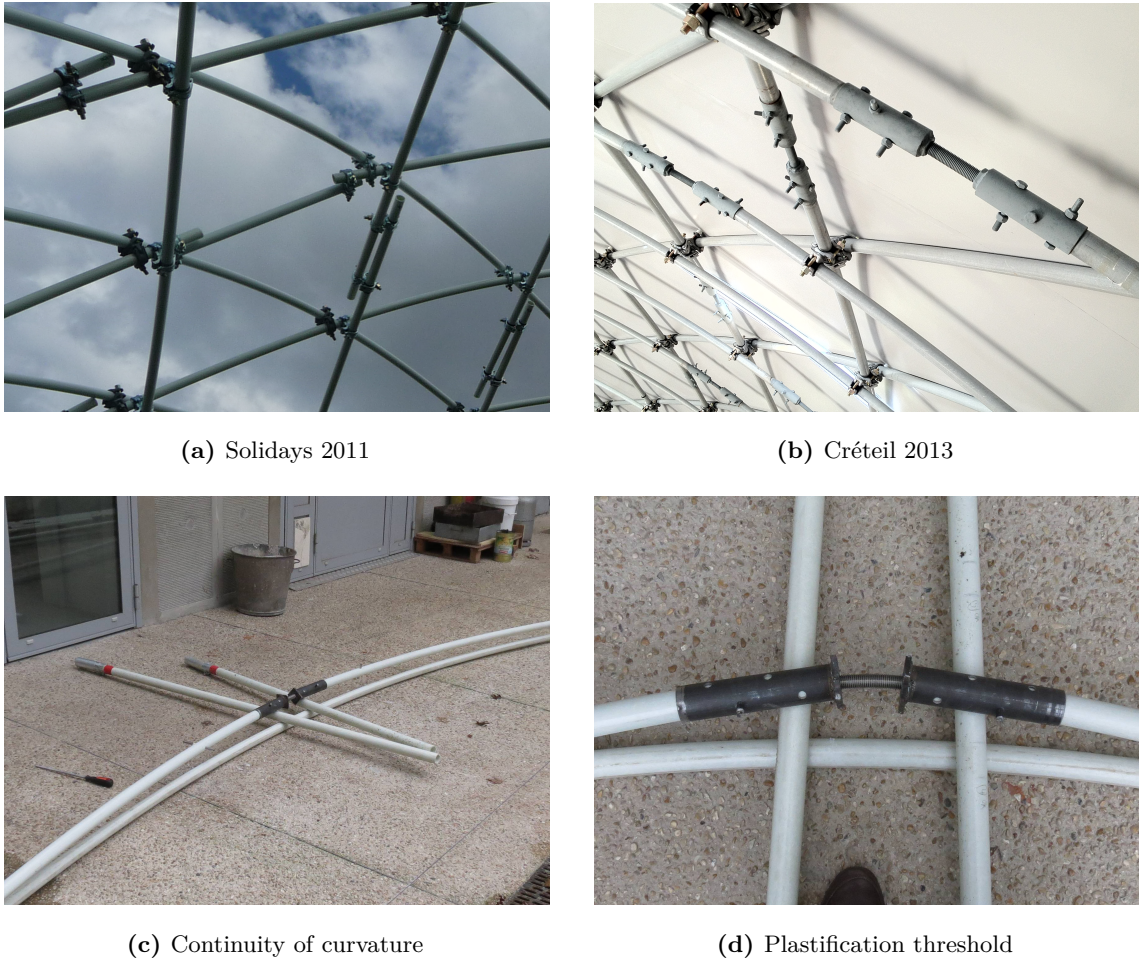


Figure 3.23 – Design and behavior of the the sleeve system.

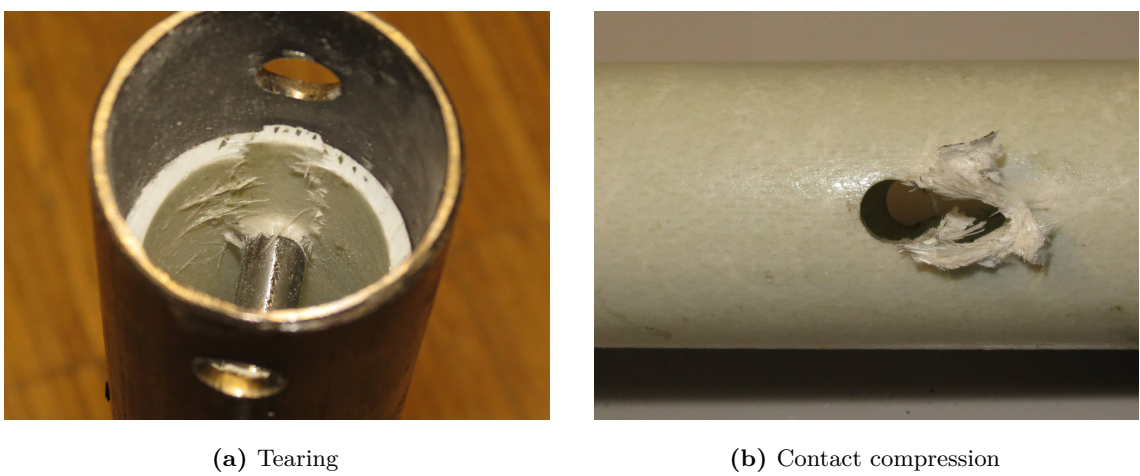


Figure 3.24 – Typical failure modes when testing the sleeve system in traction.

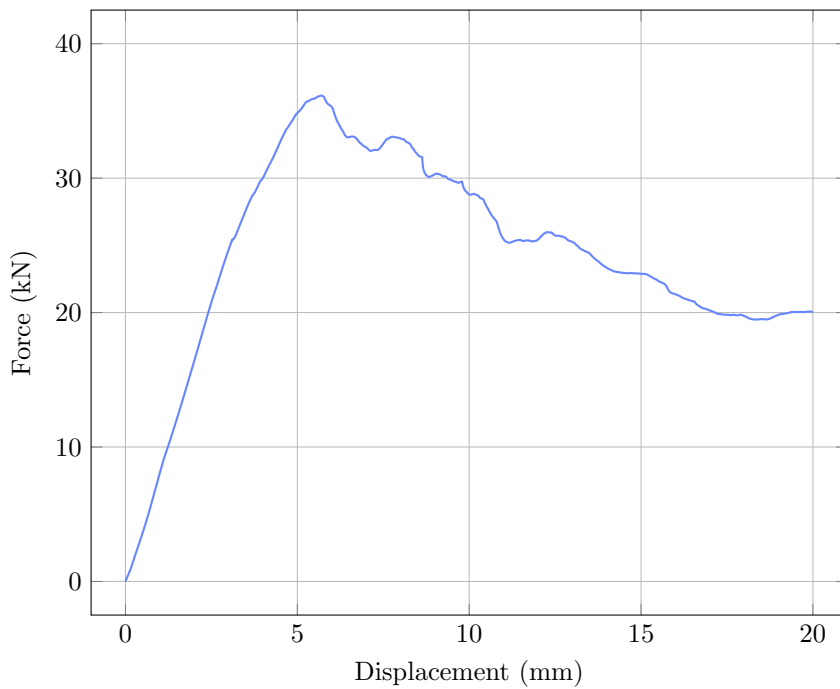


Figure 3.25 – Tensile test of the pinned connection. Results from [12].

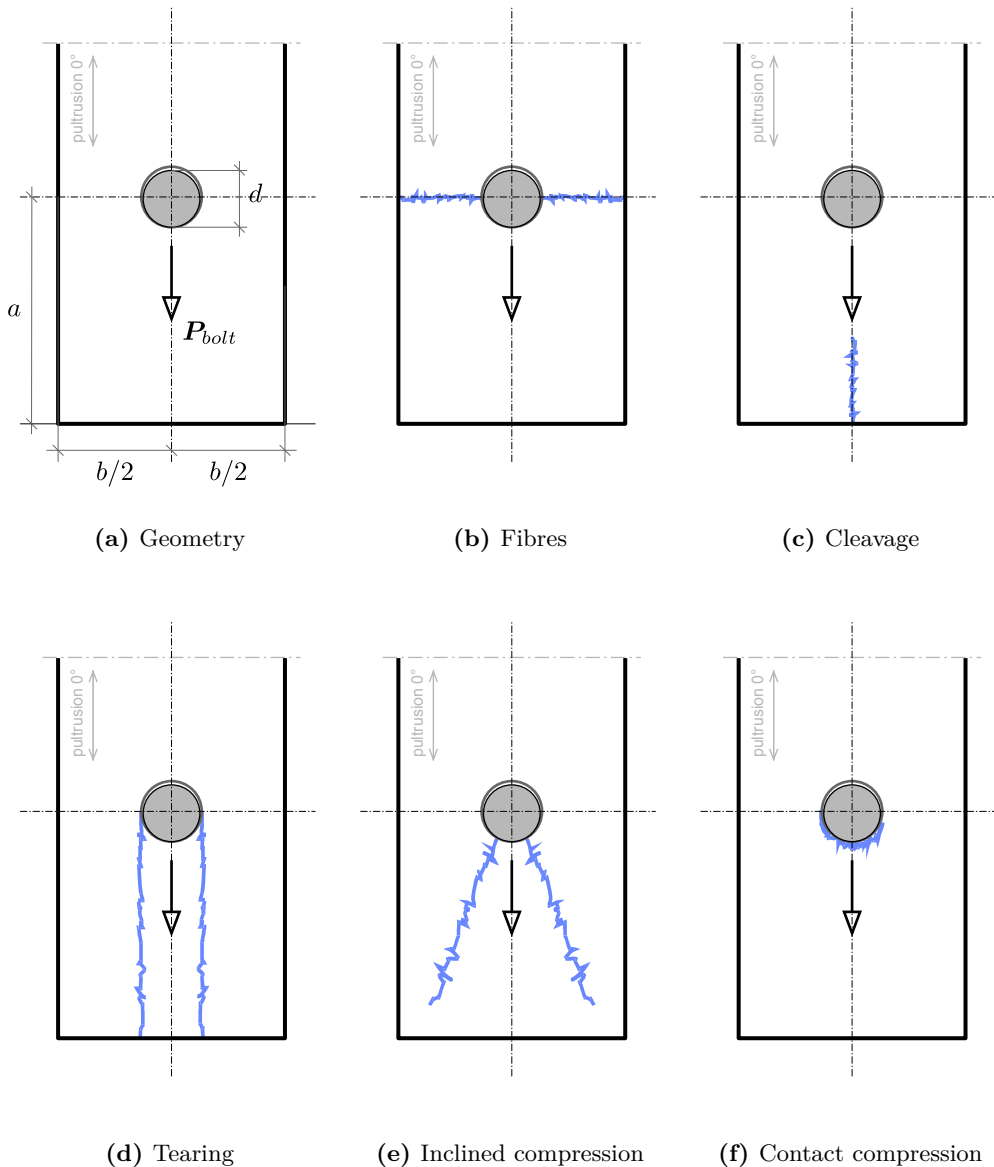


Figure 3.26 – Typical failure modes of a bolt in a pultruded element (0°).

3.6.3 Foundations

The detail of the footing was of major interest because it concentrated lots of technical difficulties and also had a strong visual impact (see [fig. 3.27](#)).

In the detail, the gridshell is fixed to the concrete strip thanks to the steel anchorages (6-15). Only the first tow layers of tubes are fixed to the ground or doors (4, 3). The anchorage is made of two parts : a steel connector (7) is pinned (6) to the composite tube (4) and equipped with a rotating steel clevis (9) ; a steel plate (15) is pinned to the concrete strip footing (26) and mounted with a vertical rotating steel clevis (11). The gridshell is connected to the ground by pinning the two parts of the anchorage. The three axis of rotations of the anchorage system – one for each clevis axis and one for the axis of the commun pin – allow to accommodate any orientations of the tube. More over, the rotation of the clevis is ensured by simple bolts (9,12) and nuts (8,13) that allow some adjustments in length. The system provides a quick and easy fixing of the gridshell capable of all the necessary adjustments required in real mounting conditions.

The membrane (1) is laced (17) to a composite rod (19). This rod is bent and clamped every 800 mm in a fixed scaffold collar (20) anchored in the concrete strip footing thanks to a steel part (21). This is a clever way to get a nice curved lacing rod at the bottom of the structure. The membrane strip (18) that ensures waterproofness is deported backward so the lacing remains visible. This has a strong and elegant visible impact. This detail runs all around the structure and is reproduced around the doors. This element is subject to heavy shear forces from the tension of the lacing (around 150 daN/lm) and this is why we chose a rod instead of a tube with a hollow section.

Thanks to the membrane strip and to a small step in the concrete slab (22) the water is evacuated into the drain, a simple trench full of gravels with two perforated flexible plastic pipes at the bottom.

3.6.4 The membrane

The membrane is nothing but a tailor-made one-piece clothing manufactured to dress up the structure. It was prefabricated based on the 3D model of the shape computed during the formfinding process (see ??) and not on some on-site geometric survey. The technical properties of the PVC coated fabric can be found in [tab. 3.3](#).

3.6. Construction details

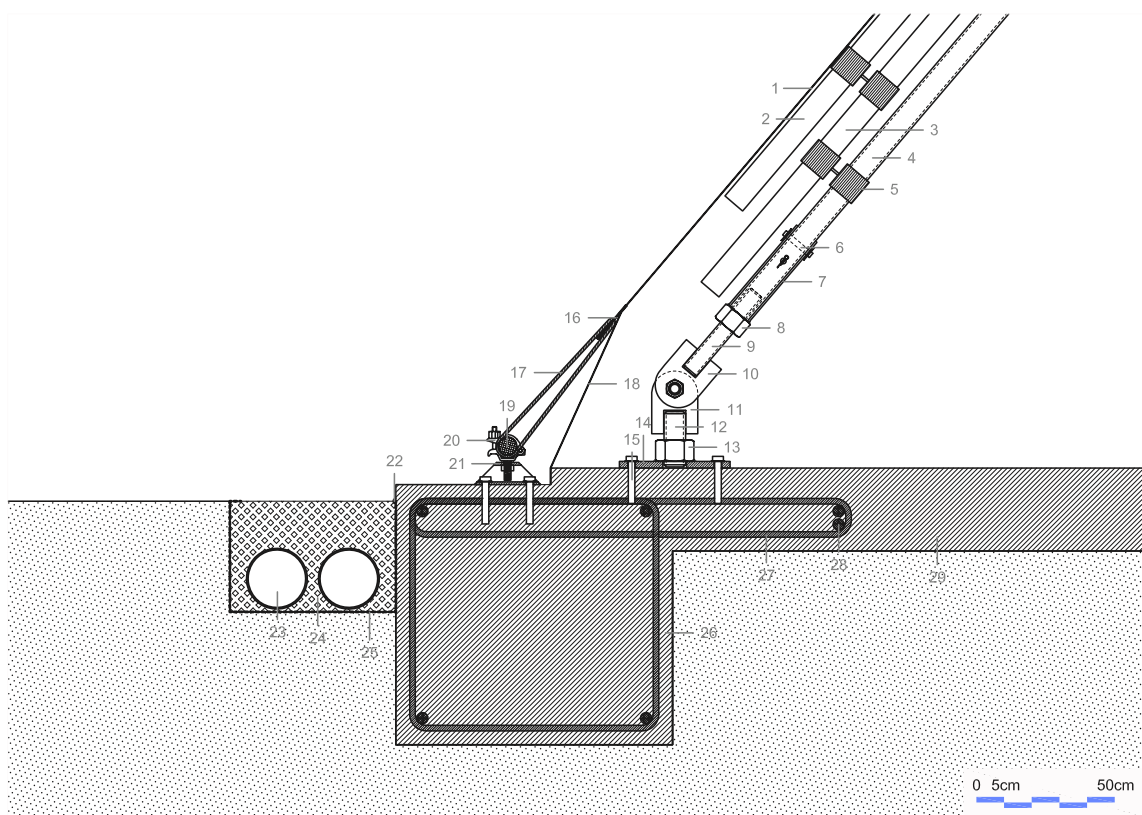


Figure 3.27 – Technical drawing of the footing.

3.7 Hygrothermal behavior

3.7.1 Temperature

During the first two years and a half of its service life, the building has shown that the thermal comfort was far from ideal as the membrane has very poor thermal properties (see [tab. 3.3](#)) :

- During winter, the comfort is ensured during mass by a forced-air heating system positioned on the equipments slab, few meters away from the main structure. This solution is adapted to infrequent occupations of the building. In that case, the energetic cost remains limited even if the solution is far from optimal because of the lack of insulation.
- During summer, the temperature raises very fast when the sun shines. The forced-air system is used to ventilate the interior volume. But the comfort level is rapidly insufficient as the interior temperature quickly exceeds 30 °C. The discomfort is amplified as the membrane gets very hot and radiates toward the inside, increasing the feeling of warm. Consequently, there was no choice but to scheduled the mass earlier at this period of the year. Cooling was not possible for economic reasons as the building was used only few hours a week.

At the time of writing, the building is being reconfigured and so its purpose is changing. A better thermal comfort is now required and solutions have to be found. Thus, a study on the thermal behavior of the structure has been done.⁹ The main results are gathered in this thesis. [fig. 3.28a](#) presents the monthly exterior temperatures observed at the site location from 8:00 AM to 7:00 PM, which corresponds to the new intended opening hours of the building. Note that the maximum value is given over one hour, that is the observed temperature exceeds this value during a one-hour-wide window in the day. The solar radiation is also given in [fig. 3.28b](#). Two scenarios are studied :

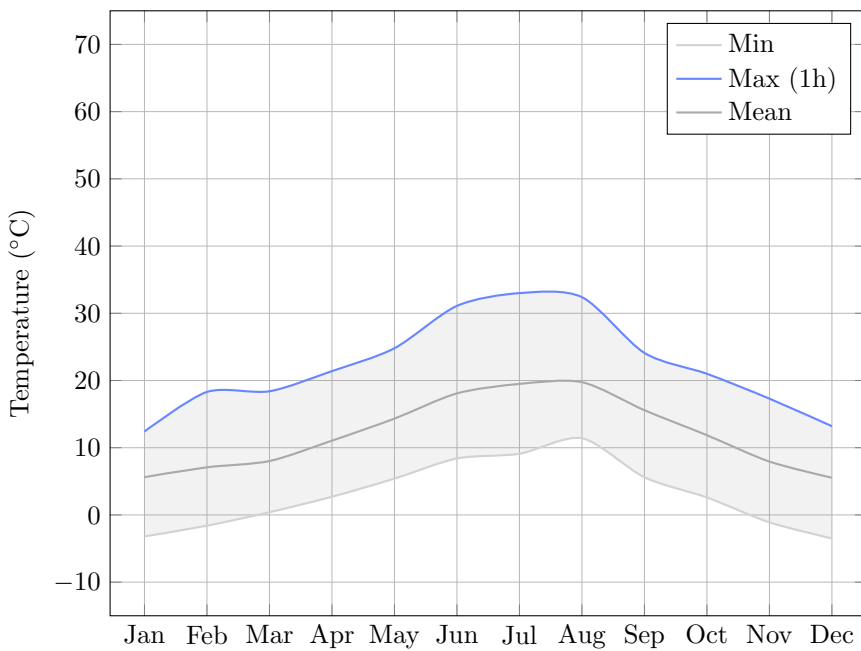
1. The structure is completely closed. No ventilation is put in place. The interior temperature can reach 70 °C (see [fig. 3.29a](#)).
2. The structure is ventilated but no cooling system is put in place. The maximum interior temperature is lowered significantly but it can still reach 50 °C (see [fig. 3.29b](#)).

This study confirms what the experience has shown : the temperature inside the building can be very high. Above 30 °C this is problematic for the comfort of the people. Above 50 °C and up to 70 °C it becomes problematic for the building itself. Indeed, this level of temperature is closed to the heat resistance of the membrane (see [tab. 3.3](#)) ; the interface layer faces a serious decrease of its capacity to resist to sliding ([fig. 3.21](#)) ; the creeping kinetics of GFRP tubes is speed up ([§3.5.1](#)).

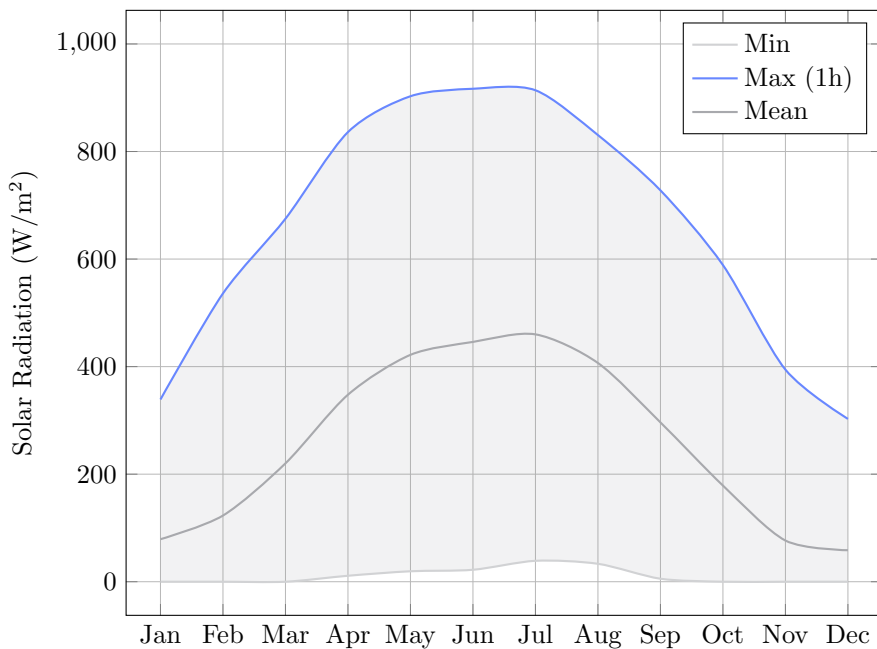
⁹This study was done in June 2017 by the design companies T/E/S/S and CHOULET for the reconfiguration project of the temporary cathedral.

3.7.2 Moisture

Condensation was also noticed in winter and shoulder season. Sometimes, droplets of water could fall abundantly and thus the wooden furnitures had to be protected. This phenomenon was particularly intense the first months because the concrete slab had not yet fully dry-out. To protect the structure and the furnitures, it was decided to maintain the inside temperature above 10 °C at all times.

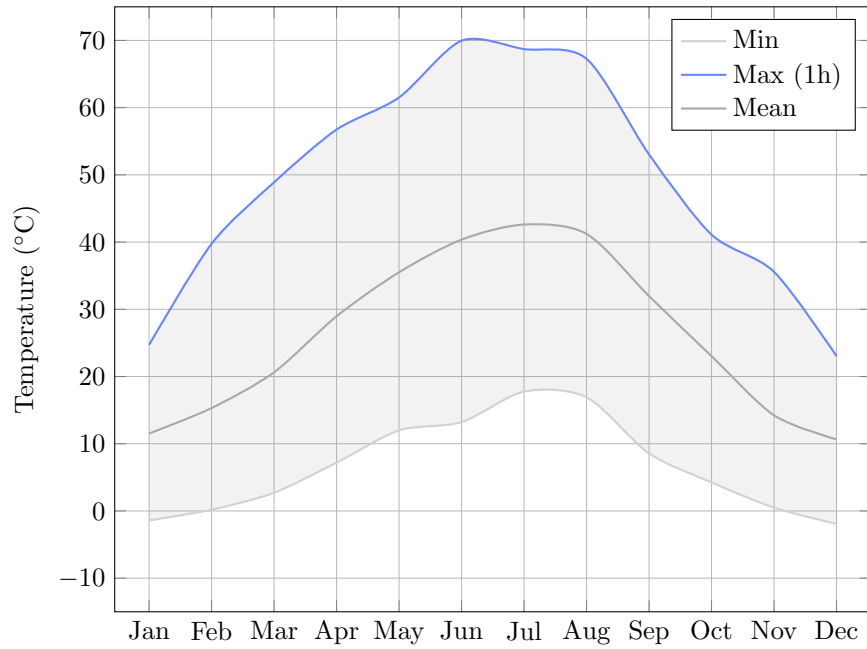


(a) Temperature.

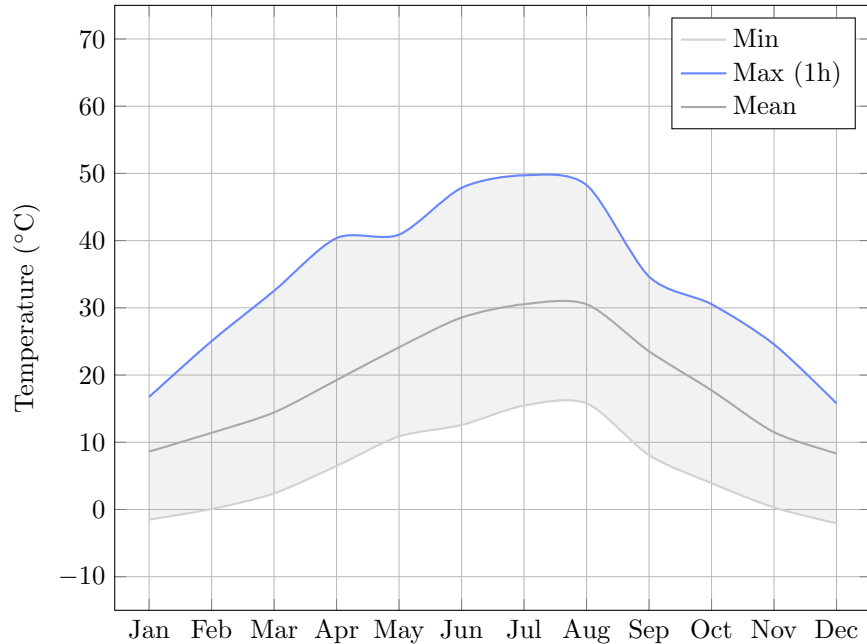


(b) Solar radiation.

Figure 3.28 – Weather data at site location during opening hours (8:00 AM to 7:00 PM).



(a) Without ventilation.



(b) With ventilation.

Figure 3.29 – Temperature inside the building during opening hours (8:00 AM to 7:00 PM).

3.8 Cost analysis

3.8.1 Overall cost for the client

The overall cost of the project – that is the amount of money paid by the client – was estimated to 324 000 € excluding taxes (see [fig. 3.30](#)). This price includes all the possible costs related to the construction of the project : the cost of the main building (masonry, doors, gridshell, envelop, fittings, heating, electricity, lightning, drainage, sewage, etc.), the cost of the service building, the cost of pedestrian pathways, the cost of the design studies, etc.

However, this cost does not take into account all the (free) man-hours spent by the volunteers to prefabricate, assemble, erect and brace the gridshell. The real cost of the gridshell system, when a cost is put on this labor, is estimated in [§3.8.2](#).

Moreover, this project required a lot of design studies and tests to verify the material properties and to validate the strength of key elements such as the swivel coupler with its EPDM layer, the sleeve system and the ground anchorage. The real cost of the studies was by far higher than what was really charged to the client and the difference must be regarded as an investment from the company T/E/S/S. In the same manner, people from the laboratory gave a consistent support during the construction stage as they were the only available experienced workers familiar with the construction of elastic gridshells in composite material [3, 27] and this labor was not charged back to the client.

The project was favorably accepted by the client based on the estimation that the cost of the gridshell would not be more expensive by 30% than renting a simple tent. The rental of a 400 m² tent with its floor was evaluated to 110 000 € for a period of time of 18 months. Retrospectively this target was met, especially as the cathedral was finally used for almost two years and a half, far more than the 18 months expected initially, and with no additional cost because the diocese owned the building

3.8.2 Cost details for the building

Here we present the cost details for the main building, that is the cathedral itself. We try to understand what is the true cost of the gridshell system in this particular project and we thus eliminate side costs (for instance the cost of fittings, the cost of the pedestrian pathways, the cost of the service building, etc.). The cost allocation is presented per square meter of covered area in [fig. 3.31](#). The total price for the building, excluding studies, is 473 €/m². It is composed of :

- 100 €/m² : the cost of masonry works (levelling, footings, slab, drainage) detailed in [tab. 3.7](#). This construction works were made by a professional contractor named BATEM.
- 248 €/m² : the cost of the superstructure (anchorages, gridshell, membrane covering and doors) detailed in [tab. 3.8](#). This price includes the labor of the volunteers

(35 €/hour) and all the costs associated to construction of the structure, including the renting of all the necessary equipments (cranes, aerial buckets, etc.).

- 126 €/m² : the cost of the envelope (lacing rod, fabric, installation) detailed in [tab. 3.8](#). This construction works were made by a professional contractor named ESMERY CARON.

Here, the global amount of studies was charged around 83 300 €, that is 248 €/m² (see [fig. 3.30](#)). This heavy cost was compensated by the fact that volunteers provided a lot of free labor (see [fig. 3.32](#)). In a more standard commercial context, the design process would be optimized too and the price of studies would go down to 15% to 20% of the price of the building, that is 70 to 95 €/m². This would bring the final price of the building to 550 €/m². This price is clearly high if only its sheltering capability is required regarding other technologies.. However, if more than sheltering is mandatory, the quality and singularity of the space created here is probably worth the price ; then this technology becomes a lot more affordable than existing traditional systems that can materialized free-forms.

3.8.3 Strengths and weaknesses

In this project the prefabrication process represents almost half of the cost in man-hours (see [fig. 3.32](#)). The manufacturing of the grid (cutting pipes, marking nodes, preassembling swivel couplers, sleeves and anchorages, etc.) could easily be automated. Composite materials such as GFRP are easy to cut, mill and drill. Small robot arms can do the job quickly with a better accuracy. This idea has been tested in a workshop at the Ecole des Ponts ParisTech in september 2016.¹⁰ More over, a numerical production process would allow to answer quickly to a variety of forms with the same equipment and industrial process.

Lots of man-hours are spent in the installation of the sleeve system (88 h). That represents 35 % of the man-hours spent in the grid prefabrication. This part should be reimplemented to allow a simpler and faster installation. Similarly, the connection should be redesigned to avoid the application of the EPDM protection layer and to allow a faster positioning and fastening as it represents 23 % of the man-hours spent in the prefabrication of the grid. This would also be a preponderant factor of improvement in the bracing stage although this cost is not detailed in [tab. 3.6](#).

At first sight it seems that the time spending assembling the grid on the construction site – which represents 22 % of the man-hours, see [fig. 3.32](#) – can not easily be reduced. However, the grid system could be divided into transportable modules. These modules would be preassembled in the factory to increase the speed and quality of the production and to minimize on-site works. Thanks to the intrinsic grid kinematic, modules can be folded for transportation. Once on site, modules are unfolded and connected to each other to form the primary flat grid. This idea was tested successfully in two wooden gridshell projects

¹⁰See the video of the construction of a 50 m² wooden gridshell in the workshop “Building Free Froms” : <http://thinkshell.fr/freeform-wooden-gridshell-2016/>.

of 50 m² each, with students of the Ecole National d'Architecture de Toulouse and Ecole National d'Architecture de Grenoble in June 2016.¹¹

Bracing is yet another costly stage as it accounts for almost 30 % of the man-hours (see fig. 3.32). This work is not easily parallelizable as it requires working at height with proper lifting equipments such as cherry pickers. Thus almost a small and qualified team can do the job. For instance, on the gridshell of Créteil, the team was composed of 6 workers using two aerial lifts. This team spent three full days to complete this task, that is the same amount of days required to assemble the grid and lift it up. Several attempt have been made during this thesis to answer this problematic. The first attempt was to use a bidirectional cable network to brace the grid. The network is installed at the ground level before the grid is deformed. Thus, work at height is reduced to a minimum. The second attempt is a larger thought on the envelope of such structures and tries to tackle two issues with a thin fibre-reinforced concrete skin : the fact that bracing with a third direction of tubes is time consuming ; and the fact that membrane covering is not adapted for permanent buildings.

¹¹Construction of two wooden gridshell pavilions : <http://www.lemoniteur.fr/article/a-toulouse-les-architectes-se-rassemblent-sous-le-meme-pavillon-32398196>.

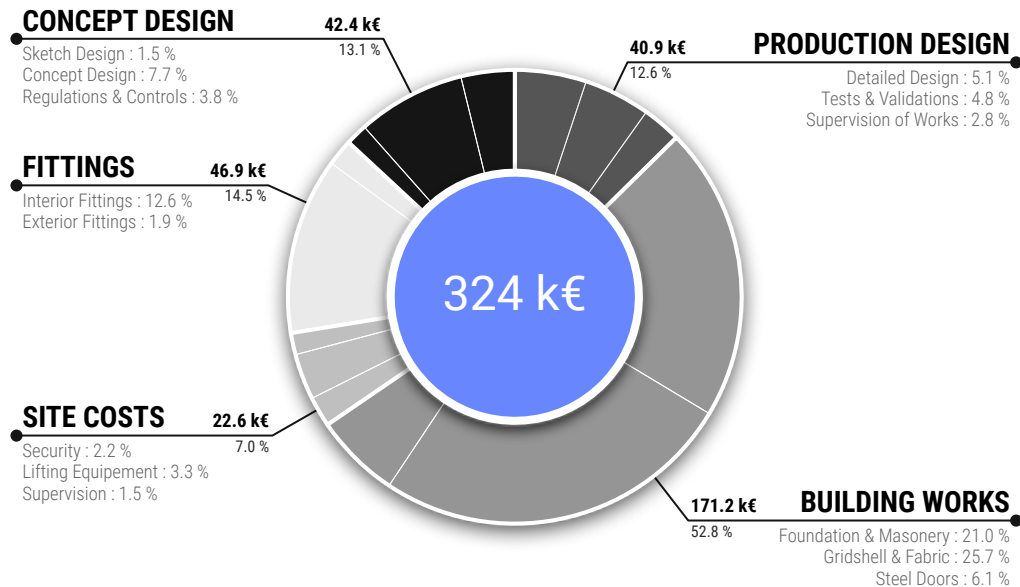


Figure 3.30 – Cost allocation for the whole project. This is the estimated overall final cost charged to the client. Prices are given excluding taxes (V.A.T).

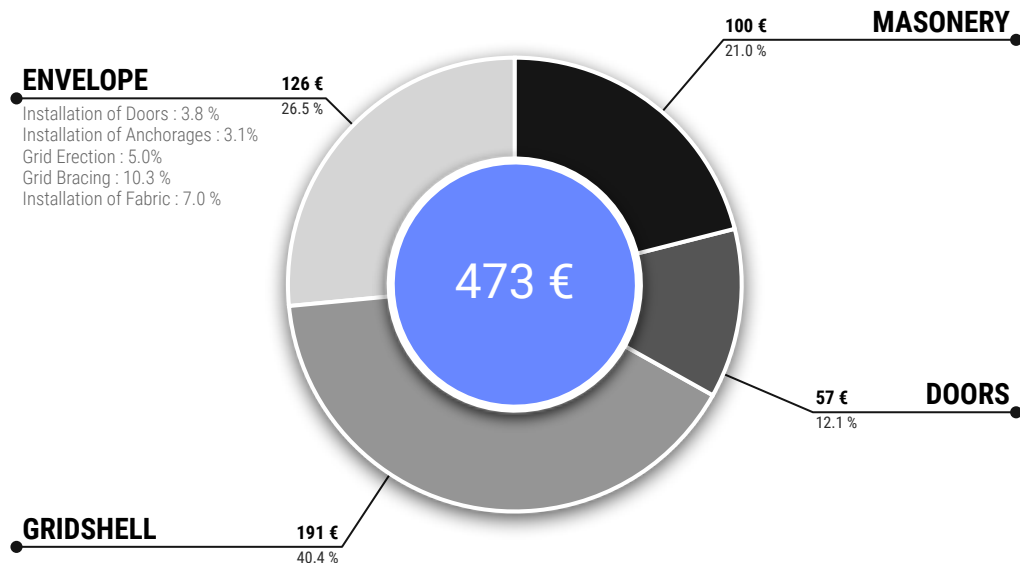


Figure 3.31 – Cost allocation per square meter of covered area. The cost of design is not included as it would not be representative. Prices are given excluding taxes (V.A.T).

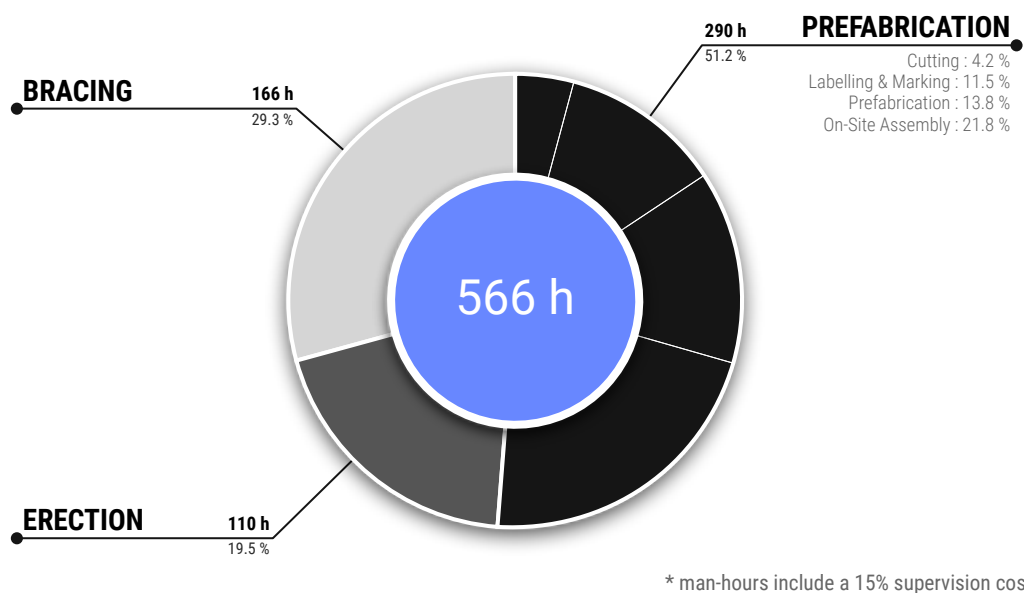


Figure 3.32 – Allocation of the man-hours spent by the volunteers on the fabrication of the gridshell. A 15% increase is considered to take into account coordination and supervision of the individual tasks. See [tab. 3.6](#) for detailed data.

3.8. Cost analysis

Item	Unit Task		Man-Hours	
	Worker	Duration	Quantity	Hours
Workstation “Cutting”	4			20.53
Pick a raw tube from the stock	2	1' 00"	176	5.87
Mark it and cut it at right length	2	2' 00"	176	11.73
Put it into the labelling stock	2	0' 30"	176	2.93
Workstation “Labelling”	5			56.64
Pick a tube from the labelling stock	2	1' 00"	176	5.87
Label it at start and end	2	1' 00"	176	5.87
Mark the position of connection collars	1	0' 30"	2260	18.83
Mark the position of sleeves	1	0' 30"	250	2.08
Mark the position of anchorages	1	0' 30"	127	21.06
Put it into the prefabrication stock	2	0' 30"	176	2.93
Workstation “Prefabrication”	6			67.75
Pick a tube from the prefabrication stock	2	1' 00"	176	5.87
Put the EPDM ribbon	1	0' 30"	2260	18.83
Prefix the swivel collar on the tube	1	0' 30"	565	4.71
Glue the sleeves	3	2' 00"	250	25.00
Drill pin holes for the sleeves	1	1' 00"	250	4.16
Fix sleeve pins	1	1' 30"	250	6.25
Put it into the final stock	2	0' 30"	176	2.93
Workstation “Site Assembly”	12			107.34
Connect the sleeves with steel rods	5	5' 00"	125	52.08
Pick a tube and position it in the grid	2	3' 00"	176	17.60
Install swivel couplers (HV)	1	2' 00"	565	18.83
Controlled tightening of couplers (HV)	1	1' 00"	1130	18.83
Workstation “Grid Erection”	12	8:00' 00"	1	96.00
Workstation “Grid Bracing”	6	8:00' 00"	3	144.00
Grid prefabrication				252.00
Grid erection				96.00
Grid bracing				144.00
Cost of supervision (15%)				74.00
Total				566.00

Table 3.6 – Man-hours spent by the volunteers on the fabrication of the gridshell. A 15% increase is considered to take into account coordination and supervision of the individual tasks. See [fig. 3.32](#) for a graphical representation of these data.

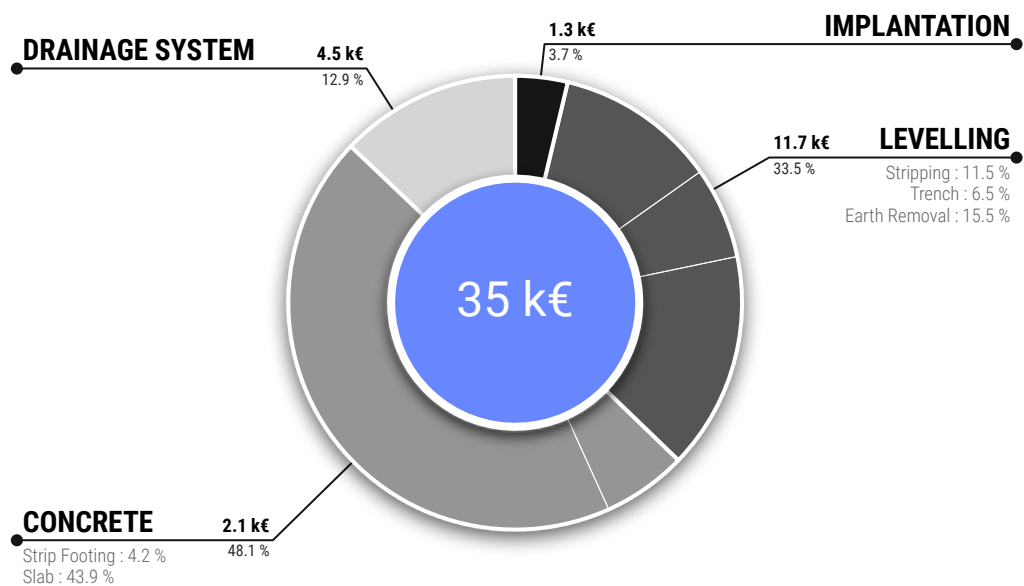


Figure 3.33 – Cost allocation for masonry works. Prices are given excluding taxes (V.A.T). Only costs associated to the structure are reported here ; for instance the works for the equipment slab and the pathways are omitted. See [tab. 3.7](#) for detailed data.

Item	Unit	Quantity	U.P. (€)	Price (€)
Building implantation		1	1 300.00	1 300.00
Leveling works				11 680.00
Top soil stripping	m ²	400	10.00	4 000.00
Trench for concrete strip footing	ml	76	30.00	2 280.00
Earth removal	m ³	180	30.00	5 400.00
Concrete				17 400.00
Concrete strip footing (200 kg/m ³ steel)	ml	70	30.00	2 100.00
Concrete slab (x2 welded wire mesh)	m ²	340	45.00	15 300.00
Drainage systems				4 500.00
French drain (x2 Ø100 mm pipes)	ml	70	30.00	2 100.00
Precast concrete inspection chamber		1	400.00	400.00
Drain line (PVC Ø125 mm pipe)	ml	30	30.00	900.00
Pre-assembled channel drain	ml	10	110.00	1 100.00
Masonry works	€/m ²	350	100	34 880.00

Table 3.7 – Cost details for masonry works. Prices are given excluding taxes (V.A.T). Only costs associated to the structure are reported here ; for instance the works for the equipment slab and the pathways are omitted. See [fig. 3.33](#) for a graphical representation of these data.

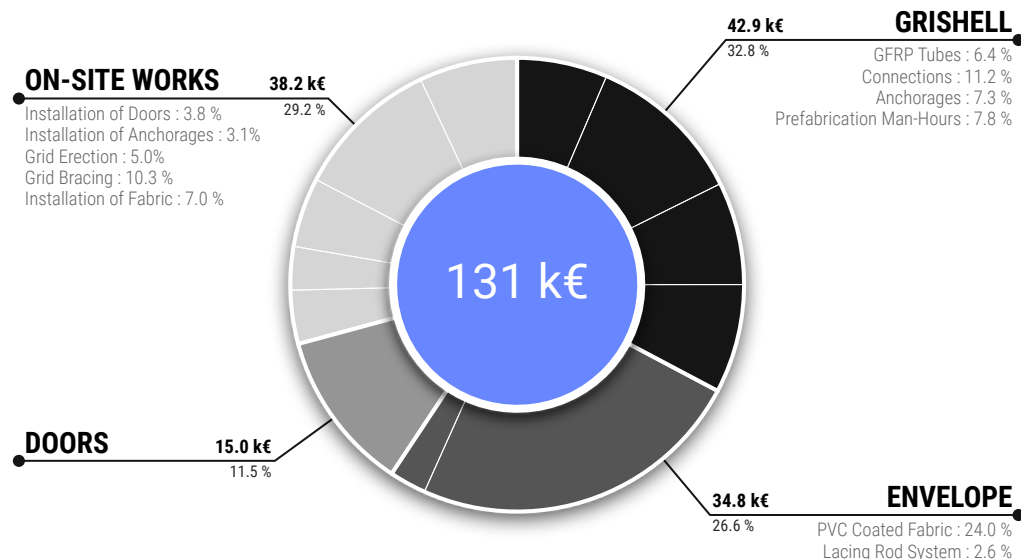


Figure 3.34 – Cost allocation for the superstructure. On-site works are isolated to identify pure manufacturing costs. To this end, the cost of the man-hours provided by the volunteers to prefabricate the grid has been assessed and allocated. See [tab. 3.8](#) for detailed data.

3.8. Cost analysis

Item	Unit	Quantity	U.P. (€)	Price (€)
Manufacturing of the gridshell				
GRFP tube (Ø42 mm)	ml	2304	3.66	8 433
Swivel connector (42x42 mm)		1295	3.95	5 115
Swivel connector (42x49 mm)		135	4.18	564
EPDM layer (1302x40x1.5 mm ribbon)		2775	0.36	1131
Welded steel sleeve system		150	50.00	7 500
ARALDIT 2047 glue (480 ml cartridge)		8	45.00	360
Ground anchorage (welded steel)		120	80.00	9 600
Man-hours (prefabrication)	h	290	35.00	10 150
Manufacturing of the envelope				
GFRP lacing rod (Ø32 mm)	ml	96	14.00	1 134
Steel clip for the rod		125	15.00	1 875
Swivel collar (Ø34 mm)		120	3.50	420
PVC coated fabric	m ²	550	50.00	27 500
Option for transparent inclusion		12	320.00	3 840
Manufacturing of the steel doors				
Main door		1	10 000.00	10 000
Small door		1	5 000.00	5 000
On-site works of installation				
Installation of the doors		1	5 000.00	5 000
Installation of the anchorages and clips	h	90	45.00	4 050
Grid erection	h	110	35.00	3 850
cranes (x2 35T)	h	24	110.00	2 640
Grid bracing	h	167	45.00	7 515
aerial bucket (x2)		1	6 000.00	6 000
Installation of fabric		1	9 165.00	9 165
Total	€/m ²	374	363	130 842
Cost of structure			265	92 622
Cost of installation			109	38 220

Table 3.8 – Cost details for the superstructure. On-site works are isolated to identify pure manufacturing costs of the gridshell, the envelope and the doors. To this end, the cost of the man-hours provided by the volunteers to prefabricate the grid has been assessed and allocated. Prices are given excluding transport costs and excluding taxes (V.A.T.). Spare quantities are included. See fig. 3.34 for a graphical representation of these data.

3.9 Conclusions

This paper has presented the different steps for the design of a gridshell in composite material : a Temporary Cathedral at Crêteil, in Paris suburb, in 2013. The first step was the optimization of the shape in order to avoid local concentrations of curvature. The second step showed a tool to automatically mesh a surface using the compass method. With this tool, the orientation of the mesh is studied according to structural and architectural criterions. The last steps showed the structural analysis of the gridshell and how to get the as-built geometry from the analysis model. Architecturally, the structure offers a very interesting space where the textual richness of the tubes against the membrane accentuates the reading of the complex curved surfaces.

This project demonstrates that gridshells in composite material are suitable for constructing freeform buildings. However, the long-term behavior of these materials needs to be better characterized to extend their lifespan.

At the moment, further developments are conducted by the laboratory to take account for torsional effects and non axisymmetric sections in such structures, as it is studied in [41].

3.10 Acknowledgements

First of all, the authors would like to thank the Catholic Church of Crêteil for their trust and their courage, which led to the initiation and successful completion of this ambitious project. Secondly, the authors would like to acknowledge the engineers from T/E/S/S, who had developed this challenging project over 18 months. They have carried out valuable work and permitted research to become a reality through this innovative edifice. Further thanks goes to Viry for the supervision of the construction works, including the delicate erection stage. Thirdly, the authors would like to thank warmly all the people involved in the construction process: the numerous parish volunteers, the technicians and researchers from the Navier laboratory and the engineers from T/E/S/S and Viry firms. Beyond the technical aspect, their enthusiasm made this project a powerful human experience. Fourth, the authors would like to thank the local firms for their work: BATEM (concrete), Eloi (steel), Esmery Caron (fabric), Solutions Composites (composite material), Axmann (connections) and ENSG.

3.11 References

- [1] B. Burkhardt, J. Hennicke, and E. Schauer, eds. *IL10 Grid Shells*. Institut für leichte Flächenträgerwerke (IL). Stuttgart, 1974.
- [3] C. Douthe, J.-F. Caron, and O. Baverel. “Gridshell structures in glass fibre reinforced polymers”. In: *Construction and Building Materials* 24.9 (2010), pp. 1580–1589.
- [10] C. Douthe. “Etude de structures élancées précontraintes en matériaux composites : application à la conception des gridshells”. PhD thesis. Université Paris Est, 2007, p. 274.
- [12] F. Tayeb. “Simulation numérique du comportement mécanique non linéaire de gridshells composés de poutres élancées en matériaux composites et de sections quelconques”. PhD thesis. 2015.
- [14] B. Addis. “‘Toys that save millions’ - A history of using physical models in structural design”. In: *The Structural Engineer* 91.4 (2013), pp. 12–27.
- [27] O. Baverel, J.-F. Caron, F. Tayeb, and L. du Peloux. “Gridshells in composite materials : construction of a 300 m² forum for the solidays’ festival in Paris”. In: *Structural Engineering International* 22.3 (2012), pp. 408–414.
- [28] L. du Peloux, F. Tayeb, O. Baverel, and J.-F. Caron. “Construction of a large composite gridshell structure: a lightweight structure made with pultruded glass fibre reinforced polymer tubes”. In: *Structural Engineering International* 26.2 (2016), pp. 160–167.
- [37] S. Adriaenssens. “Stressed spline structures”. PhD thesis. University of Bath, 2000.
- [40] S. Adriaenssens and M. Barnes. “Tensegrity spline beam and grid shell structures”. In: *Engineering Structures* 23.1 (2001), pp. 29–36.
- [41] M. Barnes, S. Adriaenssens, and M. Krupka. “A novel torsion/bending element for dynamic relaxation modeling”. In: *Computers & Structures* 119 (Apr. 2013), pp. 60–67.
- [46] B. Lefevre, C. Douthe, and O. Baverel. “Buckling of elastic gridshells”. In: *Journal of the IASS* September (2015).
- [52] L. Bouhaya, O. Baverel, and J.-F. Caron. “Optimization of gridshell bar orientation using a simplified genetic approach”. In: *Structural and Multidisciplinary Optimization* 50.5 (2014), pp. 839–848.
- [54] L. du Peloux, O. Baverel, J.-F. Caron, and F. Tayeb. “From shape to shell : a design tool to materialize freeform shapes using gridshell structures”. In: *Design Modelling Symposium*. Berlin, Deutschland, 2011.
- [61] N. Kotelnikova-Weiler. “Optimisation mécanique et énergétique d’enveloppes en matériaux composites pour les bâtiments”. PhD thesis. Université Paris-Est, 2012, p. 310.
- [67] Site Sécurité. *Règlement ERP type CTS (big tops & tents)*.
- [68] J. L. Clarke. *Eurocomp design code and handbook : structural design of polymer composites*. 2003, p. 672.

- [69] L. C. Bank. *Composites for construction : structural design with FRP materials.* 2006, p. 560.
- [70] Fiberline Composites A/S. *Fiberline design manual.* May. 2003, pp. 1–326.

Rich Kirchhoff beam model Part II

4 Geometry of smooth and discrete space curves

4.1 Introduction

In this chapter, our goal is to develop a comprehensive view of the geometry of space curves and how to frame such curves. Indeed, framed curve representations are of central importance when dealing with slender beam models, as they are often modeled using curvilinear coordinate systems. This is the kind of representation on which our beam model will be based on.

Although the theoretical beam model takes place in the smooth world, our model will be implemented in a numerical solver, hence the necessity of a discrete representation. However, the two world are intimately related to each other and this is why we chose to present them both in this chapter.¹

A comprehensive understanding of the geometry of discrete curves will enable to build a beam model with reduced degrees of freedom and capable of representing discontinuities in curvature. This last point is of particular interest when modeling real structures with complex boundary conditions and connexions where concentrated moments are transferred (that is jumps in curvature occur).

4.1.1 Overview

We start this chapter by recalling the fundamentals of smooth parametric curves (see §4.2). We introduce the *Frenet frame*, a crucial tool for the local characterization of space curves (see §4.3), and we identify two geometric invariants, the curvature and the torsion of Frenet,

¹de L'Hospital 1696 [71, preface] : “Car les courbes n'étant que des polygones d'une infinité de côtés, & ne différant entr' elles que par la différence des angles que ces côtés infiniment petits font entr'eux ; il n'appartient qu'à l'Analyse des infinité petits de déterminer la position de ces cotés pour avoir la courbure qu'ils forment [...]”.

that fully describe the geometry of a given space curve (see §4.4). We then introduce the notion of moving frame which allow to define a local orientation to each material point on a curve (see §4.5). This description will later be essential when modeling cross-section of beams. Among all the possible ways to frame a curve we look at rotation-minimizing frames. These frames are constructed thanks to the parallel transport operator, defined in the same section, which leads to the introduction of the *Bishop frame* : a torsion-free moving frame that will be at the heart of the beam model developed in the following chapters.

We then move on the discrete case and we first draw up a representation of a discrete curve as an ordered sequence of vertices linked by edges (see §4.6). We gather several definitions of the curvature for a discrete curve and we interpret them in terms of their osculating circle (see §4.7). Among these definitions, we focus on the curvatures defined respectively by the circumscribed and the inscribed osculating circles. We extend their definition to the curve endings as this is a matter of concern when dealing with mechanical boundary conditions – such as pinned or fixed endings. We study their behavior with respect to the turning angle – that is the angle between two consecutive edges – and we analyze their sensitivity to non uniform discretizations as this is a matter of concern when modeling real structures (sse §4.7.2). We then compare to what extent these curvatures can represent accurately the bending energy of typical curves, namely a circular curve and an elastica curve (see §4.7.3). For these two curvatures we demonstrate that a natural definition for the tangent vector emerges and we show how to construct it all along the discrete curve. This vector will later be associated to the cross-section normal in our Kirchhoff beam model (see §4.8). Finally, we recall two methods to parallel transport vectors or frames along a discrete curve (see §4.9). These methods will be used later to construct a twist-free reference frame fro our beam model.

4.1.2 Contributions

- We gather several definitions of the curvature for a discrete curve and we interpret them in terms of their osculating circle.
- We focus on the discrete curvatures defined respectively by the circumscribed and the inscribed osculating circles. We extend their definition to curve endings, which is crucial when modeling mechanical boundary conditions where nodes are positioned at points of interest.
- We study their behavior with respect to the turning angle and we analyze their sensitivity to non uniform discretization, which is likely to arise when modeling real structures.
- We compare to what extent these curvatures can represent accurately the bending energy of typical bended shapes (circle and elastica) regarding the sharpness of the discretization. This help us to chose what curvature representation to implement in our beam model.
- We demonstrate that a natural definition for the tangent vector at vertices emerges

for these curvatures. This will lead to a model with reduced number of degrees of freedom.

- We show how the local curvature and the tangent vector are related one to each other. This will lead to a straightforward modeling of boundary conditions and connexions. This will also allow to model discontinuities in curvature at vertices, thus enabling the modeling of applied concentrated moment and jumps in beam properties (ES , EI , GJ).

4.1.3 Related work

Delcourt 2011 [72] gives a thorough historical review of the study of space curves from Clairaut to Darboux. This history is paved with the nouns of illustre mathematicians such as Euler, Bernoulli, Monge, Fourier, Lagrange, Cauchy, Serret, Frenet, ... It reveals that the study of curves was often related to the study of physical problems (e.g. the elastica for Bernoulli & Euler, the helix for Pito).

In his lecture notes on discrete differential geometry of curves and surfaces, Hoffmann 2008 [73] presents three definitions for the discrete curvature. In his lecture notes on discrete differential geometry of plane curves, Vouga 2014 [74] constructs new discrete curvatures that mimic some of the interesting properties of the curvature in the smooth case. He remarks that none of the established discrete curvatures can reproduce all the properties of the curvature in the smooth case.

Bishop 1975 [75] remarks that the usual Frenet frame is not the only way to frame curve. He gives the skew-symmetric system of differential equations that any moving frame satisfies. He remarks that this system is governed by only three coefficient entries, which represent the components of the angular velocity vector of the frame expressed on the frame axes. He argues that the Frenet frame gains part of its significance because it is adapted to the curve and because one component of its angular velocity is null. Hence, he looks for other kind of moving frames that are both adapted and with one of the components of the angular velocity vector that is null. In particular, he looks at adapted frames that does not turn around the curve : what will be called a Bishop frame hereafter.

Klok 1986 [76] makes use of the Bishop frame to produce rotation-minimizing sweeps for visualizing 3D ribbons and cylinders. He remarks that for closed trajectories the start and end frames might not align properly. Guggenheimer 1989 [77] proposes a faster method to compute Klok's frame in relation to the Frenet frame. For that, he remarks that any frame is obtained from the Frenet frame by a rotation around the tangent vector. Bloomenthal 1990 [78] introduces the rotation method to propagate reference frames along a curve. Hanson and Ma 1995 [79] propose an algorithm to parallel transport frames along a curve using the rotation method. Poston et al. 1995 [80] propose a quadratically convergent algorithm, also based on the rotation method, to find untwisted sweeping NURBS surfaces within a given error bound ϵ .

Wang et al. 2008 [81] introduce the double reflexion method to propagate rotation min-

imizing frames. This method is supposed to be more stable than the rotation method Farouki et al. 2014 [82] investigate the use of rotation-minimizing frames that minimize the rotation around the binormal vector of the curve (compare to Bishop frame that minimize the rotation around the tangent vector of the curve).

4.2 Parametric curves

In this section we recall some fundamental results on (smooth) parametric curves.² In particular, we recall that there is more than one way to parametrize a curve. Amongst all the possible ways to parametrize a given curve, the arc length parametrization is of special interest. With this parametrization, the way a curve is described by a single parameter becomes unequivocal.³ This parametrization is naturally related to what is commonly understood as the “length of a curve”.

4.2.1 Definition

Let I be an interval of \mathbb{R} and $F: t \mapsto F(t)$ be a map of $C^0(I, \mathbb{R}^3)$. Then $\gamma = (I, F)$ is called a *parametric curve* and :

- The 2-uplet (I, F) is called a *parametrization* of γ .
- $\gamma = F(I) = \{F(t), t \in I\}$ is called the *graph* or *trace* of γ .
- γ is said to be C^k if $F \in C^k(I, \mathbb{R}^3)$.⁴

Note that for a given graph in \mathbb{R}^3 there are different possible parameterizations. Thereafter γ will simply refers to its graph $F(I)$.

4.2.2 Regularity

Let $\gamma = (I, F)$ be a parametric curve, and $t_0 \in I$ be a parameter.

- A point of parameter t_0 is called *regular* if $F'(t_0) \neq 0$.
The curve γ is called *regular* if γ is C^1 and $F'(t) \neq 0, \forall t \in I$.
- A point of parameter t_0 is called *biregular* if $F'(t_0)$ and $F''(t_0)$ are not collinear.
The curve γ is called *biregular* if γ is C^2 and $F'(t) \times F''(t) \neq 0, \forall t \in I$.

²Definition form [mathworld](#) : “A smooth curve is a curve which is a smooth function, where the word ‘curve’ is interpreted in the analytic geometry context. In particular, a smooth curve is a continuous map from a one-dimensional space to an n-dimensional space which on its domain has continuous derivatives up to a desired order.”.

³This is note rigorously exact but that is the idea. Indeed, this is true only for a given choice of orientation and to within a constant.

⁴A function f is said to be of class C^k if $f, f', f'', \dots, f^{(k)}$ exist and are continuous.

Here and thereafter, the prime symbol denotes the derivation with respect to the parameter and the product symbol denotes the cross product.

4.2.3 Reparametrization

Let $\gamma = (I, F)$ be a parametric curve of class C^k , $J \in \mathbb{R}^3$ an interval, and $\varphi: I \mapsto J$ be a C^k diffeomorphism. Let's define $G = F \circ \varphi$. Then :

- $G \in C^k(J, \mathbb{R}^3)$
- $G(J) = F(I)$
- φ is said to be an admissible *change of parameter* for γ .
- (J, G) is said to be another *admissible parametrization* for γ .

4.2.4 Natural parametrization

Let γ be a space curve of class C^1 . A parametrization (I, F) of γ is called *natural* if $\|F'(t)\| = 1, \forall t \in I$. Thus :

- The curve is necessarily regular.
- F is strictly monotonic.

4.2.5 Curve length

Let $\gamma = (I, F)$ be a parametric curve of class C^1 . The length of γ is defined as :

$$L = \int_I \|F'(t)\| dt \quad (4.1)$$

Note that as expected, the length of γ is invariant under reparametrization.

4.2.6 Arc length parametrization

Let $\gamma = (I, F)$ be a regular parametric curve. Let $t_0 \in I$ be a given parameter. The following map is said to be the *arc length of origin t_0* of γ :

$$s: t \mapsto \int_{t_0}^t \|F'(u)\| du , \quad s \in I \times \mathbb{R} \quad (4.2)$$

The arc length $s: I \mapsto s(I)$ is an admissible change of parameter for γ . Indeed, s is a C^1 diffeomorphism because it is bijective ($s' > 0$).

Let's define $G = F \circ s^{-1}$ and $J = s(I)$. Thus (J, G) is a natural reparametrization of γ and $\forall s \in J, \|G'(s)\| = 1$. This parametrization is preferred because the natural parameter

s traverses the image of γ at unit speed ($\|G'\| = 1$).⁵

Thereafter, for a regular curve γ , $\gamma(t)$ will denote the point $F(t)$ of parameter $t \in I$ while $\gamma(s)$ will denote the point $G(s)$ of arc length $s \in J = [0, L]$.

4.3 Frenet trihedron

The Frenet trihedron is a fundamental mathematical tool from the field of differential geometry to study the local characterization of planar and non-planar space curves. It is a direct orthonormal basis attached to any point P of parameter $t \in I$ on a parametric curve γ . This basis is composed of three unit vectors $\{\mathbf{t}(t), \mathbf{n}(t), \mathbf{b}(t)\}$ called respectively the *tangent*, the *normal*, and the *binormal* unit vectors.⁶

Introduced by Frenet in 1847 in his thesis “Courbes à Double Courbure” [83], it brings out intrinsic local properties of space curves : the curvature (κ) which evaluates the deviance of γ from being a straight line (see §4.4.1) ; and the torsion (τ_f) which evaluates the deviance of γ from being a planar curve (see §4.4.2).

These quantities, also known as “generalized curvatures” in modern differential geometry, are essential to understand the geometry of space curves. As stated by the *Fundamental Theorem of Space Curves*,⁷ a curve is fully determined by its curvature and torsion up to a solid movement in space (see §4.4.3).

4.3.1 Tangent vector

The first component of the Frenet trihedron is called the *unit tangent vector*. Let $\gamma = (I, F)$ be a regular parametric curve. Let $t \in I$ be a parameter. The *unit tangent vector* is defined as :

$$\mathbf{t}(t) = \frac{\gamma'(t)}{\|\gamma'(t)\|} \quad , \quad \|\mathbf{t}(t)\| = 1 \quad (4.3)$$

For a curve parametrized by arc length, this expression simply becomes :

$$\mathbf{t}(s) = \gamma'(s) \quad , \quad s \in [0, L] \quad (4.4)$$

In differential geometry, the unit tangente to the curve γ at point P_0 is obtained as the limit of the (normalized) vector $\overrightarrow{P_0 P}$, when P approches P_0 on the path γ (see fig. 4.1). For a regular curve, the left-sided and right-sided limits coïncide as P^- and P^+ approche

⁵Regular curves are also known as *unit speed* curves.

⁶Strictly speaking the map $\mathbf{t} : t \mapsto \mathbf{t}(t)$ is a *vector field* while $\mathbf{t}(t)$ is a *vector* of \mathbb{R}^3 . For the sake of simplicity, and if there is no ambiguity, these two notions will not be explicitly distinguished hereinafter.

⁷The full demonstration of this theorem is attributed to Darboux in [84, p.11].

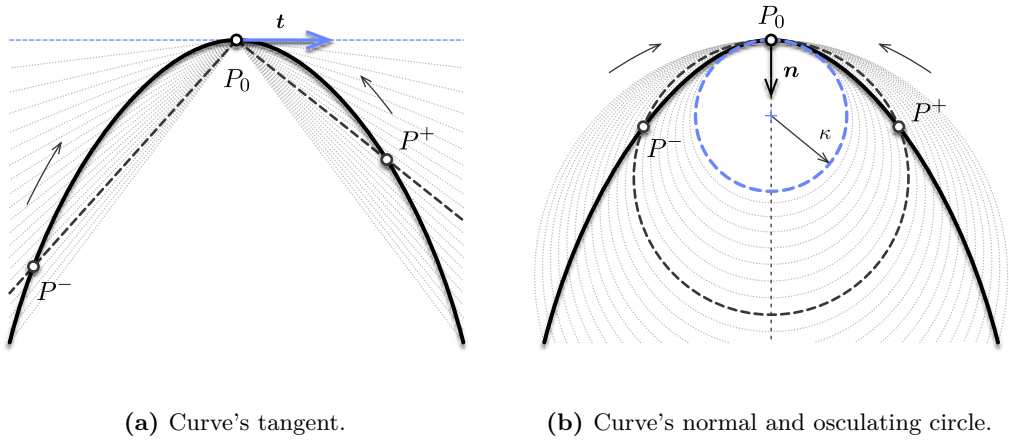


Figure 4.1 – Definition of the tangent vector and the osculating circle of a curve.

P_0 respectively from its left and right sides :

$$\mathbf{t}(P_0) = \lim_{P \rightarrow P_0} \frac{\overrightarrow{P_0P}}{\|\overrightarrow{P_0P}\|} = \lim_{P^- \rightarrow P_0} \frac{\overrightarrow{P_0P^-}}{\|\overrightarrow{P_0P^-}\|} = \lim_{P^+ \rightarrow P_0} \frac{\overrightarrow{P_0P^+}}{\|\overrightarrow{P_0P^+}\|} \quad (4.5)$$

4.3.2 Normal vector

The second component of the Frenet trihedron is called the *unit normal vector*. It is constructed from \mathbf{t}' which is necessarily orthogonal to \mathbf{t} . Indeed :

$$\|\mathbf{t}\| = 1 \Rightarrow \mathbf{t}' \cdot \mathbf{t} = 0 \Leftrightarrow \mathbf{t}' \perp \mathbf{t} \quad (4.6)$$

Remark that for a curve parametrized by arc length eq. (4.6) implies that $\gamma'(s) \cdot \gamma''(s) = 0$.

Let $\gamma = (I, F)$ be a biregular parametric curve. Let $t \in I$ be a parameter. The *unit normal vector* is defined as :⁸

$$\mathbf{n}(t) = \frac{\mathbf{t}'(t)}{\|\mathbf{t}'(t)\|} \quad , \quad \|\mathbf{n}(t)\| = 1 \quad (4.7)$$

Using eq. (4.3) in eq. (4.7) plus the usual derivation rules leads to :⁹

$$\mathbf{t}'(t) = \frac{\gamma'(t) \times (\gamma''(t) \times \gamma'(t))}{\|\gamma'(t)\|^3} \quad (4.8)$$

⁸Note that \mathbf{n} exists if and only if γ is biregular, that is \mathbf{t}' never vanishes, or equivalently γ is never locally a straight line. In that case the Frenet trihedron is undefined.

⁹Recall that $\gamma'(t) \times (\gamma''(t) \times \gamma'(t)) = \gamma''(t)(\gamma'(t) \cdot \gamma'(t)) - \gamma'(t)(\gamma''(t) \cdot \gamma'(t))$ and that $\|\gamma'(t)\| = \sqrt{\gamma'(t) \cdot \gamma'(t)}$.

Because $\gamma'(t)$ and $\gamma''(t) \times \gamma'(t)$ are perpendicular the following identity holds :

$$\|\gamma'(t) \times (\gamma''(t) \times \gamma'(t))\| = \|\gamma'(t)\| \|\gamma''(t) \times \gamma'(t)\| \quad (4.9)$$

Thus, combining eq. (4.8) and (4.9) gives :

$$\mathbf{n}(t) = \frac{\gamma'(t) \times (\gamma''(t) \times \gamma'(t))}{\|\gamma'(t)\| \|\gamma''(t) \times \gamma'(t)\|} \quad (4.10)$$

For a curve parametrized by arc length this expression becomes :

$$\mathbf{n}(s) = \frac{\gamma''(s)}{\|\gamma''(s)\|} , \quad s \in [0, L] \quad (4.11)$$

In differential geometry, the *unit normal* to the curve γ at point P_0 is obtained as the limit of the (normalized) vector $\overrightarrow{P_0P^+} - \overrightarrow{P_0P^-}$, as P^- and P^+ approach P_0 respectively from its left and right sides (fig. 4.1) :

$$\mathbf{n}(P_0) = \lim \frac{\overrightarrow{P_0P^+} - \overrightarrow{P_0P^-}}{\|\overrightarrow{P_0P^+} - \overrightarrow{P_0P^-}\|} \quad (4.12)$$

Remark that the notion of *normal vector* is ambiguous for non-planar curves as there is an infinite number of possible normal vectors lying in the plane orthogonal to the curve's tangent. In practice, the tangent derivative is a convenient choice as it allows to extend the notion of curvature from planar to non-planar space curves. However, we will see in §4.5.6 that other kinds of trihedron can be constructed regarding this choice and that one of them is especially suitable for the study of slender beams.

4.3.3 Binormal vector

The third vector of Frenet's trihedron is called the *unit binormal vector*. It is constructed from \mathbf{t} and \mathbf{n} to form an orthonormal direct basis of \mathbb{R}^3 . Let $\gamma = (I, F)$ be a biregular parametric curve. Let $t \in I$ be a parameter. The *unit binormal vector* is defined as :

$$\mathbf{b}(t) = \mathbf{t}(t) \times \mathbf{n}(t) , \quad \|\mathbf{b}(t)\| = 1 \quad (4.13)$$

Combining eq. (4.3) and eq. (4.10) with eq. (4.13) leads to :

$$\mathbf{b}(t) = \frac{\gamma'(t) \times \gamma''(t)}{\|\gamma'(t) \times \gamma''(t)\|} \quad (4.14)$$

For a curve parametrized by arc length, this expression becomes : ¹⁰

$$\mathbf{b}(s) = \mathbf{t}(s) \times \mathbf{n}(s) = \frac{\gamma'(s) \times \gamma''(s)}{\|\gamma''(s)\|} , \quad s \in [0, L] \quad (4.15)$$

¹⁰For an arc length parametrized curve the following identity holds : $\|\gamma'(s) \times \gamma''(s)\| = \|\gamma'(s)\| \|\gamma''(s)\|$.

4.3.4 Osculating plane

The tangent and normal unit vectors $\{\mathbf{t}, \mathbf{n}\}$ form an orthonormal basis of the so-called *osculating plane*, whereas the binormal vector (\mathbf{b}) is orthogonal to it. This plane is of prime importance because it is the plane in which the curve takes its curvature (see §4.4.1).

As reported in [84, p.45], the osculating plane seems to have been first introduced by Bernoulli as the plane passing through three infinitely near points on a curve.¹¹ Likewise, in modern differential geometry, the osculating plane is defined as the limit of the plane passing through the points P^- , P_0 and P^+ while P^- and P^+ approach P_0 respectively from its left and right side (fig. 4.1).

Note that the normal unit vector and the binormal unit vector $\{\mathbf{n}, \mathbf{b}\}$ define the so-called *normal plane*, while the normal tangent vector and the binormal unit vector $\{\mathbf{t}, \mathbf{b}\}$ define the so-called *rectifying plane*. These planes are secondary for the present study.

4.4 Curves of double curvature

The study of space curves belongs to the field of differential geometry. According to [84, p.28], the terminology *curve of double curvature* is attributed to Pitot around 1724.¹² However, as stated in [87, p.321] curvature and torsion were probably first thought by Monge around 1771.¹³ It is also interesting to note that, at that time, “curvature” was also referred to as “flexure”, reflecting that the study of physical problems (e.g. *the elastica*) and the study of curves of double curvature were intimately related to each other.

Space curves were historically understood as *curves of double curvature* by extension to the case of planar curves, where the curvature measures the deviance of a curve from being a straight line. The second curvature, nowadays known as the “torsion” or “second generalized curvature”, measures the deviance of a curve from being planar.

¹¹“Voco autem planum osculans, quod transit per tria curvae quaesitae puncta infinite sibi invicem propinqua” [85, p.113].

¹²“Les Anciens ont nommé cette courbe Spirale ou Hélice ; parce que la formation sur le cylindre suit la même analogie que la formation d'une spirale ordinaire sur un plan; mais elle est bien différente de la spirale ordinaire, étant une des courbes à double courbure, ou une des lignes qu'on conçoit tracée sur la surface des Solides. Peut-être que ces sortes de courbes à double courbure, ou prises sur la surface des Solides, feront un jour l'objet des recherches des géomètres. Celle que nous venons d'examiner est, je crois, la plus simple de toutes.” [86, p.28]

¹³“On appelle point d'inflexion, dans une courbe plane, le point où cette ligne, après avoir été concave dans un sens, cesse de l'être pour devenir concave dans l'autre sens. Il est évident que dans ce point, la courbe perd sa courbure, et que les deux éléments consécutifs sont en ligne droite. Mais une courbe à double courbure peut perdre chacune de ses courbures en particulier, ou les perdre toutes deux dans le même point ; c'est-à-dire, qu'il peut arriver ou que trois éléments consécutifs d'une même courbe à double courbure se trouvent dans un même plan, ou que deux de ces éléments soient en ligne droite. Il suit de là que les courbes à double courbure peuvent avoir deux espèces d'inflexions ; la première a lieu lorsque la courbe devient plane, et nous l'appellerons simple inflexion ; la seconde, que nous appellerons double inflexion, a lieu lorsque la courbe devient droite dans un de ses points.” [88, p.363].

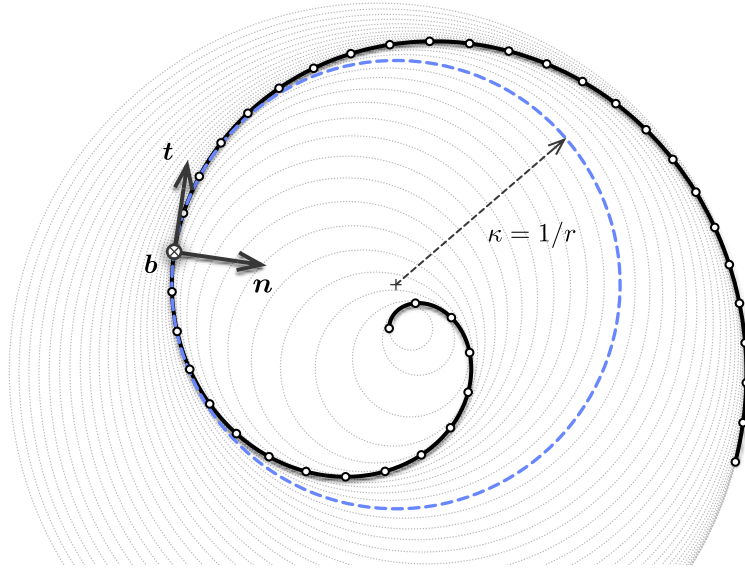


Figure 4.2 – Osculating circles for a spiral curve at different parameters.

4.4.1 First invariant : the curvature

In differential geometry, the *osculating circle* is defined as the limit of the circle passing through the points P^- , P_0 and P^+ while P^- and P^+ approach P_0 (fig. 4.1). This circle lies on the osculating plane and its radius is nothing but the inverse of the local curvature of a curve.¹⁴ While the tangent gives the best local approximation of the curve as a straight line, the osculating circle gives the best local approximation of that curve as an arc.

The curvature is also known to be the *gradient of arc length* (see [74, p.4]) and calculated as : $\nabla L = \kappa n$. Thus, the curvature gives the first-order variation in arc length when deforming a curve γ into the curve $\gamma + \epsilon\delta\gamma$:

$$L(\gamma + \epsilon\delta\gamma) = L(\gamma) + \epsilon(\nabla L \cdot \delta\gamma) + o(\epsilon) \quad (4.16a)$$

$$\nabla L \cdot \delta\gamma = \frac{d}{d\epsilon} L(\gamma + \epsilon\delta\gamma) \Big|_{\epsilon=0} = \int_0^L \kappa(\delta\gamma \cdot n) \quad (4.16b)$$

This is easily understood in the case of a circle of radius r extended to a circle of radius $r + dr$, where the total arc length variation is given by : $L(r + dr) - L(r) = \kappa dr L(r)$.

Note that due to the inner product with the normal vector, only the normal component of the deformation results in an effective extension of the curve. This point is worth to note as it will be related to the *inextensibility assumption* made later in our beam model (see ??).

¹⁴As explained by Euler himself, at a given arc length parameter (s), the osculating plane is the plane in which a curve takes its curvature : “in quo bina fili elementa proxima in curvantur” [89, p.364].

Curvature

Let γ be a regular arc length parametrized curve. Let $s \in [0, L]$ be an arc length parameter. The *curvature* is a positive scalar quantity defined as :

$$\kappa(s) = \|\mathbf{t}'(s)\| \geq 0 , \quad \mathbf{t}'(s) = \kappa(s)\mathbf{n}(s) \quad (4.17)$$

The curvature is *independent* regarding the choice of parametrization. This makes the curvature an *intrinsic property* of a given curve and that is why it is also referred to as a *geometric invariant*. Following [90, pp.203-204] it can be computed for any parametrization (I, F) of γ as :

$$\kappa(t) = \frac{\|\gamma'(t) \times \gamma''(t)\|}{\|\gamma'(t)\|^3} , \quad \mathbf{t}'(t) = \|\gamma'(t)\| \kappa(t) \mathbf{n}(t) \quad (4.18)$$

Note that in eq. (4.17) the prime symbol denotes the derivative with respect to the natural parameter (s) while in eq. (4.18) it denotes the derivative with respect to any parameter (t). Consequently, the *speed* of the curve's parametrization appears in the latter equation :

$$v(t) = \frac{ds}{dt} = \|\gamma'(t)\| = s'(t) \quad (4.19)$$

The curvature measures how much a curve bends instantaneously in its osculating plane, that is how fast the tangent vector is rotating in the osculating plane around the binormal vector. In differential geometry this is expressed for a planar curve as :

$$\kappa(s) = \lim_{ds \rightarrow 0} \frac{\angle(\mathbf{t}(s), \mathbf{t}(s + ds))}{ds} = \lim_{ds \rightarrow 0} \frac{(\mathbf{t}(s + ds) - \mathbf{t}(s)) \cdot \mathbf{n}(s)}{ds} \quad (4.20)$$

where $\angle(\mathbf{t}(s), \mathbf{t}(s + ds))$ denotes the angle between $\mathbf{t}(s)$ and $\mathbf{t}(s + ds)$. This is equivalent as measuring how fast the osculating plane itself is rotating around the binormal vector. Consequently a curve is locally a *straight line* when its curvature vanishes ($\kappa(s) = 0$).

Radius of curvature

The *radius of curvature* is defined as the inverse of the curvature ($r = 1/\kappa$). From a geometric point of view, one can demonstrate that it is the radius of the osculating circle (see fig. 4.2). Remark that where the curvature vanishes the radius of curvature goes to infinity ; that is the osculating circle becomes a line, a circle of infinite radius.

Center of curvature

The *center of curvature* is defined as the center of the osculating circle (see fig. 4.2). The locus of all the centers of curvature of a curve is called the *evolute*.

Curvature binormal vector

Finally, following [91] we define the *curvature binormal vector*. Let γ be a biregular arc length parametrized curve. Let $s \in [0, L]$ be an arc length parameter. The *curvature binormal vector* is defined as :

$$\kappa \mathbf{b}(s) = \kappa(s) \cdot \mathbf{b}(s) = \mathbf{t}(s) \times \mathbf{t}'(s) \quad , \quad \|\kappa \mathbf{b}(s)\| = \kappa(s) \quad (4.21)$$

This vector will be useful as it embed all the necessary information on the curve's curvature. We will see in §4.5.6 that this vector is associated to the angular velocity of a specific adapted moving frame attached to the curve and called the *Bishop frame*.

4.4.2 Second invariant : the torsion

Let γ be a biregular arc length parametrized curve. Let $s \in [0, L]$ be an arc length parameter. The *torsion* is a scalar quantity defined as :

$$\tau_f(s) = \mathbf{n}'(s) \cdot \mathbf{b}(s) = -\mathbf{b}'(s) \cdot \mathbf{n}(s) \quad (4.22)$$

The torsion is *independent* regarding the choice of parametrization. This makes the torsion an *intrinsic property* of a given curve and that is why it is also referred to as a *geometric invariant*. Following [90, p.204] it can be computed for any parametrization (I, F) of γ as :

$$\tau_f(t) = \frac{\gamma'(t) \cdot (\gamma''(t)) \times \gamma'''(t))}{\|\gamma'(t) \times \gamma''(t)\|^2} \quad \text{when } \kappa(t) > 0 \quad (4.23)$$

The torsion measures how much a curve goes *instantaneously out of its plane*, that is to say how fast the normal or binormal vectors are rotating in the normal plane around the tangent vector. In differential geometry this is expressed as :

$$\tau_f(s) = \lim_{ds \rightarrow 0} \frac{\angle(\mathbf{n}(s), \mathbf{n}(s + ds))}{ds} = \lim_{ds \rightarrow 0} \frac{(\mathbf{n}(s + ds) - \mathbf{n}(s)) \cdot \mathbf{b}(s)}{ds} \quad (4.24)$$

This is equivalent as measuring how fast the osculating plane is rotating around the tangent vector. Consequently a curve is locally *plane* when its torsion vanishes ($\tau_f(s) = 0$).

Remark that the *torsion* is denoted “ τ_f ” and not simply “ τ ” as the latter will be reserved to denote any angular velocity of a moving adapted frame around its tangent vector. Thus, τ_f refers to the particular angular velocity of the Frenet trihedron around its tangent vector. This torsion, which is a geometric property of the curve, will be indifferently referred to as the *Frenet torsion* or the *geometric torsion*.

4.4.3 Fundamental theorem of space curves

This two *generalized curvatures*, respectively the curvature (κ) and the torsion (τ_f), are *invariant* regarding the choice of parametrization and under *euclidean motions*. The *Fundamental theorem of space curves* states that a curve is fully described, up to a

Euclidean motion of \mathbb{R}^3 , by its positive curvature ($\kappa > 0$) and torsion (τ_f) [90, p.229].

4.4.4 Serret-Frenet formulas

The *Fundamental theorem of space curves* is somehow a consequence of the *Serret-Frenet formulas*, which is the first-order system of differential equations satisfied by the Frenet trihedron. Let γ be a biregular arc length parametrized curve. Let $s \in [0, L]$ be an arc length parameter. Then, the Frenet trihedron satisfies the following formulas :

$$\mathbf{t}'(s) = \kappa(s)\mathbf{n}(s) \quad (4.25a)$$

$$\mathbf{n}'(s) = -\kappa(s)\mathbf{t}(s) + \tau_f(s)\mathbf{b}(s) \quad (4.25b)$$

$$\mathbf{b}'(s) = -\tau_f(s)\mathbf{n}(s) \quad (4.25c)$$

This system can be seen as the *equations of motion* of the Frenet trihedron moving along the curve γ at unit speed ($\|\gamma'\| = 1$). Indeed, introducing its *angular velocity vector* also known as the *Darboux vector* (Ω_f), the previous system is expressed as :

$$\begin{bmatrix} \mathbf{t}'(s) \\ \mathbf{n}'(s) \\ \mathbf{b}'(s) \end{bmatrix} = \Omega_f(s) \times \begin{bmatrix} \mathbf{t}(s) \\ \mathbf{n}(s) \\ \mathbf{b}(s) \end{bmatrix} \quad \text{where} \quad \Omega_f(s) = \begin{bmatrix} \tau_f(s) \\ 0 \\ \kappa(s) \end{bmatrix} \quad (4.26)$$

Because the Frenet trihedron satisfies a first-order system of differential equations of parameters κ and τ_f it is possible, by integration, to reconstruct the trace of the moving frame and thus the curve, up to a constant of integration (a trihedron in this case).

Finally, those formulas can be generalized to any non unit-speed parametrization of a curve.¹⁵ Let $\gamma = (I, F)$ be a biregular parametric curve. Let $t \in I$ be a parameter. Then the following *generalized Serret-Frenet formulas* hold :

$$\mathbf{t}'(t) = v(t)\kappa(t)\mathbf{n}(t) \quad (4.27a)$$

$$\mathbf{n}'(t) = -v(t)\kappa(t)\mathbf{t}(t) + v(t)\tau_f(t)\mathbf{b}(t) \quad (4.27b)$$

$$\mathbf{b}'(t) = -v(t)\tau_f(t)\mathbf{n}(t) \quad (4.27c)$$

Again, this system can be seen as the *equations of motion* of the Frenet trihedron moving along the curve γ at non unit-speed ($v(t) = \|\gamma'(t)\|$). This time the *angular velocity vector* (Ω) is distinct from the *Darboux vector* (Ω_f) and the previous system is expressed as :

$$\begin{bmatrix} \mathbf{t}'(t) \\ \mathbf{n}'(t) \\ \mathbf{b}'(t) \end{bmatrix} = \Omega(t) \times \begin{bmatrix} \mathbf{t}(t) \\ \mathbf{n}(t) \\ \mathbf{b}(t) \end{bmatrix} \quad \text{where} \quad \Omega(t) = v(t) \begin{bmatrix} \tau_f(t) \\ 0 \\ \kappa(t) \end{bmatrix} \quad (4.28)$$

¹⁵See [90, p.203] for a complete proof.

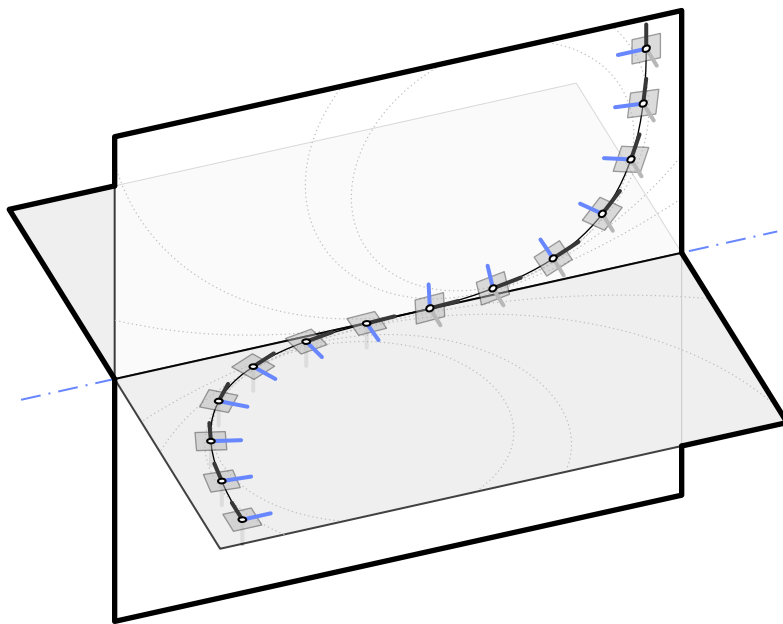


Figure 4.3 – Discontinuity of the Frenet trihedron at an inflection point where the curvature vanishes and the orientation of the osculating plane is subject to a jump of angle $\pi/2$.

4.5 Curve framing

While the Frenet trihedron “has long been the standard vehicle for analysing properties of the curve invariant¹⁶ under euclidean motions” [75, p.1], a curve can be potentially framed with any arbitrary *moving frame*, understood as an *orthonormal basis field*. Thus, the Frenet frame is not the only way to frame a curve and other frames may also exhibit some interesting properties.¹⁷

In his paper [75] Bishop establishes the differential equation that a moving frame must satisfy and remarks that, because of the orthonormality condition, the first derivatives of the frame components can be expressed in terms of themselves through a skew-symmetric coefficient matrix. For such a frame, the understanding of its motion along the curve is thus reduced to the knowledge of only three scalar coefficient functions. He remarks that most of the interesting properties that the Frenet frame exhibits are due to the fact that one of these coefficient functions is vanishing everywhere on the curve (that is the frame is *rotation-minimizing* regarding one of its components) ; and that the Frenet frame is *adapted* to the curve (that is one of its components is nothing but the unit tangent vector).

In this section we introduce the notion of *moving frame* and two properties of interest that such a frame can exhibit in addition, namely : to be *adapted* to the curve ; and to be *rotation-minimizing* regarding a given direction. We then reconsider the case of the Frenet frame regrading this mathematical framework. Finally, we introduce the *zero-twisting* frame

¹⁶Namely the curvature (κ) and the Frenet torsion (τ_f).

¹⁷Recall the title of Bishop’s paper : “There is more than one way to frame a curve” [75].

also known as the *Bishop* frame.¹⁸ This tool will be fundamental for our future study of slender beams.

4.5.1 Moving frame

Let γ be a curve parametrized by arc length. A map F which associates to each point of arc length parameter s a direct orthonormal trihedron is said to be a *moving frame* :

$$\begin{aligned} F : [0, L] &\longrightarrow \mathcal{SO}_3(\mathbb{R}) \\ s &\longmapsto F(s) = \{\mathbf{e}_3(s), \mathbf{e}_1(s), \mathbf{e}_2(s)\} \end{aligned} \quad (4.29)$$

Note that a direct orthonormal trihedron (or basis) is an element of the *rotation group* denoted \mathcal{SO}_3 . Consequently, a moving frame F attached to γ satisfies for all $s \in [0, L]$:

$$\|\mathbf{e}_i(s)\| = 1 \quad (4.30a)$$

$$\mathbf{e}_i(s) \cdot \mathbf{e}_j(s) = 0 \quad , \quad i \neq j \quad (4.30b)$$

The term “moving frame” will refer indifferently to the map itself (denoted $F = \{\mathbf{e}_3, \mathbf{e}_1, \mathbf{e}_2\}$), or to a specific evaluation of the map (denoted $F(s) = \{\mathbf{e}_3(s), \mathbf{e}_1(s), \mathbf{e}_2(s)\}$).

At first sight this indexing could seem strange but it will be convenient later in our mechanical model where \mathbf{e}_3 will be associated to the centerline’s tangent and \mathbf{e}_1 and \mathbf{e}_2 to the two cross-section principal axes of inertia. These axes will also be called *material axes*. We chose to introduce this indexing right now to maintain consistency between notations through out the chapters of this manuscript.

Governing equations

Computing the derivatives of the previous relationships leads to the following system of differential equations that the frame must satisfy for all $s \in [0, L]$:

$$\mathbf{e}'_i(s) \cdot \mathbf{e}_i(s) = 0 \quad (4.31a)$$

$$\mathbf{e}'_i(s) \cdot \mathbf{e}_j(s) = -\mathbf{e}_i(s) \cdot \mathbf{e}'_j(s) \quad , \quad i \neq j \quad (4.31b)$$

Thus, there exists 3 scalar functions (τ, k_1, k_2) such that $\{\mathbf{e}'_3, \mathbf{e}'_1, \mathbf{e}'_2\}$ can be expressed in the basis $\{\mathbf{e}_3, \mathbf{e}_1, \mathbf{e}_2\}$:

$$\mathbf{e}'_3(s) = k_2(s)\mathbf{e}_1(s) - k_1(s)\mathbf{e}_2(s) \quad (4.32a)$$

$$\mathbf{e}'_1(s) = -k_2(s)\mathbf{e}_3(s) + \tau(s)\mathbf{e}_2(s) \quad (4.32b)$$

$$\mathbf{e}'_2(s) = k_1(s)\mathbf{e}_3(s) - \tau(s)\mathbf{e}_1(s) \quad (4.32c)$$

¹⁸Named after Bishop who introduced it.

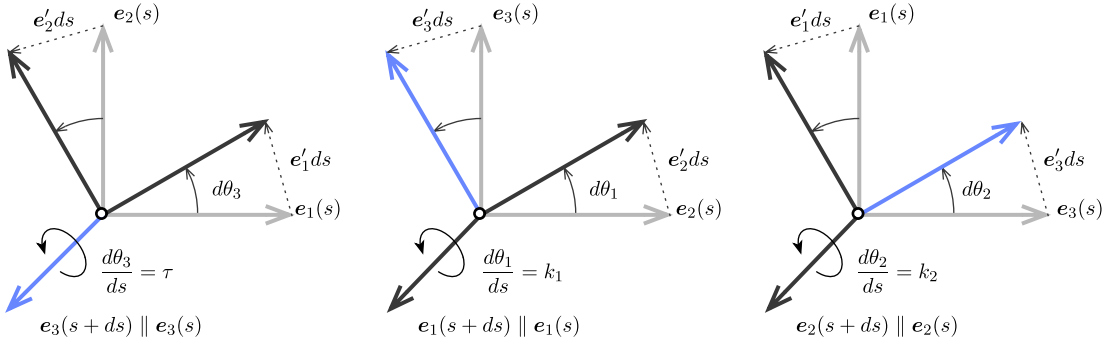


Figure 4.4 – Geometric interpretation of the angular velocity vector of a moving frame.

It is common to rewrite this first-order linear system of differential equations as a matrix equation : ^{19,20}

$$\begin{bmatrix} \mathbf{e}'_3(s) \\ \mathbf{e}'_1(s) \\ \mathbf{e}'_2(s) \end{bmatrix} = \begin{bmatrix} 0 & k_2(s) & -k_1(s) \\ -k_2(s) & 0 & \tau(s) \\ k_1(s) & -\tau(s) & 0 \end{bmatrix} \begin{bmatrix} \mathbf{e}_3(s) \\ \mathbf{e}_1(s) \\ \mathbf{e}_2(s) \end{bmatrix} \quad (4.33)$$

Since the progression of any moving frame along γ is ruled by a first-order system of differential equations, a unique triplet $\{\tau, k_1, k_2\}$ leads to a set of moving frames equal to each other within a constant of integration.²¹ Basically, with a given triplet $\{\tau, k_1, k_2\}$, one can propagate a given initial direct orthonormal trihedron (at $s = 0$ for instance) through the whole curve by integrating the system of differential equations. In general, a moving frame will be fully determined by τ, k_1 and k_2 together with the initial condition $\{\mathbf{e}_3(s = 0), \mathbf{e}_1(s = 0), \mathbf{e}_2(s = 0)\}$.

Angular velocity

This system can be seen as the *equations of motion* of the frame moving along the curve γ at unit speed ($\|\gamma'\| = 1$). Indeed, introducing its *angular velocity vector* (Ω), the previous system is expressed as :

$$\mathbf{e}'_i(s) = \boldsymbol{\Omega}(s) \times \mathbf{e}_i(s) \quad \text{avec} \quad \boldsymbol{\Omega}(s) = \begin{bmatrix} \tau(s) \\ k_1(s) \\ k_2(s) \end{bmatrix} \quad (4.34)$$

This result is straightforward deduced from eq. (4.33). Note that the cross product reveals the skew-symmetric nature of the system, which could already be seen in eq. (4.33).

¹⁹In the case of a space curve, where e_3 is chosen to be the curve tangent unit vector and e_1 is chosen to be the curve normal unit vector, this set of equations is known as the *Serret-Frenet formulas*.

²⁰In the case of a space curve drawn on a surface, where e_3 is chosen to be the curve tangent unit vector and e_1 is chosen to be the surface normal unit vector, this set of equations is known as the *Darboux-Ribaucour formulas*.

²¹This assumption reminds the *Fundamental theorem of space curves* (§4.4.3).

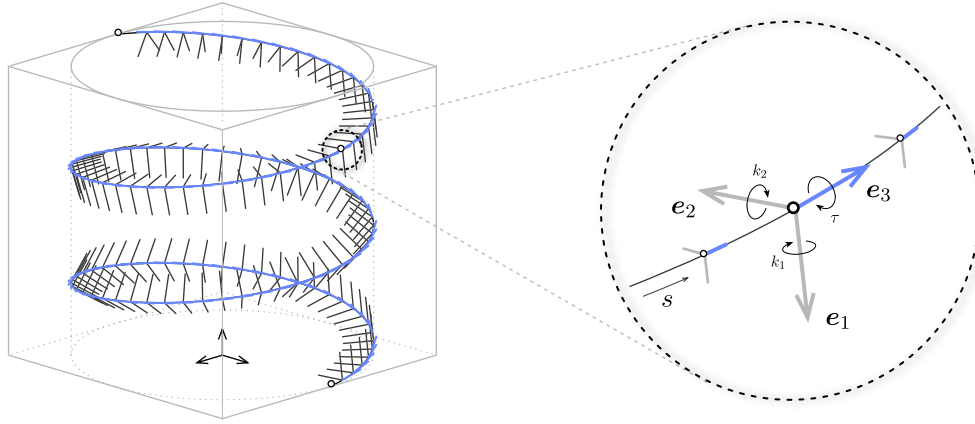


Figure 4.5 – Moving frame $F(s) = \{e_3(s), e_1(s), e_2(s)\}$ on a circular helix. The frame is adapted as $e_3(s) = t(s)$.

Geometrically, decomposing the infinitesimal rotation of the moving frame around its directors between arc length s and $s + ds$ (see fig. 4.4) shows that the scalar functions τ , k_1 and k_2 effectively correspond to the angular speed of the frame moving along γ , respectively around e_3 , e_1 and e_2 :

$$\frac{d\theta_3}{ds}(s) = \tau(s) \quad (4.35a)$$

$$\frac{d\theta_1}{ds}(s) = k_1(s) \quad (4.35b)$$

$$\frac{d\theta_2}{ds}(s) = k_2(s) \quad (4.35c)$$

4.5.2 Adapted moving frame

Let F be a moving frame as defined in the previous section. F is said to be *adapted* to γ if at each point $\gamma(s)$, $e_3(s)$ is the unit tangent vector of γ (fig. 4.5) :

$$e_3(s) = t(s) = \gamma'(s) \quad (4.36)$$

For an adapted frame, the components k_1 and k_2 of the angular velocity vector are related to the curvature of γ :²²

$$\kappa(s) = \|e'_3(s)\| = \|k_2(s)e_1(s) + k_1(s)e_2(s)\| = \sqrt{k_1(s)^2 + k_2(s)^2} \quad (4.37)$$

²²This is why for an initially straight rod with an isotropic cross-section bending and torsion are uncoupled. Indeed, in that case the bending energy does not depend on the orientation of the cross-sections anymore as it depends only on the curvature of the rod : $\mathcal{E}_b = EI_1\kappa_1^2 + EI_2\kappa_2^2 = EI\kappa^2$.

Moreover, recalling the definition of the curvature binormal vector (κb) from eq. (4.21), it is easy to see that for an adapted moving frame the following relation holds :

$$\kappa b(s) = k_1(s)e_1(s) + k_2(s)e_2(s) \quad (4.38)$$

Consequently, the angular velocity vector of an adapted moving frame can be written as :

$$\Omega(s) = \kappa b(s) + \tau(s)t(s) \quad (4.39)$$

This last result is very interesting as it shows that any adapted moving frame will differ from each other only by their twisting speed, as $\Omega_\perp = \kappa b$ only depends on the curve.

4.5.3 Rotation-minimizing frame

Following [82, 81] we introduce the *rotation-minimizing frame* notion. A frame $\{e_3, e_1, e_2\}$ is said to be *rotation-minimizing* regarding a given direction d if :

$$\Omega(s) \cdot d(s) = 0 \quad (4.40)$$

4.5.4 Parallel transport

The notion of *parallel transport* is somehow a generalization of the classical notion of collinearity in flat euclidean spaces (e.g. \mathbb{R}^2 or \mathbb{R}^3), to spaces that exhibit some non vanishing curvature (e.g. spheric or hyperbolic spaces).²³

Relatively parallel fields

Following Bishop 1975 [75], we define what is a *(relatively) parallel field*. Let γ be a regular curve parametrized by arc length. Let p be a vector field along γ . The vector field p is said to be *parallel* if its derivative is purely tangential, that is :

$$p'(s) \times t(s) = 0 \quad (4.41)$$

Consequently, for an adapted moving frame, the *normal fields* e_1 and e_2 are both *relatively parallel* if and only if the frame angular velocity is itself a normal field, that is :²⁴

$$\Omega(s) = \Omega_\perp(s) = \kappa b(s) \Leftrightarrow \Omega(s) \cdot t(s) = 0 \Leftrightarrow \tau(s) = 0 \quad (4.42)$$

In other words, a *relatively parallel normal field* : “turns, only whatever amount is necessary for it to remain normal, so it is as close to being parallel as possible without losing normality” [75].

²³<https://www.youtube.com/watch?v=p1tfZD2Bm0w>

²⁴A vector field p is said to be *normal* along a curve γ if : $\forall s \in [0, L], p \cdot t = 0$.

Parallel transport of vectors along a curve

Reciprocally, it is possible to define the *parallel transport* of a vector along a curve γ as its propagation along γ at angular speed κb . An initial vector $\mathbf{p}_0 = \mathbf{p}(s_0)$ is parallel transported at arc length parameter s into the vector $\mathbf{p}(s)$ by integrating the following first-order differential equation along γ :

$$\mathbf{p}'(s) = \kappa \mathbf{b}(s) \times \mathbf{p}(s) \quad (4.43)$$

Consequently, the resulting vector field \mathbf{p} is a parallel field. Note that a parallel field is not necessarily a normal field.

From the point of view of differential geometry, this means that the next vector $\mathbf{p}(s + ds)$ is obtained by rotating the previous one $\mathbf{p}(s)$ around the curve binormal $\mathbf{b}(s)$ by an infinitesimal angle $d\theta(s) = \kappa(s)ds$. Note that $\mathbf{b}(s)$ has the same direction as $\mathbf{t}(s) \times \mathbf{t}(s + ds)$.

Parallel transport of frames along a curve

Identically, the *parallel transport* of an adapted frame is defined as the parallel transport of its components along γ .

4.5.5 Frenet frame

The Frenet frame is a well-known particular adapted moving frame. It is defined as the map that attach to any given point of γ the corresponding Frenet trihedron $\{\mathbf{t}(s), \mathbf{n}(s), \mathbf{b}(s)\}$ where :

$$\mathbf{t}(s) = \gamma'(s) \quad (4.44a)$$

$$\mathbf{n}(s) = \frac{\mathbf{t}'(s)}{\kappa(s)} \quad (4.44b)$$

$$\mathbf{b}(s) = \mathbf{t}(s) \times \mathbf{n}(s) \quad (4.44c)$$

Governing equations

The Frenet frame satisfies the *Frenet-Serret formulas* (see §4.4.4), which govern the evolution of the frame along the curve γ :

$$\begin{bmatrix} \mathbf{t}'(s) \\ \mathbf{n}'(s) \\ \mathbf{b}'(s) \end{bmatrix} = \begin{bmatrix} 0 & \kappa(s) & 0 \\ -\kappa(s) & 0 & \tau_f(s) \\ 0 & -\tau_f(s) & 0 \end{bmatrix} \begin{bmatrix} \mathbf{t}(s) \\ \mathbf{n}(s) \\ \mathbf{b}(s) \end{bmatrix} \quad (4.45)$$

Remember the generic system of differential equations of an adapted moving frame attached to a curve, established in eq. (4.33), where $\mathbf{e}_3(s) = \mathbf{t}(s)$, $k_1(s) = 0$, $k_2(s) = \kappa(s)$ and $\tau(s) = \tau_f(s)$.

Angular velocity

Consequently, the angular velocity vector (Ω_f) of the Frenet frame, also known as the *Darboux vector* in this particular case, is given by :

$$\Omega_f(s) = \begin{bmatrix} \tau_f(s) \\ 0 \\ \kappa(s) \end{bmatrix} = \kappa b(s) + \tau_f(s) t(s) \quad (4.46)$$

Remark that the Frenet frame satisfies $\Omega_f(s) \cdot n(s) = 0$ and is thus a *rotation-minimizing* frame regarding the normal vector (n). The motion of this frame through the curve is known as *pitch-free*.

Note also that $t'(s)$ and $b'(s)$ are collinear to $n(s)$. This means that the projection of $t(s)$ and $b(s)$ is conserved from one normal plane to another, that is t and b are parallel transported along the vector field n .

Drawbacks and benefits

The Frenet frame is not continuously defined if γ is not C^2 . This is problematic for the study of slender beams as the centerline of a beam subject to punctual external forces and moments or to material discontinuities will not be C^2 but only piecewise C^2 . In that case, the centerline tangent will be continuously defined everywhere but the curvature will be subject to discontinuities, that is t' will not be continuously defined.

Moreover, even if γ is C^2 , the Frenet frame is not defined where the curvature vanishes, which obviously is an admissible configuration for a beam centerline. This issue can be partially addressed by parallel transporting the normal vector along the straight regions of the curve. Thus, the extended frame will still satisfy the governing equations exposed in [eq. \(4.45\)](#). However, if the osculating planes are not parallel on both sides of a region of null curvature, torsion will be subject to a discontinuity and so the Frenet frame ([fig. 4.3](#)).²⁵ Again, if the region of null curvature is not a point, that is the region is not an inflection point but a locus where the curve is locally a straight line, the change in torsion on both sides of the region can be accommodated by a continuous rotation from one end to the other.

One benefit of the Frenet frame is that, when transported along a *closed curve*, the frame at the end of the curve will align back with the frame at the beginning of the curve, that is the frame will return to its initial value after a complete turn. During its trip, the frame will make a total twist of $\int_0^L \tau_f(s) ds = 0[2\pi]$ around the tangent vector.

A second benefit is that any adapted frame can be obtained by a rotation of the Frenet frame around the unit tangent vector [[77](#), p.2].

²⁵This is also highlighted in [[78](#), [81](#)].

4.5.6 Bishop frame

A *Bishop frame* denoted $\{\mathbf{t}, \mathbf{u}, \mathbf{v}\}$, also known as *zero-twisting* or *parallel-transported* frame, is an adapted moving frame that has no tangential angular velocity : ²⁶

$$\boldsymbol{\Omega} \cdot \mathbf{t} = \tau = \mathbf{u}' \cdot \mathbf{v} = -\mathbf{u} \cdot \mathbf{v}' = 0 \quad (4.47)$$

Because a Bishop frame is an adapted frame, it can be defined relatively to the Frenet frame by a rotation around the unit tangent vector. A Bishop frame is a frame that cancels out the rotational movement of the Frenet frame around the tangent vector. At arc length parameter s , the Frenet frame has continuously rotated around its tangent vector of a cumulative angle : $\int_0^s \tau_f(t)dt$. Thus, any Bishop frame will be obtained, within a constant rotation angle θ_0 , through a rotation of the Frenet frame around the tangent vector by an angle :

$$\theta(s) = - \int_0^s \tau_f(t)dt + \theta_0(s) \quad (4.48)$$

Consequently, a Bishop frame can be expressed relatively to the Frenet frame as :

$$\begin{cases} \mathbf{u} = \cos \theta \mathbf{n} + \sin \theta \mathbf{b} \\ \mathbf{v} = -\sin \theta \mathbf{n} + \cos \theta \mathbf{b} \end{cases} \quad (4.49)$$

Governing equations

The Bishop frame satisfies the following system of differential equations, which governs the evolution of the frame along the curve γ :

$$\begin{bmatrix} \mathbf{t}'(s) \\ \mathbf{u}'(s) \\ \mathbf{v}'(s) \end{bmatrix} = \begin{bmatrix} 0 & \kappa(s) \sin \theta(s) & -\kappa(s) \cos \theta(s) \\ -\kappa(s) \sin \theta(s) & 0 & 0 \\ \kappa(s) \cos \theta(s) & 0 & 0 \end{bmatrix} \begin{bmatrix} \mathbf{t}(s) \\ \mathbf{u}(s) \\ \mathbf{v}(s) \end{bmatrix} \quad (4.50)$$

One can remember the generic differential equations of an adapted moving frame attached to a curve, where : ²⁷

$$k_1(s) = \kappa(s) \sin \theta(s) , \quad k_2(s) = \kappa(s) \cos \theta(s) , \quad \tau(s) = 0 \quad (4.51)$$

²⁶Bishop frames were introduced as *relatively parallel adapted frames* in [75].
²⁷

$$\tau = \mathbf{u}' \cdot \mathbf{v} = (\boldsymbol{\Omega}_f \times \mathbf{u} + \theta' \mathbf{v}) \cdot \mathbf{v} = \tau_f - \tau_f = 0$$

$$k_1 = -\mathbf{t}' \cdot \mathbf{v} = -\kappa \mathbf{n} \cdot \mathbf{v} = \kappa \sin \theta$$

$$k_2 = \mathbf{t}' \cdot \mathbf{u} = \kappa \mathbf{n} \cdot \mathbf{u} = \kappa \cos \theta$$

Angular velocity

Consequently, the angular velocity vector (Ω_b) of the Bishop frame is given by :

$$\Omega_b(s) = \begin{bmatrix} 0 \\ \kappa(s) \sin \theta(s) \\ \kappa(s) \cos \theta(s) \end{bmatrix} = \kappa b(s) \quad (4.52)$$

Remark that the Bishop frame satisfies $\Omega_b(s) \cdot t(s) = 0$ and is thus *rotation-minimizing* regarding the tangent vector. The motion of this frame through the curve is known as “roll-free”.

Because the motion of this frame is described by an angular velocity vector that is nothing but the curvature binormal vector ($\Omega_b = \kappa b$), it can be interpreted in terms of *parallel transport* as defined in §4.5.4. Thus, given an initial frame at arc length parameter $s = 0$, the Bishop frame at any arc length parameter (s) is obtained by parallel transporting the initial frame $\{t(0), u(0), v(0)\}$ along the curve from 0 to s .

Drawbacks and benefits

One of the main benefits of the Bishop frame is that its generative method : “is immune to degeneracies in the curvature vector” [78]. Although we first expressed the construction of the Bishop frame relatively to the Frenet frame (which exists wherever γ is biregular), the existence of the Bishop frame, understood in terms of parallel transport, is guaranteed wherever the curvature binormal ($\kappa b = t \times t'$) is defined. To be continuously defined over $[0, L]$, a Bishop frame only needs the curvature binormal vector to be piecewise continuously defined over $[0, L]$, which only requires that γ' is C^0 and that γ'' is piecewise C^0 . Obviously, those weaker existence conditions are profitables to bypass the drawbacks of the Frenet frame regarding the modeling of slender beams listed in §4.5.5.

Strictly speaking, a Bishop frame is not a reference frame as it is defined within an initial condition. However, we will see later that strains in a beam are modeled as a rate of change in the Bishop frame, and consequently the initial condition will disappear in the equations.

Unlike the Frenet frame, when transported along a *closed curve*, the Bishop frame at the end of the curve will not necessarily align back with the frame at the beginning of the curve.²⁸ Even if the frame returns to its initial value after a complete turn, it may return in its position after several complete turns ($2k\pi$) around the curve tangent. During its movement along the curve, the frame will make a total twist of $\int_0^L \tau_f(s) ds = \alpha[2\pi]$ around the tangent vector. This difference of angle is related to the concept of *holonomy*.

Remark also that Frenet and Bishop frames coincide for planar curves ($\tau_f = 0$), within a constant rotation around the unit tangent vector.

²⁸“it is possible for closed curves to have parallel transport frames that do not match up after one full circuit of the curve” [79].

4.5.7 Comparison between Frenet and Bishop frames

Let γ be a *circular helix* of parameter a and k . In a cartesian coordinate system, it is defined as :

$$\mathbf{r}(t) = [a \cos t, a \sin t, kt] = a \cos t \mathbf{e}_x + a \sin t \mathbf{e}_y + kt \mathbf{e}_z \quad (4.53)$$

The speed of this parametrization, the curvature and the geometric torsion are uniform and given by :

$$v(t) = \sqrt{a^2 + k^2} \quad (4.54a)$$

$$\kappa(t) = \frac{a}{a^2 + k^2} \quad (4.54b)$$

$$\tau_f(t) = \frac{k}{a^2 + k^2} \quad (4.54c)$$

The Frenet frame components are given by (with $\alpha = v\kappa$ and $\beta = v\tau_f$) :

$$\mathbf{t}(t) = [-\alpha \cos t, \alpha \sin t, \beta t] \quad (4.55a)$$

$$\mathbf{n}(t) = [-\cos t, -\sin t, 0] \quad (4.55b)$$

$$\mathbf{b}(t) = [\beta \sin t, -\beta \cos t, \alpha] \quad (4.55c)$$

And the Bishop frame components are given by :

$$\mathbf{u}(t) = [-\cos t \cos \beta t - \beta \sin t \sin \beta t, -\sin t \cos \beta t + \beta \cos t \sin \beta t, -\alpha \sin \beta t] \quad (4.56a)$$

$$\mathbf{v}(t) = [-\cos t \sin \beta t + \beta \sin t \cos \beta t, -\sin t \sin \beta t - \beta \cos t \cos \beta t, \alpha \cos \beta t] \quad (4.56b)$$

At $t = 0$ the two frames coincide. At $t > 0$ the Bishop frame is obtained from the Frenet frame by a rotation around $\mathbf{t}(t)$ of an angle $\theta(t) = -\tau_f \cdot (vt)$.

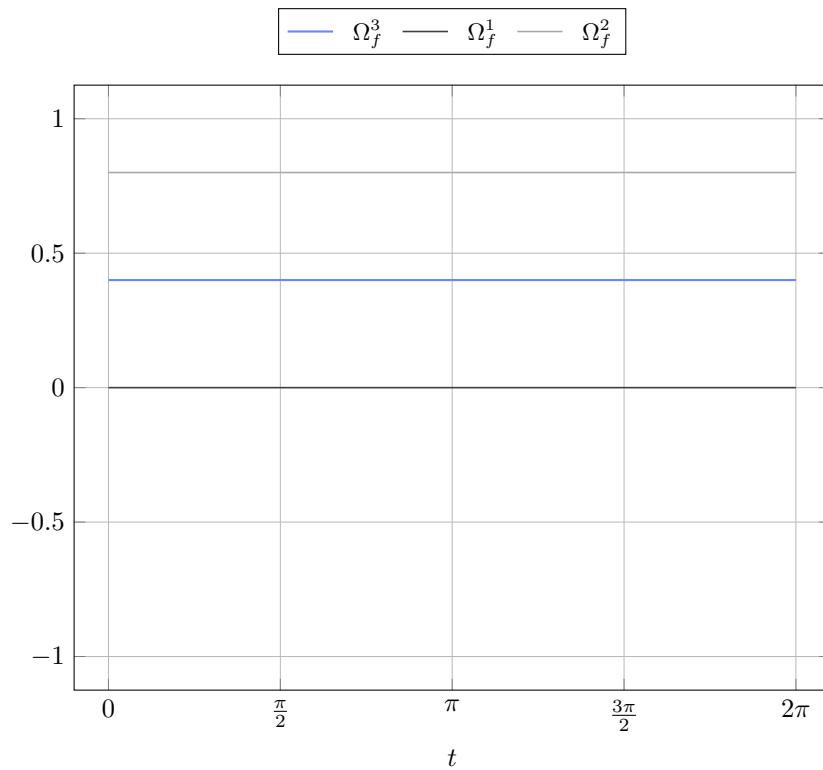
The angular velocities of the Frenet and Bishop frames are respectively given by :

$$\boldsymbol{\Omega}_f(t) = [\tau_f, 0, \kappa] \quad (4.57a)$$

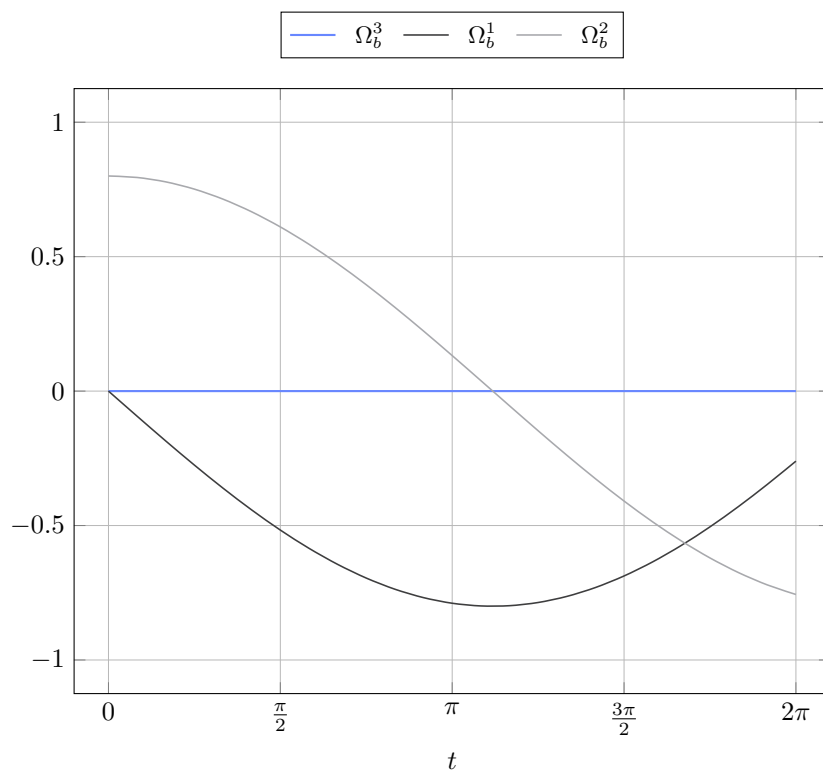
$$\boldsymbol{\Omega}_b(t) = [0, \kappa \sin \theta, \kappa \cos \theta] \quad (4.57b)$$

The components of these angular velocities are plotted in [fig. 4.6](#) for a circular helix with parameter $a = 1.0$ and $k = 0.5$ while the parameter t varies from 0 to 2π . At $t = 2\pi$ the frame has made a full turn and its altitude has increased from 0 to π .

The components of the angular velocity of the Frenet frame are constant during the movement along the curve and the frame does not rotate around the normal vector as $\Omega_f^2 = 0$ (see [fig. 4.6a](#)). The components of the angular velocity of the Bishop frame vary during the movement along the curve and the frame does not rotate around the tangent vector as $\Omega_b^3 = 0$ (see [fig. 4.6b](#)).



(a) Frenet frame



(b) Bishop frame

Figure 4.6 – Angular velocities of Frenet and Bishop frames for a circular helix ($a = 1.0$ and $k = 0.5$).

4.6 Discrete curves

The previous section has introduced the fundamental analytical tools to develop a solid understanding of the geometry of smooth space curves. These tools will be essentials for the construction of the beam model presented later in ?? and ?. In this section we look for equivalent notions in the case of discrete space curves, as the developed model will be implemented in a numerical program to solve real mechanical problems through discrete element models (see ??).

The study of those discrete equivalent notions belong to the recent field of *Discrete Differential Geometry* : “In some sense discrete differential geometry can be considered more fundamental than differential geometry since the later can be obtained from the former as a limit” [73, p.7]. In particular, we will see that there are several ways to define the discrete equivalents of the curvature and the unit tangent vector. Though these various ways are equivalent and match their smooth counterpart by passing to the limit, they exhibit different capabilities at the discrete level.

“There is no general theory or methodology in the literature, despite the ubiquitous use of discrete curves in mathematics and science. There are conflicting definitions of even basic concepts such as discrete curvature κ , discrete torsion τ , or discrete Frenet frame.” [92, p.1].

4.6.1 Definition

Let Γ be a discrete (or polygonal) space curve. Γ is defined as an ordered sequence $\Gamma = (\mathbf{x}_0, \mathbf{x}_1, \dots, \mathbf{x}_n) \in \mathbb{R}^{3(n+1)}$ of $n + 1$ pairwise disjoint *vertices* (see fig. 4.7). Consecutive pairs of vertices define n straight segments $(\mathbf{e}_0, \mathbf{e}_1, \dots, \mathbf{e}_{n-1})$ called *edges*, pointing from one vertex to the next one : $\mathbf{e}_i = \mathbf{x}_{i+1} - \mathbf{x}_i$. The midpoint of \mathbf{e}_i is a vertex denoted : $\mathbf{x}_{i+1/2} = \mathbf{x}_i + \frac{1}{2}\mathbf{e}_i$.

The length of \mathbf{e}_i is denoted $l_i = \|\mathbf{e}_i\|$. The total length of Γ is denoted $L = \sum_{i=0}^{n-1} \|\mathbf{e}_i\|$. Additionally, we define the vertex-based mean length \bar{l}_i at vertex \mathbf{x}_i :

$$\begin{cases} \bar{l}_0 = l_0 & i = 0 \\ \bar{l}_i = \frac{1}{2}(l_{i-1} + l_i) & i \in \llbracket 1, n-1 \rrbracket \\ \bar{l}_n = l_{n-1} & i = n \end{cases} \quad (4.58)$$

Discrete unit tangent vector

Edge vectors lead to a natural definition of the *discrete unit tangent vector* along each edge : $\mathbf{u}_i = \mathbf{e}_i / l_i$. However, this definition makes no sense at vertices where all the curvature is condensed and measured by the turning angle (φ_i). This is often illustrated in terms of the Gauß map, a transformation in which edges will map to points and vertices will map to

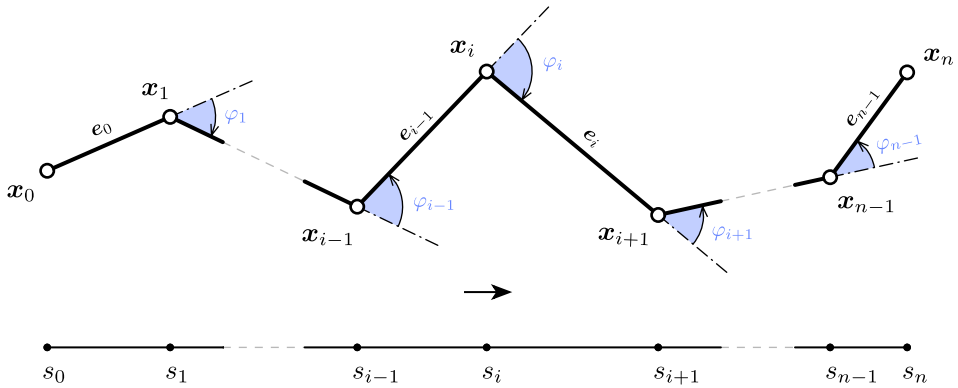


Figure 4.7 – Discrete curve representation and parametrization.

curves on the unit sphere.

Discrete osculating plane

Consecutive pairs of edges lead to a natural definition of the *discrete osculating plane*, as the plane in which Γ locally lies on. This plane is well defined by its normal vector known as the *discrete unit binormal vector* ($\mathbf{b}_i = \frac{\mathbf{e}_{i-1} \times \mathbf{e}_i}{\|\mathbf{e}_{i-1} \times \mathbf{e}_i\|}$) only if \mathbf{e}_{i-1} and \mathbf{e}_i are non-collinear ; that is the curve is not locally a straight line, or equivalently the curvature does not vanish.

Discrete turning angle

The *turning angle* is defined as the oriented angle between two adjacent edges : $\varphi_i = \angle(\mathbf{e}_{i-1}, \mathbf{e}_i)$. It is defined only for all $i \in \llbracket 1, n-1 \rrbracket$. It corresponds to the angle of rotation, in the osculating plane, around the binormal vector (\mathbf{b}_i), to align \mathbf{e}_{i-1} with \mathbf{e}_i . The sign of φ_i is taken in accordance to the right-hand rule regarding the orientation of \mathbf{b}_i . Thus, φ_i is necessarily bounded to $[0, \pi]$:

$$0 \leq \varphi_i \leq \pi \quad (4.59)$$

The next section will highlight the central role of the turning angle in the possible measurements of the discrete curvature.

Recall that for a planar curve, where φ denotes the angle between the tangent vector ($\mathbf{t} = \cos \varphi \mathbf{e}_x + \sin \varphi \mathbf{e}_y$) and the horizontal line of direction \mathbf{e}_x , the following relation holds : $\varphi(s_1) - \varphi(s_2) = \int_{s_1}^{s_2} \frac{d\varphi}{ds} ds = \int_{s_1}^{s_2} \kappa ds$.

4.6.2 Regularity

Let $\Gamma = (\mathbf{x}_0, \mathbf{x}_1, \dots, \mathbf{x}_n)$ be a discrete curve of edges $\mathbf{e}_0, \mathbf{e}_1, \dots, \mathbf{e}_{n-1}$. Γ is said to be :

- *regular* if it has no kinks : $\mathbf{e}_{i-1} + \mathbf{e}_i \neq 0 \Leftrightarrow \varphi_i \neq \pi \mid \forall i \in \llbracket 1, n-1 \rrbracket$

- *biregular* if no vertex is flat : $\mathbf{e}_{i-1} - \mathbf{e}_i \neq 0 \Leftrightarrow \varphi_i \neq 0 \mid \forall i \in \llbracket 1, n-1 \rrbracket$

4.6.3 Parametrization

In the literature, discrete curves are usually considered as maps defined on $I = \llbracket 0, n \rrbracket \in \mathbb{N}^{n+1}$. As a consequence, the discrete derivative of Γ is an edge-based quantity defined as :

$$\Gamma'_i = \frac{\Gamma(t_{i+1}) - \Gamma(t_i)}{t_{i+1} - t_i} = \mathbf{e}_i \quad , \quad \mathbf{x}_i = \Gamma(t_i) \quad , \quad t_i = i \quad (4.60)$$

Thus, as in the smooth case, a discrete curve is said to be parametrized by arc length if $\|\Gamma'\| = 1$, that is every edges are of unit length ($\|\mathbf{e}_i\| = 1$).²⁹ This constraint is sometimes relaxed to curves of constant edge length ($\|\mathbf{e}_i\| = c$) that are said to be parametrized *proportional* to arc length.

In the present work, to stick closer to the smooth case, we instead consider discrete curves as maps defined on $I = [t_0, t_1, \dots, t_n] \in \mathbb{R}^{n+1}$ where t denotes the discrete parametrization of Γ . As in the smooth case, the way to parametrize a curve is not unique.

Arc length parameter

By analogy with the smooth case, we define the curve arc length at vertices (see fig. 4.7) as :

$$\begin{cases} s_0 = 0 & i = 0 \\ s_i = \sum_{k=1}^i \|\mathbf{e}_{k-1}\| & i \in \llbracket 1, n-1 \rrbracket \\ s_n = L & i = n \end{cases} \quad (4.61)$$

This definition naturally extends to the whole domain by piecewise linear interpolation. This is not different as considering the discrete curve as a continuous polygonal curve. Indeed, for any $s \in [s_i, s_{i+1}]$ there exists a normalized parameter $t = \frac{s-s_i}{s_{i+1}-s_i} \in [0, 1]$ so that :

$$s(t) = (1-t)s_i + ts_{i+1} = s_i + tl_i \quad (4.62a)$$

$$\mathbf{x}(t) = (1-t)\mathbf{x}_i + t\mathbf{x}_{i+1} = \mathbf{x}_i + t\mathbf{e}_i \quad (4.62b)$$

Note that this parametrization satisfies $\|\Gamma'\| = 1$ on $\bigcup_{i=1}^n \llbracket s_{i-1}, s_i \rrbracket$ but Γ' remains undefined at vertices. This issue is the reason why defining the tangent vector at vertices can not be done unequivocally for discrete curves.

²⁹This assumption leads to the assertion that “A discrete curve is parameterized by arc length or it is not” [73, p.10].

4.7 Discrete curvature

Vouga 2014 [74] defines and compares three different definitions of the discrete curvature that does not suppose that $\|\mathbf{e}_i\|$ is constant. By trying to mimic some properties of the curvature in the smooth case Carroll et al. 2014 [92] and Bobenko 2015 [93] also define and compare three different definitions of the discrete curvature from the osculating circle. One main drawback of all the said proposals is that the question of the curvature at start and end points is never treated. But this is of main importance when dealing with beams as the nature of the boundary conditions can make the curvature to be null or not at its ends, depending if some moment has to be transferred or not. In this sense, the question of discrete curvature could not be treated separately with the question of the tangent vector.

4.7.1 Definition from osculating circles

Curvature is defined from the osculating circle, which is the best approximation of a curve by a circle.

Vertex-based osculating circle (circumscribed)

Let Γ be a discrete curve parametrized by arc length. The *vertex-based* (or circumscribed) osculating circle at vertex \mathbf{x}_i is defined as the unique circle passing through the points \mathbf{x}_{i-1} , \mathbf{x}_i and \mathbf{x}_{i+1} (see fig. 4.8a). This circle leads to the following definition of the curvature :³⁰

$$\kappa \mathbf{b}_i = \frac{2 \mathbf{e}_{i-1} \times \mathbf{e}_i}{\|\mathbf{e}_{i-1}\| \|\mathbf{e}_i\| \|\mathbf{e}_{i-1} + \mathbf{e}_i\|} , \quad \kappa_i = \|\kappa \mathbf{b}_i\| = \frac{2 \sin(\varphi_i)}{\|\mathbf{e}_{i-1} + \mathbf{e}_i\|} \quad (4.63)$$

This definition shows a good locality as the curvature is attached to the vertex \mathbf{x}_i , right in the place where it occurs on the discrete curve. In addition, this definition leads to a natural local spline interpolation by the circumscribed osculating circle itself. This interpolation has the advantage to pass exactly through three vertices, to lie on the osculating plane and to share the same curvature as Γ at \mathbf{x}_i . It also leads to a natural definition of the tangent vector at \mathbf{x}_i (see ??).

Moreover, while this definition is valid only on the current portion of Γ ($i \in [1, n - 1]$), it is straightforwardly extended to its endings ($i = 0, 1$), provided that a unit tangent vector \mathbf{t}_0 (respectively \mathbf{t}_n) is given at \mathbf{x}_0 (resp. \mathbf{x}_n), as the unique circle tangent to \mathbf{t}_0 (resp. \mathbf{t}_n) passing through \mathbf{x}_0 and \mathbf{x}_1 (resp. \mathbf{x}_{n-1} and \mathbf{x}_n) :

$$\kappa \mathbf{b}_0 = \frac{2 \mathbf{e}_0 \times \mathbf{t}_0}{\|\mathbf{e}_0\|^2} , \quad \kappa \mathbf{b}_n = \frac{2 \mathbf{t}_n \times \mathbf{e}_{n-1}}{\|\mathbf{e}_{n-1}\|^2} \quad (4.64)$$

This property will be very profitable in the discrete beam model developed later in the manuscript. It is examined more in details in section ?? about the definition of the tangent vector.

³⁰This curvature is also known as the *Menger curvature*.

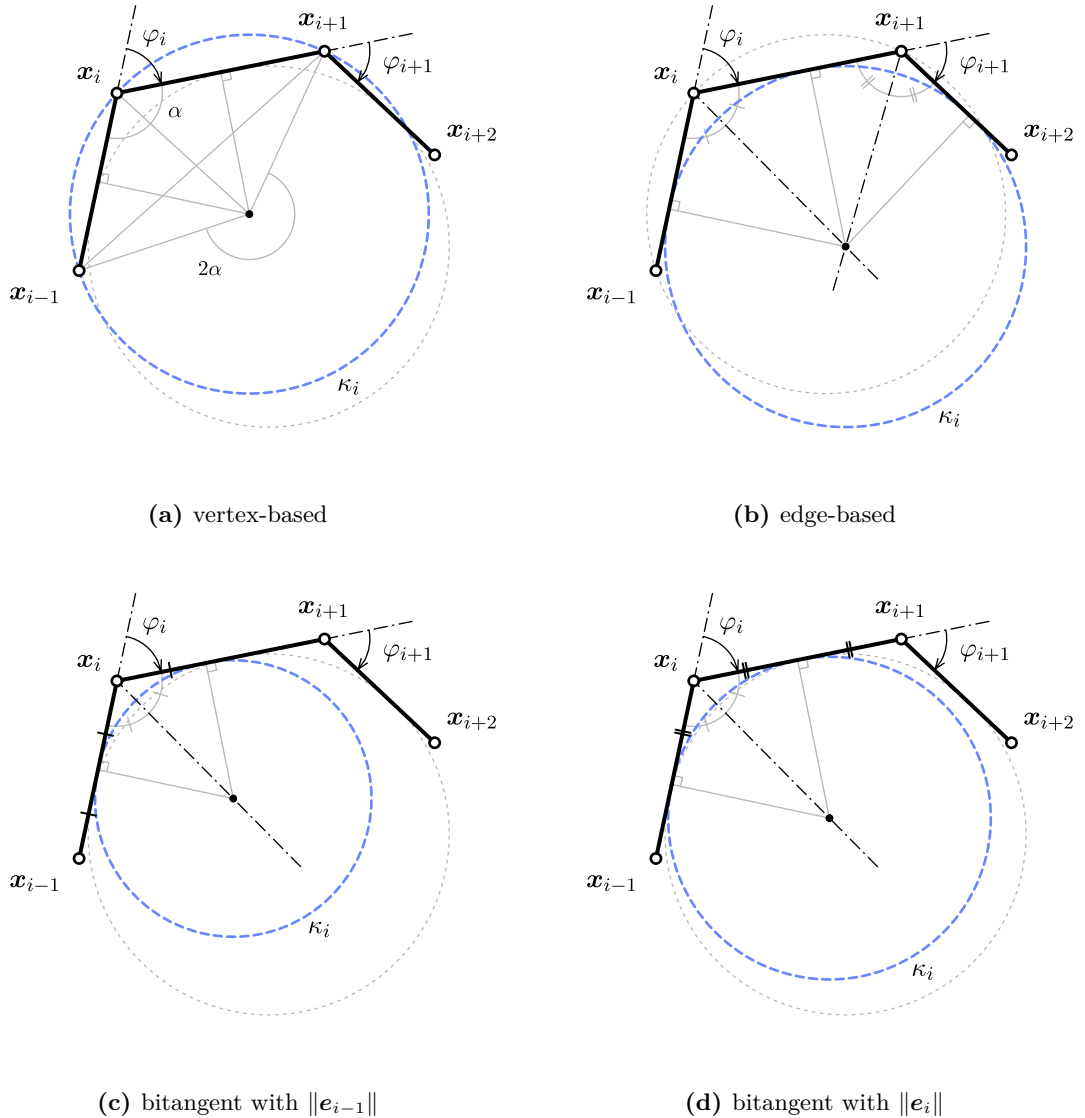


Figure 4.8 – Several ways to define the osculating circle for discrete curves, leading to different notions of discrete curvature.

Curvature (κ_i)	Locality	$\varphi \mapsto 0$	$\varphi \mapsto \pi$	Ends	Dim	Fitting
$\kappa_1 = \frac{2 \sin(\varphi_i)}{\ e_{i-1} + e_i\ }$	x_i	0	0, 2	yes	space	clothoid
$\kappa_2 = \frac{\tan(\varphi_i/2) + \tan(\varphi_{i+1}/2)}{l_i}$	e_i	0	∞	no	planar	circle
$\kappa_3 = \frac{2 \tan(\varphi_i/2)}{\bar{l}_i}$	x_i	0	∞	no	space	circles
$\kappa_4 = \frac{2 \sin(\varphi_i/2)}{\bar{l}_i}$	x_i	0	0, 2	no	space	clothoid
$\kappa_5 = \frac{\varphi_i}{\bar{l}_i}$	x_i	0	π/\bar{l}_i	no	space	elastica

Table 4.1 – Review of several discrete curvature definitions mentioned in the literature.

However, there are some important drawbacks as the curvature is bounded to $[0, 2]$ (see fig. 4.10). When the curve tends to kinks ($\varphi \mapsto \pi$), one would expect the curvature to diverge toward infinity, but instead it tends to a finite value equals to 0 ($l_{i-1} \neq l_i$) or 2 ($l_{i-1} = l_i$). This issue can be bypassed if the discretization is refined “enough”. A criterion is given in the next section (§4.7.2).

Edge-based osculating circle (inscribed)

Let Γ be a discrete curve parametrized by arc length. The *edge-based* osculating circle at edge e_i is defined as the unique circle tangent to the edges e_{i-1} , e_i and e_{i+1} (see fig. 4.8b).

$$\kappa_i = \frac{\tan(\varphi_i/2) + \tan(\varphi_{i+1}/2)}{\|e_i\|} \quad (4.65)$$

This definition shows an appropriate behavior : when the curve tends to kicks the radius of curvature tends to zero ($\tan \varphi/2 \mapsto \infty$), and when the curve tends to be a straight line the curvature tends to 0 ($\tan \varphi/2 \mapsto 0$).

However, it needs Γ to be planar which is by far too restrictive regarding our goal (the modeling of 3D slender beams). Finally, this way of defining the curvature is not as local as one would expect as it is defined relatively to the edge e_i but not where the turning occurs, at vertices.

Bitangent osculating circle (inscribed)

Let Γ be a discrete curve parametrized by arc length. Following [74] we define the curvature regarding the mean length \bar{l}_i attached to x_i as : ³¹

$$\kappa b_i = \frac{2}{\bar{l}_i} \left(\frac{\mathbf{e}_{i-1} \times \mathbf{e}_i}{\|\mathbf{e}_{i-1}\| \|\mathbf{e}_i\| + \mathbf{e}_{i-1} \cdot \mathbf{e}_i} \right) , \quad \kappa_i = \|\kappa b_i\| = \frac{2}{\bar{l}_i} \tan(\varphi_i/2) \quad (4.66)$$

This other definition combines the good locality of the vertex-based approach (see eq. (4.63)) and the proper behavior at bounds of the edge-based approach (see eq. (4.65)). Given two adjacent edges e_{i-1} and e_i , there exists an infinite number of circles that are tangent to both edges (see fig. 4.8c and fig. 4.8d for two remarkable circles among them), which center points all lie on the $\varphi_i - \pi$ angle bisector line. The corresponding osculating circle, known as the *inscribed* circle, is constructed to touch both e_{i-1} and e_i at distance \bar{l}_i from x_i . In the case of a constant edge length discrete curve, this definition of the osculating circle merges to the circles proposed in fig. 4.8c and fig. 4.8d.

However, this definition still exhibits some drawbacks. Firstly, remark that there is an infinity of possible inscribed circles (defined as a circle that is bitangent to two connected edges). Indeed, this circle is unique only if the distance between the common vertex and the points of tangency are prescribed. Although it could seem natural to take the middle

³¹This definition is also presented in [93, 92] but in the more restrictive case of constant edge length discrete curves ($l_i = cst$).

of the edges as points of tangency if they have the same length ($\|e_i\| = \|e_{i+1}\|$), there is no obvious choice at all for this parameter (compare fig. 4.8c with fig. 4.8d). Moreover, the lack of a natural interpolation spline that passes through the vertices and that is in correlation to the osculating circle is also detrimental in the context of our application.

Other definitions of osculating circles

In the literature, one can find other definitions for the discrete curvature that also correspond to the definition of an osculating circle. All these definitions are summarized in tab. 4.1. For further informations, the reader should refer to [92, 74, 93, 94].

In particular, Vouga [74] details which discrete curvature definitions parallel which property of the smooth curvature. He remarks that there is no “free-lunch” as none of the proposed definition satisfies every properties of the smooth curvature.

4.7.2 Benchmarking : sensitivity to non uniform discretization

In this section we compare the two main discrete curvature notions (circumscribed versus inscribed) regarding their sensibility to non uniform discretization.

This aspect is not treated in the actual literature, in which curves parametrized by arc length are usually treated as curves of constant edge length, though it is yet an important topic when it comes to the numerical modeling of true mechanical systems. Indeed, the presence of connexions between members will compromise the ability to enforce a constant discretization through all the elements of the structure. Additionally, vertices are obviously points of interest in a discrete model as they will be used to apply loads and enforce various constraints such as joints and support conditions. Finally, the accuracy of the discretized model is proportional to the sharpness of the discretization, whereas the computing time required to solve the model will grow as the sharpness increases. Consequently, one would distribute those points in the space as cleverly as possible and try to minimize their number as they increase the overall computation cost.

Introducing the coefficient $\alpha = \frac{\|e_{i-1}\|}{\|e_i\|}$, we rewrite the previous formulas for κ_1 and κ_3 as :

$$\begin{aligned} \kappa_1 &= \frac{2 \sin(\varphi)}{\|e_i\|(1 + \alpha^2 + 2\alpha \cos(\varphi))^{1/2}} \\ \kappa_3 &= \frac{4 \tan(\varphi/2)}{\|e_i\|(1 + \alpha)} \end{aligned} \tag{4.67}$$

These expressions lead to the following formula for the ratio κ_1/κ_3 , which relies only on α and the turning angle φ between the edges e_{i-1} and e_i :

$$\frac{\kappa_1}{\kappa_3}(\alpha) = \frac{\kappa_1}{\kappa_3}(1/\alpha) = \frac{(1 + \alpha) \cos^2(\varphi/2)}{((1 - \alpha)^2 + 4\alpha \cos^2(\varphi/2))^{1/2}} \tag{4.68}$$

Discrete curvatures are plotted in fig. 4.10 for three values of α . The thickest line is for the

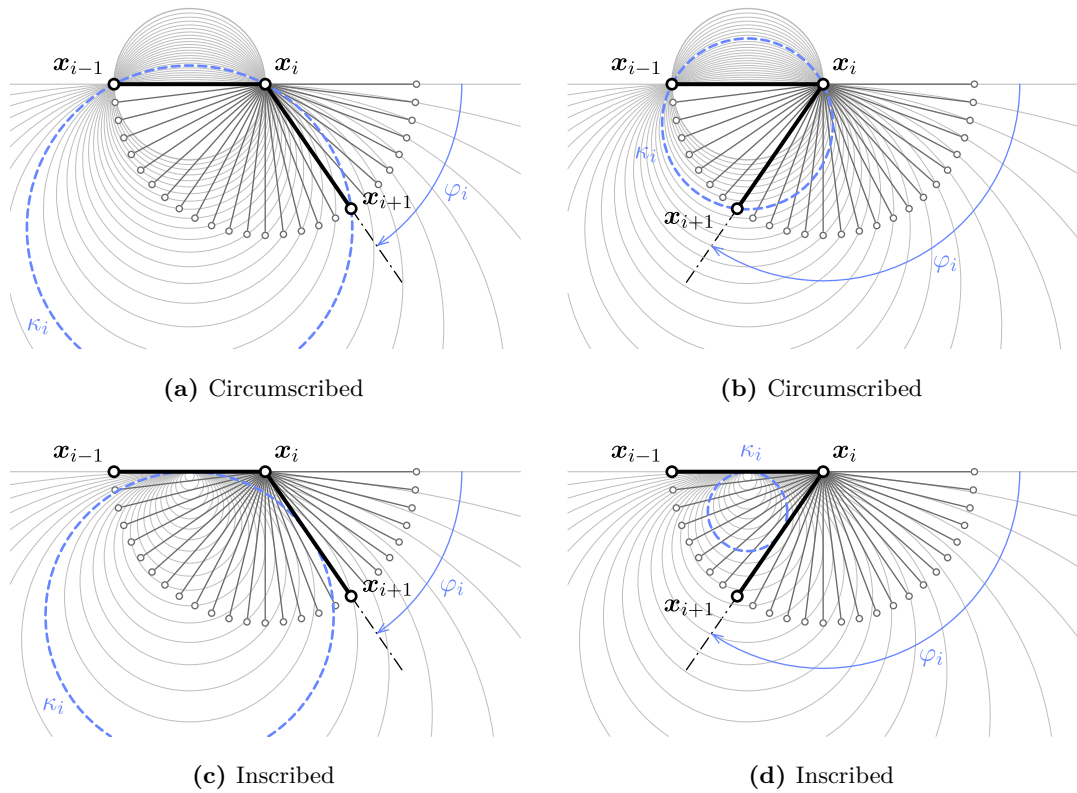


Figure 4.9 – Comparison of circumscribed and inscribed osculating circles for different values of the turning angle (φ).

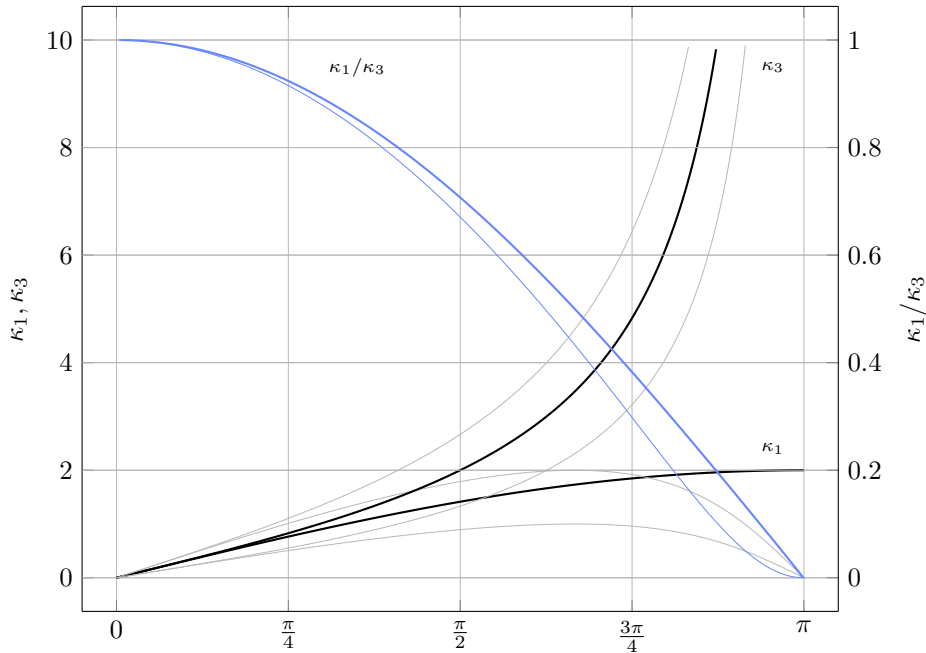


Figure 4.10 – Sensitivity of discrete curvatures to non uniform discretization ($\alpha \in [0.5, 2]$) over the whole domain of variation of the turning angle ($\varphi \in [0, \pi]$).

case of uniform discretization ($\alpha = 1$), whereas the thin lines mark the boundary cases ($\alpha = 0.5, 2$). The ratio κ_1/κ_3 is plotted in blue and leads to only one thin line (remind eq. (4.68)). The graph shows that κ_1 and κ_3 have a very close behavior for small turning angles. The variability regarding α is small when φ remains small and gets negligible as φ gets smaller.

Passing $\pi/4$ and increasing φ , κ_3 exhibits a good behavior : as the discrete curves tends to kink, κ_3 diverges towards the infinity as the smooth curvature would behave when the curve kinks. Conversely, the behavior of κ_1 is not appropriate as it converges to a fixed limit. This limit equals 2 when the edges have the same length and equals 0 when they have different lengths.

Conclusion

It appears that the discrete curvature related to the inscribed osculating circle exhibits a better behavior – that is a behavior closer to the smooth case – on the whole range of possible turning angles. This would be an advantage when modeling highly nonlinear beam configurations such as the ones encountered in hair simulations.

However, for the kind of structures we are studying here, those kind of configurations are not likely to arise. And if they do, the structure would be severely damaged and this situation is to be avoided by the designers. More over, the sharpness of the discretization could be increased to reduce the value of the turning angles and stay in the range $[0, \pi/4]$ where the circumscribed curvature gives accurate results.

4.7.3 Benchmarking : accuracy in bending energy representation

In this section we compare, for three remarkable types of curves (line, semicircle and elastica), the discrete bending energies \mathcal{E}_1 and \mathcal{E}_3 of the discrete curve, respectively based on definitions κ_1 and κ_3 (see tab. 4.1), to the bending energy \mathcal{E} of the smooth curve. We study the convergence of these energies as the sharpness of the discretization increases. The smooth and discrete bending energies are defined as :

$$\mathcal{E} = \int_0^L \kappa^2 ds \tag{4.69a}$$

$$\mathcal{E}_i = \sum_i \bar{l}_i \kappa_i^2 \tag{4.69b}$$

Straight line

Let's consider any straight line. Its smooth curvature is null. So are the discrete curvatures κ_1 and κ_3 (see tab. 4.1). In this case, the discrete bending energies perfectly match the bending energy of the smooth curve :

$$\mathcal{E} = \mathcal{E}_1 = \mathcal{E}_3 = 0 \tag{4.70}$$

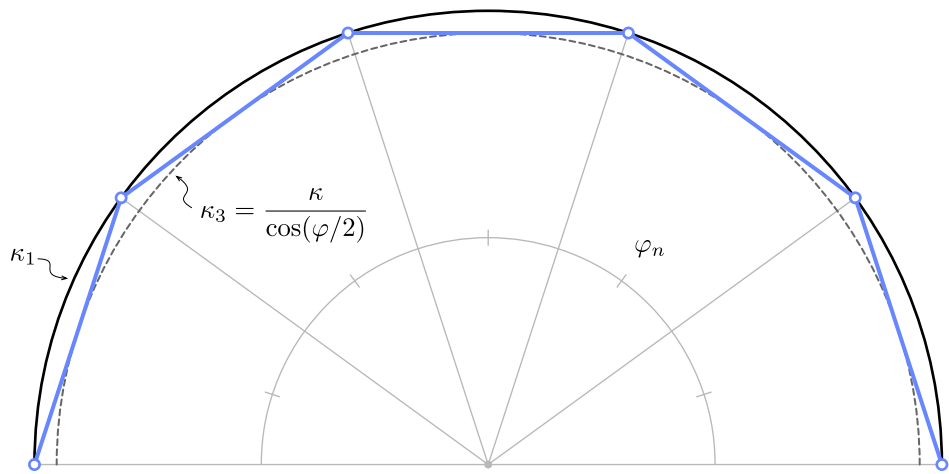


Figure 4.11 – Discretization of a semicircle and evaluation of its bending energy.

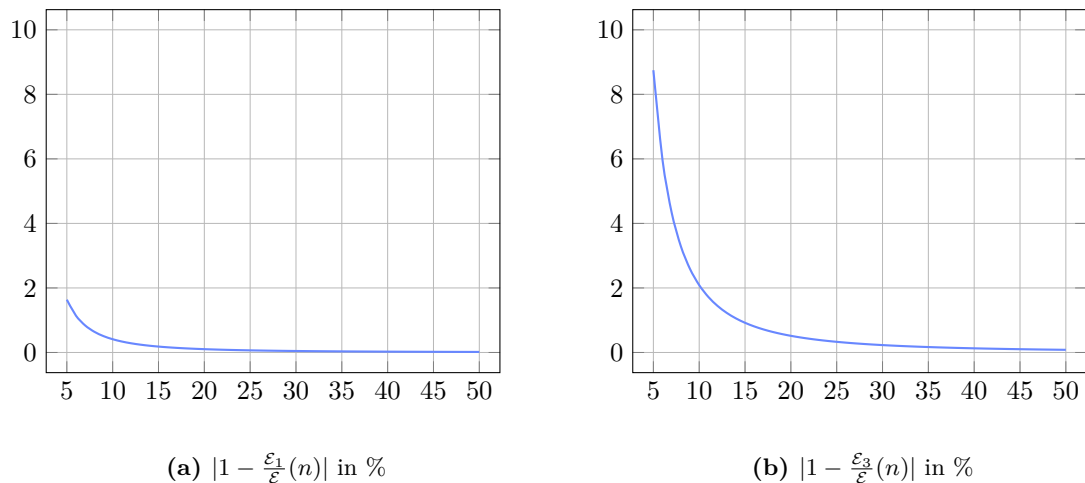


Figure 4.12 – Relative error in the estimation of the bending energy of a semicircle (\mathcal{E}) by the discrete energies \mathcal{E}_1 and \mathcal{E}_3 , regarding the sharpness of the discretization.

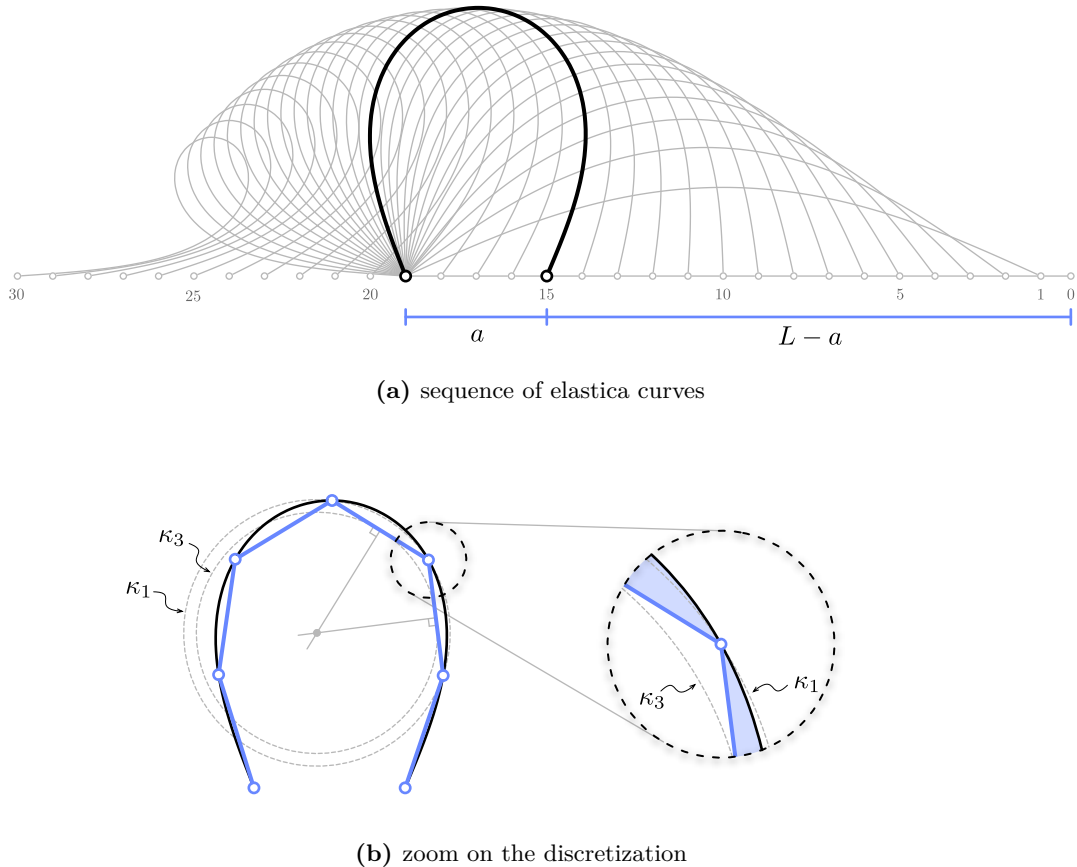


Figure 4.13 – Discretization of an elastica curve and evaluation of its bending energy.

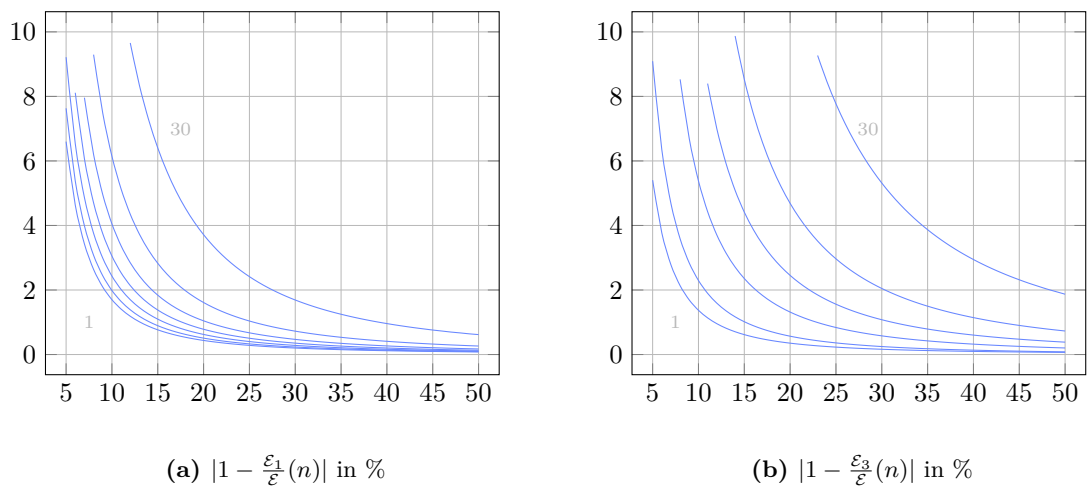


Figure 4.14 – Relative error in the estimation of the bending energy of an elastica (\mathcal{E}) by the discrete energies \mathcal{E}_1 and \mathcal{E}_3 , regarding the sharpness of the discretization. The curves (1,5,10,15,20,25,30) are chosen from [fig. 4.13a](#).

Semicircle

Let's consider a semicircle of curvature $\kappa = 1/r$ and length $L = \pi r$. This curve is discretized into n edges of equal length $|\mathbf{e}_n| = 2r \sin(\varphi/2)$ where $\varphi = \frac{\pi}{n}$ (see fig. 4.11). The total length of the discrete curve is given by : $L_n = n|\mathbf{e}_n| = L \frac{\sin(\varphi/2)}{\varphi/2}$. In this simple case, the bending energies can be expressed analytically :

$$\mathcal{E} = L\kappa^2 \quad (4.71a)$$

$$\mathcal{E}_1 = L_n \kappa_1^2 = \frac{\sin(\varphi/2)}{\varphi/2} \cdot \mathcal{E} \quad (4.71b)$$

$$\mathcal{E}_3 = L_n \kappa_3^2 = \frac{\sin(\varphi/2)}{(\varphi/2) \cos^2(\varphi/2)} \cdot \mathcal{E} \quad (4.71c)$$

Note that κ_1 equals the curvature of the smooth curve. Consequently, the estimation error is only due to the estimation of the curve length ($L_n \neq L$). The ratios $\mathcal{E}_1/\mathcal{E}$ and $\mathcal{E}_3/\mathcal{E}$ are plotted in fig. 4.12. Graphs show that \mathcal{E}_1 converges to the smooth case faster than \mathcal{E}_3 .

Elastica

Let's consider a sequence of elastica curves of fixed length L and variable curvature κ (see fig. 4.13a). These curves correspond to a buckled shape of a straight pinned-pinned beam that would have been forced to retract its span. These curves are discretized into n edges of equal length (see fig. 4.13b). This time, there is no analytical expressions available for \mathcal{E} , \mathcal{E}_1 and \mathcal{E}_3 . Results are obtained by numerical integration and plotted in fig. 4.14. Again, graphs show that \mathcal{E}_1 converges to the smooth case faster than \mathcal{E}_3 for most of the curves excepted the ones with low overall curvature (1 to 5).

Conclusion

figures 4.12 and 4.14 show that for typical curves of mechanical interest – a semicircle is the shape of a rod with constant bending moment while the elastica is the shape of a buckled rod with no end moments – the circumscribed curvature gives a better approximation of the bending energy embedded in these curves. Hence, the circumscribed curvature seems to be a good candidate to maximize accuracy while minimizing the sampling of beam elements. This will lead to models with fewer nodes and decrease the cost of the computation.

4.8 Discrete tangent vector

In this section we study how to define the discrete unit tangent vector relatively to a discrete curve. While a natural definition exists along the edges (see §4.6.1), there is no obvious choice at vertices were the curve kinks.

The ability to define a unique tangent vector is very important to define the normal of cross-sections, to control beam endings, and to relate it to curvature. You would control

the direction of the section (for a fixed/encastre support condition) or conversly, you would control the moment and seek the corresponding tangent direction (for a pin boundary condition, you know there is no end moments so the curvature is null and you are looking for the tangent).

4.8.1 Circumscribed case

We consider the case where the curvature is defined according to the circumscribed osculating circle (see fig. 4.15a).

Current portion

Let \mathbf{x}_i be a vertex in the current portion of Γ . The circumscribed osculating circle gives a smooth approximation of Γ in the vicinity of \mathbf{x}_i (see fig. 4.15a). It leads to a natural definition of a unit tangent vector for five remarkable vertices as the tangent to the osculating circle at those points (resp. \mathbf{x}_{i-1} , $\mathbf{x}_{i-1/2}$, \mathbf{x}_i , $\mathbf{x}_{i+1/2}$, \mathbf{x}_{i+1}) :

$$\mathbf{t}_i^- = 2(\mathbf{t}_i \cdot \mathbf{u}_{i-1})\mathbf{u}_{i-1} - \mathbf{t}_i \quad (4.72a)$$

$$\mathbf{t}_{i-1/2} = \mathbf{u}_{i-1} \quad (4.72b)$$

$$\mathbf{t}_i = \frac{\|\mathbf{e}_i\|}{\|\mathbf{e}_{i-1} + \mathbf{e}_i\|} \mathbf{u}_{i-1} + \frac{\|\mathbf{e}_{i-1}\|}{\|\mathbf{e}_{i-1} + \mathbf{e}_i\|} \mathbf{u}_i \quad (4.72c)$$

$$\mathbf{t}_{i+1/2} = \mathbf{u}_i \quad (4.72d)$$

$$\mathbf{t}_i^+ = 2(\mathbf{t}_i \cdot \mathbf{u}_i)\mathbf{u}_i - \mathbf{t}_i \quad (4.72e)$$

Note that \mathbf{t}_i^- (resp. \mathbf{t}_i^+) is obtained by a reflection of $-\mathbf{t}_i$ across the bisecting plane of \mathbf{e}_{i-1} (resp. \mathbf{e}_i). A very important property is that the curvature binormal vector at \mathbf{x}_i can be computed by three different ways :

$$\kappa \mathbf{b}_i = \frac{2 \mathbf{e}_{i-1} \times \mathbf{e}_i}{\|\mathbf{e}_{i-1}\| \|\mathbf{e}_i\| \|\mathbf{e}_{i-1} + \mathbf{e}_i\|} = \begin{cases} \frac{2 \mathbf{u}_{i-1} \times \mathbf{t}_i}{\|\mathbf{e}_{i-1}\|} \\ \frac{2 \mathbf{t}_i \times \mathbf{u}_i}{\|\mathbf{e}_i\|} \end{cases} \quad (4.73)$$

The first expression is interpreted as the unique circle passing through three points (\mathbf{x}_{i-1} , \mathbf{x}_i , \mathbf{x}_{i+1}) as explained in §4.7.1. Equivalently, there exist a unique circle defined by two points and a tangent vector. Precisely, the last two expressions in eq. (4.73) can be interpreted as the curvature binormal vector of the unique circle passing through \mathbf{x}_{i-1} , \mathbf{x}_i (resp. \mathbf{x}_i , \mathbf{x}_{i+1}) and tangent to \mathbf{t}_i at \mathbf{x}_i .

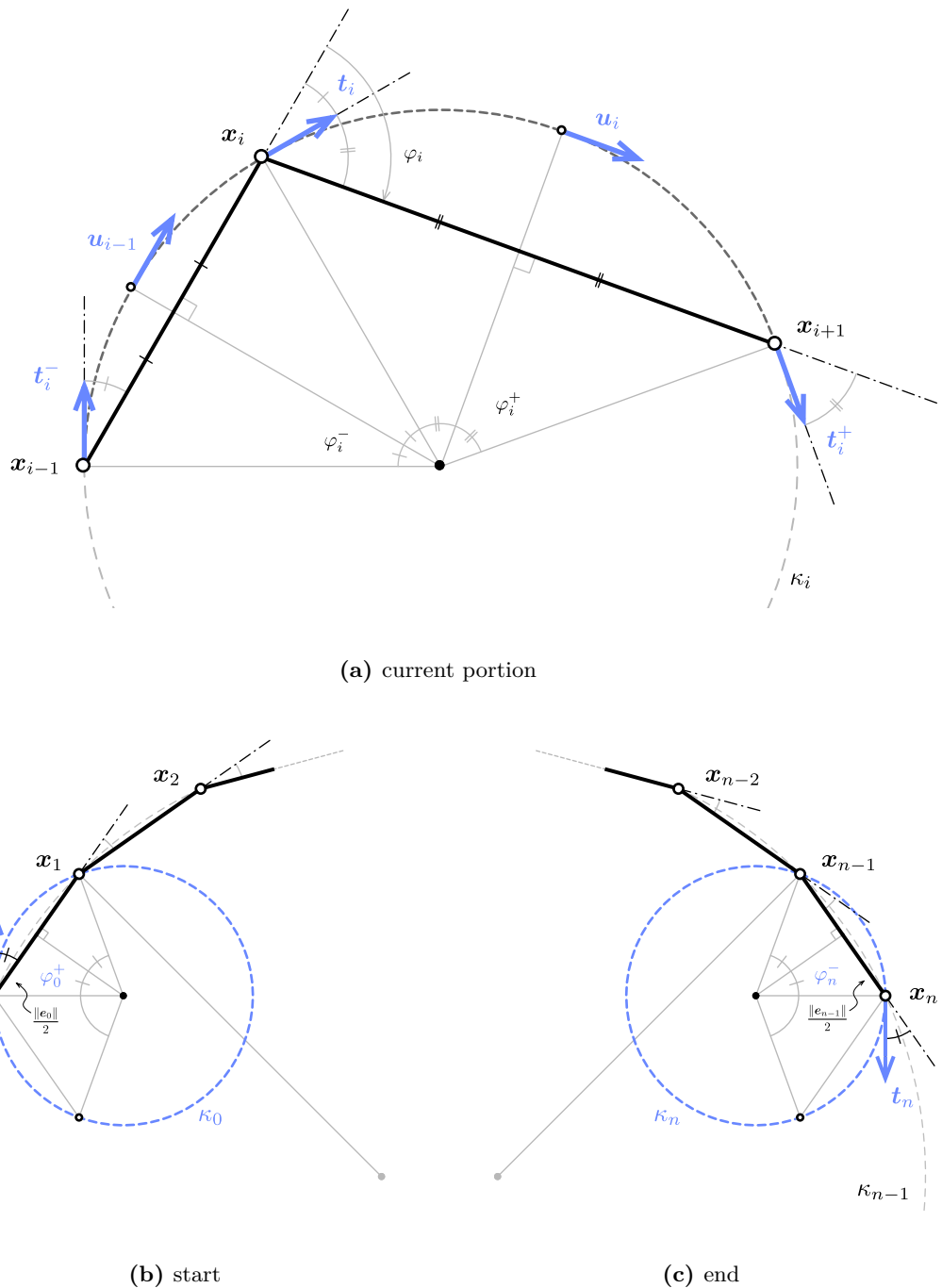


Figure 4.15 – Definition of the tangent vector (t) and related curvature binormal vector (κb) at vertices associated to the circumscribed curvature.

Discontinuity of curvature

Let \mathbf{t}_i^* be an arbitrary tangent vector at \mathbf{x}_i . Following eq. (4.73) we define the *left-sided* (resp. *right-sided*) discrete curvatures at \mathbf{x}_i in the circumscribed case as : as

$$\kappa b_i^-(\mathbf{t}_i^*) = \frac{2 \mathbf{u}_{i-1} \times \mathbf{t}_i^*}{\|\mathbf{e}_{i-1}\|} \quad (4.74a)$$

$$\kappa b_i^+(\mathbf{t}_i^*) = \frac{2 \mathbf{t}_i^* \times \mathbf{u}_i}{\|\mathbf{e}_i\|} \quad (4.74b)$$

The corresponding osculating circle will be called the *left-sided* (resp. *right-sided*) circumscribed osculating circle. When $\mathbf{t}_i^* = \mathbf{t}_i$, the limits agree one to each other ($\kappa b_i^- = \kappa b_i^+ = \kappa b_i$) and the osculating circles coincide. These definitions perfectly mimic the smooth case where, at a regular ($\|\gamma'\| \neq 0$) but not biregular ($\|\gamma''\| = 0$) point, the curvature is discontinuous while the tangent vector reminds smoothly defined.

In mechanics, this situation is likely to arise as discontinuities in material properties or punctual applied moments will necessarily lead to discontinuities in curvature (recall that $M = EI\kappa$).

Curve endings

The definition of the left and right sided curvatures given for a vertex in the current portion of Γ are still valid for the end vertices \mathbf{x}_0 and \mathbf{x}_n . Provided that a unit tangent vector \mathbf{t}_0^* (respectively \mathbf{t}_n^*) is given at \mathbf{x}_0 (resp. \mathbf{x}_n), the circumscribed osculating circle is defined as the unique circle passing through \mathbf{x}_0 and \mathbf{x}_1 (resp. \mathbf{x}_{n-1} and \mathbf{x}_n) tangent to \mathbf{t}_0^* (resp. \mathbf{t}_n^*) ; see fig. 4.15b and fig. 4.15c. It leads to the following curvature binormal vectors :

$$\kappa b_0 = \kappa b_0^+(\mathbf{t}_0^*) = \frac{2 \mathbf{t}_0^* \times \mathbf{e}_0}{\|\mathbf{e}_0\|^2} \quad (4.75a)$$

$$\kappa b_n = \kappa b_n^-(\mathbf{t}_n^*) = \frac{2 \mathbf{e}_{n-1} \times \mathbf{t}_n^*}{\|\mathbf{e}_{n-1}\|^2} \quad (4.75b)$$

Note that, contrary to the current portion, curvatures at endings are subjected to the definition of a unit tangent vector. This reflects the usual indetermination of boundary conditions. For a given beam whether the end is clamped and the tangent vector is known and one will seek the reacting moment due to the support ; whether the end is pinned and the reacting moment is null (so is the curvature) and one will seek the cross-section orientation.

4.8.2 Inscribed case

We now consider the case where the curvature is defined according to the inscribed osculating circle (see fig. 4.16a). Remark that inscribed and circumscribed osculating circles are concentric when $l_{i-1} = l_i$.

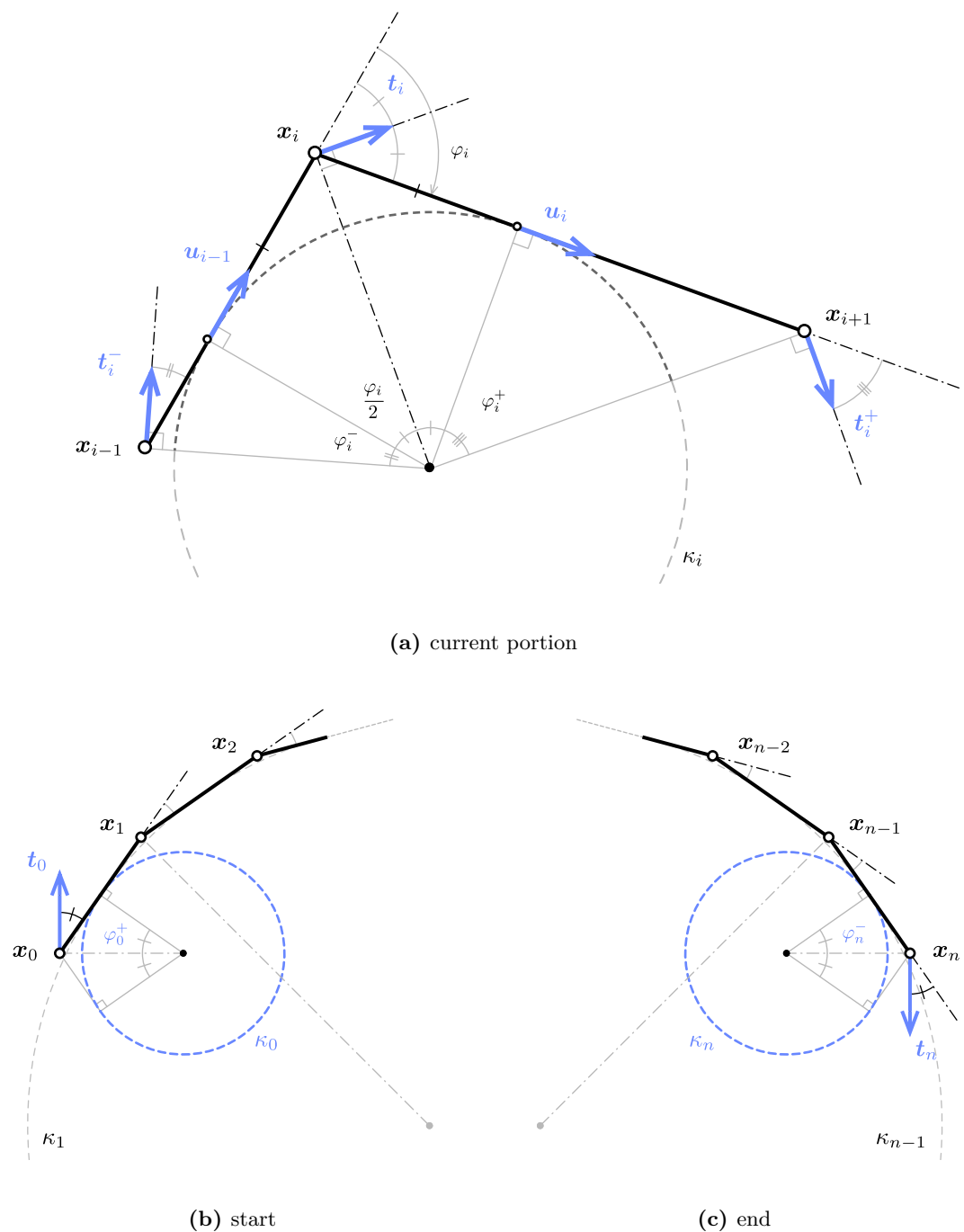


Figure 4.16 – Definition of the tangent vector (t) and related curvature binormal vector (κb) at vertices associated to the inscribed curvature.

Current portion

Let \mathbf{x}_i be a vertex in the current portion of Γ . The inscribed osculating circle gives a smooth approximation of Γ in the vicinity of \mathbf{x}_i (see fig. 4.16a) ; though this approximation does not pass through the vertices. It is again possible to construct some unit tangent vectors based on this circle, but the analytic expressions are less compact than in the circumscribed case (resp. at \mathbf{x}_{i-1} , \mathbf{x}_i , \mathbf{x}_{i+1}) :

$$\mathbf{t}_i^- = \cos\left(\frac{\varphi_i}{2} + \varphi_i^-\right) \frac{\mathbf{u}_{i-1} + \mathbf{u}_i}{\|\mathbf{u}_{i-1} + \mathbf{u}_i\|} + \sin\left(\frac{\varphi_i}{2} + \varphi_i^-\right) \frac{\mathbf{u}_{i-1} - \mathbf{u}_i}{\|\mathbf{u}_{i-1} - \mathbf{u}_i\|} \quad (4.76a)$$

$$\mathbf{t}_i^- = \frac{\mathbf{u}_{i-1} + \mathbf{u}_i}{\|\mathbf{u}_{i-1} + \mathbf{u}_i\|} \quad (4.76b)$$

$$\mathbf{t}_i^+ = \cos\left(\frac{\varphi_i}{2} + \varphi_i^+\right) \frac{\mathbf{u}_{i-1} + \mathbf{u}_i}{\|\mathbf{u}_{i-1} + \mathbf{u}_i\|} - \sin\left(\frac{\varphi_i}{2} + \varphi_i^+\right) \frac{\mathbf{u}_{i-1} - \mathbf{u}_i}{\|\mathbf{u}_{i-1} - \mathbf{u}_i\|} \quad (4.76c)$$

In this form, the expressions of \mathbf{t}_i^- and \mathbf{t}_i^+ exhibit lots of trigonometric computations. Consequently, they will be more costly to evaluate (numerically) than the ones given for the circumscribed case that exhibit only simple addition, product and division operations.

Though these points does not generally fall into mid-edge, the tangent vector can also be identified to \mathbf{u}_{i-1} (resp. \mathbf{u}_i) at point $\tilde{\mathbf{x}}_i^- = \mathbf{x}_i - \frac{1}{2}\bar{l}_i \mathbf{u}_{i-1}$ (resp. $\tilde{\mathbf{x}}_i^+ = \mathbf{x}_i + \frac{1}{2}\bar{l}_i \mathbf{u}_i$) :

$$\tilde{\mathbf{t}}_i^- = \mathbf{u}_{i-1} \quad (4.77a)$$

$$\tilde{\mathbf{t}}_i^+ = \mathbf{u}_i \quad (4.77b)$$

Similarly to the circumscribed case, one can remark that the curvature binormal vector at \mathbf{x}_i can be computed in three different manners :

$$\kappa \mathbf{b}_i = \frac{2}{\bar{l}_i} \left(\frac{\mathbf{e}_{i-1} \times \mathbf{e}_i}{\|\mathbf{e}_{i-1}\| \|\mathbf{e}_i\| + \mathbf{e}_{i-1} \cdot \mathbf{e}_i} \right) = \begin{cases} \frac{2}{\bar{l}_i} \left(\frac{\mathbf{e}_{i-1} \times \mathbf{t}_i}{\mathbf{e}_{i-1} \cdot \mathbf{t}_i} \right) \\ \frac{2}{\bar{l}_i} \left(\frac{\mathbf{t}_i \times \mathbf{e}_i}{\mathbf{t}_i \cdot \mathbf{e}_i} \right) \end{cases} \quad (4.78)$$

The first expression is interpreted as the unique circle bitangent to \mathbf{e}_{i-1} at $\tilde{\mathbf{x}}_i^-$ and \mathbf{e}_i at $\tilde{\mathbf{x}}_i^+$, as explained in §4.7.1. Equivalently, the last two expressions in eq. (4.78) can be interpreted as the curvature binormal vector of the unique circle which center is on the line normal to \mathbf{t}_i passing through \mathbf{x}_i , and that is tangent to \mathbf{e}_{i-1} (resp. \mathbf{e}_i) at $\tilde{\mathbf{x}}_i^-$ (resp. $\tilde{\mathbf{x}}_i^+$).

Discontinuity of curvature

Let \mathbf{t}_i^* be an arbitrary tangent vector at \mathbf{x}_i . Following eq. (4.78) we define the *left-sided* (resp. *right-sided*) discrete curvature at \mathbf{x}_i in the inscribed case as :

$$\kappa b_i^-(\mathbf{t}_i^*) = \frac{2}{\bar{l}_i} \left(\frac{\mathbf{e}_{i-1} \times \mathbf{t}_i^*}{\mathbf{e}_{i-1} \cdot \mathbf{t}_i^*} \right) \quad (4.79a)$$

$$\kappa b_i^+(\mathbf{t}_i^*) = \frac{2}{\bar{l}_i} \left(\frac{\mathbf{t}_i^* \times \mathbf{e}_i}{\mathbf{t}_i^* \cdot \mathbf{e}_i} \right) \quad (4.79b)$$

The corresponding osculating circle will be called the *left-sided* (resp. *right-sided*) inscribed osculating circle. When $\mathbf{t}_i^* = \mathbf{t}_i$, the limits agree one to each other ($\kappa b_i^- = \kappa b_i^+ = \kappa b_i$) and the osculating circles coincide. These definitions perfectly mimic the smooth case where, at a regular ($\|\gamma'\| \neq 0$) but not biregular ($\|\gamma''\| = 0$) point, the curvature is discontinuous while the tangent vector reminds smoothly defined.

Curve endings

The definition of the left and right sided curvatures given for a vertex in the current portion of Γ are still valid for the end vertices \mathbf{x}_0 and \mathbf{x}_n . Provided that a unit tangent vector \mathbf{t}_0^* (respectively \mathbf{t}_n^*) is given at \mathbf{x}_0 (resp. \mathbf{x}_n), the circumscribed osculating circle is defined as the unique circle passing through \mathbf{x}_0 and \mathbf{x}_1 (resp. \mathbf{x}_{n-1} and \mathbf{x}_n) tangent to \mathbf{t}_0^* (resp. \mathbf{t}_n^*) ; see fig. 4.16b and fig. 4.16c. It leads to the following curvature binormal vectors :

$$\kappa b_0 = \kappa b_0^+(\mathbf{t}_0^*) = \frac{2}{\|\mathbf{e}_0\|} \left(\frac{\mathbf{t}_0^* \times \mathbf{e}_0}{\mathbf{t}_0^* \cdot \mathbf{e}_0} \right) \quad (4.80a)$$

$$\kappa b_n = \kappa b_n^-(\mathbf{t}_n^*) = \frac{2}{\|\mathbf{e}_{n-1}\|} \left(\frac{\mathbf{e}_{n-1} \times \mathbf{t}_n^*}{\mathbf{e}_{n-1} \cdot \mathbf{t}_n^*} \right) \quad (4.80b)$$

Note that, contrary to the current portion, curvatures at endings are subjected to the definition of a unit tangent vector. This reflects the usual indetermination of boundary conditions. For a given beam whether the end is clamped, the tangent vector is known and one will seek the reacting moment due to the support ; whether the end is pinned, the reacting moment is null (so is the curvature) and one will seek the cross-section orientation.

Conclusion

We have extended the comprehension of the discrete curvature to the extremities of the curve, for both the circumscribed and inscribed definitions of the discrete curvature. We have seen that these notions lead to a natural definition of the tangent at vertices in the current portion as at the extremities.

When the curvature is prescribed at a given vertex, eq. (4.74a) and (4.74b) (circumscribed) or eq. (4.79a) and (4.79a) (inscribed) need to be solved to determine the tangent vector. Remark that both systems are linear in \mathbf{t} .

4.9 Discrete parallel transport

Discrete parallel transport can be computed by analogy to the smooth case as the minimal rotation around \mathbf{t} . However, this method gets unstable when \mathbf{t}_i and \mathbf{t}_{i+1} get almost collinear because of the cross product (although the rotation angle tends to zero, the rotation axis become very sensitive to numerical instabilities).

Note that while these definitions of parallel transport are illustrated to transport vectors in space from one location $\{\mathbf{x}, \mathbf{t}\}(s)$ to another $\{\mathbf{x}, \mathbf{t}\}(s + ds)$, it is identically transposed to parallel transport in time from one location $\{\mathbf{x}, \mathbf{t}\}(t)$ to another $\{\mathbf{x}, \mathbf{t}\}(t + dt)$ as suggested in [95].

4.9.1 The rotation method

The rotation method is given by Bloomenthal 1990 [78]. First, the frame at \mathbf{x}_i is simply translated at vertex \mathbf{x}_{i+1} . Then, the translated frame is rotated so that \mathbf{t}_i aligns with \mathbf{t}_{i+1} . The rotation axis is chosen to be $\mathbf{b} = \mathbf{t}_i \times \mathbf{t}_{i+1}$ and the angle of rotation is denoted α (see fig. 4.17a). This is analogous to the smooth case.

4.9.2 The double reflexion method

The double reflection method is given by Wang et al. 2008 [81]. It is supposed to be of order $o(h^4)$ whereas the rotation method is only $o(h^2)$, where $h = \sup_{i \in [0, n]} \|\mathbf{e}_i\|$ is the sharpness of the discretization. Though their computation cost is quite similar, the double reflection method is not subject to instability when \mathbf{t}_i and \mathbf{t}_{i+1} tend to be collinear, which is an obvious advantage.

We denote \mathcal{R}_x^n the reflection across the plane passing through the point \mathbf{x} and normal to the unit vector $\mathbf{n} = \mathbf{e}_i / \|\mathbf{e}_i\|$. Thus, \mathbf{v} is mapped through \mathcal{R} into $\mathbf{v}^* = \mathbf{v} - 2(\mathbf{v} \cdot \mathbf{n})\mathbf{n}$.

Let $\mathcal{R}_1 = \mathcal{R}_{x_{i+1/2}}^{n_1}$ be the reflection across the bisecting plane of \mathbf{e}_i ($\mathbf{n}_1 = \mathbf{u}_i$). Let $\mathbf{t}_i^* = \mathcal{R}_1(\mathbf{t}_i)$ be the image of \mathbf{t}_i by \mathcal{R}_1 . Let $\mathcal{R}_2 = \mathcal{R}_{x_{i+1}}^{n_2}$ be the reflection across the bisecting plane of the points $\mathbf{x}_{i+1} + \mathbf{t}_i^*$ and $\mathbf{x}_{i+1} + \mathbf{t}_{i+1}$. Thus, $\mathbf{n}_2 = \frac{\mathbf{t}_{i+1} - \mathbf{t}_i^*}{\|\mathbf{t}_{i+1} - \mathbf{t}_i^*\|}$ (see fig. 4.17b).

Parallel transport is defined as the *double reflection* through \mathcal{R}_1 and \mathcal{R}_2 :

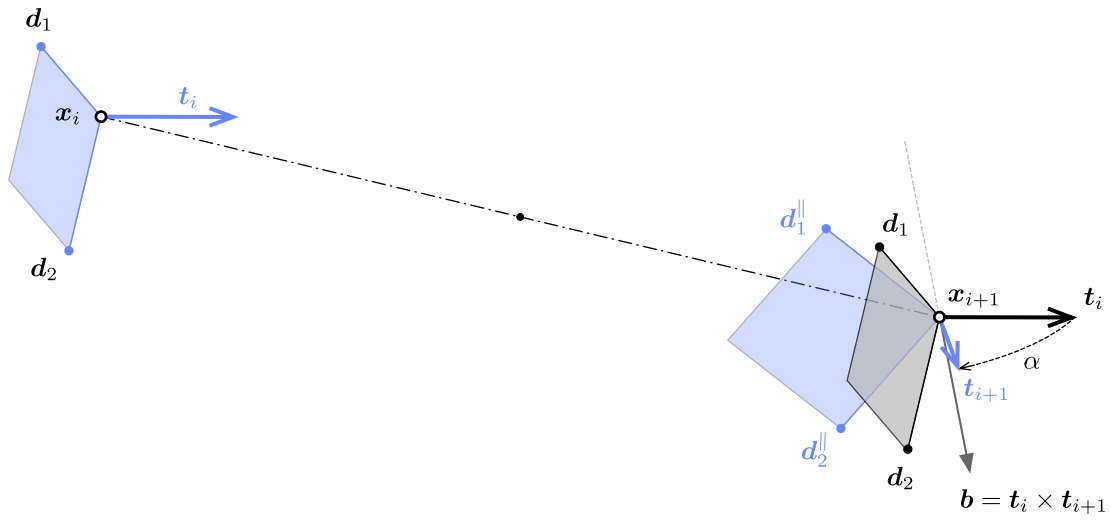
$$\mathcal{P}_{\{\mathbf{x}_i, \mathbf{t}_i\}}^{\{\mathbf{x}_{i+1}, \mathbf{t}_{i+1}\}} = \mathcal{P}_i^{i+1} = \mathcal{R}_2 \circ \mathcal{R}_1 \quad (4.81)$$

Let $\mathcal{F}_i = \{\mathbf{t}_i, \mathbf{d}_1, \mathbf{d}_2\}$ be an orthonormal frame at \mathbf{x}_i . Let $\mathcal{F}_i^* = \mathcal{R}_1(\mathcal{F}_i) = \{\mathbf{t}_i^*, \mathbf{d}_1^*, \mathbf{d}_2^*\}$ be the image of \mathcal{F}_i by \mathcal{R}_1 . Then :

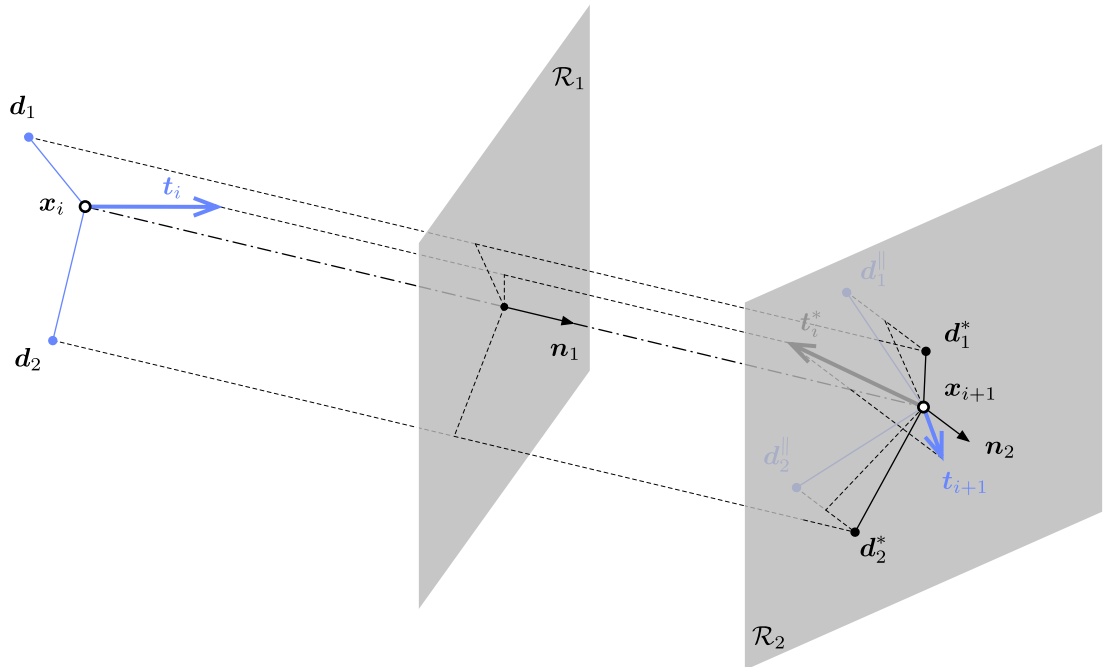
$$\mathbf{t}_i^* = \mathbf{t}_i - 2(\mathbf{t}_i \cdot \mathbf{n}_1)\mathbf{n}_1 \quad (4.82a)$$

$$\mathbf{d}_1^* = \mathbf{d}_1 - 2(\mathbf{d}_1 \cdot \mathbf{n}_1)\mathbf{n}_1 \quad (4.82b)$$

$$\mathbf{d}_2^* = \mathbf{d}_1^* \times \mathbf{t}_i^* \quad (4.82c)$$



(a) rotation method



(b) double reflection method

 Figure 4.17 – Two methods to parallel transport a vector from $\{x_i, t_i\}$ to $\{x_{i+1}, t_{i+1}\}$.

Let $\mathcal{F}_i^{\parallel} = \mathcal{R}_2(\mathcal{F}_i^*) = \{\mathbf{t}_{i+1}, \mathbf{d}_1^{\parallel}, \mathbf{d}_2^{\parallel}\}$ be the image of \mathcal{F}_i^* by \mathcal{R}_2 . Then the parallel transported vectors are given by :

$$\mathbf{d}_1^{\parallel} = \mathbf{d}_1^* - 2(\mathbf{d}_1^* \cdot \mathbf{n}_2)\mathbf{n}_2 \quad (4.83a)$$

$$\mathbf{d}_2^{\parallel} = \mathbf{t}_{i+1} \times \mathbf{d}_1^{\parallel} \quad (4.83b)$$

The double reflection is equivalent to a rotation around the line \mathcal{D} defined as the intersection of the two reflection planes, of direction $\mathbf{b} = \mathbf{n}_1 \times \mathbf{n}_2$, by an angle $\alpha = 2\angle(\mathbf{n}_1, \mathbf{n}_2) = 2\arcsin(\|\mathbf{b}\|)$.

Remark that for both the circumscribed (see fig. 4.15a) and inscribed (see fig. 4.16a) osculating circles :

$$\mathbf{t}_i = \mathcal{R}_{\mathbf{x}_{i-1/2}}^{u_{i-1}} \circ \mathcal{R}_{\mathbf{x}_i}^{t_i}(\mathbf{t}_i^-) \quad (4.84a)$$

$$\mathbf{t}_i = \mathcal{R}_{\mathbf{x}_i}^{t_i} \circ \mathcal{R}_{\mathbf{x}_{i+1/2}}^{u_i}(\mathbf{t}_i^+) \quad (4.84b)$$

4.10 Conclusion

This chapter has established all the geometrical tools required for our future discrete beam model. Our analysis show that for the type of structures we want to model the discrete curvature defined according to the circumscribed osculating circle is the most suitable as :

- it provides an unequivocal definition of the discrete curvature in the current portion and at the extremities of the curve ;
- it exhibits the fastest convergence when regarding the evaluation of the bending energy of typical curves ;
- it leads to a natural local spline interpolation passing through the curve's vertices ;
- it leads to a natural definition of the tangent vector at vertices and at midspan of edges ;
- it enables the modeling of curvature discontinuities.

4.11 References

- [71] G. F. A. de L'Hospital. "Analyse des infiniment petits, pour l'intelligence des lignes courbes". In: (1696).
- [72] J. Delcourt. "Analyse et géométrie, histoire des courbes gauches de Clairaut à Darboux". In: *Archive for History of Exact Sciences* 65.3 (2011), pp. 229–293.
- [73] T. Hoffmann. *Discrete Differential Geometry of Curves and Surfaces*. Vol. 18. 2008.
- [74] E. Vouga. "Plane Curves". In: *Lectures in discrete differential geometry*. 2014. Chap. 1, pp. 1–11.
- [75] R. Bishop. "There is more than one way to frame a curve". In: *Mathematical Association of America* (1975).
- [76] F. Klok. "Two moving coordinate frames for sweeping along a 3D trajectory". In: *Computer Aided Geometric Design* 3.3 (1986), pp. 217–229.
- [77] H. Guggenheimer. "Computing frames along a trajectory". In: *Computer Aided Geometric Design* 6.1 (1989), pp. 77–78.
- [78] J. Bloomenthal. "Calculation of reference frames along a space curve". In: *Graphics Gems*. Ed. by A. S. Glassner. Vol. 1. San Diego, CA, USA: Academic Press Professional, Inc., 1990, pp. 567–571.
- [79] A. J. Hanson and H. Ma. *Parallel Transport Approach to Curve Framing*. Tech. rep. 1995.
- [80] T. Poston, S. Fang, and W. Lawton. "Computing and approximating sweeping surfaces based on rotation minimizing frames". In: *Proceedings of the 4th International Conference on CAD/CG*. 1995, pp. 1–8.
- [81] W. Wang, B. Jüttler, D. Zheng, and Y. Liu. "Computation of rotation minimizing frames". In: *ACM Transactions on Graphics* 27.1 (2008), pp. 1–18.
- [82] R. T. Farouki, C. Giannelli, M. L. Sampoli, and A. Sestini. "Rotation-minimizing osculating frames". In: *Computer Aided Geometric Design* 31.1 (2014), pp. 27–42.
- [83] F. Frenet. "Sur les courbes à double courbure". In: *Journal de Mathématiques Pures et Appliquées* 17 (1852), pp. 437–447.
- [84] J. Delcourt. "Analyse et géométrie : les courbes gauches de Clairaut à Serret". PhD thesis. Université de Paris VI, 2007, p. 302.
- [85] J. Bernoulli. *Johannis Bernoulli... Opera omnia, tam antea sparsim edita, quam hactenus inedita*. IV. sumptibus Marci-Michaelis Bousquet, 1728, p. 584.
- [86] H. Pitot. "Quadrature de la moitié d'une courbe des arcs appelée la compagne de la cycloïde". In: *Mémoires de l'Académie Royale des Sciences (1724)* (1726), pp. 107–113.
- [87] J. L. Coolidge. *A history of geometrical methods*. Ed. by C. Corporation. Dover Books on Mathematics. Dover Publications, 2013, p. 480.
- [88] G. Monge. *Application de l'analyse à la géométrie*. 1809, p. 475.

-
- [89] L. Euler. “Continens analysin, pro incuruatione fili in fingulis punctis inueniendia”. In: *Novi Commentarii academiae scientiarum Petropolitanae* 19 (1775), pp. 340–370.
 - [90] A. Gray, E. Abbena, and S. Salamon. *Modern differential geometry of curves and surfaces with Mathematica*. Ed. by E. A. Salamon and Simon. Third. CRC Press, 2006, p. 1016.
 - [91] M. Bergou, M. Wardetzky, S. Robinson, B. Audoly, and E. Grinspun. “Discrete elastic rods”. In: *ACM SIGGRAPH* (2008), pp. 1–12.
 - [92] D. Carroll, E. Hankins, E. Kose, and I. Sterling. “A survey of the differential geometry of discrete curves”. In: *The Mathematical Intelligencer* 36.4 (2014), pp. 28–35. arXiv: [arXiv:1311.5862v1](https://arxiv.org/abs/1311.5862v1).
 - [93] A. Bobenko. *Discrete differential geometry*. Second. 2015, p. 144.
 - [94] P. Romon. *Introduction à la géométrie différentielle discrète*. Références sciences. Ellipses, 2013, p. 216.
 - [95] M. Bergou, B. Audoly, E. Vouga, M. Wardetzky, and E. Grinspun. “Discrete viscous threads”. In: *ACM Transactions on ...* (2010), pp. 1–10.

5 Elastic rod : variational approach

This chapter should be understood as an extension of the work initiated by Tayeb 2015 [12] and published by du Peloux et al. 2015 [42] and Lefevre et al. 2017 [96].

5.1 Introduction

Elastic gridshells are lightweight structures made of interconnected slender beams (see chapter 2). Modeling the deformation process of such structures is complex as it involves to take account for the geometric non linearities induced by the large displacements and rotations of the grid. More over, the large number of connexions and the coupling between flexion and torsion highly increase the complexity of the analysis.

To facilitate the design process of elastic gridshells, architects and engineers need a dedicated numerical tool that provide a good level of interactivity – which means that numerical computations must converge within a reasonable time, if not in real time – and gives deep insights on the geometry and on the mechanical behavior of the grid. This tool must be able to model complex connexions and various types of support conditions to enhance the user experience during the formfinding stage and to improve his ability to explore the space of constructible shapes.

In this chapter, our goal is to develop a beam model suitable for the modeling of grids of interconnected slender beams in order to study the mechanics of elastic gridshells. For such beams, Kirchhoff's theory of rods is considered to be appropriate. We follow recent advances in the field of computer graphics about hair modeling [91] to build a reduced degrees of freedom rod model thanks to an appropriate curve-angle representation. This representation is based on a relevant curve framing, namely the Bishop frame presented in §4.5.6. The rod will be considered inextensible. Moreover, it will be assumed that cross-sections remain normal to the rod centerline. The internal forces and moments acting on the rod will be deduced from the differentiation of the elastic energy of the beam with

respect to the degrees of freedom of the system.

This chapter is devoted to the development of the beam model. The formulation of a discrete element and its implementation in a numerical solver are treated in a dedicated chapter (see [chapter 7](#)).

5.1.1 Overview

We begin this chapter by presenting Kirchhoff model of rods based on two main hypothesis : the inextensibility and the Euler-Bernouili assumption (see [§5.2](#)). We introduce a 6-DOFs representation of the rod composed of a centerline and a material frame. Thanks to a convenient reference frame we reduce this formulation to 4-DOFs and adopt a curve-angle description of the rod (see [§5.3](#)). From there, we formulate a variational problem that will lead to the calculation of the internal forces and moments acting on the rod (see [§5.4](#)). We calculate the gradients of the elastic energy to obtain the internal twisting moment (see [§5.5](#)) and the internal forces (see [§5.6](#)). Finally, we discuss the potential of our model and suggest new possibilities (see [§5.8](#)).

5.1.2 Contributions

- We consolidate the mathematical development of the beam model by introducing the Fréchet and Gateaux derivatives in function spaces.
- We clarify the independence of the the rotational degree of freedom (θ) with respect to translational degrees of freedom (\mathbf{x}).
- We factorize the expressions of the internal forces and moments by reusing the quasi-static assumption.
- We identify the contributions of axial and shear forces, bending and torsion moments in the expressions of internal forces and moments.
- We prove the equivalence with the shear force obtained from the dynamical equations of Kirchhoff.
- We suggest that the dynamical Kirchhoff equations should be a more straight forward starting point to build up similar theories.

5.1.3 Related work

Bergou et al. 2008 [91] present a discrete treatment of adapted framed curves, parallel transport, and holonomy. Based on this framework they propose a curve-angle representation of the geometric configuration of slender rods. In this representation, the orientation of the material frame is established with respect to the Bishop frame by a single scalar angle. Upon this representation they build a mechanical model for slender elastic rods with anisotropic cross-section and arbitrary rest configuration. In the dynamic the centerline is

treated explicitly and material frames are treated as quasistatic. Bergou et al. 2010 [95] improve there previous model for the modeling of viscous threads.

Nabaei 2014 [97] implements the model developed by [91] in IPOPT, an interior point optimizer, to solve the static equilibrium of simply connected systems of twisted elastica.

Tayeb 2015 [12], du Peloux et al. 2015 [42] and Lefevre et al. 2017 [96] follow [91] to model grids of interconnected slender beams. They implement their model in a dynamic relaxation solver to formfind elastic gridshells. They formulate a special connexion.

Grégoire and Schömer 2007 [98] use the Cosserat theory of rods to simulate naturally straight hoses – for applications to wire routing or assembly simulation in the automotive industry). The material frame is parametrized by a global rotation using quaternions. The simulation is treated in a quasi-static manner. The problem is formulated as an energy minimization problem solved with newton, conjugate gradient or steepest descent method. Theetten et al. 2008 [99] formulate a geometrically exact dynamic spline model for the simulation of one dimensional objects. They handle elastic and plastic deformations as fracture. Bertails et al. 2006 [100] model the non linear behavior of hair strands with super-helices. This work is extended later by Bertails-Descoubes 2012 [101] using super-clothoids. These methods have the advantage to postulate a precise geometric interpolation at each point of the rod. Spillmann and Teschner 2007 [102] adopt a somehow similar approach. They remark that solving directly the Lagrangian equations of motion by a gradient method is too expensive. Thus, they fall back to a semi-implicit Euler integration scheme.

Jung et al. 2010 [103] provide a deep insight to the discrete mechanics of Cosserat rods, as discrete mechanics is a field of research of growing importance.

Fuller 1978 [104], Vauquelin 2000 [105], de Vries 2005 [106] and Berger 2009 [107] are worth to read to understand the variation of the parallel transport when deforming a path.

A intégrer

“Note that γ having unit speed corresponds to the rod being inextensible; this is not always assumed in the theory, nor is the material frame necessarily assumed to be orthonormal as it is here” [108, p. 607] “Natural frames and the curve angle representation of rod” [108, p. 607]

Alexander and Antman 1982 [109] : the ambiguous twist of love.

5.2 Kirchhoff rod

Kirchhoff's theory of rods is presented thoroughly in the next chapter (see [chapter 6](#)). In this chapter, although the assumptions are not exactly the ones made by Kirchhoff in his theory, we will stick to this denomination as introduced by [91]. In the present theory we will assume that :

- the rod is inextensible,
- cross-sections remain plane,
- cross-sections remain perpendicular to the centerline,
- the material deforms elastically.

5.2.1 Description of the motion

We introduce a curvilinear coordinate system to describe the motion of our Kirchhoff rod, compatible with the model assumptions. It is composed of a parametric space curve, called the *centerline*, equipped with a moving frame, called the *material frame*.

Deformed configuration

The actual geometric configuration of the rod is described by its centerline $\mathbf{x}(s)$ and its cross-sections. The centerline is a space curve parameterized by its arc length, denoted s . Cross-sections orientation are followed along the centerline by a material frame $\{\mathbf{d}_3(s), \mathbf{d}_1(s), \mathbf{d}_2(s)\}$ which is an adapted orthonormal moving frame aligned with the principal axes of inertia of the cross-section.

Recall from §4.5.2 that *adapted* means that the material frame is aligned with the tangent vector of the centerline :

$$\mathbf{d}_3(s) = \mathbf{x}'(s) = \mathbf{t}(s) \quad (5.1)$$

Here, the prime symbol denotes the derivation with respect to the arc length parameter s . Recall also from §4.2.6 that $\|\mathbf{x}'(s)\| = 1$ because \mathbf{x} is parametrized by arc length.

Stress-free configuration

Among all the possible geometric configurations of the rod we identify the *stress-free configuration* or *rest configuration*, that is the configuration in which the rod is stress-free under no external forces and moments applied top it (loads, supports, ...). This configuration is crucial as the elastic energy of a rod in a given configuration relies on both its actual and rest configuration.

Hereinafter, the symbols referring to this configuration will be denoted with an overbar (e.g. $\bar{\mathbf{x}}(s)$).

5.2.2 Inextensibility assumption

As explained by Audoly et al. 2010 [110], based on a scaling argument, two cases arise for slender beams : either the centerline stretches and bending and twisting forces become negligible compared to axial forces ; either the centerline remains inextensible. As we are

not interested in the first case – in which the beam would behave like a cable, mainly in tension – we will assume that the rod is effectively inextensible.¹

Remark that the previous description (see §5.2.1) is only valid for inextensible rods. Indeed, for an inextensible rod the centerline does not stretches and the arc length parameter for the rest configuration is also a valid arc length parameter for any other configuration.²

The inextensibility hypothesis also implies that any admissible perturbation ($\lambda \mathbf{h}_x$) of the rod's centerline (\mathbf{x}) is locally orthogonal to the centerline itself. Indeed, at each arc length s an inextensible rod must satisfies :

$$\|\mathbf{x}'\| = \|(\mathbf{x} + \lambda \mathbf{h}_x)'\| = 1 \Rightarrow \mathbf{d}_3 \cdot \mathbf{h}'_x = -\frac{\lambda^2}{2} \|\mathbf{h}'_x\|^2 = o(\lambda) \simeq 0 \quad (5.2)$$

It is worth to mention here that this property ($\mathbf{d}_3 \cdot \mathbf{h}'_x = 0$) will be used several times in the following sections.

Hereinafter, the length of the rod will be denoted L and the arc length s will vary in $[0, L]$, with no loss of generality.

5.2.3 Euler-Bernouilli assumption

Strains are supposed to remain small so that the cross-sections remain plane and the material frame remains orthonormal and adapted to the centerline during the motion of the rod. In other words the cross-sections undergo rigid body motions.³

5.2.4 Motion of the material frame

As a consequence of the Euler-Bernoulli assumption, we can differentiate the conditions of orthonormality of the material frame (see §4.5.1). This leads to the following system of differential equations governing the evolution of the *material directors* $\{\mathbf{d}_3(s), \mathbf{d}_1(s), \mathbf{d}_2(s)\}$ along the centerline :

$$\begin{bmatrix} \mathbf{d}'_3(s) \\ \mathbf{d}'_1(s) \\ \mathbf{d}'_2(s) \end{bmatrix} = \begin{bmatrix} 0 & \kappa_2(s) & -\kappa_1(s) \\ -\kappa_2(s) & 0 & \tau(s) \\ \kappa_1(s) & -\tau(s) & 0 \end{bmatrix} \begin{bmatrix} \mathbf{d}_3(s) \\ \mathbf{d}_1(s) \\ \mathbf{d}_2(s) \end{bmatrix} \quad (5.3)$$

where $\tau(s)$, $\kappa_1(s)$ and $\kappa_2(s)$ are the rates of rotation of the material frame with respect to the arc length parameter s . These equations can be formulated with the *Darboux vector* of the chosen material frame, which represents the angular velocity vector of the frame along

¹For a complete treatment of the question of inextensibility refer to §6.3.1 in chapter 6.

²For a complete treatment of the question of reparametrization refer to §6.2.1 in chapter 6.

³For a complete treatment of this point in Kirchhoff's theory refer to §6.3.1 in chapter 6.

$\boldsymbol{x}(s)$:

$$\boldsymbol{d}'_i(s) = \boldsymbol{\Omega}_m(s) \times \boldsymbol{d}_i(s) \quad (5.4a)$$

$$\boldsymbol{\Omega}_m(s) = \begin{bmatrix} \tau(s) \\ \kappa_1(s) \\ \kappa_2(s) \end{bmatrix} \quad (5.4b)$$

That means that $\tau(s)$, $\kappa_1(s)$ and $\kappa_2(s)$ are the components of the angular velocity of the material frame around its axes $\boldsymbol{d}_3(s)$, $\boldsymbol{d}_1(s)$ and $\boldsymbol{d}_2(s)$ when it travels along the centerline at unit speed.⁴

Recall from §4.4.1 how the (geometric) curvature (κ) of a spatial curve parametrized by arc length is related to the Frenet frame $\{\boldsymbol{t}(s), \boldsymbol{n}(s), \boldsymbol{b}(s)\}$ by :

$$\boldsymbol{t}'(s) = \boldsymbol{x}''(s) = \kappa(s) \cdot \boldsymbol{n}(s) \quad (5.5a)$$

$$\kappa(s) = \|\boldsymbol{t}'(s)\| = \|\boldsymbol{x}''(s)\| \quad (5.5b)$$

$$\boldsymbol{b}(s) = \boldsymbol{t}(s) \times \boldsymbol{n}(s) \quad (5.5c)$$

To describe the osculating plane in which lies the bending part of the deformation we rely on the *curvature binormal* introduced previously in eq. (4.21). We recall from eq. (4.21) and (4.37) that :

$$\boldsymbol{\kappa}\boldsymbol{b}(s) = \kappa(s) \cdot \boldsymbol{b}(s) = \boldsymbol{t}(s) \times \boldsymbol{t}'(s) = \kappa_1(s)\boldsymbol{d}_1(s) + \kappa_2(s)\boldsymbol{d}_2(s) \quad (5.6)$$

The curvature binormal is the vector of direction $\boldsymbol{b}(s)$ and norm $\kappa(s)$, and at each point of arc length s the osculating plane is normal to $\boldsymbol{\kappa}\boldsymbol{b}(s)$. Finally, recall from eq. (4.39) that, as the material frame is adapted to the centerline, the following equation holds :

$$\boldsymbol{\Omega}_m(s) = \boldsymbol{\kappa}\boldsymbol{b}(s) + \tau(s)\boldsymbol{t}(s) \quad (5.7)$$

5.2.5 Material curvatures and twist

Kirchhoff's theory assigns a physical meaning to the components of $\boldsymbol{\Omega}_m(s)$:

- $\kappa_1(s)$ and $\kappa_2(s)$ are called the *material curvatures* and represent the rod's flexion in the principal planes, respectively normal to $\boldsymbol{d}_1(s)$ and $\boldsymbol{d}_2(s)$ (see fig. 5.1a) ;
- $\tau(s)$ is called the *material twist* and represents the cross-sections rate of rotation around $\boldsymbol{d}_3(s)$ (see fig. 5.1b).

These scalar functions are directly related to the components of the strain tensor as defined in Kirchhoff's theory.⁵

⁴See fig. 4.4 in §4.5.1 for a geometric interpretation of these rates of rotation.

⁵For a complete treatment of the definition of strain in Kirchhoff's theory refer to §6.3.3 in chapter 6 or Dill 1992 [111]

Note that In the literature these quantities are sometimes called *strain rates* (Antman 2005 [112]) or *moment strains* (Reissner 1973 [113]). However, this depart from the most common definition in which the strain is a dimensionless quantity that : “[...] provides a geometrical characterization of deformation : it measures by how much the solid departs from its natural configuration.” [110, p. 19].

5.2.6 Material constitutive equations

The twisting moment (Q) and the components of the bending moment (M_1, M_2) are determined through the usual material constitutive equations :

$$Q = GJ(\tau_1 - \bar{\tau}_1) \quad (5.8a)$$

$$M_1 = EI_1(\kappa_1 - \bar{\kappa}_1) \quad (5.8b)$$

$$M_2 = EI_2(\kappa_2 - \bar{\kappa}_2) \quad (5.8c)$$

We also introduce the vector of internal moments and its as :

$$\mathbf{M} = Q\mathbf{d}_3 + M_1\mathbf{d}_1 + M_2\mathbf{d}_2 \quad (5.9a)$$

$$\mathbf{M}^\perp = M_1\mathbf{d}_1 + M_2\mathbf{d}_2 \quad (5.9b)$$

5.2.7 Elastic energy

Kirchhoff's theory assigns an elastic energy to beams according to their strain [110]. In this theory, a beam is supposed to be inextensible. Thus the elastic energy (\mathcal{E}) only accounts for bending and torsion and behaviors and is given by :

$$\mathcal{E} = \frac{1}{2} \int_0^L EI_1(\kappa_1 - \bar{\kappa}_1)^2 + EI_2(\kappa_2 - \bar{\kappa}_2)^2 ds + \frac{1}{2} \int_0^L GJ(\tau - \bar{\tau})^2 ds \quad (5.10)$$

Here, $\bar{\kappa}_1, \bar{\kappa}_2$ and $\bar{\tau}$ denote the *natural* material curvatures and material twist of the rod in its rest configuration. E and G are the elastic and shear modulus of the material. I_1 and I_2 are the moments of inertia of the cross-section. J is the torsion constant of the cross-section.

Initially straight isotropic rod : a special case

From this energy formulation an interesting and well-known result on elastic rods can be retrieved. This results stipulates that torsion is uniform in a rod with isotropic cross-section and naturally straight.⁶

Cette proposition est démontrée dans le paragraphe 273 de la théorie de l'élasticité de Love

⁶This result was already known by Love [114, § 234] and is mentioned by Adriaenssens et al. 1999 [38] and Douthe 2007 [10].

[66] ainsi que sous une forme plus condensée par S. Adriaenssens [3]

Indeed, by definition for a rod with isotropic cross-section : $EI_1 = EI_2 = EI$. If in addition the rod is straight in its rest configuration : $\bar{\kappa}_1 = \bar{\kappa}_2 = \bar{\tau} = 0$. The bending energy becomes : $\mathcal{E}_b = EI_1 \kappa_1^2 + EI_2 \kappa_2^2 = EI(\kappa_1^2 + \kappa_2^2) = EI\kappa^2$. Consequently, the elastic energy of the rod is composed of two independent terms : $\mathcal{E}_b[\mathbf{x}]$ and $\mathcal{E}_t[\theta]$. The coupling between bending and twisting disappears and the global minimum of elastic energy is reached when minimizing separately bending and twisting energies. This means that the geometry of the rod at static equilibrium (\mathbf{x}) is the one that minimized $\mathcal{E}_b[\mathbf{x}]$. And the minimum of $\mathcal{E}_t[\theta]$ is obviously achieved for a uniform twist ($\tau = cst$) along the centerline, only prescribed by the boundary conditions at the extremities of the rod (least-squares minimization).

In that particular case, the geometry of the centerline is not influenced by the amount of uniform twist (hence torsion) present in the rod.

5.3 Curve-angle representation

In the previous paragraph we have shown how the elastic energy of a rod can be computed with respect to the position of its centerline and the orientation of its cross-sections. This representation can be naturally described with six degrees of freedom (6-DOFs) : ⁷

- 3-DOFs for the position of the centerline,
- and 3-DOFs for the orientation of the cross-sections.

Following Bergou et al. 2008 [91] we introduce a reduced coordinate formulation of the rod that accounts for only 4-DOFs : ⁸

- 3-DOFs for the position of the centerline,
- and only 1-DOF for the orientation of the cross-sections.

5.3.1 Definition of the representation

This reduction of the number of DOFs relies on the choice of a suitable reference frame, namely a Bishop (or zero-twisting) frame denoted $\{\mathbf{t}(s), \mathbf{u}(s), \mathbf{v}(s)\}$. Recall from §4.5.6 in chapter 4 that this reference frame is adapted to the centerline and exhibits a null angular velocity around the centerline's tangent vector (see eq. (4.47)), which means :

$$\mathbf{u}(s) \cdot \mathbf{v}'(s) = \mathbf{u}'(s) \cdot \mathbf{v}(s) = 0 \quad (5.11)$$

⁷This is the usual choice in which the orientation of the material frame is parametrized by a rotation matrix, or equivalently a quaternion.

⁸The curve-angle representation was first introduced by [108].

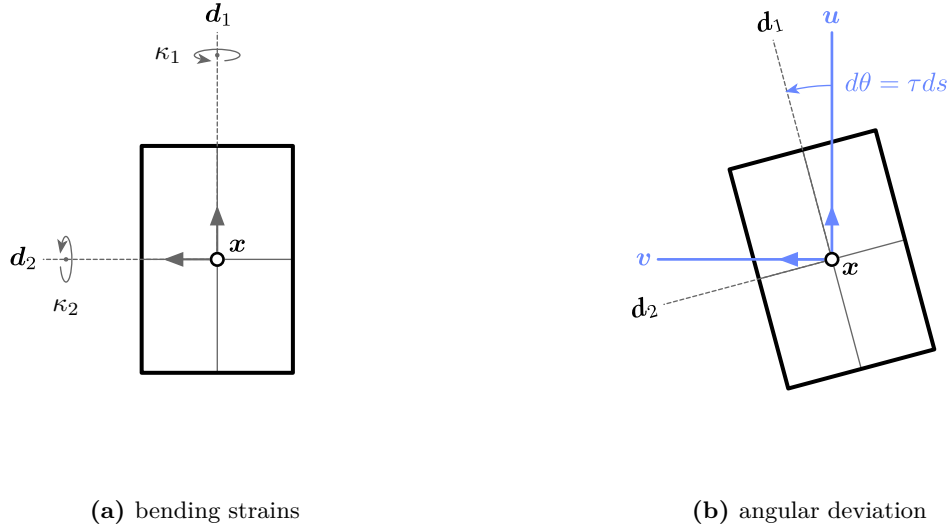


Figure 5.1 – Curve-angle representation of the rod. The orientation of the material frame is established from the reference frame by the deviation angle $\theta(s)$.

The Bishop frame only depends on x , the geometry of the centerline, and the choice of an initial condition. This reference frame is obtained all along the curve by propagating a given initial frame – usually chosen at $s = 0$ – with the parallel transport operator (see §4.5.4). By construction, this reference frame evolves along the curve with the following angular velocity :

$$\Omega_b(s) = \kappa b = t' \times t = x' \times x'' \quad (5.12a)$$

$$t'(s) = \kappa b \times t \quad (5.12b)$$

$$u'(s) = \kappa b \times u \quad (5.12c)$$

$$v'(s) = \kappa b \times v \quad (5.12d)$$

Remark that $\Omega_b(s)$ only depends on the centerline and is well defined even when the curvature vanishes, unlike the Frenet frame. In that case the parallel transport operator becomes the rotation of null angle, which is still a valid transformation.

Hence, the orientation of the cross-sections, that is the material frame $\{d_3(s), d_1(s), d_2(s)\}$, can be tracked only by the measure of a single angle $\theta(s)$ from this reference frame denoted $\{d_3(s), u(s), v(s)\}$:

$$\begin{bmatrix} d_1(s) \\ d_2(s) \end{bmatrix} = \begin{bmatrix} \cos \theta(s) & \sin \theta(s) \\ -\sin \theta(s) & \cos \theta(s) \end{bmatrix} \begin{bmatrix} u(s) \\ v(s) \end{bmatrix} \quad (5.13)$$

Note that the choice of an initial condition for the definition of the Bishop frame is not a matter of concern as only the derivative of θ appears in the elastic energy (see eq. (5.10)). Thus, we are free to choose this condition in the most convenient way.

5.3.2 Measurement of the material twist

With this 4-DOFs representation, the material twist is directly expressed in terms of the derivative of θ . Indeed, from eq. (5.12) and (5.13) we obtain :

$$\begin{aligned}\mathbf{d}'_1 &= (\cos \theta \mathbf{u} + \sin \theta \mathbf{v})' \\ &= (-\sin \theta \mathbf{u} + \cos \theta \mathbf{v}) \cdot \theta' + \cos \theta \mathbf{u}' + \sin \theta \mathbf{v}' \\ &= \theta' \mathbf{d}_2 + \cos \theta (\kappa \mathbf{b} \times \mathbf{u}) + \sin \theta (\kappa \mathbf{b} \times \mathbf{v}) \\ &= \theta' \mathbf{d}_2 + \kappa \mathbf{b} \times \mathbf{d}_1\end{aligned}\tag{5.14}$$

Finally, using the definition of τ from eq. (5.3) and the fact that $\kappa \mathbf{b}$ is perpendicular to \mathbf{d}_3 we can deduce that $\tau = \theta'$:

$$\tau = \mathbf{d}'_1 \cdot \mathbf{d}_2 = (\theta' \mathbf{d}_2 + \kappa \mathbf{b} \times \mathbf{d}_1) \cdot \mathbf{d}_2 = \theta' + \mathbf{d}_3 \cdot \kappa \mathbf{b} = \theta'\tag{5.15}$$

Here, the benefits of the curve-angle representation are revealed as the material twist is now simply given by the rate of θ with respect to the arc length parameter s . Everything happens as if the Bishop would enable a direct measurement of the mechanical torsion, getting ride of the intrinsic geometric torsion of the centerline itself (aka the torsion of Frenet).

5.3.3 Vector of material curvatures

We introduce the vector of material curvatures ($\boldsymbol{\omega}$) as the 2-dimensional vector of components κ_1 and κ_2 :

$$\boldsymbol{\omega} = \begin{bmatrix} \kappa_1 \\ \kappa_2 \end{bmatrix} = \begin{bmatrix} \kappa \mathbf{b} \cdot \mathbf{d}_1 \\ \kappa \mathbf{b} \cdot \mathbf{d}_2 \end{bmatrix} = \begin{bmatrix} -x'' \cdot \mathbf{d}_2 \\ x'' \cdot \mathbf{d}_1 \end{bmatrix}\tag{5.16}$$

5.4 Definition of the variational problem

We now have all the ingredients to build the variational problem that will lead us to the determination of the internal forces (\mathbf{f}) and the internal twisting moment (\mathbf{m}) acting on the centerline. Indeed, the quasi-static out-of-balance internal forces and twisting moment acting on the beam are calculated by differentiating the elastic energy of the system with respect to the 4 DOFs of the system, namely \mathbf{x} and θ .

5.4.1 Calculus of variations

Differentiating \mathcal{E} with respect to \mathbf{x} will yield the linear resultant of the internal forces (\mathbf{f} , see §5.5), while differentiating \mathcal{E} with respect to θ will yield the linear resultant of the internal twisting moment (\mathbf{m} , see §5.6). Main results for the calculus of variations are reminded in appendix B.

These forces and moments will be used later in a damped explicit dynamic procedure

to solve the equilibrium of the system. However, they are nothing but the gradient of the elastic energy and any other variational method can be employed to find a geometric configuration that minimize the elastic energy, that is a configuration in which the rod is at static equilibrium (our ultime goal).

Introducing ω and θ , the elastic energy defined in eq. (5.10) can be rewritten in the form :

$$\mathcal{E} = \mathcal{E}_b + \mathcal{E}_t = \frac{1}{2} \int_0^L (\omega - \bar{\omega})^T B(\omega - \bar{\omega}) ds + \frac{1}{2} \int_0^L \beta(\theta' - \bar{\theta}')^2 ds \quad (5.17)$$

where B is the bending stiffness matrix given in material frame coordinate system and β is the torsional stiffness given by :

$$B(s) = \begin{bmatrix} EI_1(s) & 0 \\ 0 & EI_2(s) \end{bmatrix}, \quad \beta(s) = (GJ)(s) \quad (5.18)$$

The matrix notation introduced in eq. (5.17) will enable more compact forms for equations. It will be used through out this chapter. Remark who the scalar product of vectors is treated as matrix multiplication with a row and column vector.

The internal shear forces and the internal twisting moment are then given by :

$$\mathbf{f} = -\frac{\partial \mathcal{E}}{\partial \mathbf{x}}[\mathbf{x}, \theta] \quad (5.19a)$$

$$\mathbf{m} = -\frac{\partial \mathcal{E}}{\partial \theta}[\mathbf{x}, \theta] \cdot \mathbf{d}_3 \quad (5.19b)$$

It is importante to notice that as the rod is supposed to be inextensible, the elastic energy does not include any term to characterized the axial strain. This assumption will have to be treated as a constraint when solving the variational problem. For instance, Bergou et al. 2008 [91] choose to enforce inextensibility at each time step with a reprojection algorithm while Lefevre et al. 2017 [96] choose to enforce this constraint thanks to a penalty energy. Hence, \mathbf{f} will give only the internal shear forces acting on the centerline.⁹

5.4.2 Prerequisite for the computation of energy gradients

To compute the energy gradients with respect to the degrees of freedom of the rod it is primordial to understand how these DOFs are chained (see fig. 5.2) :



Figure 5.2 – Succession of the degrees of freedom.

⁹This is somehow equivalent to what is remarked by Dill : “The resultant shears F_1 and F_2 are not determined by the constitutive equations. They are reactive parameters in the equations of balance of momentum as they are in the elementary beam theory.” [111].

- \boldsymbol{x} leads to the determination of the curvature binormal ($\boldsymbol{\kappa b}$) and to the determination of the reference Bishop frame $\{\boldsymbol{t}, \boldsymbol{u}, \boldsymbol{v}\}$.
- θ leads to the determination of the material frame $\{\boldsymbol{t}, \boldsymbol{d}_1, \boldsymbol{d}_2\}$ from the reference frame $\{\boldsymbol{t}, \boldsymbol{u}, \boldsymbol{v}\}$.
- κ_1 and κ_2 are the projections of $\boldsymbol{\kappa b}$ on \boldsymbol{d}_1 and \boldsymbol{d}_2 . This means that $\boldsymbol{\omega}$ depends on \boldsymbol{x} through the determination of $\boldsymbol{\kappa b}$ and the determination of $\{\boldsymbol{t}, \boldsymbol{u}, \boldsymbol{v}\}$; and depends on θ through the determination of $\{\boldsymbol{d}_1, \boldsymbol{d}_2\}$ from $\{\boldsymbol{u}, \boldsymbol{v}\}$.
- τ only depends on θ and is thus independent of \boldsymbol{x} .

5.4.3 Coupling between bending and torsion

Remark that the twisting energy (\mathcal{E}_t) only depends on θ and is independent regarding \boldsymbol{x} while the bending energy (\mathcal{E}_b) depends on both θ and \boldsymbol{x} variables (remind that κ_1 and κ_2 are the projections of $\boldsymbol{\kappa b}$ over \boldsymbol{d}_1 over \boldsymbol{d}_2). Thus, a coupling between bending and twisting appears and the minimum of the whole elastic energy is not necessarily reached for concomitant minimums of bending and twisting energies.

5.4.4 Quasistatic assumption

Following Bergou et al. 2008 [91], it is relevant to assume that the propagation of twist waves is instantaneous compared to the propagation of bending waves because for slender rods the axial stiffness is usually an order of magnitude higher than the bending stiffness. This means that the distributed internal forces (\boldsymbol{f}) and the distributed internal moment of torsion (\boldsymbol{m}) act on two different timescales in the rod dynamic.

Thus, on the timescale of action of the internal forces on the center line, driving the bending waves, the twist waves propagate instantaneously, so that :

$$\frac{\partial \mathcal{E}}{\partial \theta}[\boldsymbol{x}, \theta] = 0 \quad (5.20)$$

for the computation of \boldsymbol{f} .

This assumption is not mandatory – for instance it is not made by Nabaei 2014 [97] – but was found to lead to simpler and faster computations.

5.5 Energy gradient with respect to θ : twisting moment

For the calculus of variations, the reader is invited to refer to [appendix B](#) where the notations employed through out this section are defined and where main results are reminded.

5.5.1 Derivative of material directors with respect to θ

Recalling that θ and \mathbf{x} are independant variables and that the Bishop frame $\{\mathbf{u}, \mathbf{v}\}$ only depends on \mathbf{x} , the decomposition of the material frame directors $\{\mathbf{d}_1, \mathbf{d}_2\}$ on the Bishop frame leads directly to the following expression for the derivative of the material directors :

$$\begin{aligned} \mathbf{D}_\theta \mathbf{d}_1(s) \cdot h_\theta &= \frac{d}{d\lambda} \mathbf{d}_1[\theta + \lambda h_\theta] \Big|_{\lambda=0} \\ &= (-\sin \theta \mathbf{u} + \cos \theta \mathbf{v}) \cdot h_\theta \\ &= \mathbf{d}_2 \cdot h_\theta \end{aligned} \quad (5.21a)$$

$$\begin{aligned} \mathbf{D}_\theta \mathbf{d}_2(s) \cdot h_\theta &= \frac{d}{d\lambda} \mathbf{d}_2[\theta + \lambda h_\theta] \Big|_{\lambda=0} \\ &= (-\cos \theta \mathbf{u} - \sin \theta \mathbf{v}) \cdot h_\theta \\ &= -\mathbf{d}_1 \cdot h_\theta \end{aligned} \quad (5.21b)$$

where $h_\theta : s \mapsto h_\theta(s)$ denotes a small perturbation of θ and $\mathbf{D}_\theta \mathbf{d}_i(s)$ denotes the derivative of \mathbf{d}_i at s with respect to θ . When it is appropriate, brackets are employed to signal important functional dependencies, while parenthesis will denote the dependence with respect to the arc length parameter s .

5.5.2 Derivative of the material curvatures vector with respect to θ

Regarding the definition of the material curvatures vector and the derivative of material directors with respect to θ , it follows immediately that :

$$\begin{aligned} \mathbf{D}_\theta \boldsymbol{\omega}(s) \cdot h_\theta &= \frac{d}{d\lambda} \boldsymbol{\omega}[\theta + \lambda h_\theta] \Big|_{\lambda=0} \\ &= \begin{bmatrix} \boldsymbol{\kappa} \mathbf{b} \cdot \mathbf{d}_2 \\ -\boldsymbol{\kappa} \mathbf{b} \cdot \mathbf{d}_1 \end{bmatrix} \cdot h_\theta \\ &= -\mathbf{J} \boldsymbol{\omega} \cdot h_\theta \end{aligned} \quad (5.22)$$

where \mathbf{J} is the matrix that acts on two dimensional vectors by counter-clockwise rotation of angle $\frac{\pi}{2}$:

$$\mathbf{J} = \begin{bmatrix} 0 & -1 \\ 1 & 0 \end{bmatrix} \quad (5.23)$$

5.5.3 Computation of the twisting moment

The distributed moment of torsion is given by the functional derivative of the elastic energy with respect to θ , which can be decomposed into :

$$\begin{aligned}\langle -m(s), h_\theta \rangle &= \mathbf{D}_\theta \mathcal{E}(s) \cdot h_\theta \\ &= \mathbf{D}_\theta \mathcal{E}_b(s) \cdot h_\theta + \mathbf{D}_\theta \mathcal{E}_t(s) \cdot h_\theta\end{aligned}\tag{5.24}$$

Derivative of the torsion energy with respect to θ

We calculate the partial derivative of the twisting elastic energy with respect to θ as :

$$\begin{aligned}\mathbf{D}_\theta \mathcal{E}_t[\theta](s) \cdot h_\theta &= \frac{d}{d\lambda} \mathcal{E}_t[\theta + \lambda h_\theta] \Big|_{\lambda=0} \\ &= \frac{d}{d\lambda} \left(\frac{1}{2} \int_0^L \beta ((\theta + \lambda h_\theta)' - \bar{\theta}')^2 dt \right) \Big|_{\lambda=0} \\ &= \int_0^L \beta (\theta' - \bar{\theta}') \cdot h'_\theta dt \\ &= [\beta(\theta' - \bar{\theta}') \cdot h_\theta]_0^L - \int_0^L (\beta(\theta' - \bar{\theta}'))' \cdot h_\theta dt \\ &= \int_0^L \left(\beta(\theta' - \bar{\theta}')(\delta_L - \delta_0) - (\beta(\theta' - \bar{\theta}'))' \right) \cdot h_\theta dt\end{aligned}\tag{5.25}$$

where δ_L and δ_0 are the Dirac distributions centered respectively on $s = L$ and $s = \check{s}$.

Derivative of the bending energy with respect to θ

To compute the partial derivative of \mathcal{E}_b with respect to θ we first calculate the derivative of \mathcal{E}_b with respect to ω :

$$\begin{aligned}\mathbf{D}_\omega \mathcal{E}_b[\omega](s) \cdot h_\omega &= \frac{d}{d\lambda} \mathcal{E}_b[\omega + \lambda h_\omega] \Big|_{\lambda=0} \\ &= \frac{d}{d\lambda} \left(\frac{1}{2} \int_0^L ((\omega + \lambda h_\omega) - \bar{\omega})^T \mathbf{B} ((\omega + \lambda h_\omega) - \bar{\omega}) dt \right) \Big|_{\lambda=0} \\ &= \int_0^L (\omega - \bar{\omega})^T \mathbf{B} \cdot h_\omega dt\end{aligned}\tag{5.26}$$

where $\mathbf{h}_\omega : s \mapsto \mathbf{h}_\omega(s)$ denotes a small perturbation of ω . Then, we calculate the derivative of \mathcal{E}_b with respect to θ from the chain rule and with eq. (5.22) and (5.26) :

$$\begin{aligned}\mathbf{D}_\theta \mathcal{E}_b[\omega[\theta]](s) \cdot h_\theta &= \mathbf{D}_\omega \mathcal{E}_b[\omega](s) \cdot (\mathbf{D}_\theta \omega[\theta](s) \cdot h_\theta) \\ &= - \int_0^L (\omega - \bar{\omega})^T \mathbf{B} \mathbf{J} \omega \cdot h_\theta dt\end{aligned}\tag{5.27}$$

Twisting moment

The gradient of the elastic energy with respect to θ is obtained from eq. (5.24) with eq. (5.25) and (5.27) :

$$\begin{aligned} \langle -m(s), h_\theta \rangle &= \mathbf{D}_\theta \mathcal{E}_b[\boldsymbol{\omega}[\theta]](s) \cdot h_\theta + \mathbf{D}_\theta \mathcal{E}_t[\theta](s) \cdot h_\theta \\ &= \int_0^L \left((\beta(\theta' - \bar{\theta}')(\delta_L - \delta_0) - (\beta(\theta' - \bar{\theta}'))') - (\boldsymbol{\omega} - \bar{\boldsymbol{\omega}})^T \mathbf{B} \mathbf{J} \boldsymbol{\omega} \right) \cdot h_\theta \, dt \end{aligned} \quad (5.28)$$

Finally, we can conclude on the expression of the distributed internal twisting moment :

$$m(s) = - \left(\beta(\theta' - \bar{\theta}')(\delta_L - \delta_0) - (\beta(\theta' - \bar{\theta}'))' \right) (s) + ((\boldsymbol{\omega} - \bar{\boldsymbol{\omega}})^T \mathbf{B} \mathbf{J} \boldsymbol{\omega}) (s) \quad (5.29)$$

Remark with eq. (5.8a) and (5.15), respectively with eq. (5.8b) and (5.8c), that :

$$\beta(\theta' - \bar{\theta}') = Q \quad (5.30a)$$

$$(\boldsymbol{\omega} - \bar{\boldsymbol{\omega}})^T \mathbf{B} \mathbf{J} \boldsymbol{\omega} = \kappa_1 M_2 - \kappa_2 M_1 \quad (5.30b)$$

Hence, the quasi-static distributed internal twisting moment acting on the centerline is given for all s in $]0, L[$ by :

$$m(s) = Q'(s) + \kappa_1(s)M_2(s) - \kappa_2(s)M_1(s) \quad (5.31)$$

Quasistatic hypothesis

The quasistatic assumption (see eq. (5.20)) stipulates that the gradient of the elastic energy with respect to θ can be considered null ($\mathbf{D}_\theta \mathcal{E}(s) = 0$) for the calculation of the internal forces, which implies that for all s in $[0, L]$:

$$((\beta(\theta' - \bar{\theta}'))' + (\boldsymbol{\omega} - \bar{\boldsymbol{\omega}})^T \mathbf{B} \mathbf{J} \boldsymbol{\omega}) (s) = 0 \quad (5.32)$$

or equivalently :

$$Q'(s) + \kappa_1(s)M_2(s) - \kappa_2(s)M_1(s) = 0 \quad (5.33)$$

5.6 Energy gradient with respect to x : internal forces

For the calculus of variations, the reader is invited to refer to appendix B where the notations employed through out this section are defined and where main results are reminded.

5.6.1 Derivative of material directors with respect to x

A variation of the centerline \mathbf{x} by $\epsilon = \lambda \mathbf{h}_x$ would cause a variation of the Bishop frame because parallel transport depends on the centerline itself. As far as \mathbf{x} and θ are independent variables, this leads necessarily to a variation of the material frame. Let us denote :

- $F = \{\mathbf{t}, \mathbf{u}, \mathbf{v}\}$: the Bishop frame in the reference configuration ;
- $F_\epsilon = \{\mathbf{t}_\epsilon, \mathbf{u}_\epsilon, \mathbf{v}_\epsilon\}$: the Bishop frame in the deformed configuration ;
- $\tilde{F}_\epsilon = \{\mathbf{t}, \tilde{\mathbf{u}}_\epsilon, \tilde{\mathbf{v}}_\epsilon\}$: the frame obtained by parallel transporting F_ϵ back on F .

From [fig. 5.3](#) we start with an (arbitrary) initial reference frame defined in the rest configuration and denoted $F(0)$, positioned at arc length parameter $s = 0$:

- Firstly, the intial frame $F(0)$ is parallel transported along the centerline of the rest configuration into the frame $F(s)$ at arc length parameter s (see [fig. 5.3](#)).
- Secondly the initial frame $F(0)$ is parallel transported at the starting point of the centerline of the deformed configuration into the frame $F_\epsilon(0)$. The frame $F_\epsilon(0)$ is then parallel transported along the centerline of the deformed configuration into the frame $F_\epsilon(s)$ at arc length parameter s . Finally, $F_\epsilon(s)$ is parallel transported back onto the frame $F(s)$ of the reference configuration. This frame is denoted $\tilde{F}_\epsilon(s)$ (see [fig. 5.3](#)).

The two frames $F(s)$ and $\tilde{F}_\epsilon(s)$ are not aligned as a variation of the centerline has caused a variation of the bishop frame. We call $\Psi_\epsilon(s)$ the amount of rotation around $\mathbf{t}(s)$ needed to realign $\tilde{F}_\epsilon(s)$ onto $F(s)$ (see [fig. 5.3](#) where $\Psi_\epsilon(s) < 0$). $\Psi_\epsilon(s)$ characterizes precisely the variation of the parallel transport operator with respect to a perturbation of the centerline.

The sequence of transformations described previously and illustrated in [fig. 5.3](#) can be decomposed into only two rotations that contribute to $\Psi_\epsilon(s)$:

- $F_\epsilon \rightarrow \tilde{F}_\epsilon$: parallel transporting F_ϵ from \mathbf{t}_ϵ to \mathbf{t} . This is equivalent to a rotation around $\mathbf{b} = \mathbf{t}_\epsilon \times \mathbf{t}$ by an angle α_ϵ . This rotation is described in [fig. 5.4](#).
- $\tilde{F}_\epsilon \rightarrow F$: aligning \tilde{F}_ϵ over F . This is equivalent to a rotation around \mathbf{t} by an angle Ψ_ϵ . This rotation is described in [fig. 5.5](#).

Firstly, let's decompose $\{\mathbf{t}_\epsilon, \mathbf{u}_\epsilon, \mathbf{v}_\epsilon\}$ on the basis $\{\mathbf{t}, \tilde{\mathbf{u}}_\epsilon, \tilde{\mathbf{v}}_\epsilon\}$. Note that \tilde{F}_ϵ is expressed by rotating \tilde{F}_ϵ by an angle $\Psi_\epsilon[\mathbf{x}](s)$ around \mathbf{t} because \tilde{F}_ϵ is obtained by parallel transporting F_ϵ from \mathbf{t}_ϵ to \mathbf{t} .

Calculation of Ψ_ϵ

This variation is closely related to the writhe of closed curves. As explained by Fuller 1978 [104] when parallel transporting an adapted frame around a closed curve it might not realigned with itself after one complete loop. This “lack of alignment” is directly measured by the change of writhe which can be computed with Fuller’s Formula [104].

Note that the derivative of θ with respect to \mathbf{x} can be evaluated by the change of writhe in the curve as suggested in [106]. This approach is completely equivalent.

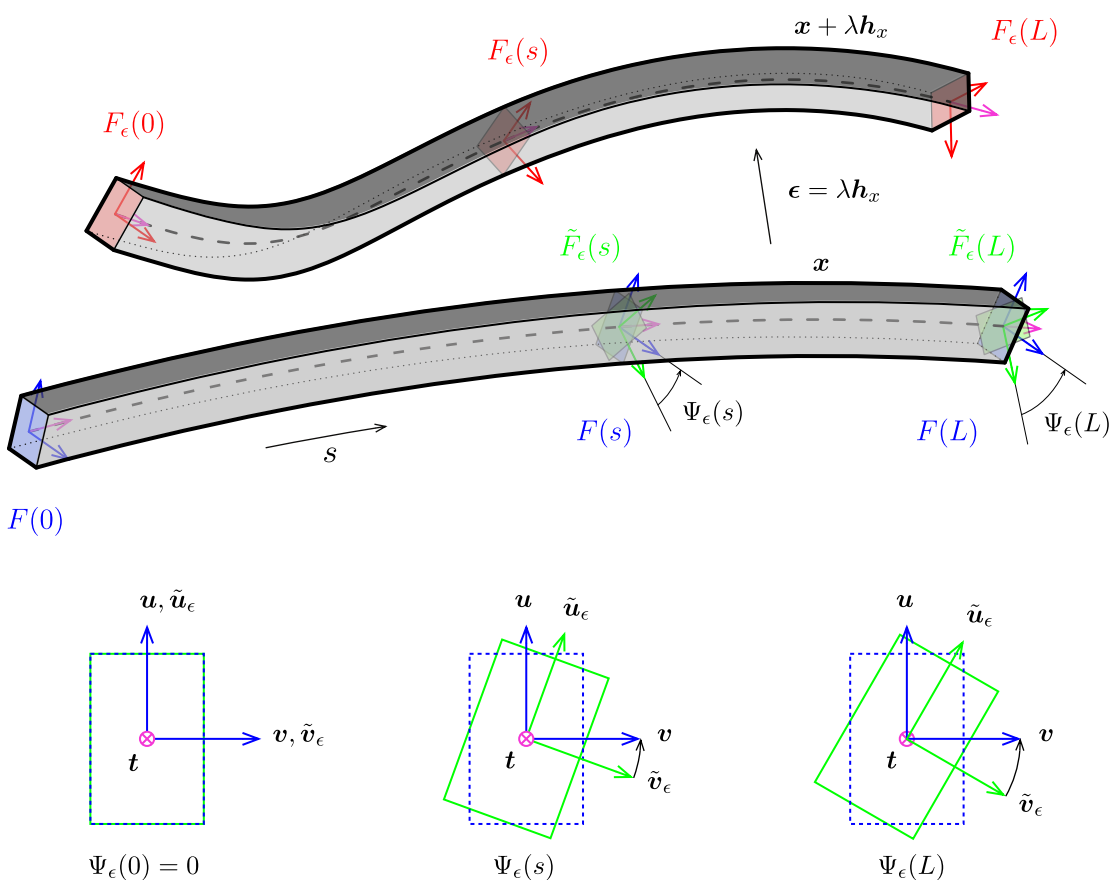


Figure 5.3 – Variation of the Bishop frame for a perturbation of the centerline.

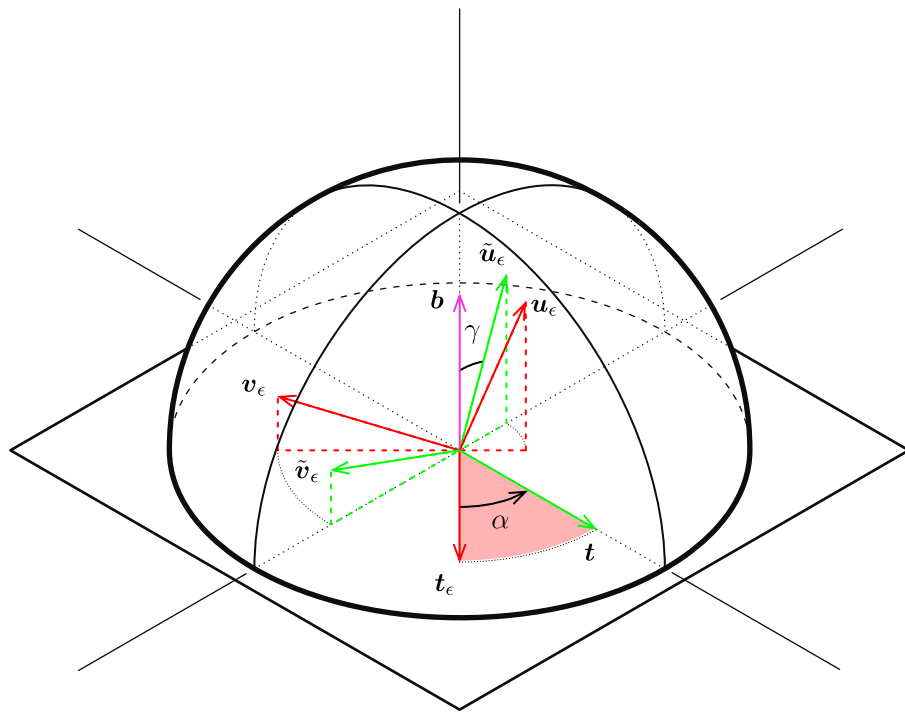


Figure 5.4 – Measuring the variation of parallel transport (α_ϵ). \tilde{F}_ϵ is obtained by parallel transporting F_ϵ from t_ϵ to t . This operation could be seen as a rotation around the axis $b = t_\epsilon \times t$ by an angle α_ϵ .

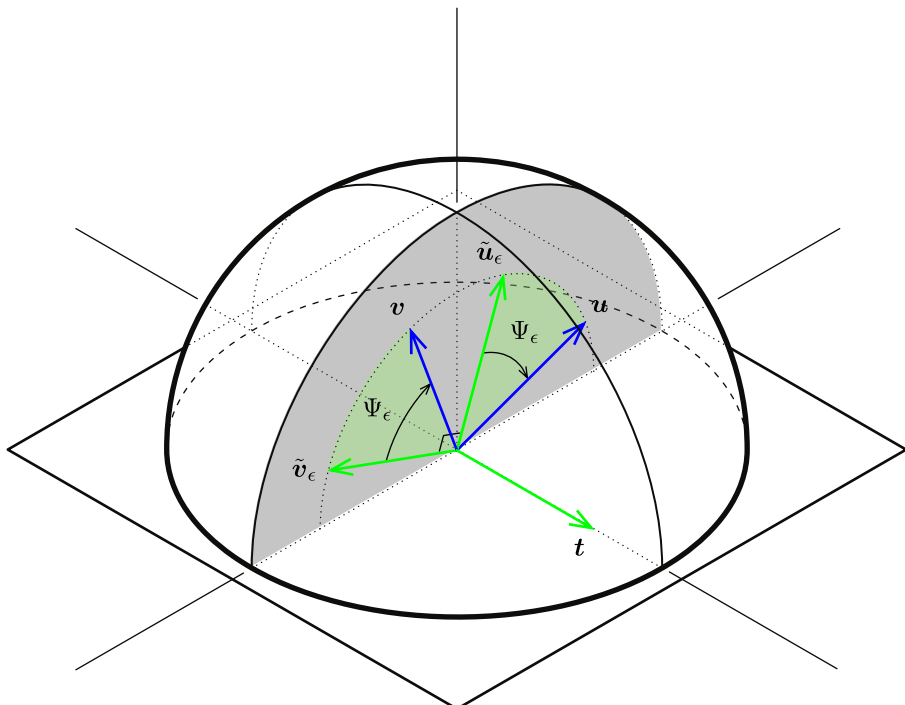


Figure 5.5 – Measuring the variation of parallel transport (Ψ_ϵ). F is obtained by rotating \tilde{F}_ϵ around t by an angle Ψ_ϵ .

5.6. Energy gradient with respect to x : internal forces

One can also see this lack of alignment in terms of rotation. Parallel transport being a propagation of frame from $s = 0$, the cumulated rotation of the Bishop frame from the deformed configuration around the initial configuration at arc length s is the cumulated angle of rotation of $\mathbf{u}[\mathbf{x} + \lambda \mathbf{h}_x]$ around $\mathbf{d}_3[\mathbf{x}]$. Recalling that the rotation rate of $\mathbf{u}[\mathbf{x} + \lambda \mathbf{h}_x]$ is $\kappa \mathbf{b}[\mathbf{x} + \lambda \mathbf{h}_x]$ by definition of zero-twisting frame, one can write :

$$\Psi_\epsilon[\mathbf{x}](s) = - \int_0^s \kappa \mathbf{b}[\mathbf{x} + \lambda \mathbf{h}_x] \cdot \mathbf{d}_3[\mathbf{x}] dt \quad (5.34)$$

The calculation of $\kappa \mathbf{b}[\mathbf{x} + \lambda \mathbf{h}_x]$ is straight forward from the definition of the curvature binormal (see eq. (5.12a)) :

$$\begin{aligned} \kappa \mathbf{b}[\mathbf{x} + \lambda \mathbf{h}_x] &= (\mathbf{x} + \lambda \mathbf{h}_x)' \times (\mathbf{x} + \lambda \mathbf{h}_x)'' \\ &= \kappa \mathbf{b}[\mathbf{x}] + \lambda(\mathbf{x}' \times \mathbf{h}_x'' + \mathbf{h}_x' \times \mathbf{x}'') + \lambda^2(\mathbf{h}_x' \times \mathbf{h}_x'') \\ &= \kappa \mathbf{b}[\mathbf{x}] + \lambda(\mathbf{x}' \times \mathbf{h}_x'' + \mathbf{h}_x' \times \mathbf{x}'') + o(\lambda) \end{aligned} \quad (5.35)$$

Thus, reminding that $\mathbf{d}_3[\mathbf{x}] = \mathbf{x}'$ and $\kappa \mathbf{b}[\mathbf{x}] \cdot \mathbf{d}_3[\mathbf{x}] = 0$, and using the invariance of circular product by cyclic permutation, one can express :

$$\begin{aligned} \Psi_\epsilon[\mathbf{x}](s) &= - \int_0^s \kappa \mathbf{b}[\mathbf{x} + \lambda \mathbf{h}_x] \cdot \mathbf{d}_3[\mathbf{x}] dt \\ &= -\lambda \int_0^s (\mathbf{x}' \times \mathbf{h}_x'' + \mathbf{h}_x' \times \mathbf{x}'') \cdot \mathbf{x}' dt + o(\lambda) \\ &= -\lambda \int_0^s \kappa \mathbf{b}[\mathbf{x}] \cdot \mathbf{h}_x' dt + o(\lambda) \end{aligned} \quad (5.36)$$

By integration by parts and dropping the implicit reference to \mathbf{x} in the notation, $\Psi_\epsilon(s)$ can be rewritten as :

$$\begin{aligned} \Psi_\epsilon(s) &= -\lambda \int_0^s \kappa \mathbf{b} \cdot \mathbf{h}_x' dt + o(\lambda) \\ &= -\lambda \left([\kappa \mathbf{b} \cdot \mathbf{h}_x]_0^s - \int_0^s \kappa \mathbf{b}' \cdot \mathbf{h}_x dt \right) + o(\lambda) \\ &= -\lambda \left(\int_0^s ((\delta_s - \delta_0) \kappa \mathbf{b} - \kappa \mathbf{b}') \cdot \mathbf{h}_x dt \right) + o(\lambda) \\ &= -\lambda \left(\int_0^L ((\delta_s - \delta_0) \kappa \mathbf{b} - (1 - H_s) \kappa \mathbf{b}') \cdot \mathbf{h}_x dt \right) + o(\lambda) \end{aligned} \quad (5.37)$$

where δ_s and H_s are the Dirac function and the Heaviside step function centered at s :

$$H_s : t \mapsto \begin{cases} 0, & t < s \\ 1, & t \geq s \end{cases} \quad (5.38a)$$

$$\delta_s : t \mapsto \delta(t - s) \quad (5.38b)$$

Note that, as expected, $\Psi_\epsilon(s)$ is in first order of λ and thus gets negligible when λ tends to zero, that is to say when the perturbation of \mathbf{x} is infinitesimal :

$$\lim_{\lambda \rightarrow 0} \Psi_\epsilon(s) = 0 \quad (5.39)$$

Calculation of α_ϵ

Recall that \tilde{F}_ϵ is obtained by parallel transporting F_ϵ from \mathbf{t}_ϵ to \mathbf{t} . \tilde{F}_ϵ results from the rotation of F_ϵ around $\mathbf{b} = \mathbf{t}_\epsilon \times \mathbf{t}$ by an angle α_ϵ .

Recall from eq. (5.2) that because the rod is supposed to be inextensible, \mathbf{t}_ϵ stays collinear to \mathbf{t} , at first order in λ , for an infinitesimal perturbation of the centerline :

$$\|\mathbf{t}\| = \|\mathbf{t}_\epsilon\| = 1 \Rightarrow (\mathbf{x} + \boldsymbol{\epsilon})' \cdot (\mathbf{x} + \boldsymbol{\epsilon})' = 1 \Leftrightarrow \mathbf{x}' \cdot \boldsymbol{\epsilon}' = -\frac{\lambda^2}{2} \|\mathbf{h}'_x\|^2 \quad (5.40)$$

Which yields :

$$\cos \alpha_\epsilon = \mathbf{t} \cdot \mathbf{t}_\epsilon = \mathbf{x}' \cdot (\mathbf{x} + \boldsymbol{\epsilon})' = 1 + \mathbf{x}' \cdot \boldsymbol{\epsilon}' = 1 - \frac{\lambda^2}{2} \|\mathbf{h}'_x\|^2 \quad (5.41)$$

Remark that the second order of the developpement is also accessible and can lead to the computation of the hessian of the system, which might be useful for improving the convergence of the minimization algorithm :

$$\cos \alpha_\epsilon = 1 - \frac{\lambda^2}{2} \|\mathbf{h}'_x\|^2 \quad (5.42a)$$

$$\sin \alpha_\epsilon = \sqrt{1 - \cos^2 \alpha_\epsilon} = \lambda \|\mathbf{h}'_x\| + o(\lambda^2) \quad (5.42b)$$

$$\sin^2 \alpha_\epsilon / 2 = \frac{\lambda^2}{4} \|\mathbf{h}'_x\|^2 \quad (5.42c)$$

Finally, it's possible to conclude that $\alpha_\epsilon(s)$ is in first order of λ and thus gets negligible when λ tends to zero :

$$\lim_{\lambda \rightarrow 0} \alpha_\epsilon(s) = 0 \quad (5.43)$$

Aligning \tilde{F}_ϵ towards F_ϵ

Recall that aligning \tilde{F}_ϵ over F is nothing but a rotation around \mathbf{t} by an angle Ψ_ϵ . This leads to :

$$\tilde{\mathbf{u}}_\epsilon = \cos \Psi_\epsilon \mathbf{u} + \sin \Psi_\epsilon \mathbf{v} \quad (5.44a)$$

$$\tilde{\mathbf{v}}_\epsilon = -\sin \Psi_\epsilon \mathbf{u} + \cos \Psi_\epsilon \mathbf{v} \quad (5.44b)$$

Aligning F_ϵ towards t

Recall that \tilde{F}_ϵ is obtained by parallel transporting F_ϵ from \mathbf{t}_ϵ to \mathbf{t} . This operation could be seen as a rotation around $\mathbf{t}_\epsilon \times \mathbf{t}$ of an angle α_ϵ . Where :

$$\mathbf{b} = \mathbf{t}_\epsilon \times \mathbf{t} = \cos \gamma \tilde{\mathbf{u}}_\epsilon + \sin \gamma \tilde{\mathbf{v}}_\epsilon = \cos \gamma \mathbf{u}_\epsilon + \sin \gamma \mathbf{v}_\epsilon \quad (5.45)$$

5.6. Energy gradient with respect to x : internal forces

Expressing F_ϵ on the basis \tilde{F}_ϵ gives for \mathbf{u}_ϵ and \mathbf{v}_ϵ :

$$\mathbf{u}_\epsilon = \sin \gamma \mathbf{b} + \cos \gamma \left(\sin \alpha_\epsilon \tilde{\mathbf{t}} + \cos \alpha_\epsilon (\cos \gamma \tilde{\mathbf{u}}_\epsilon - \sin \gamma \tilde{\mathbf{v}}_\epsilon) \right) \quad (5.46a)$$

$$\mathbf{v}_\epsilon = \cos \gamma \mathbf{b} + \sin \gamma \left(-\sin \alpha_\epsilon \tilde{\mathbf{t}} + \cos \alpha_\epsilon (\sin \gamma \tilde{\mathbf{u}}_\epsilon - \cos \gamma \tilde{\mathbf{v}}_\epsilon) \right) \quad (5.46b)$$

Which can be rearranged in :

$$\mathbf{u}_\epsilon = \cos \gamma \sin \alpha_\epsilon \mathbf{t} + (\cos \alpha_\epsilon \cos^2 \gamma + \cos^2 \gamma) \tilde{\mathbf{u}}_\epsilon + \sin \gamma \cos \gamma (1 - \cos \alpha_\epsilon) \tilde{\mathbf{v}}_\epsilon \quad (5.47a)$$

$$\mathbf{v}_\epsilon = -\sin \gamma \sin \alpha_\epsilon \mathbf{t} + \cos \gamma \sin \gamma (1 - \cos \alpha_\epsilon) \tilde{\mathbf{u}}_\epsilon + (\cos^2 \gamma + \cos \alpha_\epsilon \sin^2 \gamma) \tilde{\mathbf{v}}_\epsilon \quad (5.47b)$$

Variation of the Bishop frame with respect to x

Finally, one can express F_ϵ on the basis F as the composition of two rotations :

$$\mathbf{u}_\epsilon = \begin{bmatrix} 1 & 0 & 0 \\ 0 & \cos \Psi_\epsilon & -\sin \Psi_\epsilon \\ 0 & \sin \Psi_\epsilon & \cos \Psi_\epsilon \end{bmatrix} \begin{bmatrix} \cos \gamma \sin \alpha_\epsilon \\ 1 - 2 \cos^2 \gamma \sin^2 \alpha_\epsilon / 2 \\ 2 \sin \gamma \cos \gamma \sin^2 \alpha_\epsilon / 2 \end{bmatrix} = \begin{bmatrix} \alpha_\epsilon \cos \gamma \\ 1 \\ \Psi_\epsilon \end{bmatrix} + o(\lambda) \quad (5.48a)$$

$$\mathbf{v}_\epsilon = \begin{bmatrix} 1 & 0 & 0 \\ 0 & \cos \Psi_\epsilon & -\sin \Psi_\epsilon \\ 0 & \sin \Psi_\epsilon & \cos \Psi_\epsilon \end{bmatrix} \begin{bmatrix} -\sin \gamma \sin \alpha_\epsilon \\ 2 \sin \gamma \cos \gamma \sin^2 \alpha_\epsilon / 2 \\ 1 - 2 \sin \gamma^2 \sin^2 \alpha_\epsilon / 2 \end{bmatrix} = \begin{bmatrix} -\alpha_\epsilon \sin \gamma \\ -\Psi_\epsilon \\ 1 \end{bmatrix} + o(\lambda) \quad (5.48b)$$

Here, the expressions have been developed in first order of λ . It has been proved in eq. (5.39) and (5.43) that α_ϵ and Ψ_ϵ tend toward zero when the perturbation of the centerline is infinitesimal.

Finally, one can express the variation of the material directors with respect to an infinitesimal variation of rod's centerline by :

$$\mathbf{u}_\epsilon = \alpha_\epsilon \cos \gamma \mathbf{t} + \mathbf{u} + \Psi_\epsilon \mathbf{v} + o(\lambda) \quad (5.49a)$$

$$\mathbf{v}_\epsilon = -\alpha_\epsilon \sin \gamma \mathbf{t} + \mathbf{v} - \Psi_\epsilon \mathbf{u} + o(\lambda) \quad (5.49b)$$

Variation of the material frame with respect to x

Recalling the expression of the material frame expressed in the reference Bishop frame, it's now easy to deduce the variation of material frame with respect to a variation of the rod's centerline :

$$\mathbf{d}_1[\mathbf{x} + \lambda \mathbf{h}_x] = \cos \theta \mathbf{u}_\epsilon + \sin \theta \mathbf{v}_\epsilon \quad (5.50a)$$

$$\mathbf{d}_2[\mathbf{x} + \lambda \mathbf{h}_x] = -\sin \theta \mathbf{u}_\epsilon + \cos \theta \mathbf{v}_\epsilon \quad (5.50b)$$

Which leads according to the previous equation to :

$$\mathbf{d}_1[\mathbf{x} + \lambda \mathbf{h}_x] = \mathbf{d}_1[\mathbf{x}] + \Psi_\epsilon \mathbf{d}_2[\mathbf{x}] + \alpha_\epsilon \cos(\theta - \gamma) \mathbf{t}[\mathbf{x}] + o(\lambda) \quad (5.51a)$$

$$\mathbf{d}_2[\mathbf{x} + \lambda \mathbf{h}_x] = \mathbf{d}_2[\mathbf{x}] - \Psi_\epsilon \mathbf{d}_1[\mathbf{x}] - \alpha_\epsilon \sin(\theta + \gamma) \mathbf{t}[\mathbf{x}] + o(\lambda) \quad (5.51b)$$

5.6.2 Derivative of the vector of material curvatures with respect to x

It is now straightforward from the previous section to express the variation of the material curvatures with respect to a variation $\epsilon = \lambda \mathbf{h}_x$ of \mathbf{x} while θ remains unchanged :

$$(\mathbf{x} + \lambda \mathbf{h}_x)'' \cdot \mathbf{d}_1[\mathbf{x} + \lambda \mathbf{h}_x] = (\mathbf{x}'' + \lambda \mathbf{h}_x'') \cdot (\mathbf{d}_1 + \Psi_\epsilon \mathbf{d}_2 + \alpha_\epsilon \cos(\theta - \gamma) \mathbf{t} + o(\lambda)) \quad (5.52a)$$

$$(\mathbf{x} + \lambda \mathbf{h}_x)'' \cdot \mathbf{d}_2[\mathbf{x} + \lambda \mathbf{h}_x] = (\mathbf{x}'' + \lambda \mathbf{h}_x'') \cdot (\mathbf{d}_2 - \Psi_\epsilon \mathbf{d}_1 - \alpha_\epsilon \sin(\theta + \gamma) \mathbf{t} + o(\lambda)) \quad (5.52b)$$

Thus, recalling that $\mathbf{x}'' \cdot \mathbf{d}_3 = 0$ and that α_ϵ and Ψ_ϵ are first order quantities in λ :

$$(\mathbf{x} + \lambda \mathbf{h}_x)'' \cdot \mathbf{d}_1[\mathbf{x} + \lambda \mathbf{h}_x] = \mathbf{x}'' \cdot \mathbf{d}_1 + \Psi_\epsilon \mathbf{x}'' \cdot \mathbf{d}_2 + \lambda \mathbf{h}_x'' \cdot \mathbf{d}_1 + o(\lambda) \quad (5.53a)$$

$$(\mathbf{x} + \lambda \mathbf{h}_x)'' \cdot \mathbf{d}_2[\mathbf{x} + \lambda \mathbf{h}_x] = \mathbf{x}'' \cdot \mathbf{d}_2 - \Psi_\epsilon \mathbf{x}'' \cdot \mathbf{d}_1 + \lambda \mathbf{h}_x'' \cdot \mathbf{d}_2 + o(\lambda) \quad (5.53b)$$

Which finally leads to :

$$\boldsymbol{\omega}[\mathbf{x} + \lambda \mathbf{h}_x] = \boldsymbol{\omega}[\mathbf{x}] - \Psi_\epsilon \mathbf{J} \boldsymbol{\omega}[\mathbf{x}] + \lambda \begin{bmatrix} -\mathbf{h}_x'' \cdot \mathbf{d}_2 \\ \mathbf{h}_x'' \cdot \mathbf{d}_1 \end{bmatrix} + o(\lambda) \quad (5.54)$$

Reminding the expression of Ψ_ϵ computed in eq. (5.37), one can express the derivative of the vector of material curvatures with respect to \mathbf{x} as :

$$\mathbf{D}_x \boldsymbol{\omega}(s) \cdot \mathbf{h}_x = \left(\int_0^L ((\delta_s - \delta_0) \boldsymbol{\kappa} \mathbf{b} - (1 - H_s) \boldsymbol{\kappa} \mathbf{b}') \cdot \mathbf{h}_x dt \right) \mathbf{J} \boldsymbol{\omega} + \begin{bmatrix} -\mathbf{d}_2^T \\ \mathbf{d}_1^T \end{bmatrix} \cdot \mathbf{h}_x'' \quad (5.55)$$

Here, we have introduce a condensed matrix notation to write $\begin{bmatrix} -\mathbf{d}_2^T \\ \mathbf{d}_1^T \end{bmatrix}$ as a 2x3 matrix.

The entries of the first line are $-\mathbf{d}_2^T = [0, 0, -1]$ while the entries of the second line are $\mathbf{d}_1^T = [0, 1, 0]$. Thus, the matrix entries in the material frame coordinate system are given by :

$$\begin{bmatrix} -\mathbf{d}_2^T \\ \mathbf{d}_1^T \end{bmatrix} = \begin{bmatrix} 0 & 0 & -1 \\ 0 & 1 & 0 \end{bmatrix} \quad (5.56)$$

Remark also how the scalar product $\mathbf{h}_x'' \cdot \mathbf{d}_2$ in vector notation is treated as a product in matrix notation : $\mathbf{d}_2^T \cdot \mathbf{h}_x'' = (\mathbf{h}_x'')^T \cdot \mathbf{d}_2$.

5.6.3 Computation of the forces acting on the centerline

The distributed internal forces acting on the centerline are given by the functional derivative of the elastic energy with respect to \mathbf{x} , which can be decomposed into :

$$\begin{aligned} \langle -\mathbf{f}(s), \mathbf{h}_x \rangle &= \mathbf{D}_x \mathcal{E}(s) \cdot \mathbf{h}_x \\ &= \mathbf{D}_x \mathcal{E}_b(s) \cdot \mathbf{h}_x + \mathbf{D}_x \mathcal{E}_t(s) \cdot \mathbf{h}_x \end{aligned} \quad (5.57)$$

Derivative of the torsion energy with respect to x

Recall that the torsion energy only depends on θ which is independent of x . Thus \mathcal{E}_t is independent of x and :

$$\mathbf{D}_x \mathcal{E}_t[\mathbf{x}](s) \cdot \mathbf{h}_x = \frac{d}{d\lambda} \mathcal{E}_t[\mathbf{x} + \lambda \mathbf{h}_x] \Big|_{\lambda=0} = 0 \quad (5.58)$$

Derivative of the bending energy with respect to x

To compute the partial derivative of \mathcal{E}_b with respect to \mathbf{x} we first calculate the derivative of \mathcal{E}_b with respect to $\boldsymbol{\omega}$:

$$\mathbf{D}_{\omega} \mathcal{E}_b[\boldsymbol{\omega}](s) \cdot \mathbf{h}_{\omega} = \frac{d}{d\lambda} \mathcal{E}_b[\boldsymbol{\omega} + \lambda \mathbf{h}_{\omega}] \Big|_{\lambda=0} = \int_0^L (\boldsymbol{\omega} - \bar{\boldsymbol{\omega}})^T \mathbf{B} \cdot \mathbf{h}_{\omega} dt \quad (5.59)$$

Then, we calculate the partial derivative of \mathcal{E}_b with respect to \mathbf{x} from the chain rule and with eq. (5.55) and (5.59) :

$$\mathbf{D}_x \mathcal{E}_b[\boldsymbol{\omega}[\mathbf{x}]](s) \cdot \mathbf{h}_x = \mathbf{D}_{\omega} \mathcal{E}_b[\boldsymbol{\omega}](s) \cdot (\mathbf{D}_x \boldsymbol{\omega}[\mathbf{x}](s) \cdot \mathbf{h}_x) = \mathcal{A} + \mathcal{B} + \mathcal{C} \quad (5.60)$$

where \mathcal{A} , \mathcal{B} and \mathcal{C} are given by :

$$\mathcal{A} = \int_0^L (\boldsymbol{\omega} - \bar{\boldsymbol{\omega}})^T \mathbf{B} \begin{bmatrix} -\mathbf{d}_2^T \\ \mathbf{d}_1^T \end{bmatrix} \cdot \mathbf{h}_x'' dt \quad (5.61a)$$

$$\mathcal{B} = \int_{t=0}^L (\boldsymbol{\omega} - \bar{\boldsymbol{\omega}})^T \mathbf{B} \mathbf{J} \boldsymbol{\omega} \left(\int_{u=0}^L (\delta_t - \delta_0) \boldsymbol{\kappa} \mathbf{b} \cdot \mathbf{h}_x du \right) dt \quad (5.61b)$$

$$\mathcal{C} = \int_{t=0}^L -(\boldsymbol{\omega} - \bar{\boldsymbol{\omega}})^T \mathbf{B} \mathbf{J} \boldsymbol{\omega} \left(\int_{u=0}^L (1 - H_t) \boldsymbol{\kappa} \mathbf{b}' \cdot \mathbf{h}_x du \right) dt \quad (5.61c)$$

Calculus of \mathcal{A} :

$$\mathcal{A} = \int_0^L (\boldsymbol{\omega} - \bar{\boldsymbol{\omega}})^T \mathbf{B} \begin{bmatrix} -\mathbf{d}_2^T \\ \mathbf{d}_1^T \end{bmatrix} \cdot \mathbf{h}_x'' dt \quad (5.62)$$

One can remark that the (row) vector found in eq. (5.62) can be rewritten as : ¹⁰

$$(\boldsymbol{\omega} - \bar{\boldsymbol{\omega}})^T \mathbf{B} \begin{bmatrix} -\mathbf{d}_2^T \\ \mathbf{d}_1^T \end{bmatrix} = M_2 \mathbf{d}_1^T - M_1 \mathbf{d}_2^T = -(\mathbf{d}_3 \times \mathbf{M}^{\perp})^T \quad (5.63)$$

¹⁰Here, we mix up vector and matrix notations. The matrix form of a vector is given by the components of the vector in the material frame coordinate system. For instance, $(\mathbf{d}_3 \times \mathbf{M}^{\perp})^T$ is a row vector that writes in its matrix form : $[0, -M2, M1]$.

Thus, \mathcal{A} could be rewritten in it's vectoriel form :

$$\begin{aligned}\mathcal{A} &= - \int_0^L (\mathbf{d}_3 \times \mathbf{M}^\perp) \cdot \mathbf{h}_x'' dt \\ &= - [\mathbf{(d}_3 \times \mathbf{M}^\perp) \cdot \mathbf{h}_x']_0^L + \int_0^L (\mathbf{d}_3 \times \mathbf{M}^\perp)' \cdot \mathbf{h}_x' dt \\ &= - [\mathbf{(d}_3 \times \mathbf{M}^\perp) \cdot \mathbf{h}_x']_0^L + \int_0^L ((\mathbf{d}_3 \times \mathbf{M}^\perp') \cdot \mathbf{h}_x' + (\mathbf{h}_x' \times \mathbf{d}_3') \cdot \mathbf{M}^\perp) dt\end{aligned}\quad (5.64)$$

Recall that from eq. (5.2) that $\mathbf{h}_x' \cdot \mathbf{d}_3 = 0$ and from eq. (5.3) that $\mathbf{d}_3' \cdot \mathbf{d}_3 = 0$. Hence, $\mathbf{h}_x' \times \mathbf{d}_3'$ is colinear to \mathbf{d}_3 . Or by definition \mathbf{M}^\perp is orthogonal to \mathbf{d}_3 . Thus, $(\mathbf{h}_x' \times \mathbf{d}_3') \cdot \mathbf{M}^\perp = 0$. Finally, after a second integration by parts :

$$\begin{aligned}\mathcal{A} &= - [\mathbf{(d}_3 \times \mathbf{M}^\perp) \cdot \mathbf{h}_x']_0^L + \int_0^L (\mathbf{d}_3 \times \mathbf{M}^\perp') \cdot \mathbf{h}_x' dt \\ &= - [(\mathbf{d}_3 \times \mathbf{M}^\perp') \cdot \mathbf{h}_x'' - (\mathbf{d}_3 \times \mathbf{M}^\perp) \cdot \mathbf{h}_x']_0^L - \int_0^L (\mathbf{d}_3 \times \mathbf{M}^\perp')' \cdot \mathbf{h}_x dt\end{aligned}\quad (5.65)$$

Calculus of \mathcal{B} :

$$\begin{aligned}\mathcal{B} &= \int_{t=0}^L (\boldsymbol{\omega} - \bar{\boldsymbol{\omega}})^T \mathbf{B} \mathbf{J} \boldsymbol{\omega} \left(\int_{u=0}^L (\delta_t - \delta_0) \boldsymbol{\kappa} \mathbf{b} \cdot \mathbf{h}_x du \right) dt \\ &= - (\boldsymbol{\kappa} \mathbf{b} \cdot \mathbf{h}_x)(0) \int_{t=0}^L (\boldsymbol{\omega} - \bar{\boldsymbol{\omega}})^T \mathbf{B} \mathbf{J} \boldsymbol{\omega} dt + \int_{t=0}^L (\boldsymbol{\omega} - \bar{\boldsymbol{\omega}})^T \mathbf{B} \mathbf{J} \boldsymbol{\omega} \boldsymbol{\kappa} \mathbf{b} \cdot \mathbf{h}_x dt\end{aligned}\quad (5.66)$$

Calculus of \mathcal{C} :

$$\begin{aligned}\mathcal{C} &= \int_{t=0}^L -(\boldsymbol{\omega} - \bar{\boldsymbol{\omega}})^T \mathbf{B} \mathbf{J} \boldsymbol{\omega} \left(\int_{u=0}^L (1 - H_t) \boldsymbol{\kappa} \mathbf{b}' \cdot \mathbf{h}_x du \right) dt \\ &= \int_{u=0}^L \int_{t=u}^L -((\boldsymbol{\omega} - \bar{\boldsymbol{\omega}})^T \mathbf{B} \mathbf{J} \boldsymbol{\omega})(t) (\boldsymbol{\kappa} \mathbf{b}' \cdot \mathbf{h}_x)(u) dt du \\ &= \int_{u=0}^L - \left(\int_{t=u}^L (\boldsymbol{\omega} - \bar{\boldsymbol{\omega}})^T \mathbf{B} \mathbf{J} \boldsymbol{\omega} dt \right) (\boldsymbol{\kappa} \mathbf{b}' \cdot \mathbf{h}_x) du\end{aligned}\quad (5.67)$$

By several integration by parts, using Fubini's theorem once and supposing that the terms vanishes at $s = 0$ and $s = L$:

$$\begin{aligned}\mathcal{B} + \mathcal{C} &= \int_{t=0}^L \left((\boldsymbol{\omega} - \bar{\boldsymbol{\omega}})^T \mathbf{B} \mathbf{J} \boldsymbol{\omega} \boldsymbol{\kappa} \mathbf{b} - \left(\int_{u=t}^L (\boldsymbol{\omega} - \bar{\boldsymbol{\omega}})^T \mathbf{B} \mathbf{J} \boldsymbol{\omega} du \right) \boldsymbol{\kappa} \mathbf{b}' \right) \cdot \mathbf{h}_x dt \\ &= \int_{t=0}^L \left(- \left(\int_{u=t}^L (\boldsymbol{\omega} - \bar{\boldsymbol{\omega}})^T \mathbf{B} \mathbf{J} \boldsymbol{\omega} du \right)' \boldsymbol{\kappa} \mathbf{b} - \left(\int_{u=t}^L (\boldsymbol{\omega} - \bar{\boldsymbol{\omega}})^T \mathbf{B} \mathbf{J} \boldsymbol{\omega} du \right) \boldsymbol{\kappa} \mathbf{b}' \right) \cdot \mathbf{h}_x dt \\ &= \int_{t=0}^L \left(- \left(\int_{u=t}^L (\boldsymbol{\omega} - \bar{\boldsymbol{\omega}})^T \mathbf{B} \mathbf{J} \boldsymbol{\omega} du \right) \boldsymbol{\kappa} \mathbf{b} \right)' \cdot \mathbf{h}_x dt\end{aligned}\quad (5.68)$$

Which can be rewritted using the quasi-static hypothesis eq. (5.33) :

$$\begin{aligned}
 \mathcal{B} + \mathcal{C} &= \int_{t=0}^L \left(- \left(\int_{u=t}^L (\boldsymbol{\omega} - \bar{\boldsymbol{\omega}})^T \mathbf{B} \mathbf{J} \boldsymbol{\omega} \, du \right) \boldsymbol{\kappa} \mathbf{b} \right)' \cdot \mathbf{h}_x \, dt \\
 &= \int_{t=0}^L \left(- \left(\int_{u=t}^L \beta(\theta' - \bar{\theta}')(\delta_L - \delta_0) - (\beta(\theta' - \bar{\theta}'))' \, du \right) \boldsymbol{\kappa} \mathbf{b} \right)' \cdot \mathbf{h}_x \, dt \quad (5.69) \\
 &= \int_{t=0}^L \left(- \left(\beta(\theta' - \bar{\theta}')(L) - [\beta(\theta' - \bar{\theta}')]_t^L \right) \boldsymbol{\kappa} \mathbf{b} \right)' \cdot \mathbf{h}_x \, dt \\
 &= \int_{t=0}^L -(\beta(\theta' - \bar{\theta}') \boldsymbol{\kappa} \mathbf{b})' \cdot \mathbf{h}_x \, dt
 \end{aligned}$$

Finally, combining eq. (5.65) and (5.69) into eq. (5.60) yields :

$$\mathbf{D}_x \mathcal{E}_b[\boldsymbol{\omega}[\mathbf{x}]](s) \cdot \mathbf{h}_x = \int_0^L \left(-(\mathbf{d}_3 \times \mathbf{M}^{\perp'})' - (\beta(\theta' - \bar{\theta}') \boldsymbol{\kappa} \mathbf{b})' \right) \cdot \mathbf{h}_x \, dt \quad (5.70)$$

Internal forces

The gradient of the elastic energy with respect to \mathbf{x} is obtained from eq. (5.57) with eq. (5.58) and (5.70) :

$$\langle -\mathbf{f}(s), \mathbf{h}_x \rangle = \mathbf{D}_x \mathcal{E}(s) \cdot \mathbf{h}_x = - \int_0^L \left((\mathbf{d}_3 \times \mathbf{M}^{\perp'})' + (\beta(\theta' - \bar{\theta}') \boldsymbol{\kappa} \mathbf{b})' \right) \cdot \mathbf{h}_x \, dt \quad (5.71)$$

Finally, we can conclude on the expression of the distributed internal forces acting on the centerline :

$$\mathbf{f}(s) = (\mathbf{d}_3 \times \mathbf{M}^{\perp'}(s) + \beta(\theta' - \bar{\theta}') \boldsymbol{\kappa} \mathbf{b})'(s) \quad (5.72)$$

Remark that this expression can be rewritten thanks to eq. (5.30a) as :

$$\mathbf{f}(s) = (\mathbf{d}_3 \times \mathbf{M}^{\perp'} + Q \boldsymbol{\kappa} \mathbf{b})'(s) \quad (5.73)$$

5.7 Shear force acting on the rod

From eq. (5.31) and (5.73) we deduce the internal shear force and distributed twisting moment acting on the rod :

$$\mathbf{F} = \mathbf{d}_3 \times \mathbf{M}' \quad (5.74a)$$

$$m = Q' + \kappa_1 M_2 - \kappa_2 M_1 \quad (5.74b)$$

Remark that we fall back on the static member of the dynamical equations of rods in Kirchhoff's theory (see eq. (6.67)). Hence, we have proved the equivalence between the present approach (based on the calculus of variations and the formulation of an elastic

energy) and a more direct approach from the well-established Kirchhoff equations.¹¹

5.8 Discussion

We have build upon Bergou et al. 2008 [91] a reduced coordinate beam theory for the modeling of slender rods with anisotropic cross-section and arbitrary natural geometry. This model assumes that the rod is inextensible, that cross-sections remain plane and perpendicular to the centerline, and that the material behaves linearly.

This model is a serious step forward for the modeling of elastic gridshells compared to the actual 3-DOFs beam element developed by Adriaenssens and Barnes 2001 [40] and extended by Douthe et al. 2006 [26]. It enables the modeling of : fixed support conditions ; rectangular beams like the one used in timber gridshells; complex connections. However, nothing was done to take into account external loads and this is at that point a drawback worth to mentionne.

Unlike Bergou et al. 2008 [91] and Nabaei 2014 [97] :

- Our expressions for the internal forces and twisting moment acting on the rod have the advantage to be fully local, which leads to simpler and faster numerical evaluations.
- We have retrieved the physical meaning of the energy gradients in terms of shear, bending and twisting of the rod. This is a critical point for the post-analysis of the results given by the model as our goal is to understand and predict the behavior of real structures.
- Our model is developed in the smooth world and thus the choice of the discretization is left to the stage of the numerical implementation, which we believe gives more flexibility.

5.9 Conclusion

From this first model, we suggest to look at a different approach based on the dynamical Kirchhoff equations for rods. Although this development would be theoretically equivalent to the present approach, it would probably lead in a more straightforward manner to the calculation of the forces acting on the centerline, as suggested by §5.7. Moreover, unlike the variational approach, the dynamic equations are easy to write taking into account

¹¹It is easy from eq. (5.74a) to retrieve eq. (6.67d) and (6.67e) considering that :

$$\begin{aligned}
 \mathbf{d}_3 \times \mathbf{M}' &= \mathbf{d}_3 \times (\mathbf{M}^{\perp'} + (Q \mathbf{d}_3)') \\
 &= \mathbf{d}_3 \times (\mathbf{M}^{\perp'} + Q \mathbf{d}_3') \\
 &= \mathbf{d}_3 \times (\mathbf{M}^{\perp'} + Q (\tau \mathbf{d}_3 + \kappa \mathbf{b}) \times \mathbf{d}_3) \\
 &= \mathbf{d}_3 \times \mathbf{M}^{\perp'} + Q \kappa \mathbf{b}
 \end{aligned}$$

the action of external forces and moments acting on the rod. This would lead to a more easy-to-implement and theoretically-solid management of these actions.

Finally, this approach might be better to treat the inextensibility not as a constraint but as part as an internal force acting on the centerline.

5.10 References

- [10] C. Douthe. “Etude de structures élancées précontraintes en matériaux composites : application à la conception des gridshells”. PhD thesis. Université Paris Est, 2007, p. 274.
- [12] F. Tayeb. “Simulation numérique du comportement mécanique non linéaire de gridshells composés de poutres élancées en matériaux composites et de sections quelconques”. PhD thesis. 2015.
- [26] C. Douthe, O. Baverel, and J.-F. Caron. “Formfinding of a grid shell in composite materials”. In: *Journal of the IASS* 47 (2006), pp. 53–62.
- [38] S. Adriaenssens, M. Barnes, and C. Williams. “A new analytic and numerical basis for the form-finding and analysis of spline and gridshell structures”. In: *Computing Developments in Civil and Structural Engineering*. Ed. by B. Kumar and B. H. V. Topping. Edinburgh: Civil-Comp Press, 1999, pp. 83–91.
- [40] S. Adriaenssens and M. Barnes. “Tensegrity spline beam and grid shell structures”. In: *Engineering Structures* 23.1 (2001), pp. 29–36.
- [42] L. du Peloux, F. Tayeb, B. Lefevre, O. Baverel, and J.-F. Caron. “Formulation of a 4-DoF torsion / bending element for the formfinding of elastic gridshells”. In: *Proceedings of the International Association for Shell and Spatial Structures*. August. Amsterdam, 2015, pp. 1–14.
- [91] M. Bergou, M. Wardetzky, S. Robinson, B. Audoly, and E. Grinspun. “Discrete elastic rods”. In: *ACM SIGGRAPH* (2008), pp. 1–12.
- [95] M. Bergou, B. Audoly, E. Vouga, M. Wardetzky, and E. Grinspun. “Discrete viscous threads”. In: *ACM Transactions on ...* (2010), pp. 1–10.
- [96] B. Lefevre, F. Tayeb, L. du Peloux, and J.-F. Caron. “A 4-degree-of-freedom Kirchhoff beam model for the modeling of bending–torsion couplings in active-bending structures”. In: *International Journal of Space Structures* 32.2 (2017), pp. 69–83.
- [97] S. Nabaei. “Mechanical form-finding of timber fabric structures”. PhD thesis. EPFL, 2014.
- [98] M. Grégoire and E. Schömer. “Interactive simulation of one-dimensional flexible parts”. In: *CAD Computer Aided Design* 39.8 (2007), pp. 694–707.
- [99] A. Theetten, L. Grisoni, C. Andriot, and B. Barsky. “Geometrically exact dynamic splines”. In: *CAD Computer Aided Design* 40 (2008), pp. 35–48.
- [100] F. Bertails, B. Audoly, M.-P. Cani, B. Querleux, F. Leroy, and J.-L. Lévéque. “Super-helices for predicting the dynamics of natural hair”. In: *ACM Transactions on Graphics* 25.3 (2006), p. 1180.
- [101] F. Bertails-Descoubes. “Super-clothoids”. In: *Computer Graphics Forum* 31.2 (2012), pp. 509–518.
- [102] J. Spillmann and M. Teschner. “CORDE : Cosserat Rod Elements for the Dynamic Simulation of One-Dimensional Elastic Objects”. In: *Eurographics/ ACM SIGGRAPH Symposium on Computer Animation* (2007), pp. 1–10.

-
- [103] P. Jung, S. Leyendecker, J. Linn, and M. Ortiz. “A discrete mechanics approach to the Cosserat rod theory—Part 1: static equilibria”. eng. In: *International journal for numerical methods in engineering* 85.1 (2010), pp. 31–60.
 - [104] F. B. Fuller. “Decomposition of the linking number of a closed ribbon : A problem from molecular biology”. In: 75.8 (1978), pp. 3557–3561.
 - [105] R. Vauquelin. “Writhing Geometry at Finite Temperature : Random Walks and Geometric phases for Stiff Polymers”. In: 1 (2000).
 - [106] R. de Vries. “Evaluating changes of writhe in computer simulations of supercoiled DNA”. In: *The Journal of Chemical Physics* 122.6 (2005).
 - [107] M. Berger. “Topological Quantities: Calculating Winding, Writhing, Linking, and Higher order Invariants”. In: *Lecture Notes in Mathematics* 1973 (2009), pp. 75–97.
 - [108] J. Langer and D. Singer. “Lagrangian Aspects of the Kirchhoff elastic rod”. In: *Society for Industrial and Applied Mathematics Review* 38.4 (1996), pp. 605–618.
 - [109] J. Alexander and S. Antman. “The ambiguous twist of love”. In: *Quarterly of Applied Mathematics* 40.1 (1982), pp. 83–92.
 - [110] B. Audoly, M. Amar, and Y. Pomeau. *Elasticity and geometry*. 2010, p. 600.
 - [111] E. H. Dill. “Kirchhoff’s theory of rods”. In: *Archive for History of Exact Sciences* (1992), p. 23.
 - [112] S. Antman. *Nonlinear problems of elasticity*. Applied mathematical sciences. New York: Springer, 2005, p. 838.
 - [113] E. Reissner. “On one-dimensional large-displacement finite-strain beam theory.” In: *Studies in Applied Mathematics* 52.2 (1973), pp. 87–95.
 - [114] A. Love. *A treatise on the mathematical theory of elasticity*. Second. Cambridge University Press, 1906, p. 571.

6 Elastic rod : equilibrium approach

6.1 Introduction

In this chapter, following Dill 1992 [111], we present thoroughly the theory of slender rods developed by Kirchhoff, Clebsch and Love at the end of the XIXth century. This theory can be applied for motions where strains remain small although displacements may be large, which is perfectly suitable to the modeling of elastic gridshell structures where the material must be employed in its elastic range but the structure undergoes large displacements during the forming process.¹

We will see that this theory requires nothing more than that, and that the shear strains are negligible. In particular, the rod is not supposed to be strictly inextensible, nor the cross-sections are assumed to remain strictly plane.

The discrete beam element presented in [chapter 7](#) will directly results from the discretization of the dynamical Kirchhoff equations presented here, combined with an appropriate use of the discrete curve-angle representation (see [§5.3](#)) and the circumscribed discrete curvature (see [??](#)).

The motivations for this work were build upon the experience gained in the previous chapter (see [chapter 5](#)). Although the variational approach actually leads to the calculation of the quasi-static internal force and moment acting on the rod, these results are more straightforwardly obtained with the approach developed in this chapter, that is through writing the dynamic equilibrium of the rod. But it is not simply a matter of taste considering the perspective of the discrete element we intend to build and solve through a damped dynamic explicit time integration, namely a *dynamic relaxation* procedure (see [chapter 7](#)). Indeed, the equilibrium approach enables an immediate and full dynamic treatment of the rod, drops the stiff and unnecessary constraint of inextensibility and naturally integrates

¹This is classically referred to as “material linearity” but “geometric nonlinearity”. In the literature, *large rotation* is also employed to refer to *large displacement*.

the treatment of applied loads. It also offers a more physical and less mathematical understanding of the problem, which is a matter of concern when designing real structures.²

Finally, this approach is closer “in spirit” to what have been proposed previously in the field of active bending structures about the 3-DOFs or 6-DOFs *spline beam* elements, and first introduced by Adriaenssens and Barnes 2001 [40]. It brings a more robust background to explain how internal forces and moments are derived in those elements. For instance, in [40, 26, 29] the unbalanced shear forces acting on the rod during its motion are deduced – with no justification – from the bending moment, itself computed from the curvature of the rod. We show here that this result is a consequence of the dynamic Kirchhoff equations where some inertial terms have been neglected (see §6.3.5).

6.1.1 Overview

We begin by a short introduction on the Cosserat theory of rods (see §6.2). From this theory, we study only the way the motion of a rod is described in a very generic manner, through its force and moment strain vectors. We then restrain our study to the Kirchhoff theory of rods (see §6.3) : we specialize the description inherited from the Cosserat theory to our needs so it fulfills the specific assumptions made in Kirchhoff theory ; we establish the dynamical equations of a rod under external loading ; we recall the canonical form of the strain and stress tensors ; and finally we retrieve the usual material constitutive equations as a consequence of the small strains and elasticity assumptions. Finally, we show that the static member of the equations of motion can be retrieved from simple geometric considerations (see §6.5).

6.1.2 Contributions

- We describe the motion of a Kirchhoff rod as a particular case of the motion of a Cosserat rod. This would enable to extend the present work in order to take into account shear effects, while sticking to the same geometrical description.
- We retrieve the equations of motion of a Kirchhoff rod with a careful treatment of the assumptions, following [111].
- We highlight the pedagogical interest of this approach compared to the variational approach by showing that the static members of Kirchhoff equations are nothing but first-order balance equations.

6.1.3 Related work

The theory for slender rods presented here was developed at the end of the XIXth century by Kirchhoff [115, 116], Clebsch [117] and Love [114].

²The formalism of the energy formulation has its pros as it is more straightforwardly translated into minimization problems. Therefore, its resolution is naturally opened to a wide range of algorithms such as Newton-Raphson method, the conjugate gradient method, the steepest descent methods, ...

Dill 1992 [111] revisits the work of these pioneers and treats their theory in the framework of modern continuum mechanics. He gives the dynamic equations of balance of momentum, with a careful and precise treatment of the assumptions. In particular, he makes the correct distinction between material and geometric curvatures, a subtlety that is often hidden behind the assumption that the beam is inextensible [38, 10, 29].³ His work is mentioned by Neukirch 2009 [118].

Timoshenko 1921 [119] proposes a theory that extends Kirchhoff, Clebsch and Love works to take into account shear effects, considering that cross-sections might not stay perpendicular to the centerline of the beam. For plane problems, he measures the amount of shear through a rotation of the cross-section with respect to the beam axis.

Reissner 1973 [113] and Simo and Vu-Quoc 1991 [120] introduce the notion of *geometrically exact* beam, that is a beam model in which the description of the geometry is free of any assumption. They derive generalized Kirchhoff equations for rods that can undergo stretching, shearing, bending, torsion and even warping in [120] with the help of a 7th degree of freedom. The problem is formulated from the principle of virtual work and is fully nonlinear, which means it accounts for both large-displacements and finite-strains. A similar attempt is proposed by Antman 1974 [121]. These formulations are nothing but two-director Cosserat theories in which the material frames is constrained to remain orthonormal, but not necessary adapted to the centerline.

Antman 2005 [112] develops the *special theory of Cosserat rods*, a very generic theory applicable to the modeling of solids where one dimension is much larger than the other two. This theory is a generalization of the previous works of Antman, Reissner and Simo where the directors of the material frame are no more constrained to rigid body motions. Several authors interested in the modeling and simulation of nonlinear dynamics of rods built their work upon Antman's theory, among which we can cite Grégoire and Schömer 2007 [98], Spillmann and Teschner 2007 [102] or Cao and Tucker 2008 [122].

Lang and Linn 2009 [123] claim that Lagrangian field theory leads to a more straightforward development of the work of Simo [120] that is directly formulated using quaternions, which could be of practical interest when considering its implementation in a numerical solver.

Cisternas and Holmes 2002 [124] extend Dill and Coleman extensible rod model to take into account thermal expansion. Moulton et al. 2013 [125] offers an interesting treatment of extensible rods to model plants growth, whereas all the other papers cited here usually try to built their model upon the assumption that the rod is inextensible.

Lázaro et al. 2016 [126] presents a review of geometrically exact models for very flexible rods with the prospect of modeling bending active structures.

³“The principal normal, binormal, and torsion of the axis, viewed as an element of a space curve, have no special significance in the theory of rods. Use of those special directions as base vectors does not simplify the theory and can mislead the reader into attributing significance to them when none exists. In particular, the curvature of the rod should not be confused with the curvature of the space curve which the axis forms.” [111, p. 5]

6.2 Introduction to the special Cosserat theory of rods

This paragraph gives a very brief overview of the *special Cosserat theory of rods*, as presented by Antman 2005 [112], that accounts for bending, torsion, extension and shear behaviors of slender beams.⁴ This theory – which is a *director theory* of rods – was first introduced by [121]. It gives a larger scope to the basements of the present work – which relies on the *Kirchhoff theory of rods* – as the last is a special case of this larger theoretical framework. Thus, what is presented in this paragraph could be considered as a reasonable starting point to extend the present work, for instance to take account for shear deformations or large extensions, which might be relevant for some engineering problems or form-finding processes.

It has been largely employed in various fields [127, 95].

6.2.1 Description of the motion

The special Cosserat theory of rods consider dynamics of rods. It relies on a precise geometric description (see fig. 6.1) of rods build upon three vector-valued functions that are time dependent :

- \mathbf{x} , a position vector describing the geometry in space of a specific *fiber* called the rod *axis* or *centerline*. This function describes the rod in its longitudinal dimension. This dimension is of prime importance in the case of slender bodies such as rods as what is intend is to build a reduced theory, namely a 1-dimensional theory. This curve will often be understood as the curve passing through the cross-section centroids along the rod, although this is not mandatory in the theory.
- $\mathbf{d}_1, \mathbf{d}_2$, two unit vector fields describing the lateral spatiality of the rod and called material *directors*. These vectors will often be understood as the principal axis of the cross-section, although this is not mandatory in the theory.

Modeling the geometry of the rod in any configuration is not sufficient to build a mechanical model. Indeed, one must know a *reference* state for the solid as strains measure relative change in geometry and stresses are related to strains through the constitutive relation of the rod material. Thus, the special Cosserat theory of rods consider two configurations :

- The *actual* configuration, that is the configuration of the rod at time t during the motion.
- The *reference* configuration, that is the configuration of the rod in a specific state where its geometry (possibly curved and twisted) is known and its mechanical state (strains, stresses) under possible loads (dead weight, temperature, wind, snow , pre-stress, ...) and possible boundary conditions is known. In practice, this configuration

⁴“[we formulate] a general dynamical theory of rods that can undergo large deformations in space by suffering flexure, torsion, extension, and shear. We call the resulting geometrically exact theory the *special Cosserat theory of rods*.” [112, p. 270]

will often be chosen as a *stress-free* configuration when the beam is not subject to any loads nor restraints of any kind, although this is not mandatory in the theory.

Thus, the equations governing the motion of a *special Cosserat rod* will be based on the description of a fully known reference configuration and the description of the actual or deformed configuration of the rod at time t during its motion (see [fig. 6.1](#)). Usually, what is intended is to predict the motion of a particular rod given its reference configuration, material properties, boundary conditions, and loading. In this thesis, the equations of the motion will be integrated to converge as fast as possible to the quasi-static response of the system, as this work only deals with statics of structures. However, it is still possible to use a more convenient and accurate time integrator to compute the motion, if one wants to study the (true) dynamic of a rod and go beyond the knowledge of its static equilibrium.

Hereafter, when ambiguity is possible, symbols referring to the reference configuration will be marked with an overline while symbols referring to the actual configuration will be marked with a subscript in the variable t . Generally, scalar quantities are marked with the subscript t and vector quantities with an overline in order to avoid double subscripts when one will refer to vector components.

Actual configuration

At time t , the *actual* or *deformed* configuration of the rod $\{\mathbf{x}, \mathbf{d}_1, \mathbf{d}_2\}$ is described by its *centerline* $\gamma_t \in \mathcal{C}^1([0, L] \times \mathbb{R}^3)$, a regular space curve :

$$\begin{aligned} \gamma_t(t, \cdot) : [0, L] &\longrightarrow \mathbb{R}^3 \\ s &\longmapsto \mathbf{x}(t, s) \end{aligned} \tag{6.1}$$

and two perpendicular unit vector fields : ⁵

$$\begin{aligned} (\mathbf{d}_1, \mathbf{d}_2)(t, \cdot) : [0, L] &\longrightarrow \mathbb{R}^3 \times \mathbb{R}^3 \\ s &\longmapsto (\mathbf{d}_1(t, s), \mathbf{d}_2(t, s)) / \mathbf{d}_1(t, s) \cdot \mathbf{d}_2(t, s) = 0 \end{aligned} \tag{6.2}$$

In addition, we define a third unit vector field as :

$$\mathbf{d}_3 = \mathbf{d}_1 \times \mathbf{d}_2 \tag{6.3}$$

Thus, the centerline is framed with the orthonormal moving frame $\{\mathbf{d}_3, \mathbf{d}_1, \mathbf{d}_2\}$. The unit vectors $\mathbf{d}_i(t, s)$ are called *material directors*.

Note that the centerline is parametrized by s chosen to be the arc length parameter of the *reference* configuration. It may not coincide with the arc length parameter of the *actual* configuration denoted by $s_t = \Psi(t, s) = \Psi_t(s)$ as the rod may suffer elongation. L denotes the length of the centerline in the reference configuration. The actual length of γ_t is denoted

⁵Requiring that $\mathbf{d}_1 \perp \mathbf{d}_2$ implies that the description of the motion is convenient only for small in-plane stretching and shearing of the cross-section. This constraint can be relaxed to lead to an even more general theory, called the *2-director Cosserat theory*.

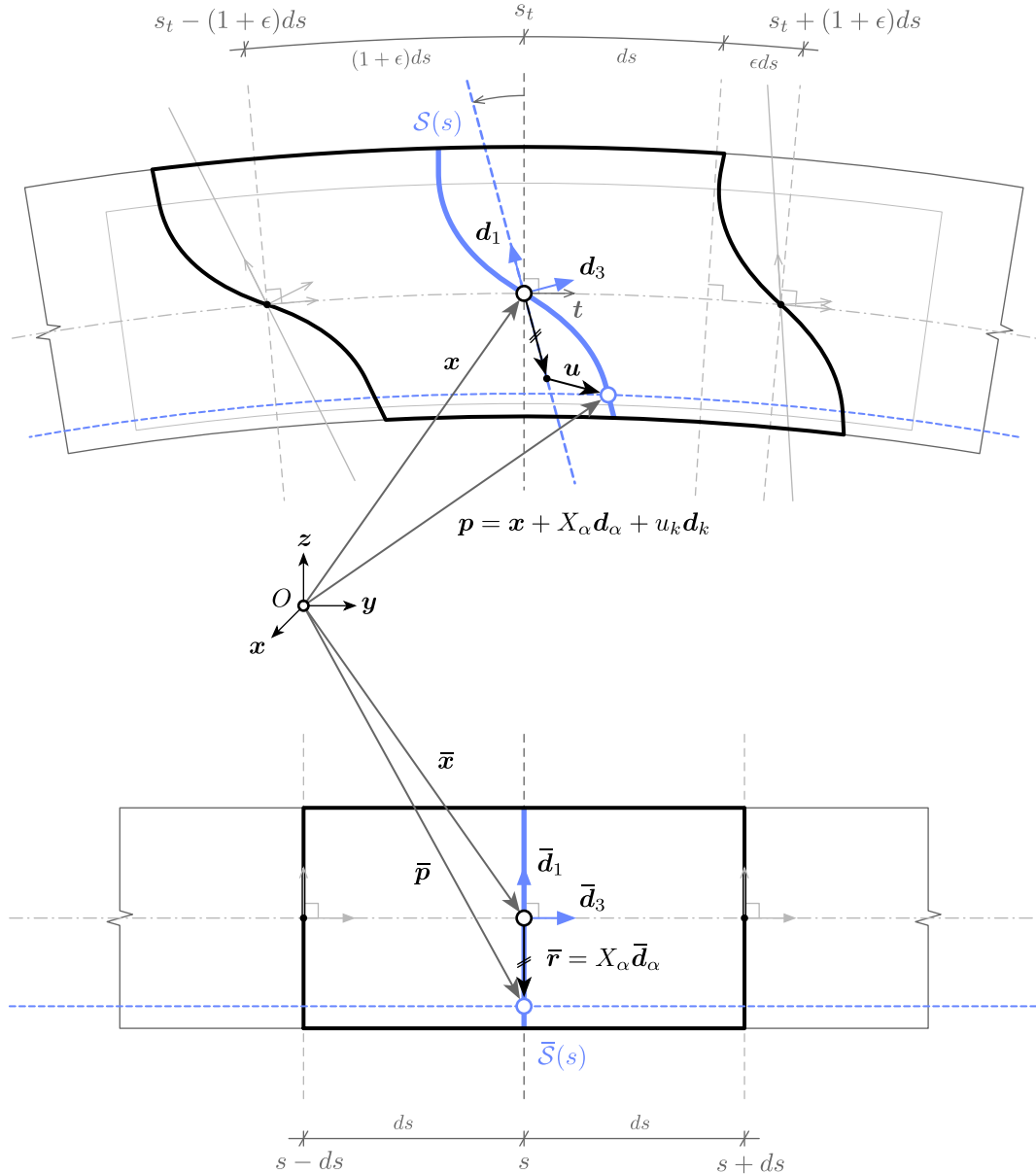


Figure 6.1 – Description of the motion for a Cosserat rod. This is a typical longitudinal section of a rectangular beam deformed from a reference configuration (bottom) to an actual configuration (top) at time t . Cross-sections are defined in the reference configuration to be planar surfaces perpendicular to the beam axis (\bar{S}). A material point $\bar{p} \in \bar{S}(s)$ is located relatively to the cross-section centroid ($\bar{x}(s)$) thanks to its material coordinates (X_1, X_2, s) . During the motion, this material point reaches a new position $p \in S(s)$. The deformed cross-section $S(s)$ is no more planar. The material frame is no more aligned with the beam axis (d_3 and t are not parallel any more). The actual position is measured from the centroid of the deformed cross-section ($x(s)$) plus an in-plane component $(X_\alpha d_\alpha)$ and a deformation vector (u). If the cross-sections deform in a rigid-body manner, then u is null everywhere.

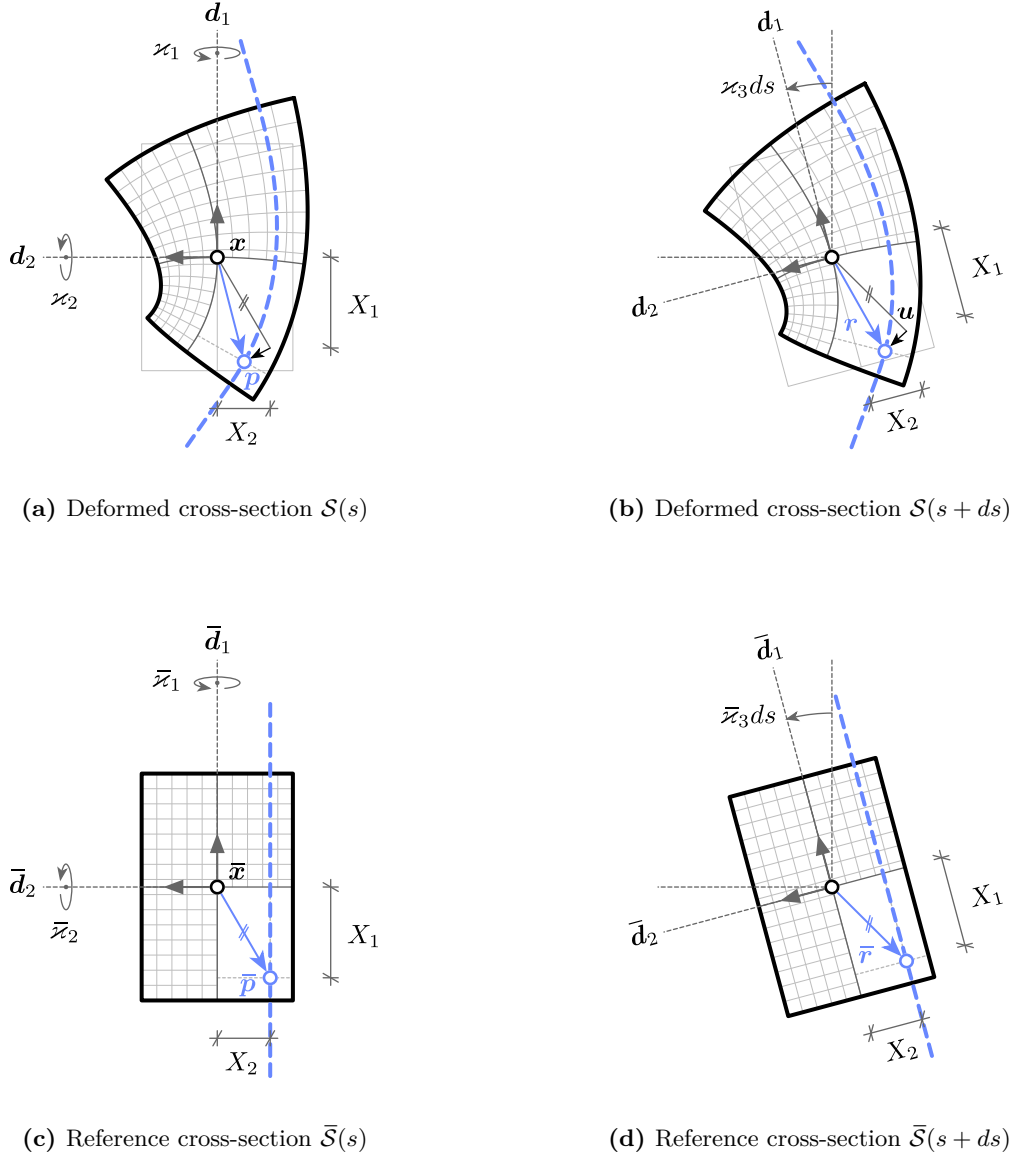


Figure 6.2 – Description of the motion for a Cosserat rod. These are the transverse sections from fig. 6.1 (however note that fig. 6.1 is drawn with $\varkappa_2 < 0$ while $\varkappa_2 > 0$ in fig. 6.2). The section curve is drawn in a dashed blue fashion. Remark how the deformed material point is located through \mathbf{x} and $\mathbf{r} = X_\alpha \mathbf{d}_\alpha + u_k \mathbf{d}_k$. Cross-sections are rotating around \mathbf{d}_3 at speed \varkappa_3 . The beam is subjected to flexion ($\varkappa_1 > 0$, $\varkappa_2 > 0$), torsion ($\varkappa_3 > 0$) and extension ($\epsilon > 0$). Fibers that are compressed – both directly by axial compression or indirectly by flexion – are subjected to transverse expansion due to the Poisson effect (see up-right of figures 6.2a and 6.2b). Reciprocally, fibers in tension – both directly by axial tension or indirectly by flexion – are subjected to transverse contraction (see bottom-left of figures 6.2a and 6.2b).

by L_t so that $s_t \in [0, L_t]$.

Finally, a material point \mathbf{p} of the body is located relatively to the centerline with the help of the local position vector \mathbf{r} such that (see figures 6.2a and 6.2b) :

$$\mathbf{p}(\bar{\mathbf{r}}, t) = \bar{\mathbf{x}}(s, t) + \bar{\mathbf{r}}(\bar{\mathbf{x}}(s, t), \bar{\mathbf{d}}_1(s, t), \bar{\mathbf{d}}_2(s, t), \bar{\mathbf{r}}, t) \quad (6.4)$$

Note that in the above expression a material point is uniquely identified – in a very generic manner – by its local position in the reference configuration ($\bar{\mathbf{r}} = \bar{\mathbf{p}} - \bar{\mathbf{x}}$).

Reference configuration

We now identify a *reference* configuration of the rod $\{\bar{\mathbf{x}}, \bar{\mathbf{d}}_1, \bar{\mathbf{d}}_2\}$ with centerline $\bar{\gamma} \in \mathcal{C}^1([0, L] \times \mathbb{R}^3)$, a regular space curve. This time, s is the arc length parameter of $\bar{\gamma}$, which leads to the important relation between $\bar{\mathbf{x}}$ and the unit tangent vector $\bar{\mathbf{t}}$ of $\bar{\gamma}$:

$$\frac{d\bar{\mathbf{x}}}{ds} = \bar{\mathbf{t}} \quad , \quad \|\bar{\mathbf{t}}\| = 1 \quad (6.5)$$

In this configuration, we define a cross-section $\mathcal{S}(s)$ as the set of material points lying in the plane perpendicular to the centerline $\bar{\gamma}$ at position $\bar{\mathbf{x}}(s)$. By definition, it is a planar surface in the reference configuration. However this surface will not necessarily remain planar in any other configuration. Moreover, and only for this configuration, it makes sense to choose the centerline as the curve passing through the cross-section centroids.

Finally, we call *material coordinates* of point $\bar{\mathbf{p}} \in \mathcal{S}(s)$ the triple $(X_3 = s, X_1, X_2)$ such that (see figures 6.2c and 6.2d) :

$$\bar{\mathbf{p}}(\bar{\mathbf{r}}) = \bar{\mathbf{x}}(s) + \bar{\mathbf{r}}(\bar{\mathbf{x}}(s), \bar{\mathbf{d}}_1(s), \bar{\mathbf{d}}_2(s), X_1, X_2) \quad (6.6a)$$

$$\bar{\mathbf{r}}(s, X_1, X_2) = X_1 \bar{\mathbf{d}}_1(s) + X_2 \bar{\mathbf{d}}_2(s) \quad (6.6b)$$

We also identify a *fiber* as the set of material points that share the same cross-section coordinates (X_1, X_2) all along the rod in the reference configuration.

Clarification about the notations

Remark that we sometimes decorate the reference configuration (with an overbar) and we sometimes decorate the actual configuration (with the subscript t). Although this could seem confusing to the reader, this is meant to produce the lighter notation possible to enhance readability.

- Thereafter, the equations will be written with respect to the arc length of the reference configuration. Hence, it was found preferable that s refers to the arc length of the reference configuration and that s_t refers to the arc length of the actual configuration.
- As a consequence of the previous item, it was found more logical that L refers to the length of the rod in the reference configuration and that L_t refers to the length of

the rod in the actual configuration.

- (X_3, X_1, X_2) refers to the same point in all configurations. Hence, there is no need to distinguish the actual configuration from the reference configuration and we drop the overbar symbol for these quantities.
- $\mathcal{S}(s)$ refers to the same set of points in all configurations. Hence, there is no need to distinguish the actual configuration from the reference configuration and we drop the overbar symbol for this quantity.

6.2.2 Time evolution

The evolution in time of the rod is simply given by the velocity of its centerline ($\dot{\mathbf{x}}$) and the *angular velocity vector* or *spin vector* ($\boldsymbol{\omega}$) of its material directors :

$$\frac{\partial \mathbf{x}}{\partial t}(s, t) = \dot{\mathbf{x}} \quad (6.7a)$$

$$\frac{\partial \mathbf{d}_k}{\partial t}(s, t) = \dot{\mathbf{d}}_k = \boldsymbol{\omega}(s, t) \times \mathbf{d}_k(s, t) \quad (6.7b)$$

From now on, the derivative with respect to time is denoted with an overdot symbol.

6.2.3 Force and moment strains

To compare rod's configurations we introduce the *force strain vector* ($\boldsymbol{\eta}$) and the *moment strain vector* ($\boldsymbol{\varkappa}$) :

$$\frac{\partial \mathbf{x}}{\partial s}(s, t) = \mathbf{x}' = \boldsymbol{\eta}(s, t) \quad (6.8a)$$

$$\frac{\partial \mathbf{d}_k}{\partial s}(s, t) = \mathbf{d}'_k = \boldsymbol{\varkappa}(s, t) \times \mathbf{d}_k(s, t) \quad (6.8b)$$

where the derivative with respect to s is denoted with a prime symbol.

The components of $\boldsymbol{\eta} = \eta_k \mathbf{d}_k$ and $\boldsymbol{\varkappa} = \varkappa_k \mathbf{d}_k$ expressed in the material frame basis $\{\mathbf{d}_3, \mathbf{d}_1, \mathbf{d}_2\}$ can be interpreted as the classical engineering strains that lead to the engineering stresses.^{6,7} In particular $\eta_3 = \mathbf{x}' \cdot (\mathbf{d}_1 \times \mathbf{d}_2)$ characterizes the change in volume of the body while η_1 and η_2 characterize the shear deformations ; \varkappa_3 is the material twist of the rod while \varkappa_1 and \varkappa_2 are the material curvatures of the rod.⁸

Observe the symmetry of eq. (6.7a) and (6.7b) and eq. (6.8a) and (6.8b) regarding the parameters s and t : $(\dot{\mathbf{x}}, \boldsymbol{\omega})$ governs the time evolution of the material frame while $(\mathbf{x}', \boldsymbol{\varkappa})$ governs the spatial evolution of the material frame along the centerline.

⁶For a complete interpretation, see [112, p. 285] or [110, ch. 3].

⁷Einstein's notation is employed here. For instance : $\boldsymbol{\eta} = \eta_k \mathbf{d}_k = \eta_3 \mathbf{d}_3 + \eta_1 \mathbf{d}_1 + \eta_2 \mathbf{d}_2$.

⁸Here, the term "material" is necessary as the material curvatures don't coincide with the geometric curvatures, although they are related one to each other. Precisely, the distinction originates in the fact that s is not a unit-speed parametrization of the centerline in the actual configuration.

Clarification about the notations

Here we have chosen to follow the denomination introduced by Reissner in [113]. This denomination is closed to the one employed by Antman in [112, p. 284] where the components of $\boldsymbol{\eta}$ are called the *strains* (aka the force strains) and the components of $\boldsymbol{\varkappa}$ are called the strain rates (aka the moment strains).⁹

It is true that $\boldsymbol{\eta}$ and $\boldsymbol{\varkappa}$ expressed the geometric configuration of the rod with respect to the arc length of the reference configuration. This description is invariant under rigid body motions. Indeed, with $\boldsymbol{\eta}$ and $\boldsymbol{\varkappa}$ given, one can rebuilt the geometry of the rod by solving the differential system of equations formed by eq. (6.8a) and (6.8b). However it seems a little improper to call them *strain* as this denomination is usually reserved to the components of the strain tensor which measure by how much a solid departs from its natural configuration and are dimensionless entries.

Material versus geometric curvature

It is worth to bring some lights in the notion of material versus geometric curvature.

6.2.4 Parametrization of the centerline

Recall that because the centerline of the reference configuration is parametrized by arc length, the unit tangent vector in this configuration is given by :

$$\bar{\mathbf{t}}(s) = \frac{d\bar{\mathbf{x}}}{ds}(\bar{s}) = \bar{\mathbf{x}}'(s) \quad , \quad \|\bar{\mathbf{x}}'\| = 1 \quad (6.9)$$

In the deformed configuration, the centerline is still parametrized by s which is no more an arc length parameter because the centerline has suffered stretch. Thus, the unit tangent vector in this configuration is given by :¹⁰

$$\mathbf{t}(s, t) = \frac{\mathbf{x}'(s, t)}{\|\mathbf{x}'(s, t)\|} \quad , \quad \|\mathbf{x}'\| = \|\boldsymbol{\eta}'\| \neq 1 \quad (6.10)$$

We introduce ϵ , the extension of the rod which characterizes the local change in length of the rod centerline, defined as :

$$\|\boldsymbol{\eta}'(s, t)\| = \frac{\partial s_t}{\partial s}(s, t) = \Psi'(s, t) = 1 + \epsilon(s, t) \quad (6.11)$$

⁹For an extensible rod, the derivative with respect to s and s_t are not equivalent. The prime notation stands only for the derivation with respect to s , the arc length parameter of the rod in the reference configuration.

¹⁰However, because s_t is an arc length parameter of γ_t : $\mathbf{t}(s, t) = \frac{\partial \mathbf{x}}{\partial s_t}(s, t)$.

Inextensibility

The rod is said to be inextensible if $\epsilon = 0$ everywhere and at all time. In this case, s is a valid arc length parameter for the centerline in every configurations. Later, we will restrict to the case of rods subjected to small extension, that is $\epsilon(t, s) \ll 1$.

Reparametrization

Although either s and s_t can be chosen as the third material coordinate to describe a rod, the definition of the material strains are given with respect to s and not s_t . This is a matter of concern as the constitutive relations – classically of the form $M = EI\kappa$, $N = ES\epsilon$, $Q = GJ\tau$ – relies upon material strains. Thus, in these equations, what takes place is a derivation with respect to s and not to s_t , which matters if the rod is not required to be inextensible.

6.2.5 To go further

The reader is invited to refer to [112] to get a deeper understanding of the *Cosserat theory for rods*, in particular to see how the governing equations are derived. Here, only the geometric description of a Cosserat rod has been presented in a very generic but still concise manner. This description will be used in the next sections in the narrower scope of the (first order) *Kirchhoff theory for rods* but could be usefully employed for richer theories.

	reference configuration	actual configuration
arc length	$s = \Psi_t^{-1}(s_t)$	$s_t = \Psi_t(s)$
length	L	L_t
centerline	$\bar{\gamma}$	γ_t
position vector	\bar{x}	x
material frame	$\{\bar{d}_3, \bar{d}_1, \bar{d}_2\}$	$\{d_3, d_1, d_2\}$
material coordinates	(s, X_1, X_2)	(s, X_1, X_2)
force strains	$\bar{\eta}$	η
moment strains	$\bar{\kappa}$	κ
spin vector	$\bar{\omega}$	ω
axial extension	$\bar{\epsilon} = 0$	$\ \eta\ = \Psi'_t(s) = 1 + \epsilon$
arc length derivative	$\frac{\partial}{\partial s} \cdot = (\cdot)'$	$\frac{\partial}{\partial s_t} \cdot = (1 + \epsilon)^{-1}(\cdot)'$
time derivative	$\frac{\partial}{\partial t} \cdot = (\dot{\cdot})$	$\frac{\partial}{\partial t} \cdot = (\dot{\cdot})$

Table 6.1 – Summary of the notations employed throughout this section.

6.3 Kirchhoff theory of rods

In this section we recall the principles of Kirchhoff theory of rods and we treat its geometrical description with the framework presented in §6.2 from Cosserat's theory.¹¹ Kirchhoff's theory accounts for finite displacements but small strains, which means that only geometric nonlinearities can be modeled. We will show in §6.3.10 that in the framework of 3D elasticity it is precisely the assumption of small strains that leads to the well-known material constitutive laws.

Our goal is to present a clean theory that leads to the dynamical equations of Kirchhoff. These equations will then be discretized in the next chapter to build a discrete element suitable for the computation of elastic gridshells.

As reported by Dill, in the literature most of the assumptions presented as the Kirchhoff assumptions were in fact not made by Kirchhoff, Clebsch nor Love. Actually a *Kirchhoff-Love* rod is a rod in which the deformed configuration differs only by *small deformations* from a configuration that satisfies the *Euler-Bernoulli* assumptions, that is : cross-sections are plane, undeformed and perpendicular to the beam centerline.^{12,13}

Hence, a Kirchhoff rod does not presuppose that the centerline is inextensible – but that the extension is small – nor that cross-sections remain plane – but that their warping deformation is small. These hypothesis, if strictly respected in the model, would not lead to the right expression of the torsion constant or the correct expression of the material curvatures.

But to what extent these deformations are considered small ? The answer is that Kirchhoff's theory is a complete *first order* theory in the parameter α :

$$\alpha = \sup_{s \in [0, L]} \{h/L, \epsilon, h\|\boldsymbol{\kappa}\|, h\|\bar{\boldsymbol{\kappa}}\|\} \quad (6.12)$$

where L is the rod length, h is the characteristic width of the cross-section, ϵ is the axial extension, $\boldsymbol{\kappa}$ and $\bar{\boldsymbol{\kappa}}$ are the vectors of material curvatures respectively in the deformed and unstressed configurations [111, 128].

¹¹“The classical elastic rod theory of Kirchhoff (1859), called the kinetic analogue, is a special case of our rod theory [...]” [112, p. 238].

¹²“Kirchhoff's theory can only apply to that class of problems for three dimensional bodies such that the loads on the sides are relatively small and slowly varying. The dominate mode of deformation must be a global bending and twisting with small axial extension. If there are substantial local variations in curvatures or substantial transverse shears, his theory of bending of rods will not provide a satisfactory first approximation.” [111, p. 18]

¹³“We discuss here the dynamical equations of a theory of elastic rods that is due to Kirchhoff and Clebsch. This properly invariant theory is applicable to motions in which the strains relative to an undistorted configuration remain small, although rotations may be large. It is constructed to be a first-order theory, i.e., a theory that is complete to within an error of order two in an appropriate dimensionless measure of thickness, curvature, twist, and extension.” [128, p. 1]

Summary of the assumptions

- The rod is slender.
- The strains are small although the displacements might be large.
- The shear strains are negligible.
- The cross-section is free to warp.
- The shear-center and the centroid of the cross-section are at the same location.
- The material and cross-section properties vary slowly along the rod.

6.3.1 Description of the motion

To describe the motion of a Kirchhoff rod, we use the framework presented in §6.2.1 for Cosserat rods.¹⁴ However, we restrict its scope by requiring that transverse shear strains are negligible quantities, which is one of the fundamental assumptions made by Kirchhoff in his theory :

$$\eta_1 \simeq 0 \tag{6.13a}$$

$$\eta_2 \simeq 0 \tag{6.13b}$$

As a consequence, the material frame remains adapted to the centerline. The rod is not supposed to be strictly inextensible. However, as strains are assumed to be small, the axial strain is supposed to be small itself ($\epsilon \ll 1$), which translates to :

$$\eta_3(s, t) = 1 + \epsilon(s, t) \tag{6.14a}$$

$$\mathbf{d}_3(s, t) = \mathbf{t}(s, t) \tag{6.14b}$$

$$\mathbf{x}'(s, t) = (1 + \epsilon)\mathbf{t}(s, t) \tag{6.14c}$$

Stress-free configuration

We now consider a *stress-free* configuration of the rod as the *reference* configuration.¹⁵ The rod is described by its centerline $\bar{\gamma}$ and its material frame $\{\bar{\mathbf{d}}_3, \bar{\mathbf{d}}_1, \bar{\mathbf{d}}_2\}$. Again, a planar cross-section is defined as the set of material points lying in the plane perpendicular to $\bar{\gamma}$ and passing through $\bar{\mathbf{x}}(s)$. The material directors $\bar{\mathbf{d}}_1$ and $\bar{\mathbf{d}}_2$ are now chosen to be aligned with the principal axes of inertia of the cross-section.¹⁶ Thus, $\bar{\mathbf{d}}_3 = \bar{\mathbf{d}}_1 \times \bar{\mathbf{d}}_2$ is normal to the plane of the cross-section and adapted to the centerline ($\bar{\mathbf{d}}_3 = \bar{\mathbf{t}}$). Moreover, the centerline

¹⁴We use the notation employed by Antman in his *special Cosserat theory of rods* : “The motion of a special Cosserat rod is defined by three vector-valued functions : $[s_1, s_2] \times \mathbb{R} \ni (s, t) \mapsto \mathbf{r}(s, t), \mathbf{d}_1(s, t), \mathbf{d}_2(s, t) \in \mathbb{E}^3$ ” [112, p. 270]. However, somme specific assumptions will be made over the directors in the context of Kirchhoff’s theory.

¹⁵See [110, p. 20] for precisions when such a configuration may not exist.

¹⁶In case of an axisymmetric section, any pair of perpendicular unit vectors lying in the cross-section plane will be valid.

is chosen to be the curve passing through the cross-section centroids and is required to be at least a regular space curve, which means that its tangent is continuously defined.

For a sufficiently slender rod, the position of material point $\bar{\mathbf{p}}$ that belongs to cross-section $\mathcal{S}(s)$ (see figures 6.1, 6.2a and 6.2b) is expressed through its material coordinates (s, X_1, X_2) as :¹⁷

$$\bar{\mathbf{p}}(s, X_1, X_2) = \bar{\mathbf{x}}(s) + \bar{\mathbf{r}}(s, X_1, X_2) \quad (6.15a)$$

$$\bar{\mathbf{r}}(s, X_1, X_2) = X_1 \bar{\mathbf{d}}_1(s) + X_2 \bar{\mathbf{d}}_2(s) \quad (6.15b)$$

Consequently, for each s in the reference configuration, (X_1, X_2) is a cartesian coordinate system for the plane $\mathcal{S}(s)$. In this system the local coordinates of the cross-section centroid are $(0, 0)$.

Finally, the cross-section is assumed to be bounded and the planar boundary curve is defined by the implicit equation : $f_s(X_1, X_2) = 0$. It is also required that the shear center and the centroid of the cross-section are at the same location, otherwise one would require a more complex kinematic description of the rod.¹⁸

Deformed configuration

We now examine the motion of a Krichhoff rod and we call *deformed* configuration its actual configuration at time t . In this configuration the rod undergoes internal stresses under body loads, external loads and constrains.

The deformed configuration of the rod at time t is described by its centerline γ_t , its material frame $\{\mathbf{d}_3, \mathbf{d}_1, \mathbf{d}_2\}$ and a local displacement field \mathbf{u} . The centerline of the rod is deformed into the space curve γ_t with position vector \mathbf{x} :

$$\begin{aligned} \gamma_t : [0, L] &\longrightarrow \mathbb{R}^3 \\ s &\longmapsto \mathbf{x}(s, t) \end{aligned} \quad (6.16)$$

A material point $\bar{\mathbf{p}}$ in the *reference* configuration is transported to position \mathbf{p} in the *actual* configuration so that (see figures 6.1, 6.2c and 6.2d) :

$$\mathbf{p}(s, X_1, X_2, t) = \mathbf{x}(s, t) + \mathbf{r}(s, X_1, X_2, t) \quad (6.17a)$$

$$\mathbf{r}(s, X_1, X_2, t) = X_1 \mathbf{d}_1(s, t) + X_2 \mathbf{d}_2(s, t) + \mathbf{u}(s, X_1, X_2, t) \quad (6.17b)$$

$$\mathbf{u}(s, X_1, X_2, t) = u_k(s, X_1, X_2, t) \mathbf{d}_k(s, t) \quad (6.17c)$$

Although the cross-section $\mathcal{S}(s)$ is a planar surface in the reference configuration, it deforms to a non-planar surface in the actual configuration since $\mathbf{u} \neq \mathbf{0}$.¹⁹ The components

¹⁷The lateral dimension of the rod must be smaller than its radius of curvature. Otherwise, this description would lead to self intersecting cross-sections.

¹⁸Some details are given in the conclusion.

¹⁹ $\mathcal{S}(s)$ refers to the same set of material points in any configurations. Sometimes a distinction is made between $\bar{\mathcal{S}}(s)$ and $\mathcal{S}(s)$ to highlight that the planarity of cross-sections is lost during the motion.

$(u_1, u_2, u_3)^T$ of the local displacement field expressed in the material frame basis are required to be small in Kirchhoff's theory of rods.²⁰ In practice, as explained by [111] this means that the considered motions must satisfy :

$$\frac{u_k}{h} = O(\alpha) \quad , \quad \frac{\partial u_k}{\partial X_1} = O(\alpha) \quad , \quad \frac{\partial u_k}{\partial X_2} = O(\alpha) \quad , \quad \frac{\partial u_k}{\partial s} = O(\alpha^2) \quad (6.18)$$

In this theory, the material frame in the reference configuration deforms in a rigid-body manner so that it remains orthonormal and aligned to the principal axes of the cross-section – within an error $O(\alpha^2)$.²¹ Remark that this is different than assuming that cross-sections deform in a rigid-body manner, which is known as the *Euler-Bernoulli* hypothesis and is equivalent to the special case $\mathbf{u} = \mathbf{0}$.

6.3.2 Reparametrization

This subsection highlights the role played by the change in length of the rod during its motion. It was found that this aspect is often treated partially or with confusion in the literature, although it is of prime importance to understand correctly the influence of axial stretch in the computation of moment strains. Indeed, for an inextensible rod, the notions of geometric curvature and (flexural) material curvatures are somehow the same notions. But this is not the case for extensible rods as explained in §6.3.3.

The rod is parametrized by s , the arc length parameter of the *reference* configuration, as the constitutive laws will be expressed relatively to this configuration. But recall once again that s is no more the arc length parameter of the *deformed* centerline as the rod may have suffered axial extension.²² Kirchhoff's theory assumes that the material frame remains adapted to the centerline during deformation, or equivalently that transverse shear strains are neglected.²³ The extension of the centerline is characterized by ϵ defined such that :

$$\bar{\mathbf{x}}' = \bar{\mathbf{d}}_3 \quad (6.19a)$$

$$\mathbf{x}' = (1 + \epsilon) \mathbf{d}_3 \quad (6.19b)$$

However, one can parametrize the deformed centerline by its own arc length parameter, denoted s_t . Let's call L_t the length of the deformed centerline and Ψ_t the \mathcal{C}^1 diffeomorphism that maps s onto s_t ($s_t = \Psi_t(s) \Leftrightarrow s = \Psi_t^{-1}(s_t)$). Thus, the centerline is equivalently

²⁰Note that this hypothesis is the one made by Kirchhoff and does not correspond to the well-known *Euler-Bernoulli* or *Navier-Bernoulli* assumption where the sections remain planar, undeformed and normal to the centerline during the rod deformation. In particular, torsion is responsible for the warping of cross-sections – that is cross-sections don't remain planar during the motion – and leads to a distinct value of the twist modulus. This is clearly stipulated in [111, 110] but is often treated with confusion in the literature.

²¹“[...] upon deformation, the principal axes of $\mathcal{S}(s)$ do remain normal to each other and to the rod axis, at least to within the approximations of the present theory, i.e., to within an error $O(\alpha^2)$.” [128, p. 344].

²²In Kirchhoff's theory, rods are not supposed to be strictly inextensible but extension has to remain small. Thus, the internal axial force is given by a constitutive law and not considered as a geometric constraint. However, some authors have remarked that it might be convenient and reasonable to solve the equations of motion considering the geometric constraint $\epsilon = 0$. See [110, p. 98] for a detailed discussion of the subject.

²³This is also known as the “unsharable” assumption. Indeed, if $\frac{\partial \mathbf{x}}{\partial s} = \eta_k \mathbf{d}_k = (1 + \epsilon) \mathbf{d}_3 \Leftrightarrow \eta_1 = \eta_2 = 0$.

described by :

$$\begin{aligned}\gamma_t : [0, L_t] &\longrightarrow \mathbb{R}^3 \\ s_t &\longmapsto \mathbf{x}(s_t)\end{aligned}\tag{6.20}$$

Because s_t is the arc length parameter of γ_t the following relations hold :

$$\frac{\partial \mathbf{x}}{\partial s_t} = \mathbf{d}_3 \tag{6.21a}$$

$$\frac{\partial s_t}{\partial s} = \eta_3 = 1 + \epsilon \tag{6.21b}$$

Consequently, one can deduced that the derivation with respect to s is proportional to the derivation with respect to s_t by a factor $1 + \epsilon$. This factor has to be taken into account when computing the material curvatures, which are no more equivalents to their geometric counterparts in the deformed configuration. This is detailed in the next section dedicated to the force and moment strain vectors.

6.3.3 Force and moment strains

This section, introduces the material force and moment strains vectors of a Kirchhoff rod. It shows how they are related – yet distinct if $\epsilon \neq 0$ – to the geometric curvature of the centerline.

Reference configuration

Since the material frame is orthonormal and adapted to the centerline, its evolution along the undeformed centerline is described thanks to the *reference material curvature vector* $\bar{\boldsymbol{\kappa}}$ defined as :

$$\bar{\mathbf{d}}'_i = \bar{\boldsymbol{\kappa}} \times \bar{\mathbf{d}}_i \tag{6.22}$$

In the reference configuration, because s is the centerline's arc length parameter, the strains vector components expressed in the material frame basis take the form : ²⁴

$$\bar{\kappa}_3 = \bar{\mathbf{d}}'_1 \cdot \bar{\mathbf{d}}_2 = \bar{\tau} = \bar{\mathbf{d}}'_1 \cdot \bar{\mathbf{d}}_2 \tag{6.23a}$$

$$\bar{\kappa}_1 = \bar{\mathbf{d}}'_3 \cdot \bar{\mathbf{d}}_2 = \bar{k}_1 = \bar{\boldsymbol{\kappa}} \bar{\mathbf{b}} \cdot \bar{\mathbf{d}}_1 \tag{6.23b}$$

$$\bar{\kappa}_2 = \bar{\mathbf{d}}'_1 \cdot \bar{\mathbf{d}}_3 = \bar{k}_2 = \bar{\boldsymbol{\kappa}} \bar{\mathbf{b}} \cdot \bar{\mathbf{d}}_2 \tag{6.23c}$$

where $\bar{\boldsymbol{\kappa}} \bar{\mathbf{b}}$ (see eq. (4.21)) is the curvature binormal vector of $\bar{\gamma}$:

$$\bar{\boldsymbol{\kappa}} \bar{\mathbf{b}} = \bar{\mathbf{t}} \times \frac{\partial \bar{\mathbf{t}}}{\partial s} = \bar{\mathbf{t}} \times \bar{\mathbf{t}} \tag{6.24}$$

²⁴Recall the following result for an adapted frame : eq. (4.38).

$\bar{\kappa}_1$ and $\bar{\kappa}_2$ are called the reference *material* curvatures. $\bar{\kappa}_3$ is called the reference *material* twist. In this configuration, $\bar{\kappa}_1$ and $\bar{\kappa}_2$ are simply computed as the projection of the curvature binormal vector along \bar{d}_1 and \bar{d}_2 .

Note the important distinction between the reference material twist ($\bar{\tau}$) and the torsion of Frenet (τ_f) of the centerline, as defined in §4.5.5.

Deformed configuration

Since the material frame is orthonormal and adapted to the centerline, its evolution along the *deformed* centerline is described thanks to the *actual* moment strain vector $\boldsymbol{\varkappa}$ defined as :

$$\frac{\partial \mathbf{d}_k}{\partial s} = \mathbf{d}'_k = \boldsymbol{\varkappa} \times \mathbf{d}_k \quad (6.25)$$

Note that the strains vector is defined relatively to the arc length s of the *reference* configuration and not the arc length s_t of the *actual* configuration. Thus the strains vector components expressed in the material frame basis are given by :

$$\varkappa_1 = \mathbf{d}'_3 \cdot \mathbf{d}_2 = (1 + \epsilon) k_1 = (1 + \epsilon) \boldsymbol{\kappa} \mathbf{b} \cdot \mathbf{d}_1 \quad (6.26a)$$

$$\varkappa_2 = \mathbf{d}'_1 \cdot \mathbf{d}_3 = (1 + \epsilon) k_2 = (1 + \epsilon) \boldsymbol{\kappa} \mathbf{b} \cdot \mathbf{d}_2 \quad (6.26b)$$

$$\varkappa_3 = \mathbf{d}'_1 \cdot \mathbf{d}_2 = (1 + \epsilon) \tau = (1 + \epsilon) \frac{\partial \mathbf{d}_1}{\partial s_t} \cdot \mathbf{d}_2 \quad (6.26c)$$

where $\boldsymbol{\kappa} \mathbf{b}$ (see eq. (4.21)) is the curvature binormal vector of γ_t given by :

$$\boldsymbol{\kappa} \mathbf{b} = \mathbf{t} \times \frac{\partial \mathbf{t}}{\partial s_t} = (1 + \epsilon) \mathbf{t} \times \mathbf{t}' \quad (6.27)$$

\varkappa_1 and \varkappa_2 are called the *material* curvatures. \varkappa_3 is called the *material* twist. Note this time the dependence of the material moment strains ($\varkappa_3, \varkappa_1, \varkappa_2$) regarding the extension of the rod. These are the strains employed in the classical constitutive laws that lead to the determination of the internal axial force ($N = E S \epsilon$), internal bending moments ($M_1 = EI_1(\varkappa_1 - \bar{\kappa}_1)$, $M_2 = EI_2(\varkappa_2 - \bar{\kappa}_2)$) and internal twisting moment ($Q = GJ((\varkappa_3 - \bar{\kappa}_3))$).

Often in the literature the flexural material curvatures are computed as the projection of the curvature binormal vector onto the first two material axes. Here it is demonstrated that this is not exact as it omits the contribution of the rod extension, although it could be a reasonable approximation when $\epsilon \ll 1$.

6.3.4 Balance of momentum

Let \mathcal{P} be the first *Piola-Kirchhoff* stress tensor. \mathcal{P} expresses how contact forces are acting in a *deformed* body, referring to its (known) *reference* configuration. Let $dS = n dS$ be an elementary oriented surface of the rod in the *reference* configuration, of centroid

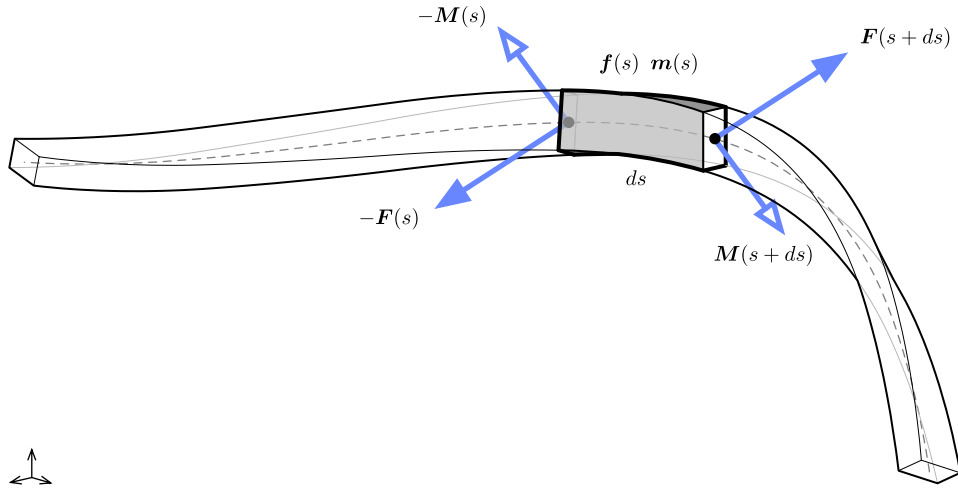


Figure 6.3 – Internal forces (\mathbf{F}) and moments (\mathbf{M}) acting on an infinitesimal beam slice of length ds . The beam is also subject to distributed external forces (\mathbf{f}) and moments (\mathbf{m}). By convention, internal forces and moments are forces and moments applied by the right part to the left part of the beam.

$\mathbf{p}(s, X_1, X_2, t) \in \mathcal{S}(s)$.²⁵ The contact forces exerted on dS are given by :

$$d\mathbf{F}(s, X_1, X_2, t) = \boldsymbol{\sigma}_n(s, X_1, X_2, t) dS \quad (6.28a)$$

$$\boldsymbol{\sigma}_n(s, X_1, X_2, t) = \mathbf{P}(s, X_1, X_2, t) \cdot \mathbf{n} \quad (6.28b)$$

The *Piola stress vector* ($\boldsymbol{\sigma}_n$) introduced in eq. (6.28b) expresses the contact forces exerted on the body per unit area of the *reference configuration*.²⁶

The generic laws for the balance of linear and angular momentums are obtained by summation over the reference configuration, where \mathbf{b} are the body forces per unit volume of the *reference configuration* :

$$\iiint_{\mathcal{V}} \rho \ddot{\mathbf{p}} dV = \iint_{\partial\mathcal{V}} \boldsymbol{\sigma}_n dS + \iiint_{\mathcal{V}} \rho \mathbf{b} dV \quad (6.29a)$$

$$\iiint_{\mathcal{V}} \rho (\mathbf{p} \times \ddot{\mathbf{p}}) dV = \iint_{\partial\mathcal{V}} \mathbf{p} \times \boldsymbol{\sigma}_n dS + \iiint_{\mathcal{V}} \rho (\mathbf{p} \times \mathbf{b}) dV \quad (6.29b)$$

Here, and subsequently, \mathcal{V} denotes the volume of a slice of the rod in the *reference configuration*, encompassed between two cross-sections ($\mathcal{S}_1 = \mathcal{S}(s_1)$, $\mathcal{S}_2 = \mathcal{S}(s_2)$, $s_1 < s_2$). We also denote \mathcal{L}_{12} the lateral surface of the rod in the *reference configuration* so that the exterior surface of the volume is : $\partial\mathcal{V} = \mathcal{S}_1 \cup \mathcal{L}_{12} \cup \mathcal{S}_2$.

The cross-section $\mathcal{S}(s)$ splits the rod in two parts. Hereafter, the downstream part of the rod over $[s, L]$ will be called the “right part”. Reciprocally, the upstream part of the rod over $[0, s]$ will be called the “left part”.

²⁵ dS is the area and \mathbf{n} is the unit normal of the elementary oriented surface dS .

²⁶For a detailed introduction to the Piola-Kirchhoff stress tensor, refer to [110, p. 52].

Internal forces and moments

At the cross-section $\mathcal{S}(s)$, the contact forces applied by the right part onto the left part of the rod yield the following resultant force \mathbf{F} and resultant moment \mathbf{M} about the centroid point $\mathbf{x}(s, t)$:

$$\mathbf{F}(s, t) = \iint_{\mathcal{S}(s)} \boldsymbol{\sigma}_n(s, X_1, X_2, t) dX_1 dX_2 \quad (6.30a)$$

$$\mathbf{M}(s, t) = \iint_{\mathcal{S}(s)} \mathbf{r}(s, X_1, X_2, t) \times \boldsymbol{\sigma}_n(s, X_1, X_2, t) dX_1 dX_2 \quad (6.30b)$$

\mathbf{F} and \mathbf{M} are commonly known as the *internal forces* and the *internal moments* of the rod.

External forces and moments

We assume that the resultant of the contact forces on \mathcal{L}_{12} and the body forces on \mathcal{V} reduce to the following forms :

$$\iint_{\mathcal{L}_{12}} \boldsymbol{\sigma}_n dS + \iiint_{\mathcal{V}} \rho \mathbf{b} dV = \int_{s_1}^{s_2} [\mathbf{f}_s + (1 + \epsilon) \mathbf{f}_{st}] ds \quad (6.31a)$$

$$\begin{aligned} \iint_{\mathcal{L}_{12}} \mathbf{p} \times \boldsymbol{\sigma}_n dS + \iiint_{\mathcal{V}} \rho (\mathbf{p} \times \mathbf{b}) dV &= \int_{s_1}^{s_2} [\mathbf{m}_s + (1 + \epsilon) \mathbf{m}_{st} \\ &\quad + \mathbf{x} \times (\mathbf{f}_s + (1 + \epsilon) \mathbf{f}_{st})] ds \end{aligned} \quad (6.31b)$$

where \mathbf{f}_s (resp. \mathbf{f}_{st}) is the distributed resultant force per unit length of the reference (resp. deformed) configuration ; and \mathbf{m}_s (resp. \mathbf{m}_{st}) is the distributed resultant moment per unit length of the reference (resp. deformed) configuration. For instance, these distributed forces and moments include external and body loads such as weight, snow, wind, ... ²⁷

Note that Kirchhoff's theory require that the stress components on the sides of the rod are small [111, p. 11] – that is $\boldsymbol{\sigma}_n \cdot \mathbf{n} = O(\alpha^2)$ over \mathcal{L}_{12} . Thus, the first two terms in the above expression will be neglected :

$$\iint_{\mathcal{L}_{12}} \boldsymbol{\sigma}_n dS \simeq 0 \quad (6.32a)$$

$$\iint_{\mathcal{L}_{12}} \mathbf{p} \times \boldsymbol{\sigma}_n dS \simeq 0 \quad (6.32b)$$

Although the continuous model does not account formally for punctual loads,²⁸ they will be introduced seamlessly in the discrete model as the dynamical equations for the motion

²⁷At this stage, although this is uncommon in the literature, it has been found convenient to mark the distinction between loads referring to the reference configuration and loads referring to the actual configuration. Indeed, various distributed loads depend on the actual length of an element such as pressure and wind loads. On the other hand, some loads are independent of the extension of the rod, such as its weight.

²⁸This is possible but would require more math. However, local effects of such loads would not be properly modeled in the theory of Kirchhoff (Saint-Venant's Principle).

of the rod will translate into rigid body equations for the discrete segments composing the rod.

Inertial forces

The inertial forces for a volume of the rod encompassed between cross-sections \mathcal{S}_1 and \mathcal{S}_2 are obtained by summation as :

$$\iiint_{\mathcal{V}} \rho \ddot{\mathbf{p}} \, dV = \iiint_{\mathcal{V}_t} \rho_t \ddot{\mathbf{p}} \, dV_t \quad (6.33a)$$

$$\iiint_{\mathcal{V}} \rho (\mathbf{p} \times \ddot{\mathbf{p}}) \, dV = \iiint_{\mathcal{V}_t} \rho_t (\mathbf{p} \times \ddot{\mathbf{p}}) \, dV_t \quad (6.33b)$$

Here, ρ (resp. ρ_t) is the mass density of the rod in the reference (resp. deformed) configuration. Expressions are given in both coordinate systems.²⁹

In the context of Kirchhoff's approximation, the local deformations (u_k) of the cross-sections can be neglected in the computation of the inertial forces [111, p. 16]. This yields :

$$\mathbf{p} \simeq \mathbf{x} + X_1 \mathbf{d}_1 + X_2 \mathbf{d}_2 \quad (6.34a)$$

$$\dot{\mathbf{p}} = \dot{\mathbf{x}} + \boldsymbol{\omega} \times (X_1 \mathbf{d}_1 + X_2 \mathbf{d}_2) \quad (6.34b)$$

$$\ddot{\mathbf{p}} = \ddot{\mathbf{x}} + \dot{\boldsymbol{\omega}} \times (X_1 \mathbf{d}_1 + X_2 \mathbf{d}_2) + \boldsymbol{\omega} \times (\boldsymbol{\omega} \times (X_1 \mathbf{d}_1 + X_2 \mathbf{d}_2)) \quad (6.34c)$$

Since X_1 and X_2 are the coordinates with respect to the centroid (\mathbf{x}) and the principal axes of the cross-section (\mathbf{d}_1 , \mathbf{d}_2), the cross-section area (S) and principal moments of inertia (I_1 , I_2) are given by :^{30,31}

$$0 = \iint_{\mathcal{S}(s)} (X_1 X_2) \, dX_1 dX_2 \quad (6.35a)$$

$$S = \iint_{\mathcal{S}(s)} dX_1 dX_2 \quad (6.35b)$$

$$I_1 = \iint_{\mathcal{S}(s)} X_2^2 \, dX_1 dX_2 \quad (6.35c)$$

$$I_2 = \iint_{\mathcal{S}(s)} X_1^2 \, dX_1 dX_2 \quad (6.35d)$$

$$I_p = \iint_{\mathcal{S}(s)} (X_1^2 + X_2^2) \, dX_1 dX_2 \quad (6.35e)$$

²⁹In [111] the change in volume and the conservation of mass is expressed through the determinants of the metric tensors of the reference and deformed configurations. Recall that this determinant is the square of the volume of the elementary cell defined by $\frac{\partial \bar{\mathbf{p}}}{\partial s}$, $\frac{\partial \bar{\mathbf{p}}}{\partial X_1}$, $\frac{\partial \bar{\mathbf{p}}}{\partial X_2}$ in the reference configuration, which is convected to the elementary cell defined by $\frac{\partial \mathbf{p}}{\partial s}$, $\frac{\partial \mathbf{p}}{\partial X_1}$, $\frac{\partial \mathbf{p}}{\partial X_2}$ in the deformed configuration.

³⁰This is exact in the reference configuration but only approximately true in the deformed configuration as the theory consider only small deformations of cross-sections.

³¹eq. (6.36a) is nothing but the definition of the centroid position. eq. (6.35a) holds because the tensor of inertia of the cross-section is diagonal in the basis $\{\mathbf{d}_3, \mathbf{d}_1, \mathbf{d}_2\}$ and thus $I_{12} = I_{21} = 0$.

Moreover, for a given cross-section the definition of the centroid yields :

$$\mathbf{0} = \iint_{\mathcal{S}(s)} (X_1 \mathbf{d}_1 + X_2 \mathbf{d}_2) dX_1 dX_2 \quad (6.36a)$$

$$0 = \iint_{\mathcal{S}(s)} X_1 dX_1 dX_2 \quad (6.36b)$$

$$0 = \iint_{\mathcal{S}(s)} X_2 dX_1 dX_2 \quad (6.36c)$$

For a thin slice of the rod ($\delta\mathcal{V}$) between cross-sections $\mathcal{S}(s)$ and $\mathcal{S}(s+ds)$, eq. (6.33a) and (6.33b) yield respectively :³²

$$\iiint_{\delta\mathcal{V}} \rho \ddot{\mathbf{p}} dV = (\rho S \ddot{\mathbf{x}}) ds \quad (6.37a)$$

$$\iiint_{\delta\mathcal{V}} \rho(\mathbf{p} \times \ddot{\mathbf{p}}) dV = \left(\rho S \ddot{\mathbf{x}} + \rho \iint_{\mathcal{S}(s)} \mathbf{r} \times \ddot{\mathbf{r}} dX_1 dX_2 \right) ds \quad (6.37b)$$

Finally, remark that :

$$\mathbf{r} \times \ddot{\mathbf{r}} = (X_1)^2 \mathbf{d}_1 \times \ddot{\mathbf{d}}_1 + (X_2)^2 \mathbf{d}_2 \times \ddot{\mathbf{d}}_2 + X_1 X_2 (\mathbf{d}_1 \times \ddot{\mathbf{d}}_2 + \mathbf{d}_2 \times \ddot{\mathbf{d}}_1) \quad (6.38)$$

Thus, reminding eq. (6.35) and (6.36), one can conclude that the inertial forces reduce to :

$$\iiint_{\delta\mathcal{V}} \rho \ddot{\mathbf{x}} dV = (\rho S \ddot{\mathbf{x}}) ds \quad (6.39a)$$

$$\iiint_{\delta\mathcal{V}} \rho(\mathbf{p} \times \ddot{\mathbf{p}}) dV = (\rho S \ddot{\mathbf{x}} + \rho I_1 \mathbf{d}_1 \times \ddot{\mathbf{d}}_1 + \rho I_2 \mathbf{d}_2 \times \ddot{\mathbf{d}}_2) ds \quad (6.39b)$$

Balance of linear momentum

For a thin slice of the rod ($\delta\mathcal{V}$) between cross-sections $\mathcal{S}(s)$ and $\mathcal{S}(s+ds)$, using eq. (6.30a) and (6.31a), the balance of linear momentum referring to the *reference configuration* expressed in eq. (6.29a) yields :

$$\begin{aligned} \iiint_{\delta\mathcal{V}} \rho \ddot{\mathbf{p}} dV &= \iint_{\partial\mathcal{V}} \boldsymbol{\sigma}_n dS + \iiint_{\delta\mathcal{V}} \rho \mathbf{b} dV \\ &= \iint_{\mathcal{S}(s)} \boldsymbol{\sigma}_n dS + \iint_{\mathcal{S}(s+ds)} \boldsymbol{\sigma}_n dS + \left(\iint_{\delta\mathcal{L}} \boldsymbol{\sigma}_n dS + \iiint_{\delta\mathcal{V}} \rho \mathbf{b} dV \right) \\ &= -\mathbf{F}(s) + \mathbf{F}(s+ds) + (\mathbf{f}_s(s) + (1+\epsilon)\mathbf{f}_{st}(s)) ds \\ &= \left(\frac{\partial \mathbf{F}}{\partial s} + \mathbf{f}_s + (1+\epsilon)\mathbf{f}_{st} \right) (s) ds \end{aligned} \quad (6.40)$$

³²Indeed, since $\iint_{\mathcal{S}(s)} \mathbf{r} dX_1 dX_2 = \mathbf{0}$ from eq. (6.36a) we have $\iint_{\mathcal{S}(s)} \ddot{\mathbf{r}} dX_1 dX_2 = \iint_{\mathcal{S}(s)} \dot{\boldsymbol{\omega}} \times \mathbf{r} + \boldsymbol{\omega} \times (\boldsymbol{\omega} \times \mathbf{r}) dX_1 dX_2 = \mathbf{0}$ and $\iint_{\mathcal{S}(s)} \mathbf{r} \times \ddot{\mathbf{x}} dX_1 dX_2 = \mathbf{0}$ as $\boldsymbol{\omega}$ and \mathbf{x} are independent of X_1 and X_2 .

Thus, using eq. (6.39a), the equation for the balance of linear momentum reduce to :³³

$$\frac{\partial \mathbf{F}}{\partial s} + \mathbf{f}_s + (1 + \epsilon) \mathbf{f}_{st} = \rho S \ddot{\mathbf{x}} \quad (6.41)$$

Balance of angular momentum

Similarly, for a thin slice of the rod ($\delta\mathcal{V}$) between cross-sections $\mathcal{S}(s)$ and $\mathcal{S}(s + ds)$, using eq. (6.30a) and (6.30b) yields :

$$\begin{aligned} \iint_{\mathcal{S}(s) \cup \mathcal{S}(s+ds)} \mathbf{p} \times \boldsymbol{\sigma}_n \, dS &= \iint_{\mathcal{S}(s) \cup \mathcal{S}(s+ds)} (\mathbf{x} + \mathbf{r}) \times \boldsymbol{\sigma}_n \, dS \\ &= -(\mathbf{x} \times \mathbf{F})(s) + (\mathbf{x} \times \mathbf{F})(s + ds) - \mathbf{M}(s) + \mathbf{M}(s + ds) \\ &= \frac{\partial}{\partial s} (\mathbf{M} + \mathbf{x} \times \mathbf{F})(s) \, ds \end{aligned} \quad (6.42)$$

Using eq. (6.31b) the balance of linear momentum referring to the *reference configuration* expressed in eq. (6.29b) yields :

$$\begin{aligned} \iiint_{\delta\mathcal{V}} \rho(\mathbf{p} \times \ddot{\mathbf{p}}) \, dV &= \iint_{\partial\delta\mathcal{V}} \mathbf{p} \times \boldsymbol{\sigma}_n \, dS + \iiint_{\delta\mathcal{V}} \rho(\mathbf{p} \times \mathbf{b}) \, dV \\ &= \frac{\partial}{\partial s} (\mathbf{M} + \mathbf{x} \times \mathbf{F})(s) \, ds + \mathbf{m}_s + (1 + \epsilon) \mathbf{m}_{st} \\ &\quad + \mathbf{x} \times (\mathbf{f}_s + (1 + \epsilon) \mathbf{f}_{st}) \, ds \end{aligned} \quad (6.43)$$

Finally, combining eq. (6.43) with eq. (6.39b) and (6.41), the equation for the balance of angular momentum reduce to :^{34,35,36}

$$\frac{\partial \mathbf{M}}{\partial s} + \frac{\partial \mathbf{x}}{\partial s} \times \mathbf{F} + \mathbf{m}_s + (1 + \epsilon) \mathbf{m}_{st} = \rho I_1 \mathbf{d}_1 \times \ddot{\mathbf{d}}_1 + \rho I_2 \mathbf{d}_2 \times \ddot{\mathbf{d}}_2 \quad (6.44)$$

³³This equation also writes : $(1 + \epsilon) \frac{\partial \mathbf{F}}{\partial s_t} + \mathbf{f}_s + (1 + \epsilon) \mathbf{f}_{st} = \rho S \ddot{\mathbf{x}}$.

³⁴Note the simplification of the term $\rho S \ddot{\mathbf{x}}$. Alternatively, the balance equations could be written for the slice considered as a rigid body. In the barycentric frame of the slice : $\frac{d}{dt}(dI_G) = \mathbf{M}(s + ds) - \mathbf{M}(s) + \mathbf{m}(s)ds + (\frac{1}{2}ds\mathbf{x}') \times \mathbf{F}(s + ds) + (-\frac{1}{2}ds\mathbf{x}') \times -\mathbf{F}(s) = (\frac{\partial \mathbf{M}}{\partial s}(s) + \mathbf{m}(s) + \mathbf{x}' \times \mathbf{F}(s))ds$ with $dI_G \simeq \rho ds(I_1 \mathbf{d}_1 + I_2 \mathbf{d}_2 + (I_1 + I_2) \mathbf{d}_3)$.

³⁵This equation also writes : $(1 + \epsilon) \left(\frac{\partial \mathbf{M}}{\partial s_t} + \frac{\partial \mathbf{x}}{\partial s_t} \times \mathbf{F} + (1 + \epsilon)^{-1} \mathbf{m}_s + \mathbf{m}_{st} \right) = \rho I_1 \mathbf{d}_1 \times \ddot{\mathbf{d}}_1 + \rho I_2 \mathbf{d}_2 \times \ddot{\mathbf{d}}_2$.

³⁶Under this form, this equation is presented by Neukirch 2009 [118].

6.3.5 Equations of motion

With some scaling arguments Dill 1992 [111] shows that terms in ω_1 and ω_2 should be negligible in the inertial forces of the rod given in eq. (6.39b), which yields to :^{37,38}

$$\rho I_1(\dot{\omega}_1 + \omega_2\omega_3) \simeq 0 \quad (6.45a)$$

$$\rho I_2(\dot{\omega}_2 - \omega_1\omega_3) \simeq 0 \quad (6.45b)$$

$$\rho(I_1 + I_2)\dot{\omega}_3 + \rho(I_2 - I_1)\omega_1\omega_2 \simeq \rho(I_1 + I_2)\dot{\omega}_3 \quad (6.45c)$$

For our application – a beam model for quasi-static analysis of gridshell structures – this approximation is clearly sufficient as what matters is the quasi-static response of the structural system and there is no need for a too accurate modeling of the transient phase. Moreover, the quasi-static response will be determined through a fictitious dynamic process appropriately damped to speed up the convergence to the steady state, and so there is no reason that the transient phase has any real physical meaning. This means that it is enough to keep only the twisting dynamic of the rod around its centerline.

Thus, the final dynamical equations for the motion of the rod to be retained are :

$$\frac{\partial \mathbf{F}}{\partial s} + \mathbf{f}_s + (1 + \epsilon)\mathbf{f}_{st} = \rho S \ddot{\mathbf{x}} \quad (6.46a)$$

$$\frac{\partial \mathbf{M}}{\partial s} + \frac{\partial \mathbf{x}}{\partial s} \times \mathbf{F} + \mathbf{m}_s + (1 + \epsilon)\mathbf{m}_{st} \simeq \rho(I_1 + I_2)\dot{\omega}_3 \mathbf{d}_3 \quad (6.46b)$$

6.3.6 Hookean elasticity

From now on we consider that the rod material is isotropic and linear elastic.³⁹ This is the framework of the so called *Hookean Elasticity*. This assumption allows the determination of the local displacement field (\mathbf{u}), the strain tensor ($\boldsymbol{\epsilon}$), the stress tensor ($\boldsymbol{\sigma}$) and the constitutive equations that link the axial force (\mathbf{F}_3), the bending moments ($\mathbf{M}_1, \mathbf{M}_2$) and the twisting moment (\mathbf{M}_3) to the strains ($\epsilon, \boldsymbol{\varkappa}, \bar{\boldsymbol{\varkappa}}$).

Such a material is characterized by a linear relation between the strain and stress tensors that takes the form :⁴⁰

$$\boldsymbol{\sigma} = 2\mu\boldsymbol{\epsilon} + \lambda Tr(\boldsymbol{\epsilon})\boldsymbol{\mathcal{I}} \quad (6.47)$$

where λ and μ are known as the elastic coefficients of Lamé. These coefficients are related

³⁷“It follows that \varkappa_1 and \varkappa_2 can be neglected in the kinetic energy [...]. However, \varkappa_3 , which provides the angular momentum about the axis of the rod, must be retained. This assumption of Kirchhoff is consistent with the technical theory of beams where rotary inertia is known to provide corrections to the natural frequencies of vibration of $O(\alpha^2)$ if the length measure is the half-wave length” [111, p. 17].

³⁸This assumption is made in numerous publications but often with ambiguous or no justifications, as of instance : “neglecting inertial momentum due to the vanishing cross-section lead to the following dynamic equations for a Kirchhoff rod” [129].

³⁹This is true at first order for small strains anyway.

⁴⁰Using Einstein notation this expression yields : $\sigma_{ij} = \lambda\epsilon_{kk}\delta_{ij} + 2\mu\epsilon_{ij}$.

to the elastic (E) and shear (G) modulus and to the Poisson ratio (ν) :

$$\mu = \frac{E}{2(1+\nu)} = G \quad (6.48a)$$

$$\lambda = \frac{2\mu\nu}{1-2\nu} \quad (6.48b)$$

A worthwhile presentation of the theory of elasticity in the specific context of elastic rods can be found in [110].

6.3.7 Deformation of cross-sections

In this paragraph, we simply recall the canonical form of the local displacement field (\mathbf{u}) for the cross-section $\mathcal{S}(s)$ in the context of Kirchhoff's approximation : ⁴¹

$$u_3 = (\varkappa_3 - \bar{\varkappa}_3)\varphi_s(X_1, X_2) \quad (6.49a)$$

$$u_1 = -\nu\epsilon X_1 - \nu(\varkappa_1 - \bar{\varkappa}_1)X_1 X_2 + \frac{1}{2}\nu(\varkappa_2 - \bar{\varkappa}_2)(X_1^2 - X_2^2) \quad (6.49b)$$

$$u_2 = -\nu\epsilon X_2 + \nu(\varkappa_2 - \bar{\varkappa}_2)X_1 X_2 + \frac{1}{2}\nu(\varkappa_1 - \bar{\varkappa}_1)(X_1^2 - X_2^2) \quad (6.49c)$$

where φ_s is the warping function in torsion of $\mathcal{S}(s)$, determined by the following differential equation and the boundary condition over the contour of the cross-section : ^{42,43}

$$0 = \frac{\partial^2 \varphi_s}{\partial X_1^2} + \frac{\partial^2 \varphi_s}{\partial X_2^2}, \quad \forall (X_1, X_2) \in \mathcal{S}(s) \quad (6.50a)$$

$$0 = \frac{\partial f_s}{\partial X_1} \left(\frac{\partial \varphi_s}{\partial X_1} - X_2 \right) + \frac{\partial f_s}{\partial X_2} \left(\frac{\partial \varphi_s}{\partial X_2} + X_1 \right), \quad f_s(X_1, X_2) = 0 \quad (6.50b)$$

These equations have known analytical solutions for classical shapes such as circles, ellipses, squares or rectangles. For other shapes, when it is not easy to find analytical solutions, the membrane analogy introduced by Prandtl 1903 [131] can be employed.⁴⁴ A careful introduction to the question of torsion in bars is proposed by Timoshenko and Goodier 1951 [133, p. 258-315].

Note that the boundary condition given by eq. (6.50b) stipulates that cross-sections are free to warp. The problem is more complex when warping is restrained. In this case, called

⁴¹Remark that the local displacement field results from the superposition of the three displacement fields obtained for pure and uniform extension, flexion and twist. For a detailed analysis of pure and uniform flexion and twist of rods refer to [110, ch. 3].

⁴²"In the traditional theory of non-uniform torsion the axial displacement field is expressed as the product of the unit twist angle and the warping function. The first one, variable along the beam axis, is obtained by a global congruence condition; the second one, instead, defined over the cross-section, is determined by solving a Neumann problem associated to the Laplace equation, as well as for the uniform torsion problem." [130].

⁴³ $\mathbf{n} = (\partial f_s / \partial X_1, \partial f_s / \partial X_2)^T$ is the unit normal vector to the boundary curve of $\mathcal{S}(s)$ defined implicitly by the equation $f_s(X_1, X_2) = 0$.

⁴⁴Recent advances [132] in the formfinding of soap films with the force density method might be of practical use to evaluate the warping function.

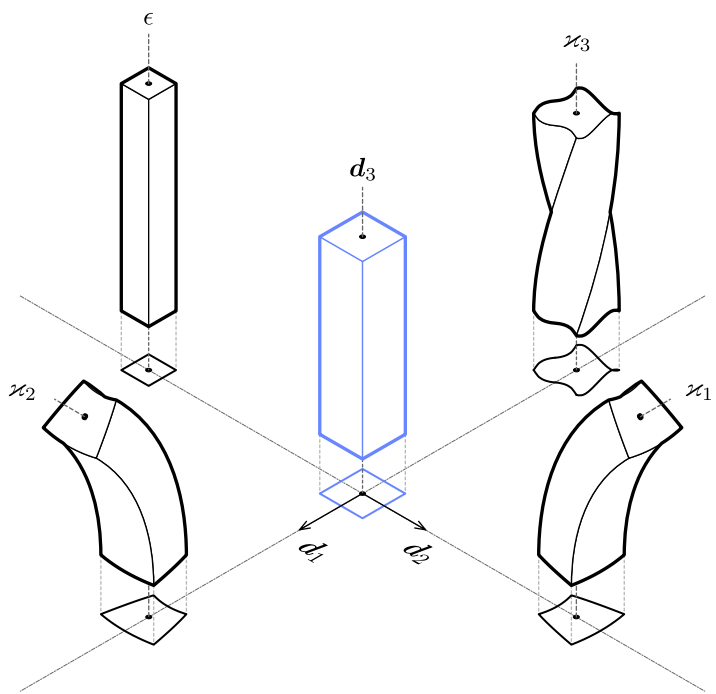


Figure 6.4 – Typical deformation modes of cross-sections in Kirchhoff's theory. Flexion around \mathbf{d}_1 (resp. \mathbf{d}_2) is measured through the material curvature κ_1 (resp. κ_2) ; torsion around \mathbf{d}_3 is measured through the material twist κ_3 ; and ϵ measures the axial extension. Remark that cross-sections are subjected to both in-plane deformations (κ_1 , κ_2 , ϵ) and out-of-plane deformations (κ_3).

non-uniform torsion, the twisting stiffness is modified.⁴⁵

To go further on the subject of non uniform torsion, which is not treated in the present work, the reader is invited to refer to [135, 136, 137].

6.3.8 Strain tensor

Here, we remind the canonical form of the strain tensor ($\boldsymbol{\epsilon}$) for the cross-section $\mathcal{S}(s)$ in the context of Kirchhoff's approximation :

$$\epsilon_{33} = \epsilon + (\varkappa_1 - \bar{\varkappa}_1)X_2 - (\varkappa_2 - \bar{\varkappa}_2)X_1 \quad (6.51a)$$

$$\epsilon_{11} = \epsilon_{22} = -\nu\epsilon_{33} \quad (6.51b)$$

$$\epsilon_{12} = 0 \quad (6.51c)$$

$$\epsilon_{31} = \frac{1}{2}(\varkappa_3 - \bar{\varkappa}_3) \left(\frac{\partial \varphi_s}{\partial X_1} - X_2 \right) \quad (6.51d)$$

$$\epsilon_{32} = \frac{1}{2}(\varkappa_3 - \bar{\varkappa}_3) \left(\frac{\partial \varphi_s}{\partial X_2} + X_1 \right) \quad (6.51e)$$

6.3.9 Stress tensor

In this paragraph, we simply give the entries of the stress tensor ($\boldsymbol{\sigma}$) defined in eq. (6.47), for the cross-section $\mathcal{S}(s)$ in the context of Kirchhoff's approximation :

$$\sigma_{33} = E\epsilon_{33} \quad (6.52a)$$

$$\sigma_{11} = \sigma_{22} = \sigma_{12} = 0 \quad (6.52b)$$

$$\sigma_{31} = 2G\epsilon_{31} \quad (6.52c)$$

$$\sigma_{32} = 2G\epsilon_{32} \quad (6.52d)$$

Thus, the Piola stress vector defined in eq. (6.28b) becomes :

$$\boldsymbol{\sigma}_n = \sigma_{31}\mathbf{d}_1 + \sigma_{32}\mathbf{d}_2 + \sigma_{33}\mathbf{d}_3 \quad (6.53)$$

6.3.10 Constitutive equations for internal forces and moments

In Kirchhoff's theory, constitutive equations for internal forces and moments should not be considered as assumptions. Indeed, as shown hereafter, they are somehow consequences of the assumptions made on the motion – that is the rod remains close to a motion where cross-sections remain planar, undistorted and perpendicular to the centerline – and on the material – the Hookean elasticity – of the rod.

⁴⁵“The problem becomes more complicated if cross sections are not free to warp or if the torque varies along the length of the bar. Warping in such cases varies along the bar and torsion is accompanied by tension or compression of longitudinal fibers. The rate of change of the angle of twist along the axis of the bar also varies, and we call this the case of non-uniform torsion.” [134].

From eq. (6.30a), (6.51a), (6.52a) and (6.53) we deduce the constitutive equation for the axial component of the internal forces : ⁴⁶

$$\begin{aligned} F_3 &= \iint_{\mathcal{S}(s)} \boldsymbol{\sigma}_n(s, X_1, X_2, t) \cdot \mathbf{d}_3 \, dX_1 dX_2 \\ &= ES\epsilon - (\varkappa_2 - \bar{\varkappa}_2) \iint_{\mathcal{S}(s)} X_1 \, dX_1 dX_2 + (\varkappa_1 - \bar{\varkappa}_1) \iint_{\mathcal{S}(s)} X_2 \, dX_1 dX_2 \quad (6.54) \\ &= ES\epsilon \end{aligned}$$

From eq. (6.30b), (6.51d), (6.51e), (6.52c), (6.52d) and (6.53) we deduce the constitutive equation for the axial component of the internal moments, that is the twisting moment :

$$\begin{aligned} M_3 &= \iint_{\mathcal{S}(s)} (\mathbf{r} \times \boldsymbol{\sigma}_n(s, X_1, X_2, t)) \cdot \mathbf{d}_3 \, dX_1 dX_2 \\ &= \iint_{\mathcal{S}(s)} \left[-X_2 \sigma_{31} + X_1 \sigma_{32} \right] \, dX_1 dX_2 \quad (6.55) \\ &= G(\varkappa_3 - \bar{\varkappa}_3) \iint_{\mathcal{S}(s)} \left[X_1 \left(\frac{\partial \varphi_s}{\partial X_2} + X_1 \right) - X_2 \left(\frac{\partial \varphi_s}{\partial X_1} - X_2 \right) \right] \, dX_1 dX_2 \end{aligned}$$

Introducing the torsional constant of St Venant (J) this equation rewrites :

$$M_3 = GJ(\varkappa_3 - \bar{\varkappa}_3) \quad (6.56a)$$

$$J = \iint_{\mathcal{S}(s)} \left[X_1 \left(\frac{\partial \varphi_s}{\partial X_2} + X_1 \right) - X_2 \left(\frac{\partial \varphi_s}{\partial X_1} - X_2 \right) \right] \, dX_1 dX_2 \quad (6.56b)$$

Remark from eq. (6.56b) that when the section does not warp ($\varphi_s=0$), the torsion constant is nothing but the polar moment of inertia of the section (I_p).

From eq. (6.30b), (6.51a), (6.52a) and (6.53) we deduce the constitutive equation for the first component of the internal moments :

$$\begin{aligned} M_1 &= \iint_{\mathcal{S}(s)} (\mathbf{r} \times \boldsymbol{\sigma}_n(s, X_1, X_2, t)) \cdot \mathbf{d}_1 \, dX_1 dX_2 \\ &= \iint_{\mathcal{S}(s)} X_2 \sigma_{33} \, dX_1 dX_2 \quad (6.57) \\ &= E(\varkappa_1 - \bar{\varkappa}_1) \iint_{\mathcal{S}(s)} X_2^2 \, dX_1 dX_2 \end{aligned}$$

From eq. (6.30b), (6.51a), (6.52a) and (6.53) we deduce the constitutive equation for the

⁴⁶Also recall from eq. (6.36) that $\iint_{\mathcal{S}(s)} X_1 \, dX_1 dX_2 = 0$ and $\iint_{\mathcal{S}(s)} X_2 \, dX_1 dX_2 = 0$.

second component of the internal moments :

$$\begin{aligned}
 M_2 &= \iint_{S(s)} (\mathbf{r} \times \boldsymbol{\sigma}_n(s, X_1, X_2, t)) \cdot \mathbf{d}_2 \, dX_1 dX_2 \\
 &= \iint_{S(s)} -X_1 \sigma_{33} \, dX_1 dX_2 \\
 &= E(\varkappa_2 - \bar{\varkappa}_2) \iint_{S(s)} X_1^2 \, dX_1 dX_2
 \end{aligned} \tag{6.58}$$

6.3.11 Discussion

Observe that the internal shear forces are reacting parameters and are given by the balance equations (see eq. (6.67d) and (6.67e)). Transverse shear deformations are neglected and the related stresses are not given by the present theory.

Cross-sections are not assumed to be subject to rigid body motions but to deform closely to such movements. Indeed, the torsion constant of St Venant (J) is found assuming the cross-sections can warp (see eq. (6.64d)). Otherwise, the constant torsion would be nothing but the polar moment of inertia, which would not lead to the correct evaluation of the torsional stiffness of the rod.

Because of the chosen description of motion (see §6.3.1), cross-sections are assumed to rotate around their center of mass. Hence, the model is only valid for sections where the shear center is located at the center of mass. This preclude thin walled open cross-sections. For further understanding of the warping of sections, refer to [137].

6.4 Summary of Kirchhoff theory

Let's summarize the assumptions and results of Kirchhoff's theory of rods on which our discret beam model (see chapter 7) will be based on.

In the reference configuration the rod is described by its reference strains :

$$\bar{\mathbf{d}}'_i = \bar{\boldsymbol{\kappa}} \times \bar{\mathbf{d}}_i \quad (6.59)$$

In the actual configuration the rod is described by its strain and spin vectors :

$$\mathbf{x}' = (1 + \epsilon)\mathbf{t} \quad (6.60a)$$

$$\mathbf{d}'_i = \boldsymbol{\kappa} \times \mathbf{d}_i \quad (6.60b)$$

$$\dot{\mathbf{d}}_i = \boldsymbol{\omega} \times \mathbf{d}_i \quad (6.60c)$$

The rod is subjected to internal forces and moments :

$$\mathbf{F} = F_1 \mathbf{d}_1 + F_2 \mathbf{d}_2 + F_3 \mathbf{d}_3 \quad (6.61a)$$

$$\mathbf{M} = M_1 \mathbf{d}_1 + M_2 \mathbf{d}_2 + M_3 \mathbf{d}_3 \quad (6.61b)$$

The rod is subjected to external and body loads described as distributed forces and moments acting on the centerline – either given per unit length of the reference configuration (\mathbf{f}_s , \mathbf{m}_s) or per unit length of the actual configuration (\mathbf{f}_{s_t} , \mathbf{m}_{s_t}) – and given by :

$$\mathbf{f} = \mathbf{f}_s + (1 + \epsilon)\mathbf{f}_{s_t} = f_1 \mathbf{d}_1 + f_2 \mathbf{d}_2 + f_3 \mathbf{d}_3 \quad (6.62a)$$

$$\mathbf{m} = \mathbf{m}_s + (1 + \epsilon)\mathbf{m}_{s_t} = m_1 \mathbf{d}_1 + m_2 \mathbf{d}_2 + m_3 \mathbf{d}_3 \quad (6.62b)$$

The internal axial force, the internal bending moments and the internal twisting moment are computed with the following constitutive equations :

$$F_3 = ES\epsilon \quad (6.63a)$$

$$M_1 = EI_1(\boldsymbol{\kappa}_1 - \bar{\boldsymbol{\kappa}}_1) \quad (6.63b)$$

$$M_2 = EI_2(\boldsymbol{\kappa}_2 - \bar{\boldsymbol{\kappa}}_2) \quad (6.63c)$$

$$M_3 = GJ(\boldsymbol{\kappa}_3 - \bar{\boldsymbol{\kappa}}_3) \quad (6.63d)$$

where S , I_1 , I_2 , J are respectively the area, the second moments of inertia and the torsional stiffness of the cross-section :

$$S = \iint_{\mathcal{S}(s)} dX_1 dX_2 \quad (6.64a)$$

$$I_1 = \iint_{\mathcal{S}(s)} X_2^2 dX_1 dX_2 \quad (6.64b)$$

$$I_2 = \iint_{\mathcal{S}(s)} X_1^2 dX_1 dX_2 \quad (6.64c)$$

$$J = \iint_{\mathcal{S}(s)} X_1 \left(\frac{\partial \varphi_s}{\partial X_2} + X_1 \right) - X_2 \left(\frac{\partial \varphi_s}{\partial X_1} - X_2 \right) dX_1 dX_2 \quad (6.64d)$$

and φ_s is the warping function of the cross-section that satisfies the differential system :

$$0 = \frac{\partial^2 \varphi_s}{\partial X_1^2} + \frac{\partial^2 \varphi_s}{\partial X_2^2}, \quad \forall (X_1, X_2) \in \mathcal{S}(s) \quad (6.65a)$$

$$0 = \frac{\partial f_s}{\partial X_1} \left(\frac{\partial \varphi_s}{\partial X_1} - X_2 \right) + \frac{\partial f_s}{\partial X_2} \left(\frac{\partial \varphi_s}{\partial X_2} + X_1 \right), \quad f_s(X_1, X_2) = 0 \quad (6.65b)$$

The dynamical equations for the motion of the rod are :

$$\frac{\partial \mathbf{F}}{\partial s} + \mathbf{f} = \rho S \ddot{\mathbf{x}} \quad (6.66a)$$

$$\frac{\partial \mathbf{M}}{\partial s} + \frac{\partial \mathbf{x}}{\partial s} \times \mathbf{F} + \mathbf{m} = \rho I_1 \mathbf{d}_1 \times \ddot{\mathbf{d}}_1 + \rho I_2 \mathbf{d}_2 \times \ddot{\mathbf{d}}_2 \quad (6.66b)$$

Neglecting the rotational dynamics around \mathbf{d}_1 and \mathbf{d}_2 the components of the above equations are written :

$$F'_1 + \varkappa_2 F_3 - \varkappa_3 F_2 + f_1 = \rho S \ddot{x}_1 \quad (6.67a)$$

$$F'_2 + \varkappa_3 F_1 - \varkappa_1 F_3 + f_2 = \rho S \ddot{x}_2 \quad (6.67b)$$

$$F'_3 + \varkappa_1 F_2 - \varkappa_2 F_1 + f_3 = \rho S \ddot{x}_3 \quad (6.67c)$$

$$M'_1 + \varkappa_2 M_3 - \varkappa_3 M_2 - (1 + \epsilon) F_2 + m_1 \simeq 0 \quad (6.67d)$$

$$M'_2 + \varkappa_3 M_1 - \varkappa_1 M_3 + (1 + \epsilon) F_1 + m_2 \simeq 0 \quad (6.67e)$$

$$M'_3 + \varkappa_1 M_2 - \varkappa_2 M_1 + m_3 \simeq \rho(I_1 + I_2)\dot{\omega}_3 \quad (6.67f)$$

The local displacements of the cross-sections are given by :

$$u_3 = (\varkappa_3 - \bar{\varkappa}_3)\varphi_s(X_1, X_2) \quad (6.68a)$$

$$u_1 = -\nu\epsilon X_1 - \nu(\varkappa_1 - \bar{\varkappa}_1)X_1 X_2 + \frac{1}{2}\nu(\varkappa_2 - \bar{\varkappa}_2)(X_1^2 - X_2^2) \quad (6.68b)$$

$$u_2 = -\nu\epsilon X_2 + \nu(\varkappa_2 - \bar{\varkappa}_2)X_1 X_2 + \frac{1}{2}\nu(\varkappa_1 - \bar{\varkappa}_1)(X_1^2 - X_2^2) \quad (6.68c)$$

The non-zero components of the strain tensor are given by :

$$\epsilon_{33} = \epsilon + (\varkappa_1 - \bar{\varkappa}_1)X_2 - (\varkappa_2 - \bar{\varkappa}_2)X_1 \quad (6.69a)$$

$$\epsilon_{31} = \frac{1}{2}(\varkappa_3 - \bar{\varkappa}_3) \left(\frac{\partial \varphi_s}{\partial X_1} - X_2 \right) \quad (6.69b)$$

$$\epsilon_{32} = \frac{1}{2}(\varkappa_3 - \bar{\varkappa}_3) \left(\frac{\partial \varphi_s}{\partial X_2} + X_1 \right) \quad (6.69c)$$

$$\epsilon_{11} = \epsilon_{22} = -\nu\epsilon_{33} \quad (6.69d)$$

The non-zero components of the stress tensor are given by :

$$\sigma_{33} = E\epsilon_{33} \quad (6.70a)$$

$$\sigma_{31} = 2G\epsilon_{31} \quad (6.70b)$$

$$\sigma_{32} = 2G\epsilon_{32} \quad (6.70c)$$

6.5 Geometric interpretation of Kirchhoff's equations

The previous equations for the motion of the rod have been established expressing the fundamental principles of balance of linear and angular momentums (see eq. (6.67a) to (6.67f)). An alternative approach, leading to the same results, consists in differentiating the elastic energy of a given configuration of the rod – assumed to be stationary – with respect to the degrees of freedom of the mechanical system (principle of virtual work). This latter approach is the one developed throughout the previous chapter (see chapter 5).⁴⁷

However, the approach through equilibrium seems easier to understand as it is (almost) just a matter of balance between forces and moments acting on infinitesimal slices of the rods (see fig. 6.5). This is of obvious pedagogical interest as it allows to understand how the geometry of the rod influences the distribution of the elastic energy between extension, flexion and torsion and how these forces are coupled together.

To emphasize this, in this section we provide the proper drawings (see figures 6.6 to 6.8) and computations for the contribution of internal forces and moments to the balance of linear and angular momentums. This is what we call here the “geometric interpretation” of Kirchhoff equations.

⁴⁷This is also the approach developed by Audoly et al. 2010 [110] for strictly inextensible rods. It was yet employed by Reissner 1973 [113].

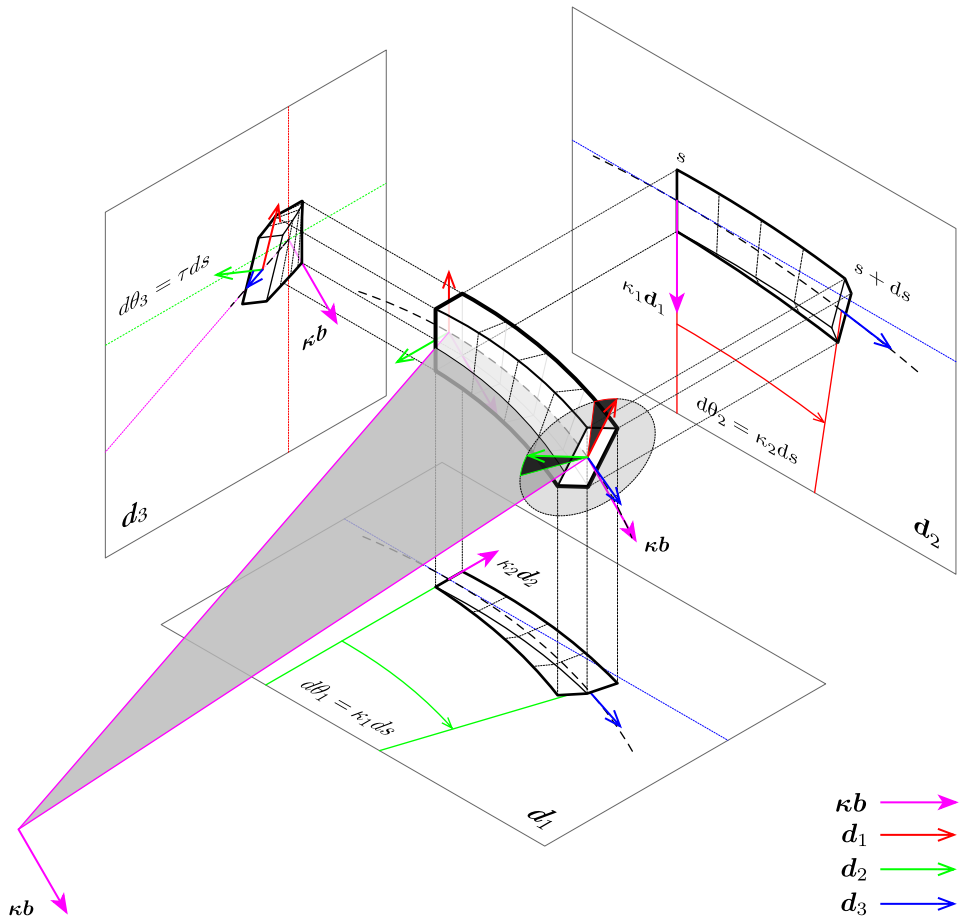
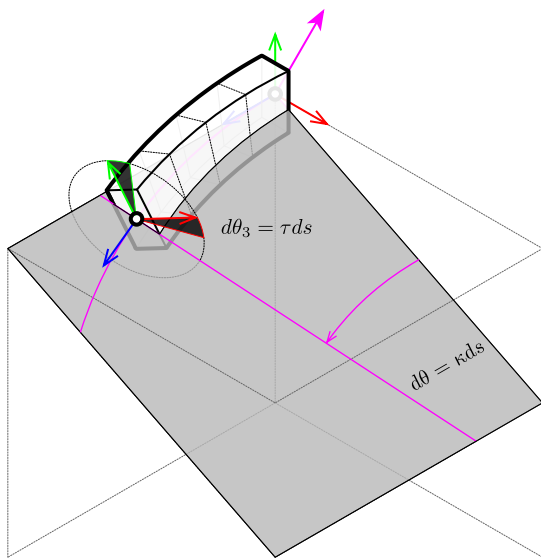
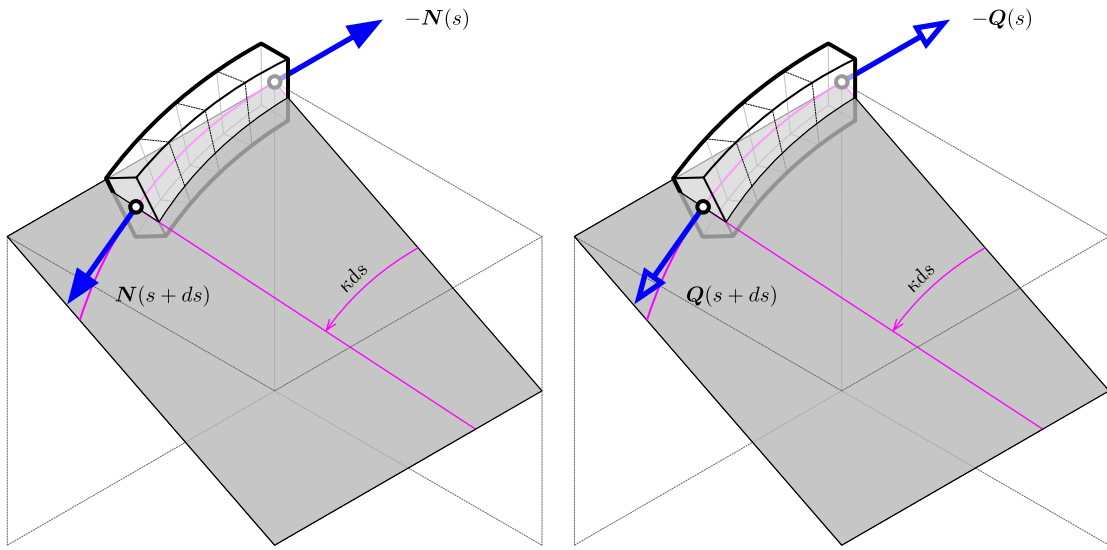


Figure 6.5 – Geometric interpretation of Kirchhoff's equations. Flexion and torsion of an elementary slice of a Kirchhoff rod of length ds . Projections of the deformations are given in the material planes perpendicular to d_1 , d_2 and d_3 . The element takes its curvature κ in the plane perpendicular to κb and represented by a gray triangle. On the figure, κb is positioned at the peak of this triangle, which is the center of the osculating circle associated to it.



(a) infinitesimal deformation



(b) contributions of the internal forces

(c) contributions of the internal moments

Figure 6.6 – Influence of the curvature (κ) in the deflection of internal forces and moments along the centerline. The osculating plane, perpendicular to κb , is represented in grey. N is the axial component of the internal force along d_3 . Q is the axial component of the internal moment, also known as the twisting moment along d_3 .

Contributions to the balance of forces

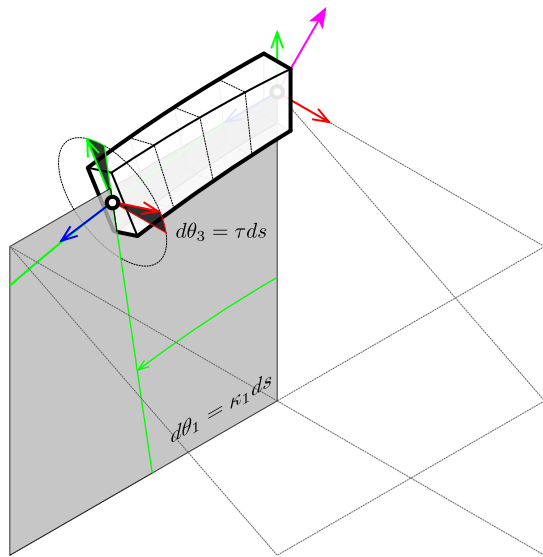
$\mathbf{N}(s + ds)$ is deflected from $\mathbf{d}_3(s)$ by the rotation of angle κds around $\boldsymbol{\kappa b}$ (fig. 6.6b). Thus, its contribution to the balance of forces onto $\mathbf{d}_3(s)$ is :

$$N(s + ds) \cos(\kappa ds) - N(s) = N'(s)ds + o(ds)$$

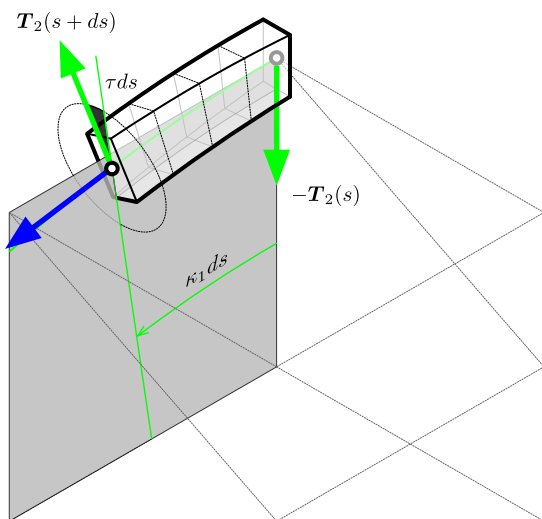
Contributions to the balance of moments

$\mathbf{Q}(s + ds)$ is deflected from $\mathbf{d}_3(s)$ by the rotation of angle κds around $\boldsymbol{\kappa b}$ (fig. 6.6c). Thus, its contribution to the balance of moments onto $\mathbf{d}_3(s)$ is :

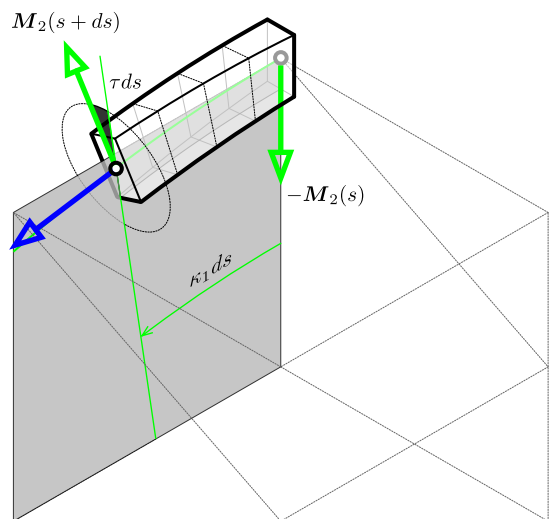
$$Q(s + ds) \cos(\kappa ds) - Q(s) = Q'(s)ds + o(ds)$$



(a) infinitesimal deformation



(b) contributions of the internal forces



(c) contributions of the internal moments

Figure 6.7 – Influence of the first material curvature (κ_1) in the deflection of internal forces and moments along the centerline. The plane perpendicular to $d_1(s)$ is represented in grey. \mathbf{F}_2 is the transverse or shear component of the internal force along d_2 . \mathbf{M}_2 is the transverse or bending component of the internal moment along d_2 .

Contributions to the balance of forces

$\mathbf{F}_2(s + ds)$ is deflected from $\mathbf{d}_2(s)$ by the combined rotations of angle τds around \mathbf{d}_3 and $\kappa_2 ds$ around \mathbf{d}_2 (fig. 6.7b). Thus, its contribution to the balance of forces onto $\mathbf{d}_1(s)$ is :

$$-F_2(s + ds) \sin(\tau ds) \cos(\kappa_2 ds) = -\tau F_2(s)ds + o(ds)$$

$\mathbf{F}_2(s + ds)$ is deflected from $\mathbf{d}_2(s)$ by the combined rotations of angle τds around \mathbf{d}_3 and $\kappa_1 ds$ around \mathbf{d}_1 (fig. 6.7b). Thus, its contribution to the balance of forces onto $\mathbf{d}_2(s)$ is :

$$-F_2(s) + F_2(s + ds) \cos(\tau ds) \cos(\kappa_1 ds) = F'_2(s)ds + o(ds)$$

$\mathbf{F}_2(s + ds)$ is deflected from $\mathbf{d}_2(s)$ by the combined rotations of angle τds around \mathbf{d}_3 and $\kappa_1 ds$ around \mathbf{d}_1 (fig. 6.7b). Thus, its contribution to the balance of forces onto $\mathbf{d}_3(s)$ is :

$$F_2(s + ds) \cos(\tau ds) \sin(\kappa_1 ds) = \kappa_1 F_2(s)ds + o(ds)$$

$\mathbf{N}(s + ds)$ is deflected from $\mathbf{d}_3(s)$ by the combined rotations of angle $\kappa_2 ds$ around \mathbf{d}_2 and $\kappa_1 ds$ around \mathbf{d}_1 (fig. 6.7b). Thus, its contribution to the balance of forces onto $\mathbf{d}_2(s)$ is :

$$-N(s + ds) \cos(\kappa_2 ds) \sin(\kappa_1 ds) = -\kappa_1 N(s)ds + o(ds)$$

Contributions to the balance of moments

$\mathbf{F}_2(s + ds)$ is deflected from the plane normal to $\mathbf{d}_1(s)$ by a rotation of angle τds around \mathbf{d}_3 (fig. 6.7b). It produces a moment around \mathbf{d}_1 with the lever arm $b = \cos(\kappa_2 ds)ds$. Thus, its contribution to the balance of moments onto $\mathbf{d}_1(s)$ is :

$$-F_2(s + ds) \cos(\tau ds)(\cos(\kappa_2 ds)ds) = -F_2(s)ds + o(ds)$$

$\mathbf{M}_2(s + ds)$ is deflected from $\mathbf{d}_2(s)$ by the combined rotations of angle τds around \mathbf{d}_3 and $\kappa_2 ds$ around \mathbf{d}_2 (fig. 6.7c). Thus, its contribution to the balance of moments onto $\mathbf{d}_1(s)$ is :

$$-M_2(s + ds) \sin(\tau ds) \cos(\kappa_2 ds) = -\tau M_2(s)ds + o(ds)$$

$\mathbf{M}_2(s + ds)$ is deflected from $\mathbf{d}_2(s)$ by the combined rotations of angle τds around \mathbf{d}_3 and $\kappa_1 ds$ around \mathbf{d}_1 (fig. 6.7c). Thus, its contribution to the balance of moments onto $\mathbf{d}_2(s)$ is :

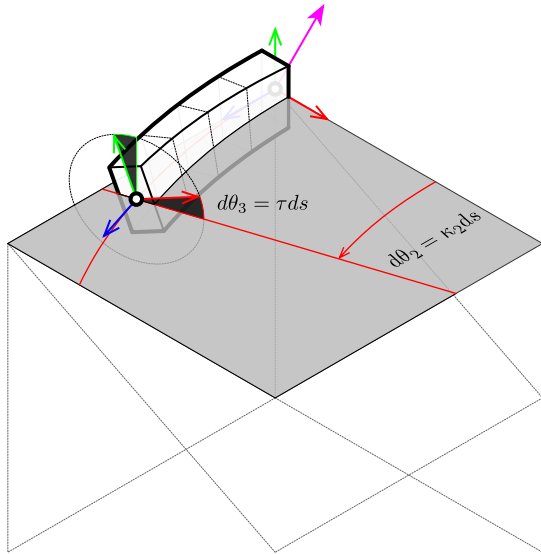
$$-M_2(s) + M_2(s + ds) \cos(\tau ds) \cos(\kappa_1 ds) = M'_2(s)ds + o(ds)$$

$\mathbf{M}_2(s + ds)$ is deflected from $\mathbf{d}_2(s)$ by the combined rotations of angle τds around \mathbf{d}_3 and $\kappa_1 ds$ around \mathbf{d}_1 (fig. 6.7c). Thus, its contribution to the balance of moments onto $\mathbf{d}_3(s)$ is :

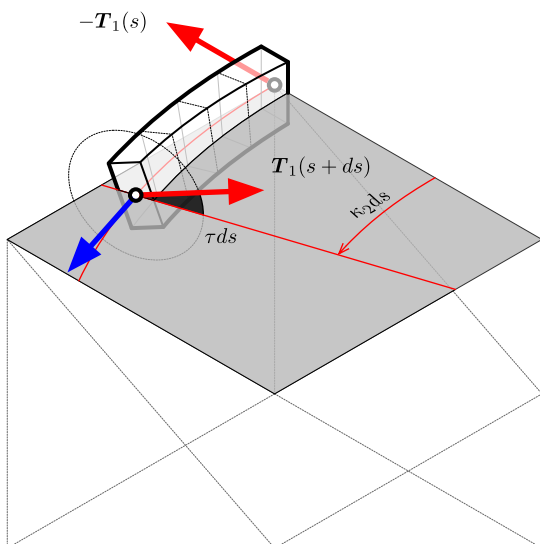
$$M_2(s + ds) \cos(\tau ds) \sin(\kappa_1 ds) = \kappa_1 M_2(s)ds + o(ds)$$

$\mathbf{Q}(s + ds)$ is deflected from $\mathbf{d}_3(s)$ by the combined rotations of angle $\kappa_2 ds$ around \mathbf{d}_2 and $\kappa_1 ds$ around \mathbf{d}_1 (fig. 6.7c). Thus, its contribution to the balance of moments onto $\mathbf{d}_2(s)$ is :

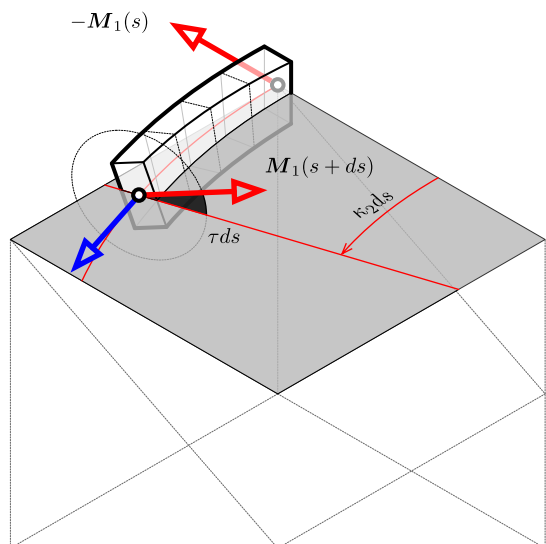
$$-Q(s + ds) \cos(\kappa_2 ds) \sin(\kappa_1 ds) = -\kappa_1 Q(s)ds + o(ds)$$



(a) infinitesimal deformation



(b) contributions of the internal forces



(c) contributions of the internal moments

Figure 6.8 – Influence of the second material curvature (κ_2) in the deflection of internal forces and moments along the centerline. The plane perpendicular to $\mathbf{d}_2(s)$ is represented in grey. \mathbf{F}_1 is the transverse or shear component of the internal force along \mathbf{d}_1 . \mathbf{M}_1 is the transverse or bending component of the internal moment along \mathbf{d}_1 .

Contributions to the balance of forces

$\mathbf{F}_1(s + ds)$ is deflected from $\mathbf{d}_1(s)$ by the combined rotations of angle τds around \mathbf{d}_3 and $\kappa_2 ds$ around \mathbf{d}_2 (fig. 6.8b). Thus, its contribution to the balance of forces onto $\mathbf{d}_1(s)$ is :

$$-F_1(s) + F_1(s + ds) \cos(\tau ds) \cos(\kappa_2 ds) = F'_1(s)ds + o(ds)$$

$\mathbf{F}_1(s + ds)$ is deflected from $\mathbf{d}_1(s)$ by the combined rotations of angle τds around \mathbf{d}_3 and $\kappa_1 ds$ around \mathbf{d}_1 (fig. 6.8b). Thus, its contribution to the balance of forces onto $\mathbf{d}_2(s)$ is :

$$F_1(s + ds) \sin(\tau ds) \cos(\kappa_1 ds) = \tau F_1(s)ds + o(ds)$$

$\mathbf{F}_1(s + ds)$ is deflected from $\mathbf{d}_1(s)$ by the combined rotations of angle τds around \mathbf{d}_3 and $\kappa_2 ds$ around \mathbf{d}_2 (fig. 6.8b). Thus, its contribution to the balance of forces onto $\mathbf{d}_3(s)$ is :

$$-F_1(s + ds) \cos(\tau ds) \sin(\kappa_2 ds) = -\kappa_2 F_1(s)ds + o(ds)$$

$\mathbf{N}(s + ds)$ is deflected from $\mathbf{d}_3(s)$ by the combined rotations of angle $\kappa_1 ds$ around \mathbf{d}_1 and $\kappa_2 ds$ around \mathbf{d}_2 (fig. 6.8b). Thus, its contribution to the balance of forces onto $\mathbf{d}_1(s)$ is :

$$N(s + ds) \cos(\kappa_1 ds) \sin(\kappa_2 ds) = \kappa_2 N(s)ds + o(ds)$$

Contributions to the balance of moments

$\mathbf{F}_1(s + ds)$ is deflected from the plane normal to $\mathbf{d}_2(s)$ by the angle τds around \mathbf{d}_3 along ds (fig. 6.8b). It produces a moment around \mathbf{d}_2 with the lever arm $b = \cos(\kappa_1 ds)ds$. Thus, its contribution to the balance of moments onto $\mathbf{d}_2(s)$ is :

$$F_1(s + ds) \cos(\tau ds)(\cos(\kappa_1 ds)ds) = F_1(s)ds + o(ds)$$

$\mathbf{M}_1(s + ds)$ is deflected from $\mathbf{d}_1(s)$ by the combined rotations of angle τds around \mathbf{d}_3 and $\kappa_2 ds$ around \mathbf{d}_2 (fig. 6.8c). Thus, its contribution to the balance of moments onto $\mathbf{d}_1(s)$ is :

$$-M_1(s) + M_1(s + ds) \cos(\tau ds) \cos(\kappa_2 ds) = M'_1(s)ds + o(ds)$$

$\mathbf{M}_1(s + ds)$ is deflected from $\mathbf{d}_1(s)$ by the combined rotations of angle τds around \mathbf{d}_3 and $\kappa_2 ds$ around \mathbf{d}_2 (fig. 6.8c). Thus, its contribution to the balance of moments onto $\mathbf{d}_2(s)$ is :

$$M_1(s + ds) \sin(\tau ds) \cos(\kappa_2 ds) = \tau M_1(s)ds + o(ds)$$

$\mathbf{M}_1(s + ds)$ is deflected from $\mathbf{d}_1(s)$ by the combined rotations of angle τds around \mathbf{d}_3 and $\kappa_2 ds$ around \mathbf{d}_2 (fig. 6.8c). Thus, its contribution to the balance of moments onto $\mathbf{d}_3(s)$ is :

$$-M_1(s + ds) \cos(\tau ds) \sin(\kappa_2 ds) = -\kappa_2 M_1(s)ds + o(ds)$$

$\mathbf{Q}(s + ds)$ is deflected from $\mathbf{d}_3(s)$ by the combined rotations of angle $\kappa_1 ds$ around \mathbf{d}_1 and $\kappa_2 ds$ around \mathbf{d}_2 (fig. 6.8c). Thus, its contribution to the balance of moments onto $\mathbf{d}_1(s)$ is :

$$Q(s + ds) \cos(\kappa_1 ds) \sin(\kappa_2 ds) = \kappa_2 Q(s)ds + o(ds)$$

6.6 Conclusion

The geometric configuration of a Kirchhoff rod has been described using a constrained Cosserat rod model, composed of a centerline curve and an orthonormal adapted frame. The assumptions upon which Kirchhoff theory for rods is built has been carefully reminded and the dynamical equations of a rod has been established. A pure geometric reasoning has been proposed to retrieve the static member of these equations, understood as first order balance laws between internal force and moment.

These theoretical clarifications give a more robust understanding of the previous works of Adriaenssens et al. 1999 [38], Douthe 2007 [10] and D'Amico et al. 2014 [29] on nonlinear rod models for the computation of elastic gridshells. Indeed, we have shown that the material curvature is the one that comes up in the calculation of the bending moment through the constitutive laws and that it is distinct from the geometric curvature, although these notions could be considered equivalent in the case of weakly extensible rods. We have also demonstrated that the shear forces acting on the rod can be straightly deduced from the dynamical equations if the angular inertia around the material directors \mathbf{d}_1 and \mathbf{d}_2 is neglected. Finally, we have remarked that the equations of motion already take into account stretching, bending and twisting of the rod. Hence, the works previously developed in [38, 10] about the 3-DOFs spline beam element are special cases of this set of dynamical equations.

In this chapter we have set up the theoretical basement to built a discrete rod model that is able to take into account axial extension, bending and torsion, and external loading. Previous works in this field can be understood as special cases of this framework and this enhance the overall understanding and the continuity between these works and the present thesis.

6.7 References

- [10] C. Douthe. “Etude de structures élancées précontraintes en matériaux composites : application à la conception des gridshells”. PhD thesis. Université Paris Est, 2007, p. 274.
- [26] C. Douthe, O. Baverel, and J.-F. Caron. “Formfinding of a grid shell in composite materials”. In: *Journal of the IASS* 47 (2006), pp. 53–62.
- [29] B. D’Amico, A. Kermani, and H. Zhang. “Form finding and structural analysis of actively bent timber grid shells”. In: *Engineering Structures* 81 (2014), pp. 195–207.
- [38] S. Adriaenssens, M. Barnes, and C. Williams. “A new analytic and numerical basis for the form-finding and analysis of spline and gridshell structures”. In: *Computing Developments in Civil and Structural Engineering*. Ed. by B. Kumar and B. H. V. Topping. Edinburgh: Civil-Comp Press, 1999, pp. 83–91.
- [40] S. Adriaenssens and M. Barnes. “Tensegrity spline beam and grid shell structures”. In: *Engineering Structures* 23.1 (2001), pp. 29–36.
- [95] M. Bergou, B. Audoly, E. Vouga, M. Wardetzky, and E. Grinspun. “Discrete viscous threads”. In: *ACM Transactions on ...* (2010), pp. 1–10.
- [98] M. Grégoire and E. Schömer. “Interactive simulation of one-dimensional flexible parts”. In: *CAD Computer Aided Design* 39.8 (2007), pp. 694–707.
- [102] J. Spillmann and M. Teschner. “CORDE : Cosserat Rod Elements for the Dynamic Simulation of One-Dimensional Elastic Objects”. In: *Eurographics/ ACM SIGGRAPH Symposium on Computer Animation* (2007), pp. 1–10.
- [110] B. Audoly, M. Amar, and Y. Pomeau. *Elasticity and geometry*. 2010, p. 600.
- [111] E. H. Dill. “Kirchhoff’s theory of rods”. In: *Archive for History of Exact Sciences* (1992), p. 23.
- [112] S. Antman. *Nonlinear problems of elasticity*. Applied mathematical sciences. New York: Springer, 2005, p. 838.
- [113] E. Reissner. “On one-dimensional large-displacement finite-strain beam theory.” In: *Studies in Applied Mathematics* 52.2 (1973), pp. 87–95.
- [114] A. Love. *A treatise on the mathematical theory of elasticity*. Second. Cambridge University Press, 1906, p. 571.
- [115] G. Kirchhoff. *Über das gleichgewicht und die bewegung einer elastischen scheibe*. Berlin, 1850, p. 38.
- [116] G. Kirchhoff. *Vorlesungen über mathematische, physik, mechanik*. Ed. by B. G. Teubner. Leipzig, 1876, p. 483.
- [117] A. Clebsch. *Théorie de l’élasticité des corps solides*. Paris: Dunod, 1883, p. 900.
- [118] S. Neukirch. “Enroulement, contact et vibrations de tiges élastiques”. PhD thesis. 2009, p. 97.
- [119] S. Timoshenko. “On the correction for shear of the differential equation for transverse vibrations of prismatic bars”. In: *Philosophical Magazine Series 6* 41.245 (1921), pp. 744–746.

- [120] J. C. Simo and L. Vu-Quoc. “A Geometrically-exact rod model incorporating shear and torsion-warping deformation”. In: *International Journal of Solids and Structures* 27.3 (1991), pp. 371–393.
- [121] S. Antman. “Kirchhoff’s problem for nonlinearly elastic rods”. In: *Quarterly of Applied Mathematics* XXXIV.3 (1974), pp. 221–240.
- [122] D. Q. Cao and R. W. Tucker. “Nonlinear dynamics of elastic rods using the Cosserat theory: Modelling and simulation”. In: *International Journal of Solids and Structures* 45.2 (2008), pp. 460–477.
- [123] H. Lang and J. Linn. “Lagrangian field theory in space-time for geometrically exact Cosserat rods”. In: 150 (2009), p. 21.
- [124] J. Cisternas and P. Holmes. “Buckling of extensible thermoelastic rods”. In: *Mathematical and Computer Modelling* 36.3 (2002), pp. 233–243.
- [125] D. Moulton, T. Lessinnes, and A. Goriely. “Morphoelastic rods. Part I : A single growing elastic rod”. In: *Journal of the Mechanics and Physics of Solids* 61.2 (2013), pp. 398–427.
- [126] C. Lázaro, S. Monleón, J. Bessini, and J. Casanova. “A review on geometrically exact models for very flexible rods”. In: *Proceedings of the IASS Annual Symposium 2016* (2016), pp. 1–10.
- [127] Y. Shi, A. E. Borovik, and J. E. Hearst. “Elastic rod model incorporating shear and extension, generalized nonlinear Schrödinger equations, and novel closed-form solutions for supercoiled DNA”. In: *The Journal of Chemical Physics* 103.8 (1995), pp. 3166–3183.
- [128] B. Coleman, E. H. Dill, M. Lembo, L. Zheng, and I. Tobias. “On the dynamics of rods in the theory of Kirchhoff and Clebsch”. In: *Archive for Rational Mechanics and Analysis* 121.4 (1993), pp. 339–359.
- [129] R. Casati and F. Bertails-descoubes. “Super space clothoids”. In: *SIGGRAPH*. 2013.
- [130] A. Campanile, M. Mandarino, V. Piscopo, and A. Pranzitelli. “On the exact solution of non-uniform torsion for beams with asymmetric cross-section”. In: *World Academy of Science, Engineering and Technology* 31 (2009), pp. 36–45.
- [131] L. Prandtl. “Zur torsion von prismatischen stäben”. In: *Physikalische Zeitschrift* 4 (1903), pp. 758–770.
- [132] K. Koohestani. “Nonlinear force density method for the form-finding of minimal surface membrane structures”. In: *Communications in Nonlinear Science and Numerical Simulation* 19.6 (2014), pp. 2071–2087.
- [133] S. Timoshenko and J. N. Goodier. *Theory of elasticity*. Second. New York: McGraw-Hill, 1951, p. 506.
- [134] S. Timoshenko. “Theory of bending, torsion and buckling of thin-walled members of open cross section : Part II.” In: *Journal of The Franklin Institute* 249.4 (1945), pp. 249–268.
- [135] V. Z. Vlasov. *Thin-walled elastic beams*. Second. National Technical Information Service, 1961.

- [136] E. Elter. “Two formulii of the shear center”. In: *Periodica Polytechnica Mechanical Engineering* 28.2-3 (1984), pp. 179–193.
- [137] J. M. Alves. “Dynamic analysis of bridge girders subjected to moving loads : Numerical and analytical beam models considering warping effects”. PhD thesis. Tecnico Lisboa, 2014, p. 129.

7 Numerical Model

7.1 Introduction

In this chapter we construct a novel discret beam element that we call the *biarc beam element*. It relies on the results from [chapter 4](#) and [chapter 6](#).

This element has a minimal number of degrees of freedom due to a reduced discrete curve-angle representation and can model extension, flexion and torsion of the rod in the framework of Kirchhoff theory. The introduction of ghost vertices enriches our previous model [42, 96] in order to better represent and localized discontinuities in the model. In particular this leads to a more accurate treatment of boundary conditions, connections and loadings. This element easily integrates inside a Dynamic Relaxation procedure to find the static equilibrium of nonlinear problems.

In the end, that makes this element very suitable for the modeling of elastic gridshells with anisotropic cross-sections and complex connections, which are known limitations of the classical 3-DOFs spline beam element [40, 26]. Moreovcer, the reduced formulation should improve both speed and stability of the numerical method compared to the classical 6-DOFs beam element [37, 29].

The interest of our approach is that the entire model is derived directly from the motion equations of the rod and thus is perfectly in the line of the pioneer works in this field [138].

7.1.1 Overview

We first construct a novel discret beam element called the *biarc model* (see §7.2). This element is based on Kirchhoff theory of slender rods presented in [chapter 6](#). The mechanical behavior of the element is derived entirely from the equations of motion [eq. \(6.67\)](#) summarized in §6.4 :

- we compute the discret force ($\boldsymbol{\eta}$) and moment ($\boldsymbol{\kappa}$) strain vectors from the geometry of the centerline ;
- we compute the bending moment (\mathbf{M}^\perp) at vertices from the material constitutive laws ;
- we compute the twisting moment (\mathbf{Q}) and the axial force (\mathbf{N}) at mid-edges from the material constitutive laws ;
- we compute the shear force (\mathbf{F}^\perp) at mid-edges from the equations of motion eq. (6.67d) and (6.67e) ;
- we interpolate the twisting moment and the axial and shear forces at vertices ;

Once the internal forces and moments acting on the vertices of the rod are known, we reinterpret the rod model as a simple *particle-spring* system (see §7.3). We study the motion of this system by integrating explicitly the motion equations of the particles with a simple finite difference scheme. The motion is artificially damped so the system falls into a state of static equilibrium. This method is called the *Dynamic Relaxation*. The dynamic itself is not a matter of concern as we are only interested in the steady state. Therefore, the parameters of the dynamic (mass and time step) are optimized to achieve *critical damping*, the damping for which the convergence is the fastest, and to ensure the numerical stability of the method.

Boundary conditions and connections between rods are treated separately (see §7.4). This topic is of special interest when modeling real structures, which is the ultimate goal.

The model has been implemented in a C# library called *Marsupilami*, intended to be a lightweight and dependence-free portable API. It is not a standalone executable software and has no graphical user-interface (GUI). To that purpose, a plugin for *Grasshopper* has also been implemented which serves as a functional GUI inside the *Rhinoceros* environnement. The core concepts of *Marsupilami* are presented in §7.5. This work was the occasion to develop a finer understanding of software architecture. Several guidelines are proposed to further develop what is more a prototype and validation code than a full-featured software.

Finally, several test cases are presented to validate the model (see §7.6).

7.1.2 Contributions

- We introduce a new 4-DOFs biarc kinematic to model the rod motion with ghost and handle vertices.
- We clarify the representation of edge and vertex quantities in a natural manner where material and cross-section properties are associated to the edges, and internal forces and moments are associated to the vertices.
- The biarc kinematic allows to model discontinuities at the junction between biarc segments.

- The mechanic of the rod is entirely derived from the motion equations.
- We give a full treatment of boundary conditions.
- We implement our element inside a Dynamic Relaxation algorithm.
- We use parallel transport only locally so that there is no more need to maintain a global reference frame for each beam.

7.1.3 Related works

Dynamic Relaxation

Day 1965 [138] introduces the *Dynamic Relaxation* method also presented by Otter et al. 1966 [139]. He remarks that for a damped system the “static equilibrium of a structure under a system of applied forces may be found by following the movement of the structure from its initial, un-deformed and unloaded, position until all vibrations resulting from its subsequent loading have died out”. He proposes to chose the damping factor to achieve critical damping, that is to obtained the fastest convergence to the steady state. He uses this computing method to study the non linear deformation of plan portal frames parametrized by two rotational degrees of freedom.

Cassel and Hobbs 1976 [140] study the stability of the method. They formulate a stability criterion expressed as a relation between the time step, the mass and the entries of the stiffness matrix. A similar criterion is formulated by Barnes 1975 [141]. Later, a proof of this criterion using Gershgorin theorem is made by Papadrakakis 1981 [142] and Underwood 1983 [143] who achieved automatic determination of the Dynamic Relaxation parameters to ensure stability but no necessarily critical damping.

Barnes 1977 [144] uses the Dynamic Relaxation to design and analyze nonlinear cable, membrane and inflatable structures. Wakefield 1980 [145] uses Dynamic Relaxation to study pretension networks with compression arches. He remarks that the method can be interpreted as a first order gradient optimization method. He first introduces a simplified planar bending element [145, p. 120], which is the parent of the classical 3-DOFs spline beam element. A review of the work from Barnes, Wakefield and Papadrakakis is available in [39].¹

Interesting investigations of the use of Dynamic Relaxation are proposed by [146] for the study of inflatable structures and by Dang and Meguid 2010 [147] for geotechnical engineering. da Silva et al. 2006 [148] shows the efficiency of the Dynamic Relaxation method compare to the Newton-Rapshon method in the nonlinear simulation of flexible lines. He highlights the robustness of the Dynamic Relaxation method, able to reach convergence where the Newton-Rapshon method fails.

Rezaiee-Pajand et al. 2012 [149] proposes a very large scope benchmark of Dynamic Relaxation method variants. His results show that the kinetic damping variant [150] has

¹Wakefield and Papadrakakis were phd students of Barnes in the late 70's.

generally the fastest convergence CPU speed, while the viscous damping variant from Underwood [143] generally converges with the smallest number of iterations.

Miki et al. 2014 [151] also interpret Dynamic Relaxation as a gradient descent method. They extend the method to integrate equality constraint conditions. However, the proposed method does not exhibit a better convergence speed than the one with kinetic damping.

Bathe is a reference author in the field of structural dynamics. He has worked on many time integration methods, either implicit or explicit [152]. His work could be a valuable starting point to pick new ideas to improve the time integration scheme presented in this thesis, if the dynamic of the structure were to be studied for instance.

Discrete element

The classical 3-DOFs spline beam element is formulated by Adriaenssens, Barnes, and Williams [39, 38, 40]. This model is used by [26] for the formfinding of elastic gridshells in composite materials. They Improve the calculation of the lumped mass to take account for the geometric bending stiffness of the element. They formulate a connection model that takes into account the eccentricity between the structural members.

Adriaenssens 2000 [37] introduces a 6-DOFs beam element compatible with the Dynamic Relaxation method. This element is implemented by Olsson and Fisher 2012 [35], Poulsen 2015 [36] and [29] in custom numerical frameworks to study nonlinear behavior of grid structures.

A first attempt to formulate a reduced model that takes into account torsion in the element is made by Barnes et al. 2013 [41]. Twisting is evaluated by the measure of the geometric torsion of the centerline, which obviously gives correct results in very special cases. Following Bergou et al. 2008 [91], Tayeb, Lefevre and du Peloux propose a novel 4-DOFs beam element suitable for the structural analysis of elastic gridshells [42, 96]. A closely related work is proposed by D'Amico et al. 2016 [43] but relies on a Catmull-Rom spline interpolation that complexifies the treatment of the element end nodes.

Duan et al. 2013 [153] developpes a geometrically exact beam model with a finite-element formulation to capture dynamic elastic deformations of slender bodies. The ordinary differential equations are solved using a multiple shooting algorithm based on numerical integration with Runge–Kutta method. Although the results show a good accuracy, the computational cost seems prohibitive for real time rendering of grid structures with a large number of connections.

7.2 Discret beam element

Let us introduce the discrete *biarc* model to describe the configuration of a beam. It is composed of a discrete curve called *centerline* (Γ) and a discrete adapted frame called *material frame* as its axes are chosen to be the principal axes of the beam cross-section

(fig. 7.1a). The centerline itself is organized in n_s consecutive adjacent *segments* which are three-vertices and two-edges elements with uniform material and section properties.

Elements can either be closed or open. The relations between the corresponding number of vertices, edges and segments are reported in §7.5.1.

7.2.1 Description of the element

Here we present how we model all the required informations involved in the element representation : its geometry (centerline, material frames, cross-sections), its materiality (elastic and shear modulus) and its mechanical state (internal forces and moments). An element is also subject to external loads (external forces and moments).

Centerline

The discrete centerline is a polygonal space curve (fig. 7.1a) defined as an ordered sequence of $n + 1$ pairwise disjoint *vertices* : $\Gamma = (\mathbf{x}_0, \mathbf{x}_1, \dots, \mathbf{x}_n) \in \mathbb{R}^{3(n+1)}$. Consecutive pairs of vertices define n straight segments $(\mathbf{e}_0, \mathbf{e}_1, \dots, \mathbf{e}_{n-1})$ called *edges* and pointing from one vertex to the next one :

$$\mathbf{e}_i = \mathbf{x}_{i+1} - \mathbf{x}_i \quad (7.1a)$$

$$l_i = \|\mathbf{e}_i\| \quad (7.1b)$$

$$\mathbf{u}_i = \mathbf{e}_i / l_i = \mathbf{d}_{3,i+1/2} \quad (7.1c)$$

The length of the i th edge is denoted l_i and its normalized direction vector is denoted \mathbf{u}_i . The arc length of the i th vertex is denoted s_i and is given by :

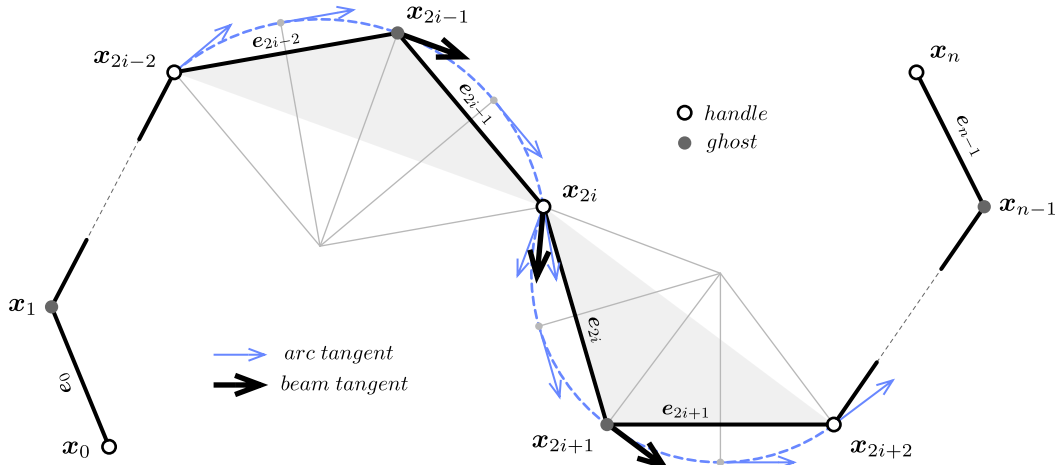
$$\begin{cases} s_0 = 0 & i = 0 \\ s_i = \sum_{k=0}^{i-1} l_k & i \in [1, n-1] \\ s_n = L & i = n \end{cases} \quad (7.2)$$

Thus, the centerline is parametrized by arc length and $\Gamma(s_i) = \mathbf{x}_i$. Additionally, we define the vertex-based mean length at vertex \mathbf{x}_i :

$$\begin{cases} \bar{l}_0 = \frac{1}{2}l_0 & i = 0 \\ \bar{l}_i = \frac{1}{2}(l_{i-1} + l_i) & i \in [1, n-1] \\ \bar{l}_n = \frac{1}{2}l_{n-1} & i = n \end{cases} \quad (7.3)$$

Segments

The discrete centerline is divided into n_s curved segments. Each segment is a three-noded element where the area covered by a segment is represented as a grey solid hatch (see fig. 7.1a). The i th segment is composed of three vertices $(\mathbf{x}_{2i}, \mathbf{x}_{2i+1}, \mathbf{x}_{2i+2})$ spanning two



(a) Centerline of the discrete biarc model.

Centerline			
Item	Symbol	Open	Closed
segments	n_s	n_s	n_s
edges	n_e	$2n_s$	$2n_s$
vertices	n	$2n_s + 1$	$2n_s$
ghosts	n_g	n_s	n_s
handles	n_h	$n_s + 1$	n_s

(b) Number of segments, edges and vertices whether the centerline is closed or open.

Figure 7.1 – Biarc model for a discrete beam element. The centerline is divided into curved segments (grey solid hatch). Each segment is defined as a three-noded element with uniform material and section properties. It has two end vertices (white) called *handle* as they are used to interact with the model, for instance to apply loads or restraints. It has one mid vertex (grey) called *ghost* as it is used only to enrich the segment kinematics and is not accessible to the end user.

edges $(\mathbf{e}_{2i}, \mathbf{e}_{2i+1})$. The $(i - 1)$ th segment and the i th segment share the same vertex \mathbf{x}_{2i} at arc length s_{2i} .

Each segment has two end vertices called *handle* ($\mathbf{x}_{2i}, \mathbf{x}_{2i+2}$) and one mid vertex called *ghost* (\mathbf{x}_{2i+1}) as this one is not accessible to the end user in order to interact with the model (link, restrain, loading, ...). Ghost vertices are used only for internal purpose to give a higher richness in the kinematic description of a segment than a two-noded segment would.

Finally, we define the *chord length* of the i th segment as the distance between \mathbf{x}_{2i} and \mathbf{x}_{2i+2} :

$$L_i = \|\mathbf{e}_{2i} + \mathbf{e}_{2i+1}\| , \quad i \in \llbracket 0, n_s - 1 \rrbracket \quad (7.4)$$

Material frames

A discrete material frame $\{\mathbf{d}_1, \mathbf{d}_2, \mathbf{d}_3\}_i$ is associated to each vertex \mathbf{x}_i . $\mathbf{d}_{1,i}$ and $\mathbf{d}_{2,i}$ are chosen to be aligned with the principle axes of the cross-section at vertex \mathbf{x}_i . At mid edge, the definition of $\mathbf{d}_{3,i+1/2}$ is consistent with the discrete curvature based on the circumscribed osculating circle (see §4.8.1).

Material and section properties

In addition, the model assumes that a segment has uniform section $(S, I_1, I_2, J)^2$ and material $(E, G)^3$ properties over its length $s \in]s_{2i}, s_{2i+2}[$. For the sake of simplicity, we introduce for further calculations the *material stiffness matrix* (\mathbf{B}_i) attached to each segment. It has the following form in the material frame basis :

$$\mathbf{B}_i = \begin{bmatrix} EI_1 & 0 & 0 \\ 0 & EI_2 & 0 \\ 0 & 0 & GJ \end{bmatrix}_i , \quad i \in \llbracket 0, n_s - 1 \rrbracket \quad (7.5)$$

where EI_1 and EI_2 are the bending stiffnesses and GJ is the torsional stiffness. The axial stiffness of the i th segment is denoted by :

$$ES_i , \quad i \in \llbracket 0, n_s - 1 \rrbracket \quad (7.6)$$

Internal forces and moments

The discrete rod is subjected to internal forces ($\mathbf{F} = F_1 \mathbf{d}_1 + F_2 \mathbf{d}_2 + N \mathbf{d}_3$) and moments ($\mathbf{M} = M_1 \mathbf{d}_1 + M_2 \mathbf{d}_2 + Q \mathbf{d}_3$). Their components in the material frame basis are named as follow :

² S is the cross-section area ; I_1, I_2 and J are the principal moments of inertia of the cross-section.

³ E is the elastic modulus and G is the shear modulus for the considered material

- The shear force : $\mathbf{F}^\perp = F_1 \mathbf{d}_1 + F_2 \mathbf{d}_2$
- The axial force : $\mathbf{N} = N \mathbf{d}_3$
- The bending moment : $\mathbf{M}^\perp = M_1 \mathbf{d}_1 + M_2 \mathbf{d}_2$
- The twisting moment : $\mathbf{Q} = Q \mathbf{d}_3$

Distributed loads

The model assumes that each segment can be loaded with some distributed forces ($\mathbf{f}^{ext} = f_k \mathbf{d}_k$) and moments ($\mathbf{m}^{ext} = m_k \mathbf{d}_k$). These forces and moments are required to be uniform over each segment but can vary from one segment to another. They can represent body loads such as self weight or thermal loads or external loads such as wind, snow, pressure, ...

Concentrated loads

Additional External concentrated forces (\mathbf{F}^{ext}) and moments (\mathbf{M}^{ext}) are applied to the segment's end vertices ($\mathbf{x}_{2i}, \mathbf{x}_{2i+2}$). Note that the model does not allow to load ghost vertices, and this is precisely why they are called "ghost".

7.2.2 Modeling of discontinuities

The model assumes that cross-section and material properties as well as distributed loads are uniform over each segment. Referring to the structure of the equations of motion, and because the centerline is required to be a regular curve in the stress-free configuration, strains, stresses, displacements, internal forces and internal moments must be piecewise continuous functions of the arc length parameter, continuous over each segment $[s_{2i}, s_{2i+2}]$. Discontinuities of these functions might occur at handle vertices (\mathbf{x}_{2i}), for instance if there is a jump in material or cross-section properties or if concentrated loads are applied at handle vertices. Moreover, the centerline curve itself will stay \mathcal{C}^1 during the motion, as it is chosen to be \mathcal{C}^1 in the reference configuration.^{4,5}

Here and subsequently, for such a function, the left and right limits at handle vertices (s_{2i}) will be denoted with superscripts f_{2i}^- and f_{2i}^+ . Possibly, the function is continuous so that the left and right limits agree ($f_{2i}^- = f_{2i}^+$).

⁴This preclude the modeling of beams with kinks as the tangent vector would not be continuously defined at these points. In such a case, the beam should be modeled in two separate parts linked together in a rigid manner.

⁵The centerline is not necessarily \mathcal{C}^2 as discontinuities in curvature may occur. For instance, if no punctual loads are applied, the bending moment is continuous over the rod. As the bending moment is linked to the curvature through the constitutive equation $M = EI\kappa$, a discontinuity in I will lead to a discontinuity in κ . Conversely, a discontinuity in κ will lead to a discontinuity in I .

7.2.3 Matrix notation

Here and subsequently, matrix notation will often be used to provide compact expressions for the equations, where the components of vector-valued functions are given in the material frame basis. This notation will be mixed with the vector notation employed more generally throughout this document. Usually, if there is no comment in the manuscript, the meaning should be obvious and with no ambiguity to the reader.

For instance, all this expressions for the curvature binormal vector and the material curvatures vector will be considered equivalent and could be mixed together in the same equation :

$$\boldsymbol{\kappa} \mathbf{b} = \kappa_1 \mathbf{d}_1 + \kappa_2 \mathbf{d}_2 = [\kappa_1 \quad \kappa_2 \quad 0]^T \quad (7.7a)$$

$$\boldsymbol{\varkappa} = \varkappa_1 \mathbf{d}_1 + \varkappa_2 \mathbf{d}_2 + \varkappa_3 \mathbf{d}_3 = [\varkappa_1 \quad \varkappa_2 \quad \varkappa_3]^T = (1 + \epsilon) [\kappa_1 \quad \kappa_2 \quad \tau]^T \quad (7.7b)$$

The force strains vector is given by :

$$\boldsymbol{\eta} = (1 + \epsilon) \mathbf{d}_3 = [0 \quad 0 \quad 1 + \epsilon]^T \quad (7.8)$$

Internal forces are composed of a shear force and an axial force given by :

$$\mathbf{F} = F_1 \mathbf{d}_1 + F_2 \mathbf{d}_2 + N \mathbf{d}_3 = [F_1 \quad F_2 \quad N]^T \quad (7.9a)$$

$$\mathbf{F}^\perp = F_1 \mathbf{d}_1 + F_2 \mathbf{d}_2 = [F_1 \quad F_2 \quad 0]^T \quad (7.9b)$$

$$\mathbf{F}^\parallel = \mathbf{N} = N \mathbf{d}_3 = [0 \quad 0 \quad N]^T \quad (7.9c)$$

Internal moments are composed of a bending moment and a twisting moment given by :

$$\mathbf{M} = M_1 \mathbf{d}_1 + M_2 \mathbf{d}_2 + Q \mathbf{d}_3 = [M_1 \quad M_2 \quad Q]^T \quad (7.10a)$$

$$\mathbf{M}^\perp = M_1 \mathbf{d}_1 + M_2 \mathbf{d}_2 = [M_1 \quad M_2 \quad 0]^T \quad (7.10b)$$

$$\mathbf{M}^\parallel = \mathbf{Q} = Q \mathbf{d}_3 = [0 \quad 0 \quad Q]^T \quad (7.10c)$$

With the help of the matrix notation, the constitutive equations eq. (6.63b) to (6.63d) together write in a single equation :

$$\mathbf{M} = \mathbf{B}(\boldsymbol{\varkappa} - \bar{\boldsymbol{\varkappa}}) = EI_1(\varkappa_1 - \bar{\varkappa}_1)\mathbf{d}_1 + EI_2(\varkappa_2 - \bar{\varkappa}_2)\mathbf{d}_2 + GJ(\varkappa_3 - \bar{\varkappa}_3)\mathbf{d}_3 \quad (7.11)$$

7.2.4 Discret extension and axial force

We assume the axial force (\mathbf{N}) to vary linearly over $[\mathbf{x}_{2i}, \mathbf{x}_{2i+2}]$ regarding the arc length parameter. The variation occurs if the segment is subject to a uniform distributed load f_3 over the segment. Consequently, the axial strain ϵ is also required to vary linearly. The

value of the axial extension at mid span of each edge is given by :

$$\epsilon_{i+1/2} = l_i / \bar{l}_i - 1 , \quad i \in [0, n_e - 1] \quad (7.12)$$

Consequently, the axial force at mid span of each edge is computed directly with the constitutive equation eq. (6.63a) as :

$$N_{2i+1/2} = N_{2i+1/2} \mathbf{u}_{2i} , \quad N_{2i+1/2} = E S_i \epsilon_{2i+1/2} \quad (7.13a)$$

$$N_{2i+3/2} = N_{2i+3/2} \mathbf{u}_{2i+1} , \quad N_{2i+3/2} = E S_i \epsilon_{2i+3/2} \quad (7.13b)$$

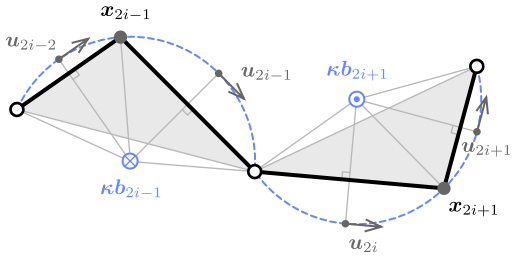
Remark the sign convention : as expected, when edge e_i suffers a positive extension ($\epsilon_{i+1/2} > 0$), vertex x_{i+1} “attracts” vertex x_i to it as $d_{3,i+1/2} = u_i$ is pointing from x_i towards x_{i+1} . Remark also that $\epsilon_{i+1/2} = 0 \Leftrightarrow l_i = \bar{l}_i$ when the rod is not stretched.

7.2.5 Discret curvature and bending moment

We assume that the internal bending moment and curvature are quadratic functions of the arc length parameter over $[x_{2i}, x_{2i+2}]$. Although they must be continuous over this interval, they might be discontinuous at handle vertices and be subjected to jump discontinuities in direction and magnitude.

Geometric curvature at ghost vertices

For a given geometry of the centerline, the curvature binormal vector at ghost vertex x_{2i-1} (resp. x_{2i+1}) is computed considering the circumscribed osculating circle passing through the vertices $(x_{2i-2}, x_{2i-1}, x_{2i})$ of the $(i-1)$ th segment – resp. through the vertices $(x_{2i}, x_{2i+1}, x_{2i+2})$ of the i th segment.

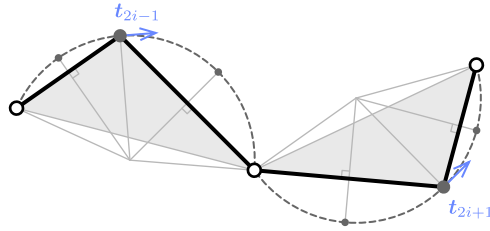


$$\kappa b_{2i-1} = \frac{2}{L_{i-1}} \mathbf{u}_{2i-2} \times \mathbf{u}_{2i-1}$$

$$\kappa b_{2i+1} = \frac{2}{L_i} \mathbf{u}_{2i} \times \mathbf{u}_{2i+1}$$

Unit tangent vector at ghost vertices

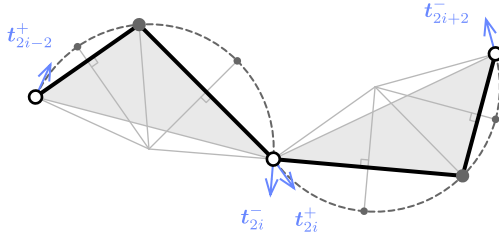
This definition of the curvature leads to a natural definition of the unit tangent vector at ghost vertex x_{2i-1} (resp. x_{2i+1}), as the unit vector tangent to the osculating circle of the $(i-1)$ th segment (resp. i th segment) at that point.



$$\begin{aligned} \mathbf{t}_{2i-1} &= \frac{l_{2i-1}}{L_{i-1}} \mathbf{u}_{2i-2} + \frac{l_{2i-2}}{L_{i-1}} \mathbf{u}_{2i-1} \\ \mathbf{t}_{2i+1} &= \frac{l_{2i+1}}{L_i} \mathbf{u}_{2i} + \frac{l_{2i}}{L_i} \mathbf{u}_{2i+1} \end{aligned}$$

Left/right unit tangent vector at handle vertices

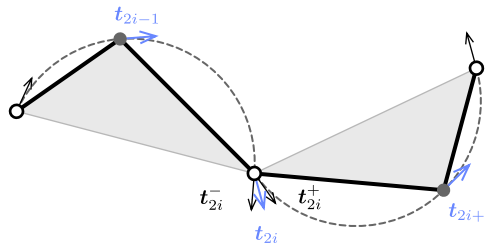
Equivalently, the definition of the osculating circles of the $(i - 1)$ th and i th segments leads to a natural definition of the left (\mathbf{t}_{2i}^-) and right (\mathbf{t}_{2i}^+) unit tangent vectors at handle vertex \mathbf{x}_{2i} , for segments of uniform curvature. When both segments have the same curvature, left and right vectors agree.



$$\begin{aligned} \mathbf{t}_{2i}^- &= 2(\mathbf{t}_{2i-1} \cdot \mathbf{u}_{2i-1}) \mathbf{u}_{2i-1} - \mathbf{t}_{2i-1} \\ \mathbf{t}_{2i}^+ &= 2(\mathbf{t}_{2i+1} \cdot \mathbf{u}_{2i}) \mathbf{u}_{2i} - \mathbf{t}_{2i+1} \end{aligned}$$

Unit tangent vector at handle vertices

The unit tangent vector \mathbf{t}_{2i} – that is the cross-section normal – at handle vertex \mathbf{x}_{2i} is chosen to be the mean of the left and right unit tangent vectors at that vertex.⁶



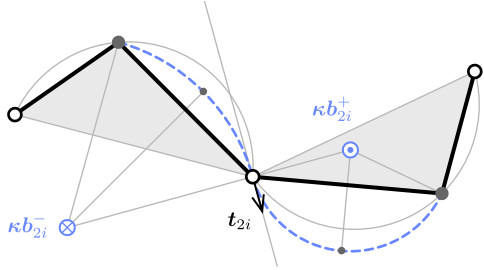
$$\mathbf{t}_{2i} = \frac{\mathbf{t}_{2i}^- + \mathbf{t}_{2i}^+}{\|\mathbf{t}_{2i}^- + \mathbf{t}_{2i}^+\|}$$

This way, the determination of the tangent vectors – or equivalently the section normals – in the static equilibrium configuration will be done in the flow of the Dynamic Relaxation process, without the need of introducing any additional degrees of freedom (for instance the usual Euler angles). The position of the vertices rules the orientation of the cross-section normals.

⁶Consequently, this model assumes that the field of tangents along the centerline is continuous and is thus unable to model cases where the centerline is not at least C^1 . In such case the beam must be considered as two parts glued together.

Left/right bending moment at handle vertices

Given the unit tangent vector \mathbf{t}_{2i} , one can define the left (κ_{2i}^-) and right (κ_{2i}^+) curvature at handle vertex \mathbf{x}_{2i} . The left curvature is initially evaluated from the left osculating circle, defined as the circle passing through \mathbf{x}_{2i-1} and \mathbf{x}_{2i} and tangent to \mathbf{t}_{2i} at \mathbf{x}_{2i} . The right curvature is initially evaluated from the right osculating circle, defined as the circle passing through \mathbf{x}_{2i} and \mathbf{x}_{2i+1} and tangent to \mathbf{t}_{2i} at \mathbf{x}_{2i} .^{7,8}



$$\begin{aligned}\kappa b_{2i}^- &= \frac{2}{l_{2i-1}} \mathbf{u}_{2i-1} \times \mathbf{t}_{2i} \\ \kappa b_{2i}^+ &= \frac{2}{l_{2i}} \mathbf{t}_{2i} \times \mathbf{u}_{2i}\end{aligned}$$

However, these values need to be adjusted so that the static condition for rotational equilibrium is satisfied at all time ($\mathbf{M}^{ext} + \mathbf{M}^+ - \mathbf{M}^- = 0$). Therefore, this condition will be satisfied in particular at the end of the solving process. To achieve this goal, we first compute a realistic mean value (\mathbf{M}_{2i}) for the internal bending moment as :

$$\mathbf{M}_{2i}^\perp = \frac{1}{2} \mathbf{B}_{i-1} (\kappa b_{2i}^- - \bar{\kappa b}_{2i}^-) + \frac{1}{2} \mathbf{B}_i (\kappa b_{2i}^+ - \bar{\kappa b}_{2i}^+) \quad (7.14)$$

To enforce the jump discontinuity in bending moment ($\mathbf{M}^{ext} = \mathbf{M}^- - \mathbf{M}^+$) across the handle vertex, we define the left and right bending moments at \mathbf{x}_{2i} as :

$$\mathbf{M}_{2i}^{\perp-} = \mathbf{M}_{2i}^\perp + \frac{1}{2} \mathbf{M}_{2i}^{\perp, ext} \quad (7.15a)$$

$$\mathbf{M}_{2i}^{\perp+} = \mathbf{M}_{2i}^\perp - \frac{1}{2} \mathbf{M}_{2i}^{\perp, ext} \quad (7.15b)$$

Note that in the case where no external concentrated bending moment is applied to the handle vertex, the internal bending moment is continuous across the vertex as expected.

⁷Remark that the centerline is now approximated with a biarc in the vicinity of \mathbf{x}_{2i} . This is the reason why this model is called the “biarc model”.

⁸This model offers the ability to represent discontinuities in curvature – thus in bending moment – at handle vertices as the left and right curvatures does not necessarily agree. This is quite different from the classical 3-dof element [39, 38, 26] which assumes that the curvature – thus the bending moment – is C^0 and can be evaluated at every vertices from the circumscribed osculating circle.

Left/right curvature at handle vertices

Finally, the left and right curvature at handle vertex \mathbf{x}_{2i} are computed back with the constitutive law :

$$\kappa b_{2i}^- = \mathbf{B}_{i-1}^{-1} \mathbf{M}_{2i}^{\perp -} + \bar{\kappa} b_{2i}^- \quad (7.16a)$$

$$\kappa b_{2i}^+ = \mathbf{B}_i^{-1} \mathbf{M}_{2i}^{\perp +} + \bar{\kappa} b_{2i}^+ \quad (7.16b)$$

Bending moment at ghost vertices

The internal bending moment at ghost vertices is simply given by the constitutive law as :

$$\mathbf{M}_{2i-1}^{\perp} = \mathbf{B}_{i-1}(\kappa b_{2i-1} - \bar{\kappa} b_{2i-1}) \quad (7.17a)$$

$$\mathbf{M}_{2i+1}^{\perp} = \mathbf{B}_i(\kappa b_{2i+1} - \bar{\kappa} b_{2i+1}) \quad (7.17b)$$

7.2.6 Discret rate of twist and twisting moment

We assume the twisting moment and the rate of twist to vary linearly over $[\mathbf{x}_{2i}, \mathbf{x}_{2i+2}]$. Thus, the material twist of the rod at mid edge is given by :

$$\tau_{i+1/2} = \frac{\Delta\theta_i}{l_i} \quad (7.18a)$$

$$\varkappa_{3,i+1/2} = \frac{\Delta\theta_i}{\bar{l}_i} \quad (7.18b)$$

To compute $\Delta\theta_i = \theta_{i+1} - \theta_i$ imagine that the rod si framed with a Bishop frame $\{\mathbf{u}, \mathbf{v}, \mathbf{t}\}$. Because the material frame $\{\mathbf{d}_1, \mathbf{d}_2, \mathbf{d}_3\}$ is also adapted to the rod centerline, it can be transformed into the Bishop frame with a single rotation of angle $\theta(s)$ around $\mathbf{d}_3(s) = \mathbf{t}(s)$. Because the Bishop frame does not twist around \mathbf{d}_3 , the rate of change of angle θ along the curve directly leads to the computation of the rate of twist as exposed in eq. (7.18b).

In the discrete case, although it is possible to frame the whole curve with a Bishop frame to achieve the computation of the rate of twist [96], it is more convenient to measure $\Delta\theta_i$ step by step using the existing material frames at vertices \mathbf{x}_i and \mathbf{x}_{i+1} . This is done in a two step process :

1. Parallel transport the material frame $\{\mathbf{d}_{1,i}, \mathbf{d}_{2,i}, \mathbf{d}_{3,i}\}$ at vertex \mathbf{x}_i onto vertex \mathbf{x}_{i+1} . We call $\{\mathbf{d}_{1,i}^{\parallel}, \mathbf{d}_{2,i}^{\parallel}, \mathbf{d}_{3,i}^{\parallel}\}$ the resulting framed positioned at \mathbf{x}_{i+1} such that $\mathbf{d}_{3,i}^{\parallel} = \mathbf{d}_{3,i+1}$.
2. Measure $\Delta\theta_i = \angle(\mathbf{d}_{1,i}^{\parallel}, \mathbf{d}_{1,i+1}) = \angle(\mathbf{d}_{2,i}^{\parallel}, \mathbf{d}_{2,i+1})$ as the oriented angle needed to align $\mathbf{d}_{1,i}^{\parallel}$ with $\mathbf{d}_{1,i+1}$ (or $\mathbf{d}_{2,i}^{\parallel}$ with $\mathbf{d}_{2,i+1}$) by a rotation of angle $\Delta\theta_i$ around $\mathbf{d}_{3,i+1} = \mathbf{t}_{i+1}$.

Consequently, the twisting moment at mid span of each edge is computed directly with the

appropriate constitutive equation :

$$\mathbf{Q}_{2i+1/2} = Q_{2i+1/2} \mathbf{u}_{2i} \quad , \quad Q_{2i+1/2} = G J_i (\varkappa_{3,2i+1/2} - \bar{\varkappa}_{3,2i+1/2}) \quad (7.19a)$$

$$\mathbf{Q}_{2i+3/2} = Q_{2i+3/2} \mathbf{u}_{2i+1} \quad , \quad Q_{2i+3/2} = G J_i (\varkappa_{3,2i+3/2} - \bar{\varkappa}_{3,2i+3/2}) \quad (7.19b)$$

Remark the sign convention : as expected, when edge e_i suffers a positive twist ($\varkappa_{3,i+1/2} > 0$), frame $\{\mathbf{d}_{1,i+1}, \mathbf{d}_{2,i+1}, \mathbf{d}_{3,i+1}\}$ makes frame $\{\mathbf{d}_{1,i}, \mathbf{d}_{2,i}, \mathbf{d}_{3,i}\}$ to rotate positively around \mathbf{u}_i as $Q_{i+1/2} > 0$.

7.2.7 Discret shear force

Recall that in Kirchhoff's theory the shear force is a reacting parameter, computed from the equilibrium equations and not from a constitutive law. Firstly, remark that the shear force can be factorized under the following expression :

$$\mathbf{F}^\perp = F_1 \mathbf{d}_1 + F_2 \mathbf{d}_2 = -\mathbf{d}_3 \times (\mathbf{d}_3 \times \mathbf{F}) \quad (7.20)$$

Then, combining eq. (6.67d) and (6.67e) – where the inertial terms are neglected – with eq. (7.20) leads to the following vectoriel form of the shear force :

$$\mathbf{F}^\perp = (1 + \epsilon)^{-1} \mathbf{d}_3 \times \left(\frac{\partial \mathbf{M}}{\partial s} + \mathbf{m} \right) = \mathbf{d}_3 \times \left(\frac{\partial \mathbf{M}}{\partial s_t} + \frac{\mathbf{m}}{1 + \epsilon} \right) \quad (7.21)$$

In the discrete case, the shear force is evaluated at mid span of each edge by :

$$\mathbf{F}_{2i+1/2}^\perp = \mathbf{u}_{2i} \times \left(\frac{\mathbf{M}_{2i+1} - \mathbf{M}_{2i}^+}{l_{2i}} + \frac{\bar{l}_{2i}}{l_{2i}} \mathbf{m}_i \right) \quad (7.22a)$$

$$\mathbf{F}_{2i+3/2}^\perp = \mathbf{u}_{2i+1} \times \left(\frac{\mathbf{M}_{2i+2}^- - \mathbf{M}_{2i+1}}{l_{2i+1}} + \frac{\bar{l}_{2i+1}}{l_{2i+1}} \mathbf{m}_i \right) \quad (7.22b)$$

Remark that the derivative of the internal moment at mid edge is evaluated by the finite difference of the moment between the two closest vertices. This is in accordance with the quadratic interpolation method of a vector-valued function given in appendix C.

Expressed in the form of eq. (7.22a) and (7.22b), the discrete shear force has the interesting property to remain strictly orthogonal to $\mathbf{d}_{3,i+1/2} = \mathbf{u}_i$. While this is true in the continuous world, this property can easily be lost in the discrete case where mean values and derivatives are evaluated through finite summations or finite differences.

Matrix notation

Because there is a derivation with respect to s in eq. (7.22a) and (7.22b), one must be very careful when writing these equations in matrix notation. Indeed, their counterparts will translate differently whether the symbols will be decomposed in the *global* frame basis or in the *material* frame basis.

If the symbols are decomposed in the *global* frame basis the translation is straightforward as the derivative of a vector is the vector of the derived components :

$$\mathbf{M} = \begin{bmatrix} M_x \\ M_y \\ M_z \end{bmatrix}, \quad \mathbf{M}' = \begin{bmatrix} M_x \\ M_y \\ M_z \end{bmatrix}' = \begin{bmatrix} M'_x \\ M'_y \\ M'_z \end{bmatrix} \quad (7.23)$$

Thus, in the discrete case, the evaluation of the derivative of the moment at mid-edge is achieved thanks to the finite difference formula :

$$\mathbf{M}'_{2i+1/2} \simeq \frac{1}{l_{2i}} \left([M_x \ M_y \ M_z]_{2i+1}^T - [M_x \ M_y \ M_z]_{2i}^T \right) \quad (7.24)$$

However, if the symbols are given in the *material* frame basis, the derivation must take into account the spatial velocity $\boldsymbol{\varkappa}$ of the material frame :

$$\mathbf{M} = \begin{bmatrix} M_1 \\ M_2 \\ Q \end{bmatrix}, \quad \mathbf{M}' = \begin{bmatrix} M_1 \\ M_2 \\ Q \end{bmatrix}' = \begin{bmatrix} M'_1 \\ M'_2 \\ Q' \end{bmatrix} + \begin{bmatrix} \boldsymbol{\varkappa}_1 \\ \boldsymbol{\varkappa}_2 \\ \boldsymbol{\varkappa}_3 \end{bmatrix} \times \begin{bmatrix} M_1 \\ M_2 \\ Q \end{bmatrix} \quad (7.25)$$

Thus, in the discrete case, the evaluation of the derivative of the moment at mid-edge is still achieved thanks to the finite difference formula, but takes a very different matrix form :

$$\begin{aligned} \mathbf{M}'_{2i+1/2} &\simeq \frac{1}{l_{2i}} \left([M_1 \ M_2 \ Q]_{2i+1}^T - [M_1 \ M_2 \ Q]_{2i}^T \right) \\ &+ \frac{1}{2} \left([\boldsymbol{\varkappa}_1 \ \boldsymbol{\varkappa}_2 \ \boldsymbol{\varkappa}_3]_{2i}^T + [\boldsymbol{\varkappa}_1 \ \boldsymbol{\varkappa}_2 \ \boldsymbol{\varkappa}_3]_{2i+1}^T \right) \\ &\times \frac{1}{2} \left([M_1 \ M_2 \ Q]_{2i}^T + [M_1 \ M_2 \ Q]_{2i+1}^T \right) \end{aligned} \quad (7.26)$$

Although this paragraph could seem superfluous to the reader, this point is a matter of concern when implementing the model into an algorithm. Indeed, the developer always has the choice between two natural data structures where vectors are represented by a triplet either in the global frame basis or in the material frame basis (see eq. (7.5)). Even more, he can decide to mix the two for practical reasons, for instance if it leads to less arithmetic computations. In particular, the stiffness matrix has a nice diagonal shape when written in the material frame basis. Thus it seems desirable to do the computation of the bending moment in this basis. On the contrary, we have just seen that it seems easier to compute the shear force in the global frame basis.

7.2.8 Interpolation of the internal forces and moments

At this point, for a given geometric configuration, we know how to compute the bending moment at vertices. But we only know how to compute the twisting moment, the axial force and the shear force at mid edges. However, our final goal is to describe the discrete rod as a particle-spring system were mass is lumped at vertices and elements are modeled as interactions between vertices. In this representation, all actions must be resumed to

vertex actions, the only conceptual entity that will have a meaning to the dynamic process.

Therefore, we need to express the value of the twisting moment, the axial force and the shear force at vertices and not only at mid edges. This can be done using [eq. \(6.67\)](#) were the inertial member is set to zero, that is neglecting the inertial forces. Although this is not exactly true during the dynamic of the rod, it is exactly true at static equilibrium, the only state we are interested in.

Axial force

From [eq. \(6.67c\)](#) we evaluate the variation of the axial force over a segment $[x_i, x_{i+1}]$ and deduce the variation of the axial strain from the constant axial stiffness ES_i of the segment :

$$\Delta N_{i+1/2} = -l_i \cdot [\kappa_1 F_2 - \kappa_2 F_1 + f_3]_{i+1/2} \quad (7.27a)$$

$$\Delta \epsilon_{i+1/2} = \Delta N_{i+1/2} / ES_i \quad (7.27b)$$

Then we conclude on the expression of the axial force at vertices :

$$N_i^+ = N_{i+1/2} - \frac{1}{2} \Delta N_{i+1/2} \quad (7.28a)$$

$$N_{i+1}^- = N_{i+1/2} + \frac{1}{2} \Delta N_{i+1/2} \quad (7.28b)$$

and the expression of the axial strain at vertices :

$$\epsilon_i^+ = \epsilon_{i+1/2} - \frac{1}{2} \Delta \epsilon_{i+1/2} \quad (7.29a)$$

$$\epsilon_{i+1}^- = \epsilon_{i+1/2} + \frac{1}{2} \Delta \epsilon_{i+1/2} \quad (7.29b)$$

Remark how a distributed external axial force (f_3) modifies the value of the axial component of the internal force at vertices, and thus is taken into account in the final static equilibrium.

Shear force

From [eq. \(6.67a\)](#) and [\(6.67b\)](#) we evaluate the variation of the shear force over a segment $[x_i, x_{i+1}]$:

$$\Delta F_{1,i+1/2} = -l_i \cdot [\kappa_2 F_3 - \kappa_3 F_2 + f_1]_{i+1/2} \quad (7.30a)$$

$$\Delta F_{2,i+1/2} = -l_i \cdot [\kappa_3 F_1 - \kappa_1 F_3 + f_2]_{i+1/2} \quad (7.30b)$$

Then we conclude on the expression of the shear force components at vertices :

$$F_{1,i}^+ = F_{1,i+1/2} - \frac{1}{2} \Delta F_{1,i+1/2} \quad (7.31a)$$

$$F_{1,i+1}^- = F_{1,i+1/2} + \frac{1}{2} \Delta F_{1,i+1/2} \quad (7.31b)$$

$$F_{2,i}^+ = F_{2,i+1/2} - \frac{1}{2} \Delta F_{2,i+1/2} \quad (7.31c)$$

$$F_{2,i+1}^- = F_{2,i+1/2} + \frac{1}{2} \Delta F_{2,i+1/2} \quad (7.31d)$$

Remark how a distributed external shear force ($\mathbf{f}^\perp = f_1 \mathbf{d}_1 + f_2 \mathbf{d}_2$) modifies the value of the shear components of the internal force at vertices, and thus is taken into account in the final static equilibrium.

Twisting moment

From eq. (6.67f) we evaluate the variation of the twisting moment over a segment $[\mathbf{x}_i, \mathbf{x}_{i+1}]$ and deduce the variation of twist from the constant torsional stiffness GJ_i of the segment :

$$\Delta Q_{i+1/2} = -l_i \cdot [\varkappa_1 M_2 - \varkappa_2 M_1 + m_3]_{i+1/2} \quad (7.32a)$$

$$\Delta \varkappa_{3,i+1/2} = \Delta Q_{i+1/2} / GJ_i \quad (7.32b)$$

Then we conclude on the expression of the twisting moment at vertices :

$$Q_i^+ = Q_{i+1/2} - \frac{1}{2} \Delta Q_{i+1/2} \quad (7.33a)$$

$$Q_{i+1}^- = Q_{i+1/2} + \frac{1}{2} \Delta Q_{i+1/2} \quad (7.33b)$$

and the expression of the rate of twist at vertices :

$$\varkappa_{3,i}^+ = \varkappa_{3,i+1/2} - \frac{1}{2} \Delta \varkappa_{3,i+1/2} \quad (7.34a)$$

$$\varkappa_{3,i+1}^- = \varkappa_{3,i+1/2} + \frac{1}{2} \Delta \varkappa_{3,i+1/2} \quad (7.34b)$$

Remark how a distributed external twisting moment (m_3) modifies the value of the axial component of the internal moment at vertices, and thus is taken into account in the final static equilibrium.

7.3 Dynamic Relaxation

From the previous section we have established the basis for a discrete rod element that can account for extension, flexion and torsion. This element is made of two types of vertices : the ghost and the handle vertices. This allows to model discontinuities at handle vertices, which is one of the main contribution of the work exposed in this chapter. We have established

a precise 4-DOFs discrete geometric representation of a slender rod. And from a given configuration we have learned to compute the internal forces and moments acting on the rod vertices using Kirchhoff's theory. Therefore, we are able to compute the resultant of the internal force and moment acting on a given vertex of the rod.⁹

We now expose a process to find the static equilibrium of a rod, which is our ultimate goal. This process is called *Dynamic Relaxation* and was first introduced by Day 1965 [138]. We assume that we know the stress-free configuration of the rod, its material properties and cross-section properties. The rod might also be subjected to known external loads such as climatic loads. Finally, we call initial configuration the actual configuration of the rod at time $t = 0$. In this configuration, the rod is (a priori) not at static equilibrium.

7.3.1 Overview of the procedure

In the Dynamic Relaxation procedure, a discretized mechanical system is dropped from a known initial configuration at time $t = 0$. Technically, the mechanical system is now idealized to a *particle-spring system* where each vertex is assimilated to a *particle*, also called *node*, represented by a material frame. Each particle has its own mass and is subjected to internal and external forces and moments. Because the system is not yet in a state of static equilibrium, the internal forces does not equilibrate the external forces. Thus, the system is subject to a motion. This motion is integrated through time and artificially damped. When all the kinetic energy is dissipated by the damping the system has reached a state of static equilibrium, which is the steady state response of the system.

Because the motion is only a mean to find a static equilibrium position of the system, the damping does not need to be realistic and should be chosen so that the system approaches the static position as fast as possible. This is also known as critical damping.

7.3.2 Resultants acting on a particle

In this section, we express the resultant force and the resultant twisting moment acting on a particle. If not balanced, these resultants will make the particle to move and rotate with respect to its degrees of freedom \boldsymbol{x} and θ .

Resultant force

The translational resultant force (\mathbf{R}_i^x) acting on a particle is the sum of two contributions. The first one (\mathbf{F}_i^{ext}) is the resultant of the concentrated forces applied to the particle such as climatic loads, support reactions or loads transferred through connections. The second one (\mathbf{F}_i^{int}) is the resultant of the internal forces applied by the upstream and downstream parts of the rod to the particle and are given by eq. (7.28) and (7.31). This leads to the

⁹Note that the internal forces and moments embed the action of distributed external forces and moments applied to the rod.

following equations : ¹⁰

$$\mathbf{R}_i^x = \mathbf{F}_i^{int} + \mathbf{F}_i^{ext} \quad (7.35a)$$

$$\mathbf{F}_i^{int} = -\mathbf{F}_i^- + \mathbf{F}_i^+ \quad (7.35b)$$

$$\mathbf{F}_i^- = F_{1,i}^- \mathbf{d}_{1,i} + F_{2,i}^- \mathbf{d}_{2,i} + N_i^- \mathbf{d}_{3,i} \quad (7.35c)$$

$$\mathbf{F}_i^+ = F_{1,i}^+ \mathbf{d}_{1,i} + F_{2,i}^+ \mathbf{d}_{2,i} + N_i^+ \mathbf{d}_{3,i} \quad (7.35d)$$

Note that the contribution of the distributed external forces (\mathbf{f}_i) is already taken into account via the interpolation of the internal force (see eq. (7.27a) and (7.30)). Likewise, the contribution of the distributed external bending moment (\mathbf{m}_i^\perp) is also taken into account via the calculation of the internal shear force (see eq. (7.22)). Finally, the contribution of the concentrated external bending moments is yet included via the expression of the discrete shear force (see eq. (7.15) and (7.22)).

Resultant twisting moment

In the same manner, the resultant twisting moment (R_i^θ) acting on a particle is the sum of two contributions.¹¹ The first one (Q_i^{ext}) is the resultant of the concentrated twisting moments applied to the particle. The second one (Q_i^{int}) is the resultant of the internal twisting moment applied by the upstream and downstream parts of the rod to the particle and given by eq. (7.33). This leads to the following equations :

$$R_i^\theta = Q_i^{int} + Q_i^{ext} \quad (7.36a)$$

$$Q_i^{int} = -Q_i^- + Q_i^+ \quad (7.36b)$$

Note that the contribution of the distributed external twisting moment (q_i^{ext}) is already taken into account via the interpolation of the internal twisting moment (see eq. (7.32a)).

7.3.3 Equations of motion

The particles of the system evolve according to the laws of motion, with respect to the 4 degrees of freedom of the system (\mathbf{x} and θ), given by :

$$m_i^x \ddot{\mathbf{x}}_i + \lambda_i^x \dot{\mathbf{x}}_i = \mathbf{R}_i^x \quad (7.37a)$$

$$m_i^\theta \ddot{\theta}_i + \lambda_i^\theta \dot{\theta}_i = R_i^\theta \quad (7.37b)$$

where $\ddot{\mathbf{x}}_i$ is the translational acceleration of the particle, $\ddot{\theta}_i$ is the rotational acceleration of the particle and λ_i^x and λ_i^θ are the viscous damping coefficients.

Hereinafter we will consider no viscous damping. Instead, we will rely on an artificial kinetic damping (see §7.3.5). For a detailed treatment of various damping methods in the

¹⁰Recall the convention from ?? : the internal force and moment are chosen to be the action of the downstream part of the rod upon the upstream part of the rod.

¹¹Actually, R_i^θ is the component of the resultant moment along $\mathbf{d}_{3,i}$. We only need to compute this component as we have only one rotational degree of freedom in our model.

Dynamic Relaxation method, refer to [143, 149].

Coupling between flexion and torsion

Although eq. (7.37a) and (7.37b) may seem uncoupled to the reader, it is not the case as the coupling occurs through the material frame (see §5.4.2). Recall that both \mathbf{R}_i^x and R_i^θ do depend on the \mathbf{x}_i and θ_i variables.

Nonlinearity

In a linear analysis the expression of the resultant force and the resultant moment would be linearized and written in the matrix form :

$$\mathbf{M}^x \ddot{\mathbf{X}} + \boldsymbol{\lambda}^x \dot{\mathbf{X}} = \mathbf{K}^x \mathbf{X} \quad (7.38a)$$

$$\mathbf{M}^\theta \ddot{\boldsymbol{\Theta}} + \boldsymbol{\lambda}^\theta \dot{\boldsymbol{\Theta}} = \mathbf{K}^\theta \boldsymbol{\Theta} \quad (7.38b)$$

where \mathbf{X} and $\boldsymbol{\Theta}$ are the column vectors of the translational (\mathbf{x}_i) and rotational (θ_i) degrees of freedom of the system ; \mathbf{M}^x and \mathbf{M}^θ are the mass matrices ; $\boldsymbol{\lambda}^x$ and $\boldsymbol{\lambda}^\theta$ are the damping matrices and \mathbf{K}^x and \mathbf{K}^θ are the stiffness matrices.¹²

Saying that the system is linearized involves that the dependence of \mathbf{R}_i^x and R_i^θ with respect to the degrees of freedom \mathbf{x}_i and θ_i will be modeled as a (linear) matrix product and that \mathbf{K}^x and \mathbf{K}^θ are computed independently of these variables. In other words, this means that \mathbf{R}_i^x and R_i^θ are calculated as a linear combination of the degrees of freedom, and that the coefficients of this combination are the matrix entries of \mathbf{K}^x and \mathbf{K}^θ .

Here, this factorization is not possible. \mathbf{R}_i^x and R_i^θ are computed from the degrees of freedom of the system but the relation is not linear (see how the internal force and moment are computed in §7.2). Therefore, the geometric system given in eq. (7.37a) and (7.37b) is effectively nonlinear.

7.3.4 Explicite time integration

In this section, we give the stages required to integrate these equations through time. The Dynamic Relaxation procedure is based on a central-difference scheme. We call h the time step. And we call *initial configuration* the configuration of the system at time $t = 0$.

Note that the time step h is not necessary constant through time and could be *adapted* during the analysis process. However, for simplicity we will treat only the case where it is constant but it is easy to extend the present work to work with a variable time step.

¹²For non linear simulation, the stiffness matrix is replaced by the *tangent* stiffness matrix and is reevaluated at each time step.

Acceleration

At time t , considering the position of the system is known (\mathbf{x}_i and $\{\mathbf{d}_{3,i}, \mathbf{d}_{1,i}, \mathbf{d}_{2,i}\}$), we can compute the resultant force (\mathbf{R}_i^x) and the resultant twisting moment (R_i^θ) acting on the particles (see §7.3.2). Using eq. (7.37) the acceleration of the particles at time t is straightforwardly deduced as :

$$\ddot{\mathbf{x}}_i^t = \frac{\mathbf{R}_i^{x,t}}{m_i^x} \quad (7.39a)$$

$$\ddot{\theta}_i^t = \frac{R_i^{\theta,t}}{m_i^\theta} \quad (7.39b)$$

Velocity

The translational and rotational velocities of a particle are evaluated with the following central difference scheme :

$$\dot{\mathbf{x}}_i^t = \frac{\dot{\mathbf{x}}_i^{t+h/2} - \dot{\mathbf{x}}_i^{t-h/2}}{h} \quad (7.40a)$$

$$\dot{\theta}_i^t = \frac{\dot{\theta}_i^{t+h/2} - \dot{\theta}_i^{t-h/2}}{h} \quad (7.40b)$$

where $\dot{\mathbf{x}}_i$ and $\dot{\theta}_i$ are the translational and rotational velocities of the particle. Thus, the velocity of a particle at time $t + h/2$ is computed from its velocity at time $t - h/2$ by :

$$\dot{\mathbf{x}}_i^{t+h/2} = \dot{\mathbf{x}}_i^{t-h/2} + h \cdot \frac{\mathbf{R}_i^{x,t}}{m_i^x} \quad (7.41a)$$

$$\dot{\theta}_i^{t+h/2} = \dot{\theta}_i^{t-h/2} + h \cdot \frac{R_i^{\theta,t}}{m_i^\theta} \quad (7.41b)$$

Position

To update the position of the system, we use the same central difference scheme but this time on the velocity :

$$\dot{\mathbf{x}}_i^{t+h/2} = \frac{\mathbf{x}_i^t - \mathbf{x}_i^{t-h}}{h} \quad (7.42a)$$

$$\dot{\theta}_i^{t+h/2} = \frac{\theta_i^t - \theta_i^{t-h}}{h} \quad (7.42b)$$

Thus, the translational and rotational positions of a particle at time $t + h$ are computed from the velocities at time $t + h/2$ by :

$$\mathbf{x}_i^{t+h} = \mathbf{x}_i^t + h \cdot \dot{\mathbf{x}}_i^{t+h/2} \quad (7.43a)$$

$$\theta_i^{t+h} = \theta_i^t + h \cdot \dot{\theta}_i^{t+h/2} \quad (7.43b)$$

Using eq. (7.41) the position at time $t + h$ can be expressed with respect to the position, velocity and resultants computed at time t as :

$$\mathbf{x}_i^{t+h} = \mathbf{x}_i^t + h \cdot \dot{\mathbf{x}}_i^{t-h/2} + h^2 \cdot \frac{\mathbf{R}_i^{x,t}}{m_i^x} \quad (7.44a)$$

$$\theta_i^{t+h} = \theta_i^t + h \cdot \dot{\theta}_i^{t-h/2} + h^2 \cdot \frac{\mathbf{R}_i^{\theta,t}}{m_i^\theta} \quad (7.44b)$$

Motion

From this new position, it is now possible to compute the new resultant force and moment acting on the particles, to update their acceleration, then to update their velocity, and then to compute the new position of the system, at time $t + 2h$. This process can be repeated indefinitely to follow the motion of the system.

Initialization

The iterative process described in this section to simulate step by step the motion of the system needs to be initialized. At the moment, eq. (7.44) only describes how to get the position of the system at $t + h$ knowing its position, velocity and acceleration at time t .

At time $t = 0$, or each time that the system will be damped (see §7.3.5), we consider that the system is released with no initial velocity, which means that :

$$\dot{\mathbf{x}}_i^0 = \frac{\mathbf{x}_i^{-h/2} + \mathbf{x}_i^{+h/2}}{2} \Rightarrow \dot{\mathbf{x}}_i^{-h/2} = -\dot{\mathbf{x}}_i^{+h/2} \quad (7.45a)$$

$$\dot{\theta}_i^0 = \frac{\theta_i^{-h/2} + \theta_i^{+h/2}}{2} \Rightarrow \dot{\theta}_i^{-h/2} = -\dot{\theta}_i^{+h/2} \quad (7.45b)$$

Therefore, the velocity at time $h/2$ given in eq. (7.41) becomes :

$$\dot{\mathbf{x}}_i^{+h/2} = \frac{1}{2}h \cdot \frac{\mathbf{R}_i^{x,t}}{m_i^x} \quad (7.46a)$$

$$\dot{\theta}_i^{+h/2} = \frac{1}{2}h \cdot \frac{\mathbf{R}_i^{\theta,t}}{m_i^\theta} \quad (7.46b)$$

and the next position at time $t + h$ is still computed from eq. (7.43).

Error propagation

Note that the motion will be realistic to the extent that the computed forces and moments will be realistic and to the extent that the time step will be small enough. Indeed, at each time step an approximation error is done in the evaluation of the velocity and the position of the system with the central difference scheme. This error is integrated through time and nothing here is done to correct it and to prevent its accumulation during the dynamic. It is not a matter of concern for us as we are only interested in the quasi-static response of the system and not in an accurate modeling of the system's motion. Moreover, higher accuracy numerical integrators would be more computationally expensive, which is against our goal to achieve real time interactive simulation of elastic gridshells.

Lots of other integration schemes exist, among which we can cite the *Explicit Euler*, the *Symplectic Euler*, the *Störmer-Verlet* and the *4th order Runge-Kutta* schemes. These schemes are briefly presented in [154]. For a complete treatment of numerical integrators refer to the book from Hairer and Wanner 2006 [155].

7.3.5 Damping

If no damping is introduced to dissipate some energy, there is no reason that the system will stop to move. Here, our goal is to dissipate the kinetic energy of the system as fast as possible to fall into a state of static equilibrium. This can be achieved with any kind of damping, among which the most well-known are *viscous damping* and *kinetic damping*.

Here, we choose to implement the kinetic damping as it is known to produce the best results for a wide range of cases [149].

Kinetic damping

Kinetic damping was first introduced by Cundall 1976 [156]. The idea behind this type of damping is simple. For a conservative system, the mechanical energy (\mathcal{E}_m) is conserved during motion and is the sum of two forms of energy : the potential energy (\mathcal{E}_p) and the kinetic energy (\mathcal{E}_k). Therefore, the potential energy of the system is minimized when its kinetic energy is maximized.

To find a state of static equilibrium, that is a state of minimal potential energy, Cundall proposes to track the kinetic energy of the system during motion. When a peak is detected, the system is frozen in its position and then released with no initial velocity, that is with no initial kinetic energy. When the system is released, the overall mechanical energy of the system has decreased and is all stocked under potential energy form. The motion starts again and part of the initial potential energy is converted to kinetic energy, until a new peak is detected. Progressively, from peak to peak, the potential energy is progressively lowered to a minimum and the system falls in a state of static equilibrium.

Because of the discrete nature of the numerical process, a peak of kinetic energy is detected

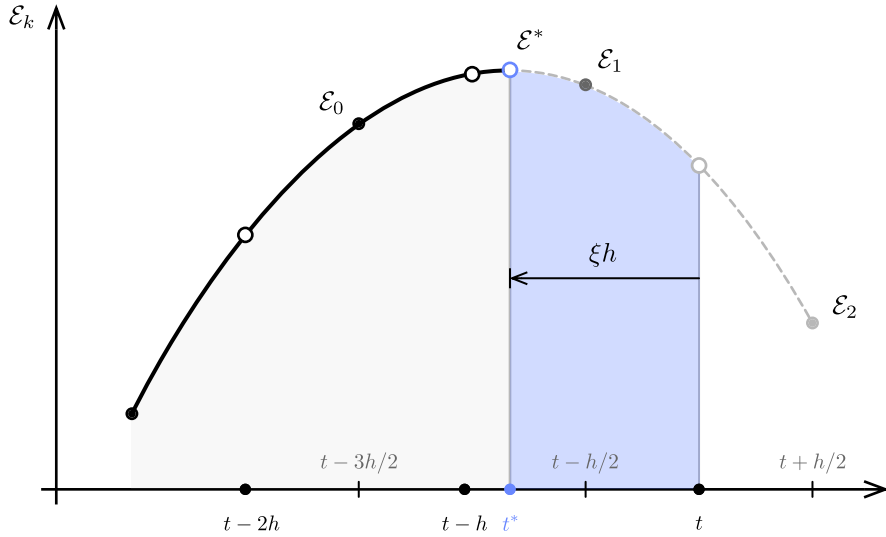


Figure 7.2 – Parabolic interpolation of the kinetic energy peak.

in the interval $[t - 3h/2, t + h/2]$ when (see fig. 7.2) :

$$\mathcal{E}_k^{t-h/2} > \mathcal{E}_k^{t+h/2} \quad (7.47)$$

where the kinetic energy of the system is computed from the mass and the velocity of the particles by :

$$\mathcal{E}_k^{x, t-h/2} = \sum_i \frac{1}{2} m_i^x \dot{x}_i^{t-h/2} \quad (7.48a)$$

$$\mathcal{E}_k^{\theta, t-h/2} = \sum_i \frac{1}{2} m_i^\theta \dot{\theta}_i^{t-h/2} \quad (7.48b)$$

$$\mathcal{E}_k^{t-h/2} = \mathcal{E}_k^{x, t-h/2} + \mathcal{E}_k^{\theta, t-h/2} \quad (7.48c)$$

Here, we have made the distinction between the translational part of the kinetic energy (\mathcal{E}_k^x) and the rotational part of the kinetic energy (\mathcal{E}_k^θ). Indeed, the kinetic damping can be triggered either considering the global kinetic energy of the system or considering separately the translational and rotational parts of the kinetic energy of the system.¹³

Peak interpolation

When a peak is detected at time $t + h/2$, the simplest way to proceed is to freeze the system in its actual position, at time t , and to release it from this position with no initial velocity. However, the peak of kinetic energy as occurred at time t^* somewhere in between times $t - h/2$ and $t + h/2$. To maximise the effect of the kinetic damping the position of the peak could be guessed using a parabolic interpolation of the kinetic energy.

¹³That is when a peak of \mathcal{E}_k^x or a peak of \mathcal{E}_k^θ is detected the kinetic damping is triggered.

Let us define \mathcal{E}_0 , \mathcal{E}_1 and \mathcal{E}_2 the last three consecutive values of the kinetic energy :

$$\mathcal{E}_0 = \mathcal{E}_k^{t-3h/2} \quad (7.49a)$$

$$\mathcal{E}_1 = \mathcal{E}_k^{t-h/2} \quad (7.49b)$$

$$\mathcal{E}_2 = \mathcal{E}_k^{t+h/2} \quad (7.49c)$$

Because a peak has just occur, the following inequalities hold :

$$\mathcal{E}_1 \geq \mathcal{E}_0 \quad (7.50a)$$

$$\mathcal{E}_1 \geq \mathcal{E}_2 \quad (7.50b)$$

We define the following parameters for the parabolic interpolation of the kinetic energy :

$$\alpha = \frac{\mathcal{E}_1 - \mathcal{E}_0}{\mathcal{E}_1 - \mathcal{E}_2} \geq 0 \quad (7.51a)$$

$$\xi = \frac{\mathcal{E}_2 - \mathcal{E}_1}{\mathcal{E}_0 - 2\mathcal{E}_1 + \mathcal{E}_2} = \frac{1}{1 + \alpha} \in [0, 1] \quad (7.51b)$$

With these parameters, the position of the peak and the value of the kinetic energy at the peak are given by :

$$t^* = t - \xi t \quad (7.52a)$$

$$\mathcal{E}^* = \mathcal{E}_1 + \frac{1 - 2\xi}{8}(\mathcal{E}_2 - \mathcal{E}_0) \geq \mathcal{E}_1 \quad (7.52b)$$

Observe that $1 - 2\xi$ and $\mathcal{E}_2 - \mathcal{E}_0$ have the same sign. Therefore, \mathcal{E}^* is always greater than \mathcal{E}_1 as expected. The system is then pushed backward to the interpolated position \mathbf{x}_i^* and θ_i^* given by :

$$\mathbf{x}_i^* = \mathbf{x}_i^t - \xi h \cdot \dot{\mathbf{x}}_i^{t-h/2} \quad (7.53a)$$

$$\theta_i^* = \theta_i^t - \xi h \cdot \dot{\theta}_i^{t-h/2} \quad (7.53b)$$

These equations can be advantageously rewritten to minimize memory allocation by avoiding the storage of the position and the speed of the system respectively at time $t - h$ and $t - h/2$:

$$\mathbf{x}_i^* = \mathbf{x}_i^t - \xi h \cdot (\dot{\mathbf{x}}_i^{t+h/2} - h \cdot \frac{\mathbf{R}_i^{x,t}}{m_i^x}) \quad (7.54a)$$

$$\theta_i^* = \theta_i^t - \xi h \cdot (\dot{\theta}_i^{t+h/2} - h \cdot \frac{\mathbf{R}_i^{\theta,t}}{m_i^\theta}) \quad (7.54b)$$

The parabolic interpolation was introduced by Barnes 1999 [39]. The advantage of this technique is double. Firstly, the damping occurs at the interpolated position, that is for a higher level of kinetic energy ($\mathcal{E}^* \geq \mathcal{E}_1$, see fig. 7.2). Hence, more kinetic energy is dissipated which should improve the convergence speed. Secondly, because of the interpolation, the

system is less subject to *time step locking* when the system moves back and forth between two positions.

7.3.6 Convergence

Several criteria exist in the literature to determine when to stop the time integration and to decide whether the algorithm has converged to a state of static equilibrium or not. It is very unlikely that the system will fall exactly in such a state but instead it will approach it and so a *convergence criteria* is required. We recall here the main ideas.

Criterion based on the resultant force

The system is at static equilibrium when all nodes are at static equilibrium. Thus, it is possible to test for convergence looking at the nodal residuals $\|\mathbf{R}_i^{x,t}\|$ and $\|\mathbf{R}_i^{\theta,t}\|$.¹⁴ For instance, convergence could be pronounced when the maximum of the residuals is less than a certain amount of force (R_ϵ^x) and moment (R_ϵ^θ) :

$$\max_i \|\mathbf{R}_i^{x,t}\| \leq R_\epsilon^x \quad (7.55a)$$

$$\max_i \|\mathbf{R}_i^{\theta,t}\| \leq R_\epsilon^\theta \quad (7.55b)$$

It can be found that this criterion is too strict and it might be preferable to rely on a more global criterion, for instance by testing the mean residual :

$$\frac{1}{N} \sum_i \|\mathbf{R}_i^{x,t}\| \leq R_\epsilon^x \quad (7.56a)$$

$$\frac{1}{N} \sum_i \|\mathbf{R}_i^{\theta,t}\| \leq R_\epsilon^\theta \quad (7.56b)$$

where N is the number of particles in the system. This approach is easily extended to any norm or generalized mean acting on the vector of residuals. For instance the p -mean could be an appropriate criterion :

$$\left(\frac{1}{N} \sum_i \|\mathbf{R}_i^{x,t}\|^p \right)^{1/p} \leq R_\epsilon^x \quad (7.57a)$$

$$\left(\frac{1}{N} \sum_i \|\mathbf{R}_i^{\theta,t}\|^p \right)^{1/p} \leq R_\epsilon^\theta \quad (7.57b)$$

Recall that when $p = -1$ it is called the *harmonic mean*, when $p = 1$ it is called the *arithmetic mean* and when $p = 2$ it is called the *quadratic mean*.

¹⁴Here, the $\|\cdot\|$ symbol denotes the usual Euclidian norm for vectors.

Criterion based on the velocity

The system is at static equilibrium when it does not move anymore, that is when the velocity of the system remains null. Thus, it is possible to test for convergence looking at the nodal velocities $\|\ddot{\mathbf{x}}_i^t\|$ and $\|\dot{\theta}_i^t\|$. The same kind of criteria can be formed.

Criterion based on the displacement

Displacement criteria are very similar to velocity criteria. The convergence is pronounced when the displacement of the system is considered negligible. The same kind of criteria can be formed.

Criterion based on the kinetic energy

The kinetic energy can also be employed to form convergence criteria. Somehow, it is nothing but a velocity criteria weighted by the fictitious mass of the particles. It makes sense as particles contribute to the motion proportionally to their mass. All the criteria exposed previously can be formed with the kinetic energy $\frac{1}{2}m_i^x \dot{\mathbf{x}}_i^t$ and $\frac{1}{2}m_i^\theta \dot{\theta}_i^t$ of the particles.

Relative and adaptative criterion

It can be useful to proportionate the convergence criteria to the size of the system. For the same level of convergence a system with 1000 elements is likely to have a higher kinetic energy than a system with 1 element. The first answer to this issue is to consider a mean value over the particles, as proposed in eq. (7.56) and (7.57).

Some authors have proposed another option to address this problem [141, 10]. They define the kinetic energy convergence threshold as a fraction (f) of the maximum kinetic energy observed previously during the motion :

$$\sum_i \frac{1}{2}m_i^x \dot{\mathbf{x}}_i^t \leq f \cdot \max_{[0,t]} \mathcal{E}_k^{x,t} \quad (7.58a)$$

$$\sum_i \frac{1}{2}m_i^\theta \dot{\theta}_i^t \leq f \cdot \max_{[0,t]} \mathcal{E}_k^{\theta,t} \quad (7.58b)$$

Hence, this criterion is *adaptative* and also *relative* to the size of the problem. The same approach can be adopted for force, velocity or displacement based criteria.

7.3.7 Stability and critical damping

Because we are not interested by the motion itself but by the quasi-static response of the system when properly damped, the time step (h) and the mass of the particles (m_i^x, m_i^θ) should be chosen in order :

- to ensure that the algorithm will converge to a state of static equilibrium (stability) ;

- to produce the fastest convergence possible (critical damping).

Translational fictitious mass

Barnes 1999 [39] studies the vibration modes of a simple unidimensional mass-spring system to postulate that the optimal fictitious mass of a particle is related to the time step and the stiffness lumped at the particle by :

$$m_i = \frac{h^2}{2} K_i \quad (7.59)$$

A demonstration of this result is proposed by Papadrakakis 1981 [142] and Underwood 1983 [143] for an automatic evaluation of the fictitious mass of the particles. K_i should be understood as the greatest direct stiffness that can occur during the simulation process at the i th particle. For a structure with only tension and compression members, Barnes computes the stiffness lumped at a particle according to the geometric and material stiffness of all the members (j) that are connected to this particle :

$$K_i = \sum_j \left[\frac{ES}{L_0} + g \frac{N}{L} \right] \quad (7.60)$$

ES/L_0 is the axial stiffness of the element while N/L is its geometric stiffness. Because the geometric stiffness varies along the simulation, Barnes introduces a multiplication factor ($g > 1$). This factor must be chosen by the end user to ensure that when gN/L is evaluated it is effectively an upper bound to N/L at all time.

Douthe 2007 [10] extends the formulation of Barnes to account for flexural stiffness :

$$\frac{h^2}{2} \sum_j \left[\frac{ES}{L_0} + g \left(\frac{N}{L} + \frac{EI}{L^3} \right) \right] \quad (7.61)$$

In practice, the bending stiffness is negligible in front of the axial stiffness. Additional informations can be found in [157, 146].

Rotational fictitious mass

By analogy to these works, following [96] we define the twisting fictitious mass as :

$$K_i = \sum_j \left[\frac{GJ}{L_0} + g \frac{Q}{L} \right] \quad (7.62)$$

Fictitious mass update

in practice, as remarked in [10] the fictitious masses do not evolve a lot between two peaks of kinetic energy. Therefore, they can be reevaluated only after each peak to minimize the computational cost of the algorithm.

7.3.8 Application to the simple plane pendulum

The simple pendulum – where a weight is suspended from a pivot so that it can swing freely – is of practical interest to illustrate how the Dynamic Relaxation procedure works. We recall the analytical solution for this nonlinear problem. We then explore the progress of the Dynamic Relaxation method to find the position of static equilibriul of the pendulum.

Equation of motion

Let us call m the mass and l the length of the pendulum (see fig. 7.3a). The angle $\theta(t)$ gives the position of the pendulum at time t from the vertical axis. The motion of the pendulum is given by the following differential equation :

$$\ddot{\theta} + \omega_0^2 \sin \theta = 0 \quad (7.63)$$

In addition, we call $\theta_0 = \theta(0)$ the initial position of the pendulum where it is dropped with no initial velocity ($\dot{\theta}(0) = 0$). Remark that m is not involved in eq. (7.63).¹⁵

The kinetic, potential and mechanical energies of the pendulum are given by :

$$\mathcal{E}_k = \frac{1}{2} m \dot{\theta}^2 \quad (7.64a)$$

$$\mathcal{E}_p = mgl(1 - \cos \theta) \quad (7.64b)$$

Linearisation for small oscillations

For a small initial angle ($\theta_0 \ll 1$) eq. (7.63) simplifies to :

$$\ddot{\theta} + \omega_0^2 \theta = 0 \quad (7.65)$$

and the period T_0 and the angular frequency ω_0 of the pendulum are given by :

$$T_0 = \frac{2\pi}{\omega_0} \quad (7.66a)$$

$$\omega_0 = \left(\frac{g}{l}\right)^{1/2} \quad (7.66b)$$

Therefore, for small angles the period is independent of the initial angle θ_0 .

¹⁵We could have introduced a fictitious mass (m_f) for the weight to optimize the convergence of the algorithm (see §7.3.7). In this case, the reference pulsation of the pendulum would writes : $\omega_0 = \sqrt{(m/m_f) \cdot (g/l)}$. The real mass of the weight is the one that give access to the force exerted to the pendulum while the fictitious mass is freely chosen to speed up the convergence of the method.

Exact solution

For greater initial angles, the solution is nonlinear and requires elliptic functions to be solved analytically [158, 159].

The period of the pendulum is given in terms of the elliptic integral K by :

$$T/T_0 = \frac{2}{\pi} K(k) \quad (7.67a)$$

$$k = \sin(\theta_0/2) \quad (7.67b)$$

$$K(m) = \int_0^1 \frac{dz}{\sqrt{(1-z^2)(1-mz^2)}} \quad (7.67c)$$

The position of the pendulum over time is expressed in terms of the *Jacobi elliptic function* $sn(u, m)$ by :

$$\theta(t) = 2 \arcsin \left(k \, sn(\omega_0 \cdot (T/4 - t), k) \right) \quad (7.68)$$

The angular velocity of the pendulum is calculated from the conservation of mechanical energy as :

$$\dot{\theta}(t) = 2\omega_0 \left(\sin^2(\theta_0/2) - \sin^2(\theta/2) \right)^{1/2} \quad (7.69)$$

Finding the position of static equilibrium

A pendule of mass $m = 1.0 \text{ kg}$ is dropped with no initial velocity at angle $\theta_0 = 135^\circ$. The length of the pendulum is defined so that its angular frequency is $\omega_0 = 1.0 \text{ s}^{-1}$. The gravity is $g = 9.81 \text{ m/s}^2$.

The motion of the pendulum is simulated by the Dynamic Relaxation method with kinetic damping. Interpolation of kinetic energy peaks is not implemented in this example. When a peak is detected, the pendulum is pushed backward to its previous position, frozen and dropped again with no initial velocity. The time step is set to $h = 0.1 \text{ s}$ and the simulation is stopped when the kinetic energy of the pendulum less than $\mathcal{E}_k^{lim} = 10^{-20}$.

The course of the pendulum for the first iterations is represented in fig. 7.3a. The pendulum is dropped with no velocity at angle θ_0 . Driven by the gravity, it starts to move down slowly and its velocity increases over time. Progressively, its potential energy is transformed into kinetic energy but the overall mechanical energy is conserved because the motion is undamped until a peak of kinetic energy is reached (see fig. 7.4a).

The potential energy of the pendulum decreases until it reaches the vertical axis (see fig. 7.3b). But because of the discrete nature of the algorithm, the pendulum jumps over the equilibrium position and starts to move up few time steps. Accordingly its velocity starts to decrease and so its kinetic energy. Quickly, a peak of kinetic energy is detected

and the kinetic damping is triggered.

The process is repeated but with a lower initial position θ_0 . The mechanical energy of the system has decreased and so has the upper bound of the potential energy. From peak to peak, this bound is lowered through kinetic damping and in the end the potential energy of the pendulum is reduced to zero within the convergence tolerance \mathcal{E}_k^{lim} (see fig. 7.4a).

The convergence process is also monitored with the phase diagram of the motion (see fig. 7.4b). Each closed curve is an iso-curve which corresponds to a given level of mechanical energy defined by $\mathcal{E}_m = \mathcal{E}_p(\theta_0)$. An undamped pendulum travels along an iso-curve and makes a full turn every period of time T . Here, until a kinetic energy peak is reached the level of mechanical energy is preserved during the motion and the pendulum moves along the corresponding iso-curve in the phase diagram.

Observe in fig. 7.4b that the pendulum slightly deviates from its theoretical movement. The velocity is slightly under estimated from its theoretical value. This error is due to the central difference approximation of the velocity and is integrated during the motion, thus accumulating over time. When the kinetic damping is triggered this error is dissipated. This kind of diagram is very useful to compare time integrators as proposed in [155]. In the phase diagram, the effect of the kinetic damping is to jump from one iso-curve to another with a lower mechanical energy level (see fig. 7.4b).

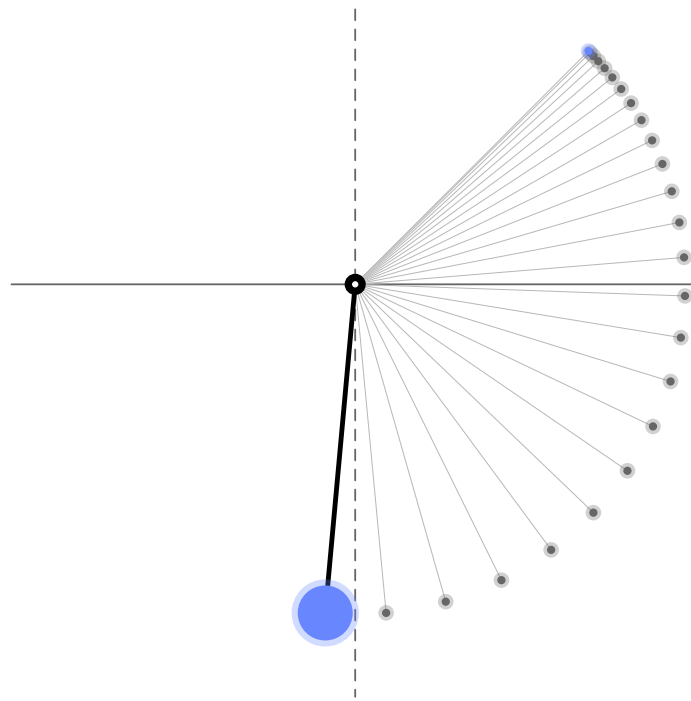
This application is also useful to understand the relation between accuracy, stability and critical damping :

- When $h \ll T$ the method sticks closely to the theoretical movement. The process is stable and peaks of kinetic energy are determined with accuracy. However the method requires a huge amount of iterations which increases the computation time.
- When $h \gg T$ the method gets unstable as the dynamic is updated at a lower rate than the typical reaction time of the system. The process fails to capture a plausible motion and bolting is likely to occur. In this case the pendulum will start to swirl.

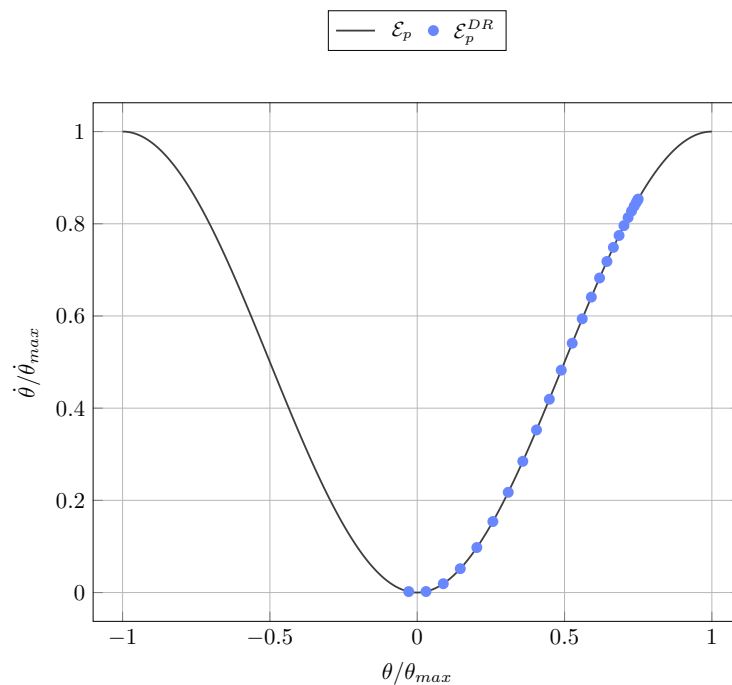
7.4 Enriching the model

7.4.1 Support

7.4.2 Connexion

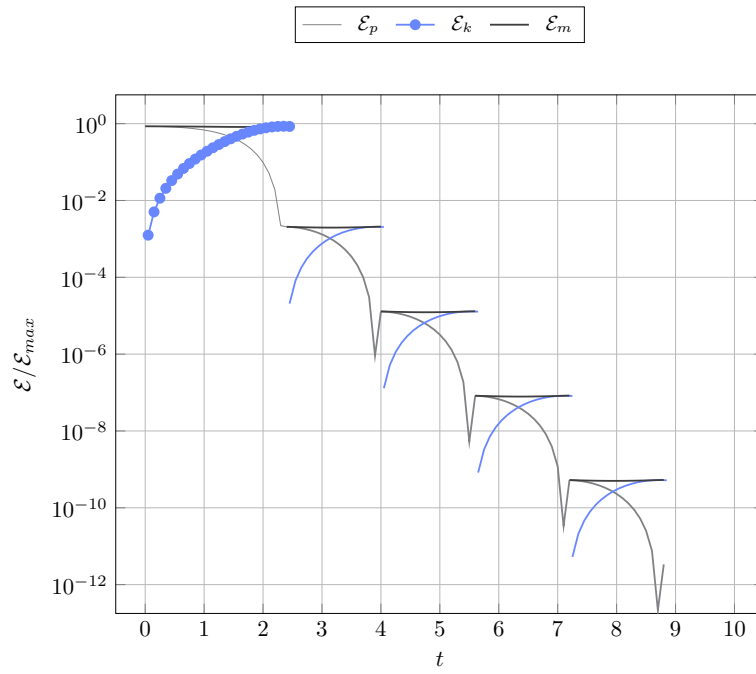


(a) First steps until the first peak of \mathcal{E}_k is reached.

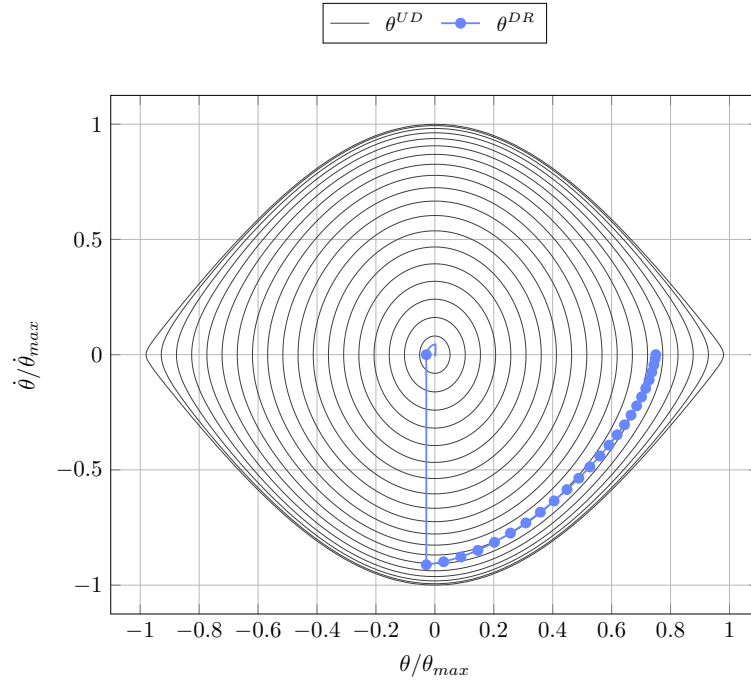


(b) Potential energy of the pendulum for the first steps.

Figure 7.3 – Application of the DR process to the simple plane pendulum.



(a) Typical profile of the kinetic damping.



(b) Convergence of the DR process in the phase space.

Figure 7.4 – Convergence of the DR process for the simple plane pendulum.

7.5 Software

The present model has been implemented in a numerical software called *Marsupilami*. A first version of this software, based on the 3-DOFs spline beam element, was used successfully in the structural design of the Ephemeral Cathedral of Créteil (see ??) and other smaller timber gridshells (see fig. 2.19). During this thesis *Marsupilami* has been completely redeveloped to include rotational DOFs capabilities. Lots of new features have been

7.5.1 Architecture of the software

The code of *Marsupilami* is divided into three libraries presented hereinafter : *Marsupilami.Math*, *Marsupilami.CoreLib* and *Marsupilami.Gh*.

Marsupilami.Math.dll

This is a small standalone math library. It defines three data types : *MPoint*, *MVector* and *MFrame*. *MPoint* and *MVector* types store three coordinates *X*, *Y* and *Z* in double-precision floating-point format (see fig. 7.5). *Frame* type is composed of a *MPoint* called *Origin* and three *MVector* called *XAxis*, *YAxis* and *ZAxis*. The *MFrame* type serves to represent a material frame where *XAxis* and *YAxis* are the first and second material axis of the cross-section, and the *ZAxis* is the normal vector of the cross-section.

Although some math libraries already exist for C#, it was found useful to build our own library so that it can be customized to our needs without restrictions. In particular, when it comes to software optimization for such a CPU-bound application you would better know exactly what is done inside the math routines. Having your own math library facilitates benchmarking several variants of the math routines and select the optimal one.

Marsupilami.CoreLib.dll

This is the core library. It defines structured objects such as element, section, material, model, solver. It is conceived as an API that third-party software can use to provide computation (for instance Excel, Rhino Grasshopper, Dynamo, ...).

Marsupilami.Gh.gha

This is a grasshopper plugin that exposes the logic of *Marsupilami.CoreLib.dll*. Marsupilami types are mapped to Grasshopper types. Display methods are provided. Easier to build and construct some models

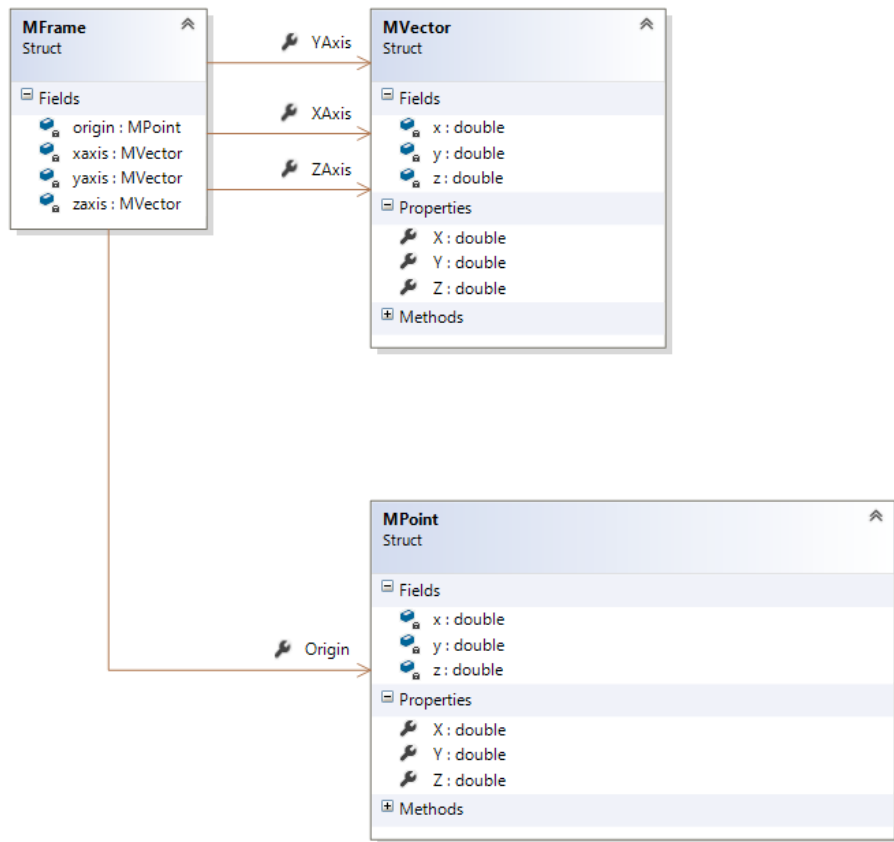


Figure 7.5 – Partial class diagram of *Marsupilami.Math.dll*.

	add	sub	mul	div	sqrt
cost	1	1	4	10	20

Table 7.1 – Simple cost model for arithmetic operations.

7.5.2 Key aspects

Implementation details : [35], [36]

Language

Why C# ?

Code abstraction

Modularité : evaluation courbure, schéma d'intégration, autorefine, autobreak, plasticity
 Design pattern [160] : An object-oriented architecture for extensible structural design software [161] : design patterns

Event driven

Events-driven vs asynchronous vs parallel. Evènement vs procédural

The events-driven paradigm means that an object called an "event" is sent to the program whenever something happens, without that "something" having to be polled in regular intervals to discover whether it has happened. That "event" may be trapped by the program to perform some actions (i.e. a "handler") – either synchronous or asynchronous. Therefore, handling of events can either be synchronous or asynchronous. JavaScript, for example, uses a synchronous eventing system. Asynchronous means that actions can happen independent of the current "main" execution stream. Mind you, it does NOT mean "parallel", or "different thread". An "asynchronous" action may actually run on the main thread, blocking the "main" execution stream in the meantime. So don't confuse "asynchronous" with "multi-threading". You may say that, technically speaking, an asynchronous operation automatically assumes eventing – at least "completed", "faulted" or "aborted/cancelled" events (one or more of these) are sent to the instigator of the operation (or the underlying O/S itself) to signal that the operation has ceased. Thus, async is always event-driven, but not the other way round.

Serialization

SQLite, JSON, XML.

7.5.3 Performance

Software optimization is both a very active field of research and a nightmare for non specialists. It is virtually impossible to find good rules of thumb in the literature to orient critical implementation decisions. For instance a question that looks so simple as : "Should I use a Struct of Arrays or and Array of Structs ?" ... is not so simple at all ; and the answer is generally "It depends ...". And indeed, it depends on the coding language you chose, the coding skills you have to make the language talk to the processor in the way you want and not in the way you think it will. It also depends on complex hardware considerations. Optimizations can be made at all levels of abstraction of a software, from the highest level (algorithm) to the lowest level (assembly code).

To embrace the complexity of this problematic the reader is invited to refer to the excellent book *Writing High-Performance .NET Code* [162].

Know what things cost

When it comes to software performance, the first stage should always be to measure what things cost (See [know what things cost](#)).¹⁶ Once the bottlenecks are identified, then the optimization of the critical pieces of code can begin. To this end, two tools were employed during the development of *Marsupilami* :

- Cost Model : a very simple cost model was established to assign a performance rating to each base math routine, based on the number of arithmetic and trigonometric operations it performs (see [tab. 7.1](#)). This cost model was established through micro benchmarks with the [BenchmarkDotNet](#) library.
- Measure : performance measurements were conducted on full analysis of several test cases with the library [PerfView](#).

Algorithmic optimization

The analyses made with PerfView showed that rotation and parallel transportation of frames are critical operations for the performance of the program. A thorough work was done to optimize all the costly math routines by using the minimal logic to perform the operations.

Further improvements might be achieved using polynomial representations of trigonometric functions but not time was left to dig seriously into this direction [163, 164].[165]. The optimization of math routines and in particular trigonometric functions is a field of research to itself [165].

Vectorization

Marsupilami leverages the built-in capabilities offered by the .Net framework to parallelize some of the work. At the moment, the computation of the internal forces and moments of the elements is made inside a parallel loop. Still, a lot remains to be explored in this area :

- Single Instruction Multiple Data (SIMD) instructions allow vectorization of arithmetic and trigonometric operations at the CPU level and can offer up to a x8 speed up.
- Dynamic relaxation is very suitable for parallelization [166]. New hardware capabilities such as multicore CPU or GPU cards with hundreds of cores can be leveraged to speed up the computation [167, 168].

However, this technologies are relatively recent and still complex to implement as they require low level coding. They are note easily implementable from C# and *Marsupilami* does not rely on any of these technology.

¹⁶<https://msdn.microsoft.com/en-us/library/ms973852.aspx>

Code abstraction

“In-depth performance optimization will often defy code abstractions.” [162, p. 155]

7.5.4 Further guidelines

Tips

- abstract model
- NLOpt, Ipopt that have a C# wrapper, accord-framework, alglib
- Proprietary solver Knitro, Mosek
- webAPI C# Julia Javascript [169] : Software Tools for Nonlinear Optimization
-

Neos The NEOS Server is a free internet-based service for solving numerical optimization problems. It is able to take models specified in a variety of formats (including AMPL, GAMS and MPS) and pass them to a range of both free and commercial solvers (including Gurobi, CPLEX and Cbc). See here for the full list of solvers and input formats that NEOS supports. <https://github.com/odow/NEOS.jl> <http://www.juliaopt.org/>

DifferentialEquations.jl

([Manual](#) | [GitHub](#)) Time integration, custom mass matrix, call back to implement kinetic damping, custom integrator

MathOptInterface.jl :

An abstraction layer for mathematical optimization solvers ([Manual](#) | [GitHub](#)) MathProgBase.jl : This package provides high-level one-shot functions for linear and mixed-integer programming (linprog and mixintprog), as well as a solver-independent low-level interface for implementing advanced techniques that require efficiently solving a sequence of linear programming problems. <http://mathprobbasejl.readthedocs.io/en/latest/index.html>

OOP vs structured programming : <https://softwareengineering.stackexchange.com/questions/125753/does-object-orientation-really-affect-algorithm-performance> AoS vs OoS particle vs Collection of Particle.

Structure of the algorithm

Algorithm 1: Dynamic Relaxation algorithm as implemented in *Marsupilami*.

```

1 Function Run():
2     foreach node in model do                                /*  $dx = v_x dt$ ,  $d\theta = v_\theta dt$  */
3         | Move( $dx, d\theta$ ) ;
4     end
5     /* Elements calculate internal forces and moments          */
6     foreach element in model do
7         | CalcInternalForces( $x, d_1, d_2, d_3$ ) ;           /*  $\mathbf{F}^{int}(x, d_1, d_2, d_3)$  */
8         | CalcInternalMoments( $x, d_1, d_2, d_3$ ) ;        /*  $\mathbf{M}^{int}(x, d_1, d_2, d_3)$  */
9     end
10    /* Joints coordinate the dynamic of several nodes          */
11    foreach joint in model do
12        | AggregateForcesAndMoments() ;
13        | AggregateMasses() ;
14        | SynchronizeForcesAndMoments() ;
15        | SynchronizeMasses() ;
16    end
17    /* Calculate translational kinetic energy                   */
18    foreach node in model do
19        | CalcAcceleration( $m_x, \mathbf{F}$ )                  /*  $\mathbf{a}_x(t) = \mathbf{R}_x/m_x$  */
20        | CalcVelocity( $\mathbf{a}_x, dt$ )                     /*  $\mathbf{v}_x(t + \frac{dt}{2}) = \mathbf{v}_x(t - \frac{dt}{2}) + dt\mathbf{a}_x(t)$  */
21        | CalcKEnergy( $v_x$ )                          /*  $E_x(t + \frac{dt}{2}) = \frac{1}{2} \sum m_x v_x^2(t + \frac{dt}{2})$  */
22    end
23    /* Detect pic of kinetic energy                         */
24    if  $E_x(t + \frac{dt}{2}) < E_x(t - \frac{dt}{2})$  then
25        | InterpolatePosition() ;
26        | Reset() ;
27    end
28    /* Calculate rotational kinetic energy                 */
29    foreach node in model do
30        | CalcAcceleration( $m_\theta, \mathbf{M}$ )            /*  $\mathbf{a}_\theta(t) = \mathbf{R}_\theta/m_\theta$  */
31        | CalcVelocity( $\mathbf{a}_\theta, dt$ )             /*  $\mathbf{v}_\theta(t + \frac{dt}{2}) = \mathbf{v}_\theta(t - \frac{dt}{2}) + dt\mathbf{a}_\theta(t)$  */
32        | CalcKEnergy( $v_\theta$ )                      /*  $E_\theta = \frac{1}{2} \sum m v_\theta^2(t + \frac{dt}{2})$  */
33    end
34    /* Detect pic of kinetic energy                         */
35    if  $E_\theta(t + \frac{dt}{2}) < E_\theta(t - \frac{dt}{2})$  then
36        | InterpolatePosition() ;
37        | Reset() ;
38    end
39 return

```

7.6 Test case

7.7 Conclusion

7.8 References

- [10] C. Douthe. “Etude de structures élancées précontraintes en matériaux composites : application à la conception des gridshells”. PhD thesis. Université Paris Est, 2007, p. 274.
- [26] C. Douthe, O. Baverel, and J.-F. Caron. “Formfinding of a grid shell in composite materials”. In: *Journal of the IASS* 47 (2006), pp. 53–62.
- [29] B. D’Amico, A. Kermani, and H. Zhang. “Form finding and structural analysis of actively bent timber grid shells”. In: *Engineering Structures* 81 (2014), pp. 195–207.
- [35] J. Olsson and A. Fisher. “Form finding and size optimization - Implementation of beam elements and size optimization in real time”. PhD thesis. Chalmers University of Technology, 2012, p. 97.
- [36] E. Poulsen. “Structural design and analysis of elastically bent gridshells”. PhD thesis. Chalmers University of Technology, Gothenburg Sweden, 2015.
- [37] S. Adriaenssens. “Stressed spline structures”. PhD thesis. University of Bath, 2000.
- [38] S. Adriaenssens, M. Barnes, and C. Williams. “A new analytic and numerical basis for the form-finding and analysis of spline and gridshell structures”. In: *Computing Developments in Civil and Structural Engineering*. Ed. by B. Kumar and B. H. V. Topping. Edinburgh: Civil-Comp Press, 1999, pp. 83–91.
- [39] M. Barnes. “Form finding and analysis of tension structures by dynamic relaxation”. In: *International Journal of Space Structures* 14.2 (1999), pp. 89–104.
- [40] S. Adriaenssens and M. Barnes. “Tensegrity spline beam and grid shell structures”. In: *Engineering Structures* 23.1 (2001), pp. 29–36.
- [41] M. Barnes, S. Adriaenssens, and M. Krupka. “A novel torsion/bending element for dynamic relaxation modeling”. In: *Computers & Structures* 119 (Apr. 2013), pp. 60–67.
- [42] L. du Peloux, F. Tayeb, B. Lefevre, O. Baverel, and J.-F. Caron. “Formulation of a 4-DoF torsion / bending element for the formfinding of elastic gridshells”. In: *Proceedings of the International Association for Shell and Spatial Structures*. August. Amsterdam, 2015, pp. 1–14.
- [43] B. D’Amico, H. Zhang, and A. Kermani. “A finite-difference formulation of elastic rod for the design of actively bent structures”. In: *Engineering Structures* 117 (2016), pp. 518–527.
- [91] M. Bergou, M. Wardetzky, S. Robinson, B. Audoly, and E. Grinspun. “Discrete elastic rods”. In: *ACM SIGGRAPH* (2008), pp. 1–12.
- [96] B. Lefevre, F. Tayeb, L. du Peloux, and J.-F. Caron. “A 4-degree-of-freedom Kirchhoff beam model for the modeling of bending–torsion couplings in active-bending structures”. In: *International Journal of Space Structures* 32.2 (2017), pp. 69–83.
- [138] A. Day. “An Introduction to dynamic relaxation”. In: *The Engineer* (1965).

- [139] J. Otter, A. Cassel, and R. Hobbs. “Dynamic Relaxation”. In: *Proceedings of the Institution of Civil Engineers* 35.4 (1966), pp. 633–656.
- [140] A. Cassel and R. Hobbs. “Numerical stability of dynamic relaxation analysis of non-linear structures”. In: *Numerical Methods in Engineering* October (1976), pp. 1407–1410.
- [141] M. Barnes. “Applications of dynamic relaxation to the topological design and analysis of cable, membrane and pneumatic structures”. In: *International Conference on Space Structures*. Guildford, 1975.
- [142] M. Papadrakakis. “A method for the automatic evaluation of the dynamic relaxation parameters”. In: (1981).
- [143] P. Underwood. “Dynamic relaxation”. In: *Computational methods for transient analysis*. 1983, p. 524.
- [144] M. Barnes. “Form finding and analysis of tension space structures by dynamic relaxation”. PhD thesis. City University London, 1977.
- [145] D. Wakefield. “Dynamic relaxation analysis of pretensioned networks supported by compression arches”. PhD thesis. City University London, 1980, p. 281.
- [146] J. Rodriguez, G. Rio, J. M. Cadou, and J. Troufflard. “Numerical study of dynamic relaxation with kinetic damping applied to inflatable fabric structures with extensions for 3D solid element and non-linear behavior”. In: *Thin-Walled Structures* 49.11 (2011), pp. 1468–1474.
- [147] H. K. Dang and M. A. Meguid. “Evaluating the performance of an explicit dynamic relaxation technique in analyzing non-linear geotechnical engineering problems”. In: *Computers and Geotechnics* 37.1-2 (2010), pp. 125–131.
- [148] D. M. L. da Silva, B. P. Jacob, and M. V. Rodrigues. “Implicit and explicit implementation of the dynamic relaxation method for the definition of initial equilibrium configurations of flexible lines”. In: *25st International Conference on Offshore Mechanics and Arctic Engineering, Hamburg, Germany* September 2016 (2006), pp. 1–10.
- [149] M. Rezaiee-Pajand, S. R. Sarafrazi, and H. Rezaiee. “Efficiency of dynamic relaxation methods in nonlinear analysis of truss and frame structures”. In: *Computers and Structures* 112-113 (2012), pp. 295–310.
- [150] B. H. V. Topping and P. Ivanyi. *Computer Aided Design of Cable-membrane Structures*. 2007.
- [151] M. Miki, S. Adriaenssens, T. Igarashi, and K. Kawaguchi. “The geodesic dynamic relaxation method for problems of equilibrium with equality constraint conditions”. In: *International Journal for Numerical Methods in Engineering* 99.9 (2014), pp. 682–710.
- [152] G. Noh and K.-j. Bathe. “An explicit time integration scheme for the analysis of wave propagations”. In: *Computers and Structures* 129 (2013), pp. 178–193.
- [153] Y. Duan, D. Li, and P. F. Pai. “Geometrically exact physics-based modeling and computer animation of highly flexible 1D mechanical systems”. In: *Graphical Models* 75.2 (2013), pp. 56–68.

- [154] B. Fierz. “Stabilizing explicit dynamic finite element simulations”. PhD thesis. 2013.
- [155] E. Hairer and G. Wanner. *Geometric numerical integration algorithms for ordinary differential equations*. Springer Verlag, 2006, p. 644.
- [156] P. Cundall. “Explicit-finite difference methods in geomechanics.” In: *Numerical Methods in Geomechanics*. Blacksburg, Virginia, United States, 1976, pp. 132–150.
- [157] W. Lewis. *Tension structures: form and behaviour*. Telford, Thomas, 2003, p. 201.
- [158] R. Borghi. “Simple pendulum dynamics: revisiting the Fourier-based approach to the solution”. In: (2013), pp. 1–16. arXiv: [1303.5023](https://arxiv.org/abs/1303.5023).
- [159] A. Beléndez, C. Pascual, D. Méndez, T. Beléndez, and C. Neipp. “Exact solution for the nonlinear pendulum”. In: *Revista Brasileira de Ensino de Física* 29.4 (2007), pp. 645–648.
- [160] R. Clune, J. J. Connor, J. Ochsendorf, and D. Kelliher. “An object-oriented architecture for extensible structural design software”. In: *Computers and Structures* 100-101 (2012), pp. 1–17.
- [161] J. Bishop. *C# 3.0 Design Patterns*. 2008.
- [162] B. Watson. *Writing High-Performance .NET Code*. 2014.
- [163] L. N. Trefethen. “Computing numerically with functions instead of numbers”. In: *Mathematics in Computer Science* 1.1 (2007), pp. 9–19.
- [164] S. Chevillard, M. Jolde\cs, and C. Lauter. “Sollya: An Environment for the Development of Numerical Codes”. In: *Mathematical Software - ICMS 2010*. Ed. by K. Fukuda, J. van der Hoeven, M. Joswig, and N. Takayama. Vol. 6327. Lecture Notes in Computer Science. Heidelberg, Germany: Springer, 2010, pp. 28–31.
- [165] R. Green. “Faster Math Functions”. In: *Proc. of Game Developers Conference* (2003).
- [166] B. H. V. Topping and A. I. Khan. “Article information : PARALLEL COMPUTATION SCHEMES FOR”. In: *Engineering Computations* 11.6 (1994), pp. 513–548.
- [167] V. Rek and I. Němec. “Parallel Computing Procedure for Dynamic Relaxation Method on GPU Using NVIDIA’s CUDA”. In: *Applied Mechanics and Materials* 821.1 (2016), pp. 331–337.
- [168] A. Liew, T. VanMele, and P. Block. “Vectorised graphics processing unit accelerated dynamic relaxation for bar and beam elements”. In: *Structures* 8 (2016), pp. 111–120.
- [169] T. Moulard, B. Chrétien, and E. Yoshida. “Software Tools for Nonlinear Optimization”. In: *Journal of the Robotics Society of Japan* 32.6 (2014), pp. 536–541.

8 Conclusion

Conclusion

Appendix Part III

A Review of built elastic gridshells

Appendix A. Review of built elastic gridshells

N	Year	Nickname	Type	City	Country	Ref.
1	1962	Experimental structure	Workshop	Berkeley	USA	[1]
2	1962	Exhibition pavilion	Pavilion	Essen	Germany	[1]
3	1967	German Pavilion	Pavilion	Montreal	Canada	[1]
4	1973	Seibu	Experiment	Tokyo	Japan	[4]
5	1974	Basket shell	Experiment	Amehabad	India	[1]
6	1974	Experimental structure	Experiment	London	England	[1]
7	1975	Mannheim Multihalle	Building	Mannheim	Germany	[1]
8	1973	Ferrocement gridshell	Building	Ahmedabad	India	[4]
9	1976	AA Bamboo Latice Shell	Workshop	London	England	[4]
10	1976	Test structure of a gridshell	Experiment	Stuttgart	Germany	[1]
11	1977	Small Pavilion	Workshop	Mexico City	Mexico	[4]
12	1977	Small Greenhouse	Workshop	Zitacuaro	Mexico	[4]
13	1977	Experimental structure	Workshop	Mexico City	Mexico	[4]
14	1977	Experimental structure	Workshop	Mexico City	Mexico	[4]
15	1995	Westminster Lodge	Building	Dorset	England	[17]
16	1998	Earth Center	Building	Doncaster	England	
17	2000	Japan Pavilion	Pavilion	Hannover	Germany	[18]
18	2002	Downland	Building	Downland	England	[16]
19	2002	Life Science Centre Trust	Building	Pishwanton	England	
20	2003	Woodland Center	Building	Filmwell	England	
21	2006	Savill	Building	Savill	England	[24]
22	2007	Chiddingstone Orangery	Roofing	Kent	England	
23	2007	ENPC	Experiment	Noisy-Champs	France	[26]
24	2011	Solidays	Pavilion	Paris	France	[27]
25	2012	Toledo	Workshop	Naples	Italy	[29]
26	2013	Créteil	Building	Créteil	France	[28]
27	2013	ZA	Workshop	Cluj	Romania	
28	2014	F2	Workshop	San Antonio	USA	
29	2014	Toledo 2.0	Workshop	Naples	Italy	[30]
30	2015	Booby	Experiment	Noisy-Champs	France	[8]
31	2016	JPO	Pavilion	Toulouse	France	
32	2016	FAV	Pavilion	Montpellier	France	
33	2016	CLC	Workshop	Noisy-Champs	France	
34	2016	Trondheim	Workshop	Trondheim	Norway	[32]

Table A.1 – Project review - general informations.

N	Material	Layer	Pitch m	Surface m^2	Span m	Section mm
1	steel	single	0.82	52	7.8	double Ø21.7
2	hemelock pine	single	0.48	198	16.8	60x40
3	hemelock pine	single	0.50	365	17.5	42x35 - 42x28
4	aluminium	single	0.50	72	8.5	20x20x2
5	bamboo	single	0.48	225	15.0	Ø25.4
6	yellow pine	single	0.45	82	6.0	14x19
7	hemelock pine	double	0.50	7400	60.0	50x50
8	steel	single	0.50	80	8.0	Ø19x1.2
9	bamboo	single	0.7	63	7.0	Ø25.4
10	hemelock pine	single	0.50	38	6.7	15x15
11	pine	single	0.50	62	6.0	16x24
12	wood	double	0.4	81	9.0	20x22
13	aluminium	single	0.50	58	7.3	double Ø8.0
14	steel	single		17	4.0	double Ø5.0
15	roundwood thinnings	double				Ø100.0
16	oak	single	0.4	36	6.0	32x15
17	cardboard	single	1.0	2500	35.0	Ø120x22
18	oak	double	1.0 - 0.5	710	16.0	50x35
19	larch	single	0.6	80	10.0	35x25
20	chestnut	single	0.6	300	12.0	75x25
21	larch	double	1.0	2000	24.0	80x50
22	sweet chestnut	double	1.0	50	5.0	40x30
23	GFRP	single	1.0	170	13.0	Ø41.7x3.5
24	GFRP	single	1.0	280	15.0	Ø41.7x3.5
25	wood	double	0.50	75	6.5	
26	GFRP	single	1.0	350	17.5	Ø41.7x3.5
27	larch	double	0.7	234	13.0	70x20
28	wood	double		144	12.0	
29	larch	double	0.50	100	10.0	50x20
30	GFRP	single	0.25	10	3.4	Ø10
31	pine	double	0.6	50	7.0	48x12
32	pine	double	0.6	50	7.0	48x12
33	pine	double	0.6	50	7.0	48x12
34	spruce	double	0.50	100	10.0	48x23

Table A.2 – Project review - key numbers.

A.1 References

- [1] B. Burkhardt, J. Hennicke, and E. Schauer, eds. *IL10 Grid Shells*. Institut für leichte Flächentragwerke (IL). Stuttgart, 1974.
- [4] B. Burkhardt, M. Chaitos, J. Langner, W. Langner, and G. Lubberger, eds. *IL13 Multihalle Mannheim*. Institut für leichte Flächentragwerke (IL). Stuttgart, 1978.
- [8] P. Cuvilliers, C. Douthe, L. du Peloux, and R. Le Roy. “Hybrid structural skin : prototype of an elastic gridshell braced by a fibre-reinforced concrete envelope”. In: *Journal of The International Association for Shell and Spatial Structures* (2017), pp. 1–12.
- [16] R. Harris, J. Romer, O. Kelly, and S. Johnson. “Design and construction of the Downland Gridshell”. eng. In: *Building research and information* 31.6 (2003), pp. 427–454.
- [17] R. Burton, M. Dickson, and R. Harris. “The use of roundwood thinnings in buildings : a case study”. In: *Building Research & Information* 26.2 (1998), pp. 76–93.
- [18] M. McQuaid, F. Otto, and S. Ban. “Building the Japan pavilion”. In: *Shigeru Ban*. Phaidon Press, 2006, pp. 8–11.
- [24] R. Harris, S. Haskins, and J. Roynon. “The Savill Garden gridshell : Design and construction”. In: *The Structural Engineer* 86.17 (2008), pp. 27–34.
- [26] C. Douthe, O. Baverel, and J.-F. Caron. “Formfinding of a grid shell in composite materials”. In: *Journal of the IASS* 47 (2006), pp. 53–62.
- [27] O. Baverel, J.-F. Caron, F. Tayeb, and L. du Peloux. “Gridshells in composite materials : construction of a 300 m² forum for the solidays’ festival in Paris”. In: *Structural Engineering International* 22.3 (2012), pp. 408–414.
- [28] L. du Peloux, F. Tayeb, O. Baverel, and J.-F. Caron. “Construction of a large composite gridshell structure: a lightweight structure made with pultruded glass fibre reinforced polymer tubes”. In: *Structural Engineering International* 26.2 (2016), pp. 160–167.
- [29] B. D’Amico, A. Kermani, and H. Zhang. “Form finding and structural analysis of actively bent timber grid shells”. In: *Engineering Structures* 81 (2014), pp. 195–207.
- [30] B. D’Amico, A. Kermani, H. Zhang, A. Pugnale, S. Colabella, and S. Pone. “Timber gridshells: Numerical simulation, design and construction of a full scale structure”. In: *Structures* 3.May 2016 (2015), pp. 227–235.
- [32] J. Haddal Mork, S. Dyvik Hillersøy, B. Manum, A. Rønnquit, and N. Labonnote. “Introducing the Segment Lath - a Simplified Modular Timber Gridshell Built in Trondheim Norway”. In: *World Conference on Timber Engineering*. 3. Vienna, Austria, 2016.

B Calculus of variations

B.1 Introduction

In this appendix we drawback essential mathematical concepts for the calculus of variations. Recall how the notion of energy, gradients are extended to function spaces.

[170]

B.2 Spaces

B.2.1 Normed space

A *normed space* $V(\mathbb{K})$ is a vector space V over the scalar field \mathbb{K} with a norm $\|\cdot\|$.

A *norm* is a map $\|\cdot\| : V \times V \mapsto \mathbb{K}$ which satisfies :

$$\forall x \in V, \quad \|x\| = 0_{\mathbb{K}} \Rightarrow x = 0_V \quad (\text{B.1a})$$

$$\forall x \in V, \forall \lambda \in \mathbb{K}, \quad \|\lambda x\| = |\lambda| \|x\| \quad (\text{B.1b})$$

$$\forall (x, y) \in V^2, \quad \|x + y\| \leq \|x\| + \|y\| \quad (\text{B.1c})$$

B.2.2 Inner product space

A *inner product space* or *pre-hilbert space* $E(\mathbb{K})$ is a vector space E over the scalar field \mathbb{K} with an inner product.

An *inner product* is a map $\langle ; \rangle : E \times E \mapsto \mathbb{K}$ which is bilinear, symmetric and positive-

Appendix B. Calculus of variations

definite :

$$\forall(x, y, z) \in E^3, \forall(\lambda, \mu) \in \mathbb{K}^2, \quad \begin{aligned} \langle \lambda x + \mu y ; z \rangle &= \lambda \langle x ; z \rangle + \mu \langle y ; z \rangle \\ \langle x ; \lambda y + \mu z \rangle &= \lambda \langle x ; y \rangle + \mu \langle x ; z \rangle \end{aligned} \quad (\text{B.2a})$$

$$\forall(x, y) \in E^2, \quad \langle x ; y \rangle = \langle y ; x \rangle \quad (\text{B.2b})$$

$$\forall x \in E, \quad \langle x ; x \rangle \geqslant 0_{\mathbb{K}} \quad (\text{B.2c})$$

$$\forall x \in E, \quad \langle x ; x \rangle = 0_{\mathbb{K}} \Rightarrow x = 0_E \quad (\text{B.2d})$$

Moreover, an inner product naturally induces a norm on E defined by :

$$\forall x \in E, \quad \|x\| = \sqrt{\langle x ; x \rangle} \quad (\text{B.3})$$

Thus, an inner product vector space is also naturally a normed vector space.

B.2.3 Euclidean space

An *Euclidean space* $\mathcal{E}(\mathbb{R})$ is a finite-dimensional real vector space with an inner product. Thus, distances and angles between vectors could be defined and measured regarding to the norm associated with the chosen inner product.

An Euclidean space is nothing but a finite-dimensional real pre-hilbert space.

B.2.4 Banach space

A *Banach space* $\mathcal{B}(\mathbb{K})$ is a complete normed vector space, which means that it is a normed vector space in which every Cauchy sequence of \mathcal{B} converges in \mathcal{B} for the given norm.

Thus, a Banach space is a vector space with a metric that allows the computation of vector length and distance between vectors and is complete in the sense that a Cauchy sequence of vectors always converges to a well defined limit in that space.

B.2.5 Hilbert space

A *Hilbert space* is an inner product vector space $\mathcal{H}(\mathbb{K})$ such that the natural norm induced by the inner product turns \mathcal{H} into a complete metric space (i.e. every Cauchy sequence of \mathcal{H} converges in \mathcal{H}).

The Hilbert space concept is a generalization of the Euclidean space concept. In physics it's common to encounter Hilbert spaces as infinite-dimensional function spaces.

Hilbert spaces are Banach spaces, but the converse does not hold generally.

For example, $\mathcal{L}^2([a, b])$ is an infinite-dimensional Hilbert space with the canonical inner product $\langle f ; g \rangle = \int_a^b fg$.

Note that \mathcal{L}^2 is the only Hilbert space among the \mathcal{L}^p spaces.

B.3 Derivative

The well known notion of function derivative in \mathbb{R}^n can be extended to maps between Banach spaces. This is useful in physics when formulating problems as variational problems, usually in terms of energy minimization. Indeed, energy is generally defined over a functional vector space and not simply over the real line.

In this case, the research of minimal values of a potential energy rests on the calculus of variations of the energy function compared to variations to other functions defining the problem (geometry, materials, boundary conditions, ...).

Mathematical concepts extended well-known notions of derivative, jacobian and hessian in Euclidean spaces (typically \mathbb{R}^2 or \mathbb{R}^3) for Banach functional spaces.

B.3.1 Fréchet derivative

Differentiability

Let \mathcal{B}_V and \mathcal{B}_W be two Banach spaces and $U \subset \mathcal{B}_V$ an open subset of \mathcal{B}_V . Let $f : u \mapsto f(u)$ be a function of $U^{\mathcal{B}_W}$. f is said to be *Fréchet differentiable* at $u_0 \in U$ if there exists a continuous linear operator $\mathbf{D}f(u_0) \in \mathcal{L}(\mathcal{B}_V, \mathcal{B}_W)$ such that :

$$\lim_{h \rightarrow 0} \frac{f(u_0 + h) - f(u_0) - \mathbf{D}f(u_0) \cdot h}{\|h\|} = 0 \quad (\text{B.4a})$$

Or, equivalently :

$$f(u_0 + h) = f(u_0) + \mathbf{D}f(u_0) \cdot h + o(h) \quad , \quad \lim_{h \rightarrow 0} \frac{o(h)}{\|h\|} = 0 \quad (\text{B.4b})$$

In the literature, it is common to find the following notations : $df = \mathbf{D}f(u_0) \cdot h = \mathbf{D}f_{u_0}(h) = \mathbf{D}f(u_0, h)$ for the differential of f , which means nothing but $\mathbf{D}f(u_0)$ is linear regarding h . The dot denotes the evaluation of $\mathbf{D}f(u_0)$ at h . This notation can be ambiguous as far as the linearity of $\mathbf{D}f(u_0)$ in h is denoted as a product which is not explicitly defined.

Derivative

If f is Fréchet differentiable at $u_0 \in U$, the continuous linear operator $\mathbf{D}f(u_0) \in \mathcal{L}(\mathcal{B}_V, \mathcal{B}_W)$ is called the *Fréchet derivative* of f at u_0 and is also denoted :

$$f'(u_0) = \mathbf{D}f(u_0) \quad (\text{B.5})$$

Appendix B. Calculus of variations

f is said to be \mathcal{C}^1 in the sens of Fréchet if f is Fréchet differentiable for all $u \in U$ and the function $\mathbf{D}f : u \mapsto f'(u)$ of $U^{\mathcal{L}(\mathcal{B}_V, \mathcal{B}_W)}$ is continuous.

Differential or total derivative

$df = \mathbf{D}f(u_0) \cdot h$ is sometimes called the *differential* or *total derivative* of f and represents the change in the function f for a perturbation h from u_0 .

Higer derivatives

Because the differential of f is a linear map from \mathcal{B}_V to $\mathcal{L}(\mathcal{B}_V, \mathcal{B}_W)$ it is possible to look for the differentiability of $\mathbf{D}f$. If it exists, it is denoted \mathbf{D}^2f and maps \mathcal{B}_V to $\mathcal{L}(\mathcal{B}_V, \mathcal{L}(\mathcal{B}_V, \mathcal{B}_W))$.

B.3.2 Gâteaux derivative

Directional derivative

Let \mathcal{B}_V and \mathcal{B}_W be two Banach spaces and $U \subset \mathcal{B}_V$ an open subset of \mathcal{B}_V . Let $f : u \mapsto f(u)$ be a function of $U^{\mathcal{B}_W}$. f is said to have a *derivative in the direction* $h \in \mathcal{B}_V$ at $u_0 \in U$ if :

$$\frac{d}{d\lambda} f(u_0 + \lambda h) \Big|_{\lambda=0} = \lim_{\lambda \rightarrow 0} \frac{f(u_0 + \lambda h) - f(u_0)}{\lambda} \quad (\text{B.6})$$

exists. This element of \mathcal{B}_W is called the *directional derivative* of f in the direction h at u_0 .

Differentiability

Let \mathcal{B}_V and \mathcal{B}_W be two Banach spaces and $U \subset \mathcal{B}_V$ an open subset of \mathcal{B}_V . Let $f : u \mapsto f(u)$ be a function of $U^{\mathcal{B}_W}$. f is said to be *Gâteaux differentiable* at $u_0 \in U$ if there exists a continious linear operator $\mathbf{D}f(u_0) \in \mathcal{L}(\mathcal{B}_V, \mathcal{B}_W)$ such that :

$$\forall h \in \mathcal{U}, \quad \lim_{\lambda \rightarrow 0} \frac{f(u_0 + \lambda h) - f(u_0)}{\lambda} = \frac{d}{d\lambda} f(u_0 + \lambda h) \Big|_{\lambda=0} = \mathbf{D}f(u_0) \cdot h \quad (\text{B.7a})$$

Or, equivalently :

$$\forall h \in \mathcal{U}, \quad f(u + \lambda h) = f(u) + \lambda \mathbf{D}f(u_0) \cdot h + o(\lambda) \quad , \quad \lim_{\lambda \rightarrow 0} \frac{o(\lambda)}{\lambda} = 0 \quad (\text{B.7b})$$

In other words, it means that all the directional derivatives of f exist at u_0 .

Derivative

If f is Gâteaux differentiable at $u_0 \in U$, the continuous linear operator $\mathbf{D}f(u_0) \in \mathcal{L}(\mathcal{B}_V, \mathcal{B}_W)$ is called the *Gâteaux derivative* of f at u_0 and is also denoted :

$$f'(u_0) = \mathbf{D}f(u_0) \quad (\text{B.8})$$

f is said to be \mathcal{C}^1 in the sens of Gâteaux if f is Gâteaux differentiable for all $u \in U$ and the function $\mathbf{D}f : u \mapsto f'(u)$ of $U^{\mathcal{L}(\mathcal{B}_V, \mathcal{B}_W)}$ is continuous.

The Gâteaux derivative is a weaker form of derivative than the Fréchet derivative. If f is Fréchet differentiable, then it is also Gâteaux differentiable and its Fréchet and Gâteaux derivatives agree, but the converse does not hold generally.

B.3.3 Useful properties

Let $\mathcal{B}_V, \mathcal{B}_W$ and \mathcal{B}_Z be three Banach spaces. Let $f, g : \mathcal{B}_V \rightarrow \mathcal{B}_W$ and $h : \mathcal{B}_W \rightarrow \mathcal{B}_Z$ be three Gâteaux differentiable functions. Then, the following useful properties holds :

$$\mathbf{D}(f + g)(u) = \mathbf{D}f(u) + \mathbf{D}g(u) \quad (\text{B.9})$$

$$\mathbf{D}(f \circ h)(u) = \mathbf{D}h(f(u)) \circ \mathbf{D}f(u) = \mathbf{D}h(f(u)) \cdot \mathbf{D}f(u) \quad (\text{B.10})$$

Recall that the composition of $\mathbf{D}h(f(u))$ with $\mathbf{D}f(u)$ means “ $\mathbf{D}h(f(u))$ applied to $\mathbf{D}f(u)$ ” and is also denoted by \cdot as explained previously.

B.3.4 Partial derivative

Following [170] the main results on partial derivatives of two-variables functions are presented here. They are generalizable to n-variables functions.

Definition

Let $\mathcal{B}_{V_1}, \mathcal{B}_{V_2}$ and \mathcal{B}_W be three Banach spaces and $U \subset \mathcal{B}_{V_1} \oplus \mathcal{B}_{V_2}$ an open subset of $\mathcal{B}_{V_1} \oplus \mathcal{B}_{V_2}$. Let $f : u \mapsto f(u)$ be a function of $U^{\mathcal{B}_W}$. Let $u_0 = (u_{01}, u_{02}) \in U$. If the derivatives of the following functions exist :

$$\begin{aligned} f_1 : \mathcal{B}_{V_1} &\longrightarrow \mathcal{B}_W \\ u_1 &\mapsto f(u_1, u_{02}) \end{aligned} \quad , \quad \begin{aligned} f_2 : \mathcal{B}_{V_2} &\longrightarrow \mathcal{B}_W \\ u_2 &\mapsto f(u_{01}, u_2) \end{aligned} \quad (\text{B.11})$$

they are called *partial derivatives* of f at u_0 and are denoted $\mathbf{D}_1 f(u_0) \in \mathcal{L}(\mathcal{B}_{V_1}, \mathcal{B}_W)$ and $\mathbf{D}_2 f(u_0) \in \mathcal{L}(\mathcal{B}_{V_2}, \mathcal{B}_W)$.

Differentiability

Let \mathcal{B}_{V_1} , \mathcal{B}_{V_2} and \mathcal{B}_W be three Banach spaces and $U \subset \mathcal{B}_{V_1} \oplus \mathcal{B}_{V_2}$ an open subset of $\mathcal{B}_{V_1} \oplus \mathcal{B}_{V_2}$. Let $f : u \mapsto f(u)$ be a function of $U^{\mathcal{B}_W}$. If f is differentiable, then the partial derivatives exist and satisfy for all $h = (h_1, h_2) \in \mathcal{B}_{V_1} \oplus \mathcal{B}_{V_2}$:

$$\mathbf{D}_1 f(u) \cdot h_1 = \mathbf{D}f(u) \cdot (h_1, 0) \quad (\text{B.12})$$

$$\mathbf{D}_2 f(u) \cdot h_2 = \mathbf{D}f(u) \cdot (0, h_2) \quad (\text{B.13})$$

$$\mathbf{D}f(u) \cdot (h_1, h_2) = \mathbf{D}_1 f(u) \cdot h_1 + \mathbf{D}_2 f(u) \cdot h_2 \quad (\text{B.14})$$

B.4 Gradient vector

Let \mathcal{H} be a Hilbert space with the inner product denoted $\langle \cdot, \cdot \rangle$. Let $U \subset \mathcal{H}$ an open subset of \mathcal{H} . Let $F : u \mapsto F(u)$ be a scalar function of $U^{\mathbb{R}}$. The *gradient* of F is the map $\text{grad } F : x \mapsto (\text{grad } F)(x)$ of $U^{\mathcal{H}}$ such that :

$$\forall h \in \mathcal{H}, \quad \langle (\text{grad } F)(x), h \rangle = \mathbf{D}F(x) \cdot h \quad (\text{B.15})$$

Note that the gradient vector depends on the chosen inner product. For $\mathcal{H} = \mathbb{R}^n$ with the canonical inner product, one can recall the usual definition of the gradient vector and the corresponding linear approximation of F :

$$\mathbf{F}_{x+h} = \mathbf{F}_x + (\text{grad } F)_x^T H + o(H) \quad , \quad \text{grad } F_x = \begin{bmatrix} \frac{\partial F}{\partial x_1} \\ \vdots \\ \frac{\partial F}{\partial x_n} \end{bmatrix} \in \mathbb{R}^n \quad (\text{B.16})$$

Recall that the canonical inner product on \mathbb{R}^n is such that $\langle x, y \rangle = X^T Y$ in a column vector representation. In this case it is common to denote $\text{grad } F = \nabla F$.

For function spaces the usual definition of the gradient can be extended. For instance if F is a scalar function on \mathcal{L}^2 , the gradient of F is the unique function (if it exists) from \mathcal{L}^2 which satisfies :

$$\forall h \in \mathcal{L}^2, \quad \mathbf{D}F(x) \cdot h = \langle (\text{grad } F)(x), h \rangle = \int (\text{grad } F) h \quad (\text{B.17})$$

In this case it is common to denote $\text{grad } F = \frac{\delta F}{\delta x}$. The gradient is also known as the *functional derivative*. The existence and unicity of $\text{grad } F$ is ensured by the *Riesz representation theorem*.

B.5 Jacobian matrix

Let f be a differentiable function from \mathbb{R}^n to \mathbb{R}^m . The *differential* or *total derivative* of such a fonction is a linear application from \mathbb{R}^n to \mathbb{R}^m which could be represented with the

following matrix called the *jacobian matrix* :

$$\mathbf{D}f(x) = \mathbf{J}_x = \frac{df}{dx} = \begin{bmatrix} \frac{\partial f}{\partial x_1} & \cdots & \frac{\partial f}{\partial x_n} \end{bmatrix} = \begin{bmatrix} \frac{\partial f_1}{\partial x_1} & \cdots & \frac{\partial f_1}{\partial x_n} \\ \vdots & \ddots & \vdots \\ \frac{\partial f_m}{\partial x_1} & \cdots & \frac{\partial f_m}{\partial x_n} \end{bmatrix} \in \mathcal{M}_{m,n}(\mathbb{R}) \quad (\text{B.18})$$

Thus, with the matrix notation, the Taylor expansion takes the following form :

$$\mathbf{F}_{x+h} = \mathbf{F}_x + \mathbf{J}_x H + o(H) \quad (\text{B.19})$$

In the cas $m = 1$, the jacobian matrix of the functional F is nothing but the gradient vector transpose itself :

$$\mathbf{D}F(x) = \mathbf{J}_x = \frac{dF}{dx} = \begin{bmatrix} \frac{\partial F}{\partial x_1} & \cdots & \frac{\partial F}{\partial x_n} \end{bmatrix} = \nabla F^T \quad (\text{B.20})$$

B.6 Hessian

Let F be a differentiable scalar function from \mathbb{R}^n to \mathbb{R} . The second order differential of such a fonction is a linear application from \mathbb{R}^n to \mathbb{R}^n which could be represented with the following matrix called the *hessian matrix* :

$$\mathbf{D}^2F(x) = \mathbf{H}_x = \frac{d^2F}{dx}(x) = \begin{bmatrix} \frac{\partial F_1^2}{\partial x_1^2} & \frac{\partial F_1^2}{\partial x_1 \partial x_2} & \cdots & \frac{\partial F_1^2}{\partial x_1 \partial x_n} \\ \frac{\partial F_1^2}{\partial x_2 \partial x_1} & \frac{\partial F_1^2}{\partial x_2^2} & \cdots & \frac{\partial F_1^2}{\partial x_2 \partial x_n} \\ \vdots & \ddots & \ddots & \vdots \\ \frac{\partial F_p^2}{\partial x_n \partial x_1} & \frac{\partial F_p^2}{\partial x_n \partial x_2} & \cdots & \frac{\partial F_p^2}{\partial x_n^2} \end{bmatrix} \in \mathcal{M}_{n,n}(\mathbb{R}) \quad (\text{B.21})$$

Thus, with the matrix notation, the Taylor expansion takes the following form :

$$\mathbf{F}_{x+h} = \mathbf{F}_x + \mathbf{J}_x H + \frac{1}{2}H^T \mathbf{H}_x H + o(H) \quad (\text{B.22})$$

B.7 Functional

A *functional* is a map from a vector space $E(\mathbb{K})$ into its underlying scalar field \mathbb{K} . Here $\mathcal{E}_p[\mathbf{x}, \theta]$ is a functional depending over \mathbf{x} and θ .

B.8 References

- [170] R. Abraham, J. E. Marsde, and T. Ratiu. *Manifolds, Tensor Analysis, and Applications (Ralph Abraham, Jerrold E. Marsden and Tudor Ratiu)*. 2002, p. 617.

C Parabolic interpolation

C.1 Introduction

In this appendix, we give the required formulas to conduct a parabolic interpolation of a scalar or vector-valued function over an interval.

We look for a polynomial interpolation of order 2 of a continuous scalar or vector-valued function $\mathbf{V}: t \mapsto \mathbf{V}(t)$ over the interval $[t_0, t_2]$; supposing that the value of the function is known for three distinct parameters $t_0 < t_1 < t_2$:

$$\mathbf{V}(t_0) = \mathbf{V}_0 \tag{C.1a}$$

$$\mathbf{V}(t_1) = \mathbf{V}_1 \tag{C.1b}$$

$$\mathbf{V}(t_2) = \mathbf{V}_2 \tag{C.1c}$$

This interpolation method is employed several times in this thesis, for instance to evaluate the position of a kinetic energy peak during the dynamic relaxation process. It is also employed for evaluating the bending moment and the curvature of a discrete rod at mid-edge, knowing its values at vertices.

Note that this interpolation method is valid if the basis in which \mathbf{V} is decomposed does not depend on the parameter t . Otherwise, the classical transportation term should be considered ($\boldsymbol{\omega} \times \mathbf{V}$).

C.2 Lagrange interpolating polynomial

The Lagrange interpolation of order two is given by the following polynomial :

$$\mathbf{V}(t) = \mathbf{V}_0 \frac{(t - t_1)(t - t_2)}{(t_0 - t_1)(t_0 - t_2)} + \mathbf{V}_1 \frac{(t - t_0)(t - t_2)}{(t_1 - t_0)(t_1 - t_2)} + \mathbf{V}_2 \frac{(t - t_0)(t - t_1)}{(t_2 - t_0)(t_2 - t_1)} \tag{C.2}$$

C.3 Reparametrization

Lets introduce the distances l_0 and l_1 in the parametric space :

$$l_0 = t_1 - t_0 \quad (\text{C.3a})$$

$$l_1 = t_2 - t_1 \quad (\text{C.3b})$$

Lets introduce the change of variable $u = t - t_1$. The polynomial in [eq. \(C.2\)](#) can be rewritten in the form :

$$\mathbf{V}(u) = \mathbf{V}_0 \frac{u(u - l_1)}{l_0(l_0 + l_1)} - \mathbf{V}_1 \frac{(u + l_0)(u - l_1)}{l_0 l_1} + \mathbf{V}_2 \frac{u(u + l_0)}{l_1(l_0 + l_1)} \quad (\text{C.4})$$

where :

$$u_0 = -l_0 \quad (\text{C.5a})$$

$$u_1 = 0 \quad (\text{C.5b})$$

$$u_2 = l_1 \quad (\text{C.5c})$$

The derivative of this polynomial is also required to determine the extremum value of \mathbf{V} . Differentiating [eq. \(C.4\)](#) gives :

$$\mathbf{V}'(u) = \mathbf{V}_0 \frac{2u - l_1}{l_0(l_0 + l_1)} - \mathbf{V}_1 \frac{2u + (l_0 - l_1)}{l_0 l_1} + \mathbf{V}_2 \frac{2u + l_0}{l_1(l_0 + l_1)} \quad (\text{C.6})$$

This expression can be factorized to give the more compact form :

$$\mathbf{V}'(u) = \left(\frac{\mathbf{V}_1 - \mathbf{V}_0}{l_0} \right) \frac{l_1 - 2u}{l_0 + l_1} + \left(\frac{\mathbf{V}_2 - \mathbf{V}_1}{l_1} \right) \frac{l_0 + 2u}{l_0 + l_1} \quad (\text{C.7})$$

C.4 Characteristic values

Using [eq. \(C.4\)](#) the interpolated values of \mathbf{V} at mid distance between t_0 and t_1 ($u = -l_0/2$), and at mid distance between t_1 and t_2 ($u = +l_1/2$) are given by :

$$\mathbf{V}_{01} = \mathbf{V}_0 \frac{l_0 + 2l_1}{4(l_0 + l_1)} + \mathbf{V}_1 \frac{l_0 + 2l_1}{4l_1} - \mathbf{V}_2 \frac{l_0^2}{4l_1(l_0 + l_1)} \quad (\text{C.8a})$$

$$\mathbf{V}_{12} = -\mathbf{V}_0 \frac{l_1^2}{4l_0(l_0 + l_1)} + \mathbf{V}_1 \frac{2l_0 + l_1}{4l_0} + \mathbf{V}_2 \frac{2l_0 + l_1}{4(l_0 + l_1)} \quad (\text{C.8b})$$

Using [eq. \(C.7\)](#) the interpolated values of \mathbf{V}' at mid distance between t_0 and t_1 ($u = -l_0/2$), and at mid distance between t_1 and t_2 ($u = +l_1/2$) are given by :

$$\mathbf{V}'_{01} = \frac{\mathbf{V}_1 - \mathbf{V}_0}{l_0} \quad (\text{C.9a})$$

$$\mathbf{V}'_{12} = \frac{\mathbf{V}_2 - \mathbf{V}_1}{l_1} \quad (\text{C.9b})$$

Remark that this is an interesting result as at these parameters the evaluation of \mathbf{V}' boils down to a finite difference scheme.

Using eq. (C.7) and introducing $\alpha = \frac{l_0}{l_0+l_1}$ the interpolated values of \mathbf{V}' at t_0 , t_1 and t_2 are given by :

$$\mathbf{V}'_0 = (1 + \alpha)\mathbf{V}'_{01} - \alpha\mathbf{V}'_{12} \quad (\text{C.10a})$$

$$\mathbf{V}'_1 = (1 - \alpha)\mathbf{V}'_{01} + \alpha\mathbf{V}'_{12} \quad (\text{C.10b})$$

$$\mathbf{V}'_2 = (\alpha - 1)\mathbf{V}'_{01} + (2 - \alpha)\mathbf{V}'_{12} \quad (\text{C.10c})$$

Lets rewrite eq. (C.8a) and (C.8b) with the help of α :

$$\mathbf{V}_{01} = \frac{1}{4} \left((2 - \alpha)\mathbf{V}_0 + \frac{2 - \alpha}{1 - \alpha}\mathbf{V}_1 - \frac{\alpha^2}{1 - \alpha}\mathbf{V}_2 \right) \quad (\text{C.11a})$$

$$\mathbf{V}_{01} = \frac{1}{4} \left(-\frac{(1 - \alpha)^2}{\alpha}\mathbf{V}_0 + \frac{1 + \alpha}{\alpha}\mathbf{V}_1 + (1 + \alpha)\mathbf{V}_2 \right) \quad (\text{C.11b})$$

C.5 Extremum value

The extremum value of the parabola is obtained for $\mathbf{V}'(u^*) = 0$. It's a minimum if $\mathbf{V}'_{12} > \mathbf{V}'_{01}$ and it's a maximum if $\mathbf{V}'_{12} < \mathbf{V}'_{01}$:

$$u^* = \frac{l_1\mathbf{V}'_{01} + l_0\mathbf{V}'_{12}}{2(\mathbf{V}'_{01} - \mathbf{V}'_{12})} \quad (\text{C.12})$$

Remark that if $\mathbf{V}'_{12} = \mathbf{V}'_{01}$ it does not make sens to compute u^* as in this case the parabola degenerates into a line. The value of the function at this parameter is given by :

$$\mathbf{V}(u^*) = \mathbf{V}_1 + \frac{(l_1\mathbf{V}'_{01} + l_0\mathbf{V}'_{12})^2}{4(l_0 + l_1)(\mathbf{V}'_{01} - \mathbf{V}'_{12})} \quad (\text{C.13})$$

The parabola in eq. (C.4) now writes :

$$\mathbf{V}(u) = -\frac{\mathbf{V}'_{01} - \mathbf{V}'_{12}}{l_0 + l_1}(u - u^*)^2 + \mathbf{V}(u^*) \quad (\text{C.14})$$

The extremum is located in $[t_0, t_2]$ if the sign of \mathbf{V}' changes on this interval. This condition is satisfied whenever $\mathbf{V}'_{01} \cdot \mathbf{V}'_{12} < 0$.

Finally, in the special case of a uniform discretization where $l_0 = l_1 = l$, eq. (C.12) and (C.13) become :

$$u^* = \frac{l}{2} \left(\frac{\mathbf{V}_0 - \mathbf{V}_2}{\mathbf{V}_0 - 2\mathbf{V}_1 + \mathbf{V}_2} \right) \quad (\text{C.15a})$$

$$\mathbf{V}(u^*) = \mathbf{V}_1 - \frac{u^*}{4l}(\mathbf{V}_2 - \mathbf{V}_0) \quad (\text{C.15b})$$

Bibliography

- [1] B. Burkhardt, J. Hennicke, and E. Schauer, eds. *IL10 Grid Shells*. Institut für leichte Flächentragwerke (IL). Stuttgart, 1974.
- [2] E. Happold and I. Liddell. “Timber lattice roof for the Mannheim Bundesgartenschau”. In: *The structural engineer* 53.3 (1975), pp. 99–135.
- [3] C. Douthe, J.-F. Caron, and O. Baverel. “Gridshell structures in glass fibre reinforced polymers”. In: *Construction and Building Materials* 24.9 (2010), pp. 1580–1589.
- [4] B. Burkhardt, M. Chaitos, J. Langner, W. Langner, and G. Lubberger, eds. *IL13 Multihalle Mannheim*. Institut für leichte Flächentragwerke (IL). Stuttgart, 1978.
- [5] J. Chilton and G. Tang. *Timber Gridshells: Architecture, structure and craft*. Routledge, 2017.
- [6] M. Collins and T. Cosgrove. “A Review of the State of the Art of Timber Gridshell Design and Construction”. In: *Civil Engineering Research in Ireland*. 2016.
- [7] G. Quinn and C. Gengnagel. “A review of elastic grid shells, their erection methods and the potential use of pneumatic formwork”. In: *WIT Transactions on the Built Environment* 136 (2014), pp. 129–144.
- [8] P. Cuvilliers, C. Douthe, L. du Peloux, and R. Le Roy. “Hybrid structural skin : prototype of an elastic gridshell braced by a fibre-reinforced concrete envelope”. In: *Journal of The International Association for Shell and Spatial Structures* (2017), pp. 1–12.
- [9] L. Kim-Lan Vaulot. “Form-Finding of Elastic Gridshells”. PhD thesis. Massachusetts Institute of Technology, 2016.
- [10] C. Douthe. “Etude de structures élancées précontraintes en matériaux composites : application à la conception des gridshells”. PhD thesis. Université Paris Est, 2007, p. 274.
- [11] L. Bouhana. “Optimisation structurelle des gridshells”. PhD thesis. Université Paris-Est, 2010, p. 154.
- [12] F. Tayeb. “Simulation numérique du comportement mécanique non linéaire de gridshells composés de poutres élancées en matériaux composites et de sections quelconques”. PhD thesis. 2015.

Bibliography

- [13] E. Lafuente Hernández. "Design and Optimisation of Elastic Gridshells". PhD thesis. Universität der Künste Berlin, 2015.
- [14] B. Addis. "'Toys that save millions' - A history of using physical models in structural design". In: *The Structural Engineer* 91.4 (2013), pp. 12–27.
- [15] I. Liddell. "Frei Otto and the development of gridshells". In: *Case Studies in Structural Engineering* 4 (2015), pp. 39–49.
- [16] R. Harris, J. Romer, O. Kelly, and S. Johnson. "Design and construction of the Downland Gridshell". eng. In: *Building research and information* 31.6 (2003), pp. 427–454.
- [17] R. Burton, M. Dickson, and R. Harris. "The use of roundwood thinnings in buildings : a case study". In: *Building Research & Information* 26.2 (1998), pp. 76–93.
- [18] M. McQuaid, F. Otto, and S. Ban. "Building the Japan pavilion". In: *Shigeru Ban*. Phaidon Press, 2006, pp. 8–11.
- [19] R. Harris and O. Kelly. "The structural engineering of the Downland gridshell". In: *Space Structures* 5 1.April 2002 (2002), pp. 161–172.
- [20] O. Lowenstein. "Lothian Gridshell". In: *Building for a Future Winter* (2002), p. 29.
- [21] Bdonline.co.uk. *The other gridshell*. 2002.
- [22] O. Lowenstein. "Gridshells in England. Ideas from the U.K. make stunning use of small timber". In: *Wood Design & Building* (2004).
- [23] Fourthdoor.org. *Growing and making Flimwell's chestnut gridshell*. 2003.
- [24] R. Harris, S. Haskins, and J. Roynon. "The Savill Garden gridshell : Design and construction". In: *The Structural Engineer* 86.17 (2008), pp. 27–34.
- [25] Trada. "The Savill Building. A visitor centre with a timber gridshell roof Gridshell structures". In: *TRADA* (2006), pp. 1–7.
- [26] C. Douthe, O. Baverel, and J.-F. Caron. "Formfinding of a grid shell in composite materials". In: *Journal of the IASS* 47 (2006), pp. 53–62.
- [27] O. Baverel, J.-F. Caron, F. Tayeb, and L. du Peloux. "Gridshells in composite materials : construction of a 300 m² forum for the solidays' festival in Paris". In: *Structural Engineering International* 22.3 (2012), pp. 408–414.
- [28] L. du Peloux, F. Tayeb, O. Baverel, and J.-F. Caron. "Construction of a large composite gridshell structure: a lightweight structure made with pultruded glass fibre reinforced polymer tubes". In: *Structural Engineering International* 26.2 (2016), pp. 160–167.
- [29] B. D'Amico, A. Kermani, and H. Zhang. "Form finding and structural analysis of actively bent timber grid shells". In: *Engineering Structures* 81 (2014), pp. 195–207.
- [30] B. D'Amico, A. Kermani, H. Zhang, A. Pugnale, S. Colabella, and S. Pone. "Timber gridshells: Numerical simulation, design and construction of a full scale structure". In: *Structures* 3.May 2016 (2015), pp. 227–235.
- [31] D. Naicu, R. Harris, and C. Williams. "Timber Gridshells: Design methods and their application to a temporary pavilion". In: *World Conference on Timber Engineering* (2014), pp. 1–2.

- [32] J. Haddal Mork, S. Dyvik Hillersøy, B. Manum, A. Rønnquit, and N. Labonnote. “Introducing the Segment Lath - a Simplified Modular Timber Gridshell Built in Trondheim Norway”. In: *World Conference on Timber Engineering*. 3. Vienna, Austria, 2016.
- [33] N. Labonnote, J. H. Mork, S. H. Dyvik, A. Rønnquist, and B. Manum. “Experimental and Numerical Study of the Structural Performance of a Timber Gridshell”. In: *World Conference on Timber Engineering*. 2. Vienna, Austria, 2016, pp. 3–10.
- [34] M. Toussaint. “A design tool for timber gridshells”. PhD thesis. Technische Universiteit Delft, 2007.
- [35] J. Olsson and A. Fisher. “Form finding and size optimization - Implementation of beam elements and size optimization in real time”. PhD thesis. Chalmers University of Technology, 2012, p. 97.
- [36] E. Poulsen. “Structural design and analysis of elastically bent gridshells”. PhD thesis. Chalmers University of Technology, Gothenburg Sweden, 2015.
- [37] S. Adriaenssens. “Stressed spline structures”. PhD thesis. University of Bath, 2000.
- [38] S. Adriaenssens, M. Barnes, and C. Williams. “A new analytic and numerical basis for the form-finding and analysis of spline and gridshell structures”. In: *Computing Developments in Civil and Structural Engineering*. Ed. by B. Kumar and B. H. V. Topping. Edinburgh: Civil-Comp Press, 1999, pp. 83–91.
- [39] M. Barnes. “Form finding and analysis of tension structures by dynamic relaxation”. In: *International Journal of Space Structures* 14.2 (1999), pp. 89–104.
- [40] S. Adriaenssens and M. Barnes. “Tensegrity spline beam and grid shell structures”. In: *Engineering Structures* 23.1 (2001), pp. 29–36.
- [41] M. Barnes, S. Adriaenssens, and M. Krupka. “A novel torsion/bending element for dynamic relaxation modeling”. In: *Computers & Structures* 119 (Apr. 2013), pp. 60–67.
- [42] L. du Peloux, F. Tayeb, B. Lefevre, O. Baverel, and J.-F. Caron. “Formulation of a 4-DoF torsion / bending element for the formfinding of elastic gridshells”. In: *Proceedings of the International Association for Shell and Spatial Structures*. August. Amsterdam, 2015, pp. 1–14.
- [43] B. D’Amico, H. Zhang, and A. Kermani. “A finite-difference formulation of elastic rod for the design of actively bent structures”. In: *Engineering Structures* 117 (2016), pp. 518–527.
- [44] T. Bulenda and J. Knippers. “Stability of grid shells”. In: *Computers and Structures* 79.12 (2001), pp. 1161–1174.
- [45] R. Mesnil, J. Ochsendorf, and C. Douthe. “Stability of Elastic Grid Shells”. In: *International Journal of Space Structures* 30.1 (2015), pp. 27–36.
- [46] B. Lefevre, C. Douthe, and O. Baverel. “Buckling of elastic gridshells”. In: *Journal of the IASS* September (2015).
- [47] S. R. Malek. “The effect of geometry and topology on the mechanics of grid shells”. PhD thesis. MIT, 2012.

Bibliography

- [48] T. Jensen, O. Baverel, and C. Douthe. “Morphological and mechanical investigation of interconnected elastic gridshells”. In: *International Journal of Space Structures* 28.3-4 (2013), pp. 175–186.
- [49] G. Filz and D. Naicu. “2 Landscapes – interaction of 2 gridshells based on a modified Stewart - Gough - principle”. In: *Proceedings of the IASS Working Groups 12 + 18*. Tokyo, Japan, 2015.
- [50] F. Tayeb, J.-F. Caron, O. Baverel, and L. du Peloux. “Stability and robustness of a 300m² composite gridshell structure”. In: *Construction & Building Materials* (2013).
- [51] L. Bouhana, O. Baverel, and J.-F. Caron. “Mapping two-way continuous elastic grid on an imposed surface : application to grid shells”. In: *IASS 2009*. Valencia, Spain, 2009, pp. 989–998.
- [52] L. Bouhana, O. Baverel, and J.-F. Caron. “Optimization of gridshell bar orientation using a simplified genetic approach”. In: *Structural and Multidisciplinary Optimization* 50.5 (2014), pp. 839–848.
- [53] E. Lafuente Hernández, S. Sechelmann, T. Rörig, and C. Gengnagl. “Topology optimisation of regular and irregular elastic gridshells by means of a non-linear variational method”. In: *Advances in Architectural Geometry*. 2012, pp. 147–160.
- [54] L. du Peloux, O. Baverel, J.-F. Caron, and F. Tayeb. “From shape to shell : a design tool to materialize freeform shapes using gridshell structures”. In: *Design Modelling Symposium*. Berlin, Deutschland, 2011.
- [55] Y. Masson and L. Monasse. “Existence of global Chebyshev nets on surfaces of absolute Gaussian curvature less than 2 pi”. In: *Journal of Geometry* 108.1 (2017), pp. 25–32.
- [56] Y. Masson. “Existence et construction de réseaux de Chebyshev avec singularités et application aux gridshells”. PhD thesis. Université Paris-Est, 2017.
- [57] S. Pone, G. Mirra, E. Pignatelli, D. Lancia, and S. Colabella. “Specialised algorithms for different project stages in a post-formed timber gridshell design”. In: *Structures and Architecture* September (2016), pp. 259–266.
- [58] C. Douthe, R. Mesnil, H. Orts, and O. Baverel. “New shapes for elastic gridshells covered by planar facets”. In: *Proceedings of the IASS Annual Symposium*. October. Tokyo, Japan, 2016, pp. 1–9.
- [59] R. Mesnil. “Structural explorations of fabrication-aware design spaces for non-standard architecture”. PhD thesis. Paris-Est University, 2017, p. 231.
- [60] N. Kotelnikova-Weiler, C. Douthe, E. Lafuente Hernández, O. Baverel, C. Gengnagel, and J.-F. Caron. “Materials for actively-Bent structures”. In: *International Journal of Space Structures* 28.3-4 (2013), pp. 229–240.
- [61] N. Kotelnikova-Weiler. “Optimisation mécanique et énergétique d’enveloppes en matériaux composites pour les bâtiments”. PhD thesis. Université Paris-Est, 2012, p. 310.

- [62] G. Quinn, C. Gengnagel, and K.-U. Bletzinger. “imulatin ng Pneumatic Reaction of a Strained Grid Shells via v Dynamic Relaxation”. In: *Proceedings of the IASS Annual Symposium*. October. Tokyo, Japan, 2016.
- [63] Liuti, A. Pugnale, and B. D’Amico. “Building timber gridshells with air : Numerical simulations and technique challenges”. In: *Structures and Architecture* (2016).
- [64] E. Lafuente Hernández and C. Gengnagel. “A new hybrid: Elastic gridshells braced by membranes”. In: *WIT Transactions on the Built Environment* 136 (2014), pp. 157–170.
- [65] B. D’Amico, A. Kermani, H. Zhang, P. Sheperd, and C. Williams. “Optimisation of cross-section of actively bent grid shells with strength and geometric compatibility constraints”. In: *Computers & Structures* 154 (2015), pp. 163–176.
- [66] A. Menges, O. D. Krieg, and T. Schwinn. *Advancing Wood Architecture. A computational approach*. Routledge, July 2016, p. 256.
- [67] Site Sécurité. *Règlement ERP type CTS (big tops & tents)*.
- [68] J. L. Clarke. *Eurocomp design code and handbook : structural design of polymer composites*. 2003, p. 672.
- [69] L. C. Bank. *Composites for construction : structural design with FRP materials*. 2006, p. 560.
- [70] Fiberline Composites A/S. *Fiberline design manual*. May. 2003, pp. 1–326.
- [71] G. F. A. de L’Hospital. “Analyse des infiniment petits, pour l’intelligence des lignes courbes”. In: (1696).
- [72] J. Delcourt. “Analyse et géométrie, histoire des courbes gauches de Clairaut à Darboux”. In: *Archive for History of Exact Sciences* 65.3 (2011), pp. 229–293.
- [73] T. Hoffmann. *Discrete Differential Geometry of Curves and Surfaces*. Vol. 18. 2008.
- [74] E. Vouga. “Plane Curves”. In: *Lectures in discrete differential geometry*. 2014. Chap. 1, pp. 1–11.
- [75] R. Bishop. “There is more than one way to frame a curve”. In: *Mathematical Association of America* (1975).
- [76] F. Klok. “Two moving coordinate frames for sweeping along a 3D trajectory”. In: *Computer Aided Geometric Design* 3.3 (1986), pp. 217–229.
- [77] H. Guggenheimer. “Computing frames along a trajectory”. In: *Computer Aided Geometric Design* 6.1 (1989), pp. 77–78.
- [78] J. Bloomenthal. “Calculation of reference frames along a space curve”. In: *Graphics Gems*. Ed. by A. S. Glassner. Vol. 1. San Diego, CA, USA: Academic Press Professional, Inc., 1990, pp. 567–571.
- [79] A. J. Hanson and H. Ma. *Parallel Transport Approach to Curve Framing*. Tech. rep. 1995.
- [80] T. Poston, S. Fang, and W. Lawton. “Computing and approximating sweeping surfaces based on rotation minimizing frames”. In: *Proceedings of the 4th International Conference on CAD/CG*. 1995, pp. 1–8.

Bibliography

- [81] W. Wang, B. Jüttler, D. Zheng, and Y. Liu. “Computation of rotation minimizing frames”. In: *ACM Transactions on Graphics* 27.1 (2008), pp. 1–18.
- [82] R. T. Farouki, C. Giannelli, M. L. Sampoli, and A. Sestini. “Rotation-minimizing osculating frames”. In: *Computer Aided Geometric Design* 31.1 (2014), pp. 27–42.
- [83] F. Frenet. “Sur les courbes à double courbure”. In: *Journal de Mathématiques Pures et Appliquées* 17 (1852), pp. 437–447.
- [84] J. Delcourt. “Analyse et géométrie : les courbes gauches de Clairaut à Serret”. PhD thesis. Université de Paris VI, 2007, p. 302.
- [85] J. Bernoulli. *Johannis Bernoulli... Opera omnia, tam antea sparsim edita, quam hactenus inedita*. IV. sumptibus Marci-Michaelis Bousquet, 1728, p. 584.
- [86] H. Pitot. “Quadrature de la moitié d’une courbe des arcs appelée la compagne de la cycloïde”. In: *Mémoires de l’Académie Royale des Sciences (1724)* (1726), pp. 107–113.
- [87] J. L. Coolidge. *A history of geometrical methods*. Ed. by C. Corporation. Dover Books on Mathematics. Dover Publications, 2013, p. 480.
- [88] G. Monge. *Application de l’analyse à la géométrie*. 1809, p. 475.
- [89] L. Euler. “Continens analysin, pro incuruatione fili in fingulis punctis inueniendia”. In: *Novi Commentarii academiae scientiarum Petropolitanae* 19 (1775), pp. 340–370.
- [90] A. Gray, E. Abbena, and S. Salamon. *Modern differential geometry of curves and surfaces with Mathematica*. Ed. by E. A. Salamon and Simon. Third. CRC Press, 2006, p. 1016.
- [91] M. Bergou, M. Wardetzky, S. Robinson, B. Audoly, and E. Grinspun. “Discrete elastic rods”. In: *ACM SIGGRAPH* (2008), pp. 1–12.
- [92] D. Carroll, E. Hankins, E. Kose, and I. Sterling. “A survey of the differential geometry of discrete curves”. In: *The Mathematical Intelligencer* 36.4 (2014), pp. 28–35. arXiv: [arXiv:1311.5862v1](https://arxiv.org/abs/1311.5862v1).
- [93] A. Bobenko. *Discrete differential geometry*. Second. 2015, p. 144.
- [94] P. Romon. *Introduction à la géométrie différentielle discrète*. Références sciences. Ellipses, 2013, p. 216.
- [95] M. Bergou, B. Audoly, E. Vouga, M. Wardetzky, and E. Grinspun. “Discrete viscous threads”. In: *ACM Transactions on ...* (2010), pp. 1–10.
- [96] B. Lefevre, F. Tayeb, L. du Peloux, and J.-F. Caron. “A 4-degree-of-freedom Kirchhoff beam model for the modeling of bending–torsion couplings in active-bending structures”. In: *International Journal of Space Structures* 32.2 (2017), pp. 69–83.
- [97] S. Nabaei. “Mechanical form-finding of timber fabric structures”. PhD thesis. EPFL, 2014.
- [98] M. Grégoire and E. Schömer. “Interactive simulation of one-dimensional flexible parts”. In: *CAD Computer Aided Design* 39.8 (2007), pp. 694–707.

- [99] A. Theetten, L. Grisoni, C. Andriot, and B. Barsky. “Geometrically exact dynamic splines”. In: *CAD Computer Aided Design* 40 (2008), pp. 35–48.
- [100] F. Bertails, B. Audoly, M.-P. Cani, B. Querleux, F. Leroy, and J.-L. Lévéque. “Super-helices for predicting the dynamics of natural hair”. In: *ACM Transactions on Graphics* 25.3 (2006), p. 1180.
- [101] F. Bertails-Descoubes. “Super-clothoids”. In: *Computer Graphics Forum* 31.2 (2012), pp. 509–518.
- [102] J. Spillmann and M. Teschner. “CORDE : Cosserat Rod Elements for the Dynamic Simulation of One-Dimensional Elastic Objects”. In: *Eurographics/ ACM SIGGRAPH Symposium on Computer Animation* (2007), pp. 1–10.
- [103] P. Jung, S. Leyendecker, J. Linn, and M. Ortiz. “A discrete mechanics approach to the Cosserat rod theory—Part 1: static equilibria”. eng. In: *International journal for numerical methods in engineering* 85.1 (2010), pp. 31–60.
- [104] F. B. Fuller. “Decomposition of the linking number of a closed ribbon : A problem from molecular biology”. In: 75.8 (1978), pp. 3557–3561.
- [105] R. Vauquelin. “Writhing Geometry at Finite Temperature : Random Walks and Geometric phases for Stiff Polymers”. In: 1 (2000).
- [106] R. de Vries. “Evaluating changes of writhe in computer simulations of supercoiled DNA”. In: *The Journal of Chemical Physics* 122.6 (2005).
- [107] M. Berger. “Topological Quantities: Calculating Winding, Writhing, Linking, and Higher order Invariants”. In: *Lecture Notes in Mathematics* 1973 (2009), pp. 75–97.
- [108] J. Langer and D. Singer. “Lagrangian Aspects of the Kirchhoff elastic rod”. In: *Society for Industrial and Applied Mathematics Review* 38.4 (1996), pp. 605–618.
- [109] J. Alexander and S. Antman. “The ambiguous twist of love”. In: *Quarterly of Applied Mathematics* 40.1 (1982), pp. 83–92.
- [110] B. Audoly, M. Amar, and Y. Pomeau. *Elasticity and geometry*. 2010, p. 600.
- [111] E. H. Dill. “Kirchhoff’s theory of rods”. In: *Archive for History of Exact Sciences* (1992), p. 23.
- [112] S. Antman. *Nonlinear problems of elasticity*. Applied mathematical sciences. New York: Springer, 2005, p. 838.
- [113] E. Reissner. “On one-dimensional large-displacement finite-strain beam theory.” In: *Studies in Applied Mathematics* 52.2 (1973), pp. 87–95.
- [114] A. Love. *A treatise on the mathematical theory of elasticity*. Second. Cambridge University Press, 1906, p. 571.
- [115] G. Kirchhoff. *Über das gleichgewicht und die bewegung einer elastischen scheibe*. Berlin, 1850, p. 38.
- [116] G. Kirchhoff. *Vorlesungen über mathematische, physik, mechanik*. Ed. by B. G. Teubner. Leipzig, 1876, p. 483.
- [117] A. Clebsch. *Théorie de l’elasticité des corps solides*. Paris: Dunod, 1883, p. 900.

Bibliography

- [118] S. Neukirch. “Enroulement, contact et vibrations de tiges élastiques”. PhD thesis. 2009, p. 97.
- [119] S. Timoshenko. “On the correction for shear of the differential equation for transverse vibrations of prismatic bars”. In: *Philosophical Magazine Series 6* 41.245 (1921), pp. 744–746.
- [120] J. C. Simo and L. Vu-Quoc. “A Geometrically-exact rod model incorporating shear and torsion-warping deformation”. In: *International Journal of Solids and Structures* 27.3 (1991), pp. 371–393.
- [121] S. Antman. “Kirchhoff’s problem for nonlinearly elastic rods”. In: *Quarterly of Applied Mathematics* XXXIV.3 (1974), pp. 221–240.
- [122] D. Q. Cao and R. W. Tucker. “Nonlinear dynamics of elastic rods using the Cosserat theory: Modelling and simulation”. In: *International Journal of Solids and Structures* 45.2 (2008), pp. 460–477.
- [123] H. Lang and J. Linn. “Lagrangian field theory in space-time for geometrically exact Cosserat rods”. In: 150 (2009), p. 21.
- [124] J. Cisternas and P. Holmes. “Buckling of extensible thermoelastic rods”. In: *Mathematical and Computer Modelling* 36.3 (2002), pp. 233–243.
- [125] D. Moulton, T. Lessinnes, and A. Goriely. “Morphoelastic rods. Part I : A single growing elastic rod”. In: *Journal of the Mechanics and Physics of Solids* 61.2 (2013), pp. 398–427.
- [126] C. Lázaro, S. Monleón, J. Bessini, and J. Casanova. “A review on geometrically exact models for very flexible rods”. In: *Proceedings of the IASS Annual Symposium 2016* (2016), pp. 1–10.
- [127] Y. Shi, A. E. Borovik, and J. E. Hearst. “Elastic rod model incorporating shear and extension, generalized nonlinear Schrödinger equations, and novel closed-form solutions for supercoiled DNA”. In: *The Journal of Chemical Physics* 103.8 (1995), pp. 3166–3183.
- [128] B. Coleman, E. H. Dill, M. Lembo, L. Zheng, and I. Tobias. “On the dynamics of rods in the theory of Kirchhoff and Clebsch”. In: *Archive for Rational Mechanics and Analysis* 121.4 (1993), pp. 339–359.
- [129] R. Casati and F. Bertails-descoubes. “Super space clothoids”. In: *SIGGRAPH*. 2013.
- [130] A. Campanile, M. Mandarino, V. Piscopo, and A. Pranzitelli. “On the exact solution of non-uniform torsion for beams with asymmetric cross-section”. In: *World Academy of Science, Engineering and Technology* 31 (2009), pp. 36–45.
- [131] L. Prandtl. “Zur torsion von prismatischen stäben”. In: *Physikalische Zeitschrift* 4 (1903), pp. 758–770.
- [132] K. Koohestani. “Nonlinear force density method for the form-finding of minimal surface membrane structures”. In: *Communications in Nonlinear Science and Numerical Simulation* 19.6 (2014), pp. 2071–2087.
- [133] S. Timoshenko and J. N. Goodier. *Theory of elasticity*. Second. New York: McGraw-Hill, 1951, p. 506.

- [134] S. Timoshenko. “Theory of bending, torsion and buckling of thin-walled members of open cross section : Part II.” In: *Journal of The Franklin Institute* 249.4 (1945), pp. 249–268.
- [135] V. Z. Vlasov. *Thin-walled elastic beams*. Second. National Technical Information Service, 1961.
- [136] E. Elter. “Two formulii of the shear center”. In: *Periodica Polytechnica Mechanical Engineering* 28.2-3 (1984), pp. 179–193.
- [137] J. M. Alves. “Dynamic analysis of bridge girders subjected to moving loads : Numerical and analytical beam models considering warping effects”. PhD thesis. Tecnico Lisboa, 2014, p. 129.
- [138] A. Day. “An Introduction to dynamic relaxation”. In: *The Engineer* (1965).
- [139] J. Otter, A. Cassel, and R. Hobbs. “Dynamic Relaxation”. In: *Proceedings of the Institution of Civil Engineers* 35.4 (1966), pp. 633–656.
- [140] A. Cassel and R. Hobbs. “Numerical stability of dynamic relaxation analysis of non-linear structures”. In: *Numerical Methods in Engineering* October (1976), pp. 1407–1410.
- [141] M. Barnes. “Applications of dynamic relaxation to the topological design and analysis of cable, membrane and pneumatic structures”. In: *International Conference on Space Structures*. Guildford, 1975.
- [142] M. Papadrakakis. “A method for the automatic evaluation of the dynamic relaxation parameters”. In: (1981).
- [143] P. Underwood. “Dynamic relaxation”. In: *Computational methods for transient analysis*. 1983, p. 524.
- [144] M. Barnes. “Form finding and analysis of tension space structures by dynamic relaxation”. PhD thesis. City University London, 1977.
- [145] D. Wakefield. “Dynamic relaxation analysis of pretensioned networks supported by compression arches”. PhD thesis. City University London, 1980, p. 281.
- [146] J. Rodriguez, G. Rio, J. M. Cadou, and J. Troufflard. “Numerical study of dynamic relaxation with kinetic damping applied to inflatable fabric structures with extensions for 3D solid element and non-linear behavior”. In: *Thin-Walled Structures* 49.11 (2011), pp. 1468–1474.
- [147] H. K. Dang and M. A. Meguid. “Evaluating the performance of an explicit dynamic relaxation technique in analyzing non-linear geotechnical engineering problems”. In: *Computers and Geotechnics* 37.1-2 (2010), pp. 125–131.
- [148] D. M. L. da Silva, B. P. Jacob, and M. V. Rodrigues. “Implicit and explicit implementation of the dynamic relaxation method for the definition of initial equilibrium configurations of flexible lines”. In: *25st International Conference on Offshore Mechanics and Arctic Engineering, Hamburg, Germany September 2016* (2006), pp. 1–10.

Bibliography

- [149] M. Rezaiee-Pajand, S. R. Sarafrazi, and H. Rezaiee. “Efficiency of dynamic relaxation methods in nonlinear analysis of truss and frame structures”. In: *Computers and Structures* 112-113 (2012), pp. 295–310.
- [150] B. H. V. Topping and P. Ivanyi. *Computer Aided Design of Cable-membrane Structures*. 2007.
- [151] M. Miki, S. Adriaenssens, T. Igarashi, and K. Kawaguchi. “The geodesic dynamic relaxation method for problems of equilibrium with equality constraint conditions”. In: *International Journal for Numerical Methods in Engineering* 99.9 (2014), pp. 682–710.
- [152] G. Noh and K.-j. Bathe. “An explicit time integration scheme for the analysis of wave propagations”. In: *Computers and Structures* 129 (2013), pp. 178–193.
- [153] Y. Duan, D. Li, and P. F. Pai. “Geometrically exact physics-based modeling and computer animation of highly flexible 1D mechanical systems”. In: *Graphical Models* 75.2 (2013), pp. 56–68.
- [154] B. Fierz. “Stabilizing explicit dynamic finite element simulations”. PhD thesis. 2013.
- [155] E. Hairer and G. Wanner. *Geometric numerical integration algorithms for ordinary differential equations*. Springer Verlag, 2006, p. 644.
- [156] P. Cundall. “Explicit-finite difference methods in geomechanics.” In: *Numerical Methods in Geomechanics*. Blacksburg, Virginia, United States, 1976, pp. 132–150.
- [157] W. Lewis. *Tension structures: form and behaviour*. Telford, Thomas, 2003, p. 201.
- [158] R. Borghi. “Simple pendulum dynamics: revisiting the Fourier-based approach to the solution”. In: (2013), pp. 1–16. arXiv: [1303.5023](https://arxiv.org/abs/1303.5023).
- [159] A. Beléndez, C. Pascual, D. Méndez, T. Beléndez, and C. Neipp. “Exact solution for the nonlinear pendulum”. In: *Revista Brasileira de Ensino de Física* 29.4 (2007), pp. 645–648.
- [160] R. Clune, J. J. Connor, J. Ochsendorf, and D. Kelliher. “An object-oriented architecture for extensible structural design software”. In: *Computers and Structures* 100-101 (2012), pp. 1–17.
- [161] J. Bishop. *C# 3.0 Design Patterns*. 2008.
- [162] B. Watson. *Writing High-Performance .NET Code*. 2014.
- [163] L. N. Trefethen. “Computing numerically with functions instead of numbers”. In: *Mathematics in Computer Science* 1.1 (2007), pp. 9–19.
- [164] S. Chevillard, M. Jolde\cs, and C. Lauter. “Sollya: An Environment for the Development of Numerical Codes”. In: *Mathematical Software - ICMS 2010*. Ed. by K.~Fukuda, J.~van~der~Hoeven, M.~Joswig, and N.~Takayama. Vol. 6327. Lecture Notes in Computer Science. Heidelberg, Germany: Springer, 2010, pp. 28–31.
- [165] R. Green. “Faster Math Functions”. In: *Proc. of Game Developers Conference* (2003).
- [166] B. H. V. Topping and A. I. Khan. “Article information : PARALLEL COMPUTATION SCHEMES FOR”. In: *Engineering Computations* 11.6 (1994), pp. 513–548.

- [167] V. Rek and I. Němec. “Parallel Computing Procedure for Dynamic Relaxation Method on GPU Using NVIDIA’s CUDA”. In: *Applied Mechanics and Materials* 821.1 (2016), pp. 331–337.
- [168] A. Liew, T. VanMele, and P. Block. “Vectorised graphics processing unit accelerated dynamic relaxation for bar and beam elements”. In: *Structures* 8 (2016), pp. 111–120.
- [169] T. Moulard, B. Chrétien, and E. Yoshida. “Software Tools for Nonlinear Optimization”. In: *Journal of the Robotics Society of Japan* 32.6 (2014), pp. 536–541.
- [170] R. Abraham, J. E. Marsden, and T. Ratiu. *Manifolds, Tensor Analysis, and Applications (Ralph Abraham, Jerrold E. Marsden and Tudor Ratiu)*. 2002, p. 617.